

# **Manufacturing and characterization of open-cell metal foams with high strut porosity**

## **Dissertation**

zur Erlangung des akademischen Grades

## **Doktoringenieurin (Dr.-Ing.)**

von M. Sc. Alina Sutygina

geb. am 6. August 1993 im Tomsk (Russland)

genehmigt durch die Fakultät für Maschinenbau  
der Otto-von-Guericke-Universität Magdeburg

Gutachter:

Prof. Dr. rer. nat. Michael Scheffler

Prof. Dr.-Ing. habil. Christos Aneziris

Prof. Dr. rer. nat. Franziska Scheffler

Promotionskolloquium am 28.03.2022

## Abstract

Aluminum and copper foams were manufactured by the sponge replication technique and a combination of the sponge replication technique with two additional freezing steps, freezing and freeze-drying, in order to generate additional lamellar strut pores. The effect of the starting powder particle characteristics, the thermal processing parameters, the polymeric template foam cell size, and the additional strut porosity on the macrostructure, the porosity, the mechanical properties, the thermal conductivity, and the specific surface area was studied.

Foams prepared with the additional freeze processing steps possess additional pores with a lamellar shape in the struts, and they showed a higher strut porosity and a higher specific surface area. The lamellar pores in the foam struts had a thickness between 24  $\mu\text{m}$  and 56  $\mu\text{m}$  and a random orientation, which had a significant influence on the compressive strength, the absorbed energy during compression testing, and the thermal conductivity of the metal foams.

Since those foams are potential supports for microporous materials due to their unique heat transport and fluid dynamic properties, the zeolite SAPO-34 was crystallized directly on aluminum foams and the MOF material HKUST-1 was crystallized directly on copper foams. These microporous components were found on the outer surface of the foam struts, in the hollow cavities of the foam struts, and in the lamellar pores generated by additional freezing steps.

## Kurzfassung

Aluminium- und Kupferschäume wurden durch das Replika-Verfahren und mittels Kombination des Replika-Verfahrens mit Gefrieren und Gefriertrocknung, hergestellt, um zusätzliche lamellare Stegporen zu erzeugen. Untersucht wurden die Auswirkungen der Eigenschaften der Ausgangspulverpartikel, der thermischen Verarbeitungsparameter, der Zellgröße der Polymerschäumtemplate und der zusätzlichen Stegporosität auf die Makrostruktur, die Porosität, die mechanischen Eigenschaften, die Wärmeleitfähigkeit und die spezifische Oberfläche.

Schäume, die mit den zusätzlichen Gefrierbehandlungsschritten hergestellt wurden, wiesen zusätzliche Poren mit einer lamellaren Struktur in den Stegen auf, und sie zeigten eine höhere Stegporosität und eine höhere spezifische Oberfläche. Die lamellaren Poren in den Stegen hatten eine Dicke zwischen 24  $\mu\text{m}$  und 56  $\mu\text{m}$  und eine zufällige Orientierung, was einen signifikanten Einfluss auf die Druckfestigkeit, die absorbierte Energie während des Drucktests und die Wärmeleitfähigkeit der Metallschäume hatte.

Da diese Schäume aufgrund ihrer einzigartigen Wärmetransport- und Fluidynamikeigenschaften potenzielle Träger für mikroporöse Materialien sind, wurde der Zeolith SAPO-34 direkt auf Aluminiumschäumen und das MOF-Material HKUST-1 direkt auf Kupferschäumen kristallisiert. Diese mikroporösen Komponenten befanden sich auf der äußeren Oberfläche der Stege, in den Hohlsteinen der Schäume und in den zusätzlichen lamellaren Poren.

# Table of Contents

<b>Abstract</b> .....	<b>II</b>
<b>Kurzfassung</b> .....	<b>III</b>
<b>List of figures</b> .....	<b>VII</b>
<b>List of tables</b> .....	<b>XI</b>
<b>List of abbreviations</b> .....	<b>XII</b>
<b>1 Introduction</b> .....	<b>1</b>
<b>2 Theoretical part</b> .....	<b>3</b>
2.1 Types of metal foams and their structure .....	3
2.2 Mechanical properties of open-cell metal foams.....	4
2.3 Manufacturing techniques of open-cell metal foams .....	6
2.3.1 Open-cell metal foams prepared by the sponge replication technique .....	9
2.4 Freeze-drying as a method to manufacture porous materials .....	11
2.4.1 Basic principles: anisotropic and isotropic freezing .....	12
2.4.2 Influence of freezing parameters, solid loading, solvents and additives on the microstructure of freeze-dried porous materials .....	14
2.4.3 Application of freeze-casted ceramic and metal porous materials .....	18
2.4.4 Freeze-drying of metals .....	20
2.5 Manufacturing of open-cell foams via sponge replication technique and freeze- drying.....	22
2.6 Micro-macroporous composite materials based on open-cell foams .....	25
2.6.1 SAPO-34: Hydrothermal synthesis, properties, and application .....	26
2.6.2 HKUST-1: Properties, crystallization on open-cell foams, and applications ....	28
<b>3 Materials</b> .....	<b>31</b>
3.1 Specimen preparation of metal foams .....	31
3.1.1 Starting aluminum and copper powders .....	31
3.1.2 Specimen preparation of aluminum and copper foams by the sponge replication technique .....	32
3.1.3 Specimen preparation of aluminum and copper foams by a combination of sponge replication and freezing techniques .....	33
3.2 Direct crystallization of zeolites and MOFs onto the surface of aluminum and copper foams .....	34
3.2.1 Direct crystallization of SAPO-34 onto the surface of aluminum foams .....	34
3.2.2 Direct crystallization of HKUST-1 onto the surface of copper foams .....	35
<b>4 Characterization</b> .....	<b>37</b>
4.1 Thermal analysis.....	37

4.1.1	Differential scanning calorimetry and thermogravimetric analysis.....	37
4.1.2	Thermal conductivity .....	37
4.2	Micro- and macrostructure characterization.....	39
4.2.1	X-ray diffraction analysis .....	39
4.2.2	Scanning electron microscopy .....	39
4.2.3	Microcomputer tomography .....	41
4.2.4	Determination of the foam porosity .....	43
4.3	Mechanical properties .....	45
4.4	Analysis of the microporous-component HKUST-I and SAPO-34 and water adsorption capacity .....	47
4.5	Determination of the specific surface area by the BET-method of foam composites .....	47
<b>5</b>	<b>Results and discussion.....</b>	<b>49</b>
5.1	Aluminum foams manufactured by the sponge replication technique and investigation of their properties.....	49
5.1.1	As-received aluminum powders .....	49
5.1.2	Aluminum foams prepared from different starting powders .....	51
5.1.3	Chapter summary .....	54
5.1.4	Aluminum foams thermally processed in different atmospheres .....	55
5.1.5	Aluminum foams manufactured by the sponge replication technique at different temperatures in Ar atmosphere .....	60
5.1.6	Aluminum foams manufactured by the sponge replication technique with different total porosity .....	66
5.1.7	Chapter summary .....	68
5.2	Aluminum foams manufactured by a combination of sponge replication and freezing techniques .....	69
5.2.1	Aluminum foams manufactured by a combination of sponge replication and freezing techniques at different temperatures and solid loading .....	70
5.2.2	Aluminum foams manufactured by a combination of sponge replication and freezing techniques with different cell size .....	71
5.2.3	Aluminum foams: sponge replication vs. combination of sponge replication and freezing techniques .....	77
5.2.4	Chapter summary .....	81
5.3	Copper foams manufactured by the sponge replication technique and a combination of sponge replication and freezing techniques .....	82
5.3.1	As-received copper powder .....	83
5.3.2	Copper foams manufactured by the sponge replication technique at different temperatures.....	84

5.3.3	Copper foams manufactured by the sponge replication technique with different cell size .....	87
5.3.4	Copper foams manufactured by a combination of sponge replication and freezing techniques with different cell size .....	92
5.3.5	Chapter summary .....	98
5.4	Direct crystallization of active coatings onto the surface of aluminum and copper foams .....	99
5.4.1	Direct crystallization of SAPO-34 onto the surface of aluminum foams .....	100
5.4.2	Direct crystallization of HKUST-1 onto the surface of copper foams .....	106
5.4.3	Chapter summary .....	110
<b>6</b>	<b>Summary and outlook.....</b>	<b>112</b>
	<b>References .....</b>	<b>115</b>
	<b>A Appendix .....</b>	<b>130</b>
	<b>Declaration of Honour .....</b>	<b>132</b>
	<b>Curriculum Vitae .....</b>	<b>133</b>
	<b>List of publications .....</b>	<b>134</b>

## List of figures

Figure 1 Metal foams with open cells (a) (adapted from [13]) and closed cells (b) [14].	3
Figure 2 Schematic representation of a compressive stress-strain curve for a metal open-cell foam indicating the linear elastic behavior, the stress plateau and the densification regimes (a); deformation of an elastic-plastic cellular structure (b, c) and an elastic-brittle cellular structure (d).	5
Figure 3 Schematic illustration of the production of open-cell metal foams by investment casting (adapted from [36]).	6
Figure 4 Schematic illustration of the fabrication of open-cell metal foams by space holder casting (adapted from [36]).	7
Figure 5 Schematic illustration of manufacturing of open-cell metal foams by the sponge replication technique (adapted from [36]).	8
Figure 6 SEM image of a typical strut and cross-section of metal foams prepared by the sponge replication technique (here: aluminum foams).	10
Figure 7 Tomographic imaging of the strut before loading, showing the sutured area of the strut (black arrow) (a); strut after loading at 4 % deformation strain, showing unzipping along the struts (white arrow) (b); development of cracks around the pore: unloaded strut (black arrow) (c) and crack development around the pore after loading at 1.4 % strain (unzipping (*) is marked) (d) [45].	11
Figure 8 An anisotropic freeze casting process consisting of placing a suspension in a thermally insulated mould (a), freezing the suspension (b), accumulation and pushing the particles out of the liquid into the interdendritic space (c) and their incorporation (d), sublimation of frozen samples (e), and densification of the sample via sintering (f) [50].	13
Figure 9 An isotropic freeze casting process consisting of placing a suspension in a thermally insulated mould (a), solid nucleation in suspension (b), random solidification (c), sublimation of frozen samples (d) and densification via sintering (e) [50].	13
Figure 10 Schematic representation of pores in sublimated materials during anisotropic (top) and isotropic freezing (bottom). The colored areas indicate the region with solidified liquid, which determines the morphology of the pores after sublimation. The dark areas are the solid material particles [50].	14
Figure 11 Wavelength variation of the material structure as a function of the ice front velocity. The SEM image of the cross-section of the sample parallel to the ice front with the smallest lamellae thickness of $\sim 2 \mu\text{m}$ is shown in inset (a) [53].	15
Figure 12 Microstructure of unidirectionally aligned pore channels in YSZ ceramics at different distances from the cooled plate from 15 mm to 3 mm and at freezing temperatures varied from $-30 \text{ }^\circ\text{C}$ to $-196 \text{ }^\circ\text{C}$ [56].	15
Figure 13 SEM micrograph of a cross-section parallel to the ice front showing the effect of the suspension water content on the microstructure; total porosity of the samples: (a) 70 %, (b) 40 %, (c) 24 % [53].	16
Figure 14 Zeolite framework structure for zeolite A, formed by joining sodalite cages (yellow) through four-membered and six-membered rings. The diameter of the pore opening (orange) is 0.41 nm (the cations in the pores are not specified in the frame structure) [6].	25
Figure 15 A MOF example HKUST-1: the porous structure consists of $[\text{Cu}\cdots\text{Cu}]^{4+}$ dumbbells that are connected by trimesate anions (pore diameter 1.0 nm, yellow spheres) [6].	26
Figure 16 Schematic illustration of RP foams preparation.	32
Figure 17 Schematic illustration of RP/FP foam preparation.	33
Figure 18 Schematic illustration of a PTFE-lined stainless steel autoclave with a Teflon distance holder after crystallization of SAPO-34 on the surface of aluminum foam (a); RP/FP aluminum foam with SAPO-34 after calcination for 15 h without (b) and on (c) Teflon distance holder; RP/FP aluminum foam with SAPO-34 and collected SAPO-34 powder after calcination (d).	35
Figure 19 Schematic illustration of the thermal conductivity measurement.	38

Figure 20. Example of a 2D image reconstruction after thresholding (a,b) and after filling and despeckle (c,d) of a foam manufactured by the sponge replication technique (a,c) and of a foam manufactured by the combination of sponge replication and freezing techniques (b,d). Schematic illustration of wall strut thickness ( $D_{ws}$ ), thickness of material lamellae ( $D_{ml}$ ), lamellar pore thickness ( $D_{lp}$ ), and strut thickness ( $D_s$ ) measurements (adapted from [13])..	42
Figure 21 Compressive stress-strain curves of copper foams manufactured by the sponge replication technique, where $\sigma$ is the compressive yield strength and $\varepsilon_D$ is the densification strain.....	46
Figure 22 SEM images of the Aldrich (a) and Ecka (b) powders; XRD diffractograms of as-received Aldrich powder (red curves) and Ecka powder (green curves) (c) (adapted from [157]).....	50
Figure 23 TG (green) and DSC (red) curves of as received Aldrich (straight line) and Ecka (dash dot line) powders in air; the heating rate was 10 K min <sup>-1</sup> (adapted from [157]).....	51
Figure 24 SEM images of selectively broken struts and cross sections of the foams made from the Aldrich powder (a, b) and from the Ecka powder (c, d) after thermal processing at 750 °C for 3h in vacuum; PU template foams with a cell size of 20 ppi (adapted from [157]).....	52
Figure 25 X-ray diffraction analysis (a) and an example of the compressive strength curve (b,c) of the foams prepared from the Aldrich powder and from the Ecka powder after thermal processing at 750 °C for 3h in vacuum; PU template foams with a cell size of 20 ppi (adapted from [157]).....	53
Figure 26 Aluminum foams after thermal processing for 3h at 750 °C in air, vacuum and Ar atmosphere; PU template foams with a cell size of 20 ppi (adapted from [158]).....	56
Figure 27 SEM images of aluminum RP foams thermally processed for 3h at 750 °C in air (a,d), in vacuum (b,e), and in Ar (c,f); PU template foams with a cell size of 20 ppi.....	56
Figure 28 X-ray diffraction patterns of as received aluminum powder and RP aluminum foams after thermal processing in air, vacuum and Ar at 750 °C for 3 h.....	57
Figure 29 RP aluminum foams after compressive strength test (top) and stress-strain curves (bottom) typical for foams thermally processed in air, vacuum, and Ar at 750 °C for 3 h; PU template foams with a cell size of 20 ppi (adapted from [158]).....	59
Figure 30 Aluminum foams before PU burn-out and after thermal processing for 3 h in Ar at 600 °C to 750 °C; PU template foams with a cell size of 20 ppi. ....	60
Figure 31 SEM images of aluminum RP foams thermally processed for 3 h in Ar at 600 °C (a,b), 650 °C in (c,d), 750 °C (e,f), 800 °C (g,h), and 850 °C (j,k); PU template foams with a cell size of 20 ppi (adapted from [158]).....	62
Figure 32 X-ray diffraction patterns of as received aluminum powder and RP aluminum foams after thermal processing for 3 h in Ar at 600 °C to 900 °C (adapted from [158]). ....	63
Figure 33 Compressive stress-strain curves of the RP aluminum foams after processing at 600 °C (a), 650 °C (b), and 750 °C (c) for 3 h in Ar for PU template foams with a cell size of 20 ppi..	65
Figure 34 $\mu$ -CT reconstruction image of the RP aluminum foams with $P_{total} \approx 90.5\%$ (a); distributions of the wall strut thickness and the strut thickness (b) and the cell size (c) of the RP aluminum foams with $P_{total} \approx 90.5\%$ (red) and $P_{total} \approx 86.6\%$ (green), both thermally processed at 650 °C for 3h; specific surface area after thresholding (green) and after filling and despeckle (gray) (d); PU template foams with a cell size of 20 ppi.....	68
Figure 35 RP/FP aluminum foams before binder and PU burn-out and after thermal processing for 3 h in Ar at 650 °C and 750 °C; PU template foams with a cell size of 20 ppi. ....	70
Figure 36 RP foam and RP/FP foam with 70 vol. % of water and RP/FP foam with 80 vol. % of water after thermal processing for 3 h in Ar at 650 °C; PU template foams with a cell size of 20 ppi. ....	71
Figure 37 SEM images of the surface of RP/FP aluminum foams (a) and their cross sections after thermal processing for 3h in Ar at 650 °C (b–d).....	72
Figure 38 $\mu$ -CT reconstruction images of the RP/FP aluminum foams after thermal processing at 650 °C in Ar for 3 h as a function of the PU template foam cell size: 10 ppi (a–c), 20 ppi (d–f), and 30 ppi (g–j). ....	74
Figure 39 Distributions of the cell size (a), strut thickness (b), material lamellae thickness (c), and lamellar pore thickness (d) of the RP/FP aluminum foams thermally processed at 650 °C for 3h in Ar; the PU template foam cell size was 10 ppi, 20 ppi, and 30 ppi (adapted from [159]). ....	75

Figure 40	Specific surface area of the RP/FP aluminum foams thermally processed at 650 °C for 3h in Ar depending on the cell size of the PU template foam (10 ppi, 20 ppi, and 30 ppi); measured using $\mu$ -CT (adapted from [159]).	76
Figure 41	Compressive stress-strain curves of RP/FP aluminum foams after thermal processing at 650 °C for 3 h in Ar; PU template foams cell sizes were 10 ppi, 20 ppi, and 30 ppi.	77
Figure 42	Distributions of the cell size (a) and the strut thickness (b) of the RP (red) and RP/FP (green) aluminum foams; specific surface area of the RP and RP/FP aluminum foams after thresholding (green) and filling and despeckle (gray) (c) measured using $\mu$ -CT; PU template foams with a cell size of 20 ppi (adapted from [159]).	79
Figure 43	Relationship between the relative compressive strength and the relative density of RP (red dots) and RP/FP (green dots) aluminum foams thermally processed at 650 °C for 3 h in an Ar atmosphere; the Gibson-Ashby models were obtained by fitting experimental results with $C$ and $n$ variables (red line for RP foams and green line for RP/FP foams); and Gibson-Ashby model with $C = 0.3$ , $n = 1.5$ (black dash line); PU template foams with a cell size of 20 ppi (adapted from [159]).	81
Figure 44	As-received copper powder: XRD phase analyse (a), TG and DSC curves in air (b) and SEM image of the powder (c); the heating rate was 10 K min <sup>-1</sup> (adapted from [13]).	84
Figure 45	X-ray diffraction patterns of the RP copper foams after PU burn-out in air (a); photographs of the RP copper foams before and after binder and PU burn-out and after thermal processing at 900 °C for 6 h in Ar/H <sub>2</sub> atmosphere (b); PU template foams with a cell size of 20 ppi (adapted from [13]).	85
Figure 46	SEM images of RP copper foams: before (a,f) and after (b,g) binder and PU burn-out; after processing at 500 °C (c,h) and 900 °C (d,i) for 6 h in Ar/H <sub>2</sub> (adapted from [13]).	86
Figure 47	Compressive stress-strain curves of the RP copper foams after processing at 500 °C (green) and 900 °C (black) for 6 h in Ar/H <sub>2</sub> ( $\sigma$ – compressive yield strength, $\epsilon_D$ – densification strain); PU template foams with a cell size of 20 ppi (adapted from [13]).	87
Figure 48	3D reconstructed images of the RP copper foams after thermal processing at 900 °C for 6 h in Ar/H <sub>2</sub> atmosphere for different cell sizes of the PU template foams: 10 ppi (a,d), 20 ppi (b,e), and 30 ppi (c,f).	89
Figure 49	Distributions of the cell size (a), wall strut thickness (b), and strut thickness (c) of the RP copper foams thermally processed at 900 °C for 6 h in Ar/H <sub>2</sub> atmosphere for different PU template foam sizes (10 ppi, 20 ppi, and 30 ppi); data obtained from $\mu$ -CT measurements.	90
Figure 50	Relationship between the relative compressive strength and the relative density of the RP copper foams thermally processed at 900 °C for 6 h in Ar/H <sub>2</sub> atmosphere for different cell sizes of the PU template foams (10 ppi, 20 ppi, and 30 ppi); Gibson-Ashby models obtained by fitting experimental results with $C = 0.3$ and variable $n$ ; and Gibson-Ashby model with $C = 0.3$ , $n = 1.5$ (black dash line).	92
Figure 51	SEM images of the cross section of RP/FP copper foams for 20 ppi templated foams (a–c) and their surfaces (d–f) after thermal processing for 6h in Ar/H <sub>2</sub> at 900 °C (adapted from [13]).	93
Figure 52	$\mu$ -CT reconstruction images of the RP/FP copper foams after thermal processing at 900 °C for 6 h in Ar/H <sub>2</sub> atmosphere; different cell sizes of the PU template foams: 10 ppi (a,d), 20 ppi (b,e), and 30 ppi (c,f).	95
Figure 53	Distributions of the cell size (a), the strut thickness (b), the material lamellae (c), and lamellar pores (d) of the RP/FP copper foams thermally processed at 900 °C for 6 h in Ar/H <sub>2</sub> atmosphere for foams templated with different cell sizes of the PU foams (10 ppi, 20 ppi, and 30 ppi); measurements were carried out with $\mu$ -CT (adapted from [160]).	96
Figure 54	Specific surface area of the RP/FP copper foams thermally processed at 900 °C for 6 h in Ar/H <sub>2</sub> atmosphere for different template cell sizes of the PU foams (10 ppi, 20 ppi, and 30 ppi); data obtained from $\mu$ -CT analysis.	97
Figure 55	Relationship between the relative compressive strength and the relative density of the RP/FP copper foams thermally processed at 900 °C for 6 h in Ar/H <sub>2</sub> atmosphere; foams from different cell size of the PU template foams (10 ppi, 20 ppi, and 30 ppi); Gibson-Ashby models obtained by fitting experimental results with $C = 0.3$ and variable $n$ ; and Gibson-Ashby model with $C = 0.3$ , $n = 1.5$ (black dash line).	98

Figure 56 SEM images of the RP/FP aluminum foams after crystallization of SAPO-34 for 5 h (a–d), 15 h (e–h), and 24 h (i–l). .....	101
Figure 57 X-ray diffraction patterns of SAPO-34 calculated patterns (black), after crystallization for 5 h (green), 15 h (red), and 24 h (grey). .....	102
Figure 58 SEM cross section images of the RP (top) and RP/FP (bottom) aluminum foams after crystallization of SAPO-34 for 5 h (a,d), 15 h (b,e), and 24 h (c,f); PU template foams with a cell size of 20 ppi. ....	103
Figure 59 Dependence of the SAPO-34 loading on crystallization time (a), and water uptake of the SAPO-34 aluminum composite foams as a function of SAPO-34 loading (b) for the RP (black) and RP/FP foams (green); PU template foams with a cell size of 20 ppi. ....	104
Figure 60 SEM images of aluminum foams with SAPO-34 crystallized for 5 h (a) and for 24 h (b) after water adsorption for three cycles (a) and one cycle (b); PU template foams with a cell size of 20 ppi. The cycle time for the water adsorption was 24 h. ....	105
Figure 61 SEM images of the surface of RP/FP copper foams after crystallization of HKUST-1 for 6 h (a–c), 14 h (d–f), 24 h (g–h), and 96 h (j–l); HKUST-1 powder after crystallization for 24 h (i). ....	107
Figure 62 X-ray diffraction patterns of HKUST-1: calculated patterns (black); after crystallization for 6 h (red), 24 h (green), and 96 h (grey). ....	108
Figure 63 SEM cross-section images of RP/FP copper foam after crystallization of HKUST-1 for 96 h. ....	108
Figure 64 Dependence of HKUST-1 loading on crystallization time (a) and the water uptake of the HKUST-1 copper composite foams as a function of the HKUST-1 loading (b) for the RP (black rectangles) and RP/FP (green rectangles) foams; RP/FP copper foam with HKUST-1 after crystallization for 14 h (c); PU template foams with a cell size of 20 ppi. ....	109
Figure 65 SEM images of the surface of the RP copper foams after crystallization of HKUST-1 for 96 h and water adsorption for 7 days and long-term storage. ....	110
Figure A 1 SEM images of the strut surface of RP aluminum foams thermally processed for 3 h at 750 °C in air (a), vacuum (b), and Ar (c) (adapted from [158]). ....	130
Figure A 2 Aluminum foams after thermal processing for 3 h in Ar at 750–900 °C [158]. ....	130
Figure A 3 SEM images of RP aluminum foams strut surface thermally processed for 3h in Ar at 650 °C (a), 750 °C (b), 800 °C (c), and 850 °C (d) (adapted from [158]). ....	130

## List of tables

Table 1 Influence of freezing direction, freezing front velocity, temperature, solid loading, solvents and additives on the microstructure of freeze-dried porous materials. ....	18
Table 2 Slurry content and thermal processing conditions of RP foams.....	32
Table 3 Slurry content and thermal processing conditions of RP/FP foams. ....	34
Table 4 Porosity and compressive yield strength of the aluminum foams prepared from Aldrich powder and from Ecka powder; PU template foams with a cell size of 20 ppi. ....	54
Table 5 Oxide concertation, volumetric shrinkage, porosity, compressive yield strength and thermal conductivity of RP aluminum foams thermally processed in air, vacuum and Ar atmospheres at 750 °C for 3 h; PU template foams with a cell size of 20 ppi.....	58
Table 6 Volumetric shrinkage, porosity, compressive yield strength, and thermal conductivity of Al foams thermally processed for 3 h in Ar at 600 °C, 650 °C, and 750 °C; PU template foams with a cell size of 20 ppi. ....	61
Table 7 Phase composition of the as-received powder and the aluminum foams thermally processed for 3 h in Ar at 600–900 °C. ....	63
Table 8 Porosity, geometrical characteristics, mechanical and thermal properties of RP aluminum foams thermally processed for 3 h at 650 °C in Ar with total porosity 90.5 % and 86.6 % for PU template foams with a cell size of 20 ppi.....	67
Table 9 Geometrical, mechanical and thermal properties of RP/FP aluminum foams thermally processed for 3 h at 650 °C in Ar for PU template foams with a cell size of 10 ppi, 20 ppi, and 30 ppi.....	73
Table 10 Geometrical, mechanical and thermal properties of RP and RP/FP aluminum foams thermally processed for 3 h at 650 °C in Ar, templated with PU foams with a cell size of 20 ppi.....	78
Table 11 Volumetric shrinkage, porosity and mechanical properties of the RP copper foams thermally processed for 6 h at 500 °C and 900 °C in Ar/H <sub>2</sub> ; PU template foams with a cell size of 20 ppi. ....	86
Table 12 Geometrical, mechanical and thermal properties of the RP copper foams thermally processed for 6 h at 900 °C in Ar/H <sub>2</sub> for PU template foams with a cell size of 10 ppi, 20 ppi, and 30 ppi. ....	88
Table 13 Geometrical, mechanical, and thermal properties of RR/FP copper foams thermally processed for 6 h at 900 °C in Ar/H <sub>2</sub> atmosphere; templated with different cell sizes of the PU foams (10 ppi, 20 ppi, and 30 ppi).....	94
Table 14 Properties of selected RP and RP/FP aluminum foams after crystallization for 5 and 24 h; PU template foams with a cell size of 20 ppi.....	105
Table 15 Water uptake of RP/FP aluminum foam after crystallization for 5 h with a SAPO-34 loading of ~27.3 wt. % after three water adsorption/desorption cycles; PU template foams with a cell size of 20 ppi.....	106
Table A 1 Oxide concertation, volumetric shrinkage, porosity, compressive yield strength, and thermal conductivity of Al foams thermally processed for 3 h in Ar at 750–850 °C; PU template foams with a cell size of 20 ppi and a geometric size of 20 mm × 20 mm × 20 mm.....	131

## List of abbreviations

Al	Aluminum
BET	Brunauer-Emmett-Teller
BTC	Benzenetricarboxylate
Cu	Copper
DSC	Differential scanning calorimetry
EDX	Energy dispersive X-ray spectroscopy
LMC	Liquid metal cooling
$\mu$ -CT	Microcomputer tomography
MOFs	Metal-organic frameworks
PAM	Polyacrylamide
PEG	Polyethylene glycol
Ppi	Pores per linear inch
PTFE	Polytetrafluoroethylene
PU	Polyurethane
PVA	Polyvinyl alcohol
PVF	Polyvinylfluoride
TBA	Tert-butyl alcohol
TG	Thermogravimetric
RP	Replication processed
RP/FP	Replication processed and freeze-dried processed
SEM	Scanning electron microscope
XRD	X-ray diffraction
YSZ	Yttria-stabilized zirconia

## List of symbols

$E$	Strain	[-]
$\varepsilon_D$	Densification strain	[-]
$P$	Density	[g cm <sup>-3</sup> ]
$\rho^*$	Density of foams	[g cm <sup>-3</sup> ]
$\rho_{rel}$	Relative density	[-]
$\rho_{water}$	Density of water	[g cm <sup>-3</sup> ]
$\Sigma$	Compressive yield strength	[MPa]
$\sigma_{pl}^*$	Plastic collapse strength	[MPa]
$\sigma_b^*$	Yield strength of bulk material	[MPa]
$\lambda_b$	Thermal conductivity of bulk material	[W·m <sup>-1</sup> K <sup>-1</sup> ]
$\lambda_g$	Thermal conductivity of gas phase	[W·m <sup>-1</sup> K <sup>-1</sup> ]
$\lambda_f$	Thermal conductivity of foam	[W·m <sup>-1</sup> K <sup>-1</sup> ]
$\lambda_s$	Thermal conductivity of porous strut material	[W·m <sup>-1</sup> K <sup>-1</sup> ]
$C$	Constant related to pore geometry effect	[-]
$D_{lp}$	Lamellar pore thickness	[μm]
$D_{ml}$	Material lamellae thickness	[μm]
$D_s$	Strut thickness	[mm]
$D_{ws}$	Wall strut thickness	[mm]
$d_{50}$	Median diameter of particle size distribution	[μm]
$m_{dry}$	Weight of sample in air	[g]
$m_{sub}$	Weight of submerged sample	[g]
$m_{wet}$	Weight of soaked sample	[g]
$m_{foam}$	Weight of the initial foam after thermal processing	[g]
$m_{foam+material}$	Weight of the foam after crystallization	[g]
$m_{after\ water\ adsorption}$	Weight of foams with crystallized material after water adsorption	[g]
$N$	Density exponent	[-]
$Obj.S/Obj.V.$	Surface-area-to-volume ratio	[cm <sup>-1</sup> ]
$P_{cell}$	Cell porosity	[%]
$P_{closed}$	Closed porosity of foam	[%]
$P_{open}$	Open porosity of foam	[%]

$P_s$	Strut porosity	[%]
$P_{total}$	Total porosity	[%]
$S_{BET}$	BET surface area	[m <sup>2</sup> ·g <sup>-1</sup> ]
$T_m$	Melting temperature	[°C]
$V_{foam}$	Total foam volume	[cm <sup>3</sup> ]
$V_{hollow\ strut\ pores}$	Volume of hollow struts pores or cavities	[cm <sup>3</sup> ]
$V_{material}$	Volume of material without any pores	[cm <sup>3</sup> ]
$V_{material\ pores}$	Volume of open and closed materials pores	[cm <sup>3</sup> ]
$V_{pores}$	Total pore volume	[cm <sup>3</sup> ]
$W$	Energy absorption	[MJ·m <sup>-3</sup> ]

# 1 Introduction

Highly porous metallic and ceramic foams possess a combination of properties such as high stiffness-to-weight ratio, high energy and sound absorption capability, and a low specific gravity [1–3]. The combination of these properties made porous materials candidates for widespread applications in industry. Closed-cell metallic foams, for example, are mainly used in aerospace industry for noise reduction, in architecture as lightweight structures and heat/sound insulation materials, in automotive industry in engine brackets or gear wheels with anti-vibration layer out of aluminum foams [4,5]. Open-cell metal foams, due to a combination of properties such as high thermal/electrical conductivity with a high specific surface area and permeability to liquids and gases, have found applications in filters, heat exchangers, heat pumps, and substrates in catalysis, where foams often are coated with active materials [4–6]. For these kind of applications, the efficiency of a metal foam-based system depends strongly on parameters such as cell size and specific surface area, which influence the active-material loading, the thermal and mechanical properties.

Open-cell metal foams can be manufactured by the sponge replication method, also called the Schwartzwalder process [1,7–9]. Those foams are characterized by their open-cellular structure, a high total porosity, high gas and liquid permeability, and they possess comparatively high stability and strength. The foams also have a high specific surface area, which can be varied by the pore size of the polymeric foam templates from which they are made. A distinctive feature of sponge replicated foams compared to other preparation methods is the hollow strut structure formed after template burn-out. This increases the specific surface area but brings challenges for the coating processes of the hollow struts with active materials.

A potential solution for foam processing to access the inner surface of their struts and to increase the specific surface area by creating additional strut porosity is the combination of the sponge replication technique with the freeze-drying process; as shown in [10,11]. Freeze-drying or freeze-casting is a method for manufacturing porous structures with a high specific surface area [12]. This method is based on the formation of pores in materials by freezing a suspension consisting of solids and solvent or dispersant. Sublimation is applied to remove the frozen solvent or dispersant leaving behind pores after solidification.

The aim of this work is to develop manufacturing routes for porous open-cell aluminum and copper foams by the sponge replication technique and a combination of the sponge replication

technique with freezing techniques to generate a higher porosity, preferably in the strut material of the open-cellular reticulated metal foams. For this purpose, sponge replicated foams were prepared and the most relevant processing parameters were identified to obtain stable foams. In a second step, the sponge replication technique was combined with the freezing technique to generate pores on the foam struts. After identification of the most relevant process parameters of the combination of these two different pore-forming processes, the resulting metal foams were coated with microporous metal-organic framework compounds or with zeolites by a direct-crystallization process. All materials were investigated by means of solid state characterization.

## 2 Theoretical part

This chapter describes the macrostructure and manufacturing processes of open-cell foams, focusing on the replication technique as well as the freezing method to obtain highly porous materials. The influence of the pore size of the initial polyurethane (PU) template, additives, powder loading, freezing temperature, and freezing rate on the porosity, pore direction, and mechanical properties of the foams are discussed. An overview of relevant works related to the manufacturing of sponge replicated foams and the freeze-dried foams, as well as ceramic foams obtained by a combination of these methods, is presented. The second part of the chapter describes the possibilities of using highly porous metallic foams as a support for microporous, sorption-active materials such as metal-organic frameworks (MOFs) and zeolites. The structures and properties of the active microporous materials SAPO-34 and HKUST-1 are reviewed.

### 2.1 Types of metal foams and their structure

Metallic and ceramic foams are characterized by a cellular structure and are divided into open-cell and closed-cell foams (Figure 1). The structure of both, open-cell and closed-cell foams, consists of a set of polyhedral cells, which are irregularly shaped and surrounded by a three-dimensional strut network [2]. In the case of open-cell foam, the cells are connected by edges or struts, and the cell-to-cell connection occurs through open faces, also addressed as windows. In closed-cell foams, the cells are connected by a solid body without interconnection between them. The main purpose of this work is to obtain open-cell foams, so further work will focus only on open-cell foams.

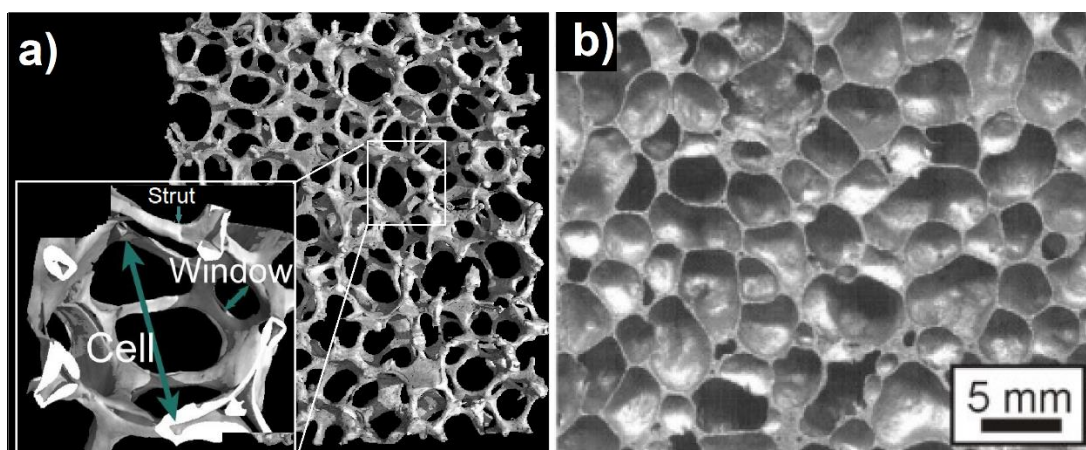


Figure 1 Metal foams with open cells (a) (adapted from [13]) and closed cells (b) [14].

Open-cell foams have high porosity, which has a major influence on their permeability and fluid dynamic behavior [15,16]. Their porosity is mainly based on the volume of voids (cells) enclosed between the struts. However, additional strut porosity such as material pores and hollow struts after PU burn-out may be present in the structure of open-cell foams, which are formed during the manufacturing process. The cell size is one of the important parameters in the design and manufacture of open-cell foams. It is common to use the number of pores per inch (ppi), which is obtained by counting the cells over a distance of a linear inch, to indicate the cell size. Other relevant characteristics of open-cell foams are their high specific surface area and the resulting ratio of surface area to volume, which influence the heat and mass transfer and, therefore, is important when they are used e.g. as catalysts, filters, and heat exchangers [5,16–18].

## 2.2 Mechanical properties of open-cell metal foams

The properties of metal foams depend on three dominant factors: 1) the material of foams determines the mechanical, thermal, and electrical properties; 2) the cell topology, open or closed, and pore shape influence the bending or stretch dominated behavior of the stress-strain curve; and 3) the relative density ( $\rho_{rel}$ ), which is derived as the ratio of foam density ( $\rho^*$ ) to bulk material density ( $\rho$ ) [19].

Mechanical properties of metal foams, such as compressive strength or energy absorption capability, are strongly dependent on the relative density of the foam, pore size, pore shape, and the ratio of open and closed cells. The characteristics of the compressive strength of foams are characterized by an elastic-plastic deformation of the stress-strain curves (Figure 2 a), which can be generally divided into three regions [20,21]: the region of elastic deformation, characterized by a linear increase in stress-strain until the plastic collapse stress ( $\sigma_{pl}^*$ ) is exceeded, the region of plastic deformation (plateau area) with the plastic collapse of cells as a result of yielding, buckling, or cell crushing, and the densification region at the densification strain point  $\varepsilon_D$ , where opposing cell walls start to come into contact and crush together [19,20].

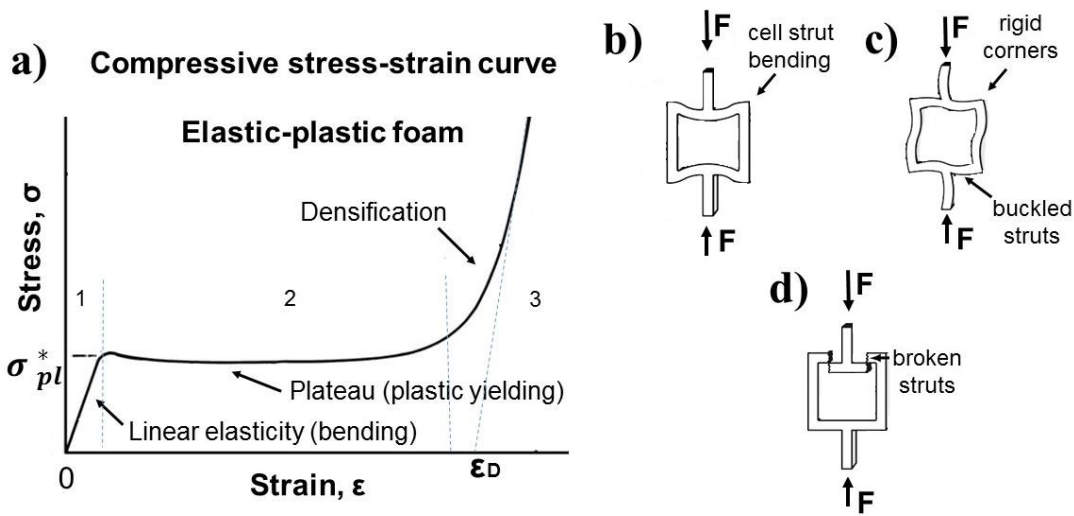


Figure 2 Schematic representation of a compressive stress-strain curve for a metal open-cell foam indicating the linear elastic behavior, the stress plateau and the densification regimes (a); deformation of an elastic-plastic cellular structure (b, c) and an elastic-brittle cellular structure (d).

Figure 2 shows the deformation under compressive loading for an elastic-plastic metal cell structure (b, c) and an elastic-brittle cell structure (ceramic, d) [19,20,22]. At the beginning of loading, the cell struts begin to bend, resulting in bending deflection (b). When the load applied to the cell walls exceeding their full plastic moment, they begin to yield. A further increase in compressive load causes the metal foam to collapse by the elastic buckling of the cell struts (c). Ductile foams are destroyed by plastic bending of the cell struts (broken struts, d).

The Gibson-Ashby model can be used to find a relationship between microstructure (cell size, porosity etc.) and the mechanical strength [19,20]. It can predict the compressive strength of open-cell metal foams assuming that struts undergo bending deformation. According to this model, the data  $\sigma_{pl}^*/\sigma_b^*$  can be plotted as a function of the relative density  $\rho_{rel}$  according to the following equation:

$$\frac{\sigma_{pl}^*}{\sigma_b^*} = C \cdot \left(\frac{\rho^*}{\rho}\right)^n, \quad (1)$$

where  $\rho^*$  is the density of foams,  $\sigma_b^*$  and  $\rho$  are the compressive yield strength and the density of bulk material, respectively. The proportionality constant  $C$  is related to the pore geometry effect and the density exponent  $n$  shows the deformation mechanism. The empirical values of these constants for open-cell metal foams are  $C \approx 0.3$  and  $n \approx 1.5$  [19,20,23,24].

### 2.3 Manufacturing techniques of open-cell metal foams

There is a variety of methods to manufacture open-cell metal foams. The most widespread and established methods are investment casting, casting around hollow spheres, and space holder or infiltration casting [25–27]. There are other less common methods such as layer by layer electrodeposition on a polymer pre-form [28], direct foaming [29] or sponge replication technique [8,25,30,31]. All of the manufacturing routes have their specific production characteristics, advantages and limitations, which significantly affect mechanical properties, total porosity, pore size, pore shape, and specific surface area of foams.

**Manufacturing of open-cell metal foams by investment casting** consists of four main steps (Figure 3) [2,32]. In the first step, a PU foam is dipped in a mould slurry as ceramic or gypsum. The PU foam is then burnt out after the mould material has dried and solidified. This produces pores or open voids in the mould material that follow the shape of the PU foam. In the third step, molten metal is filled into this mould material by capillary infiltration. Then, in the final step, after the metal has solidified, the mould material is removed by high-pressure water jets or by dissolution in acids or by leaching, to produce a metal foam that follows the shape of the original PU foam. The investment casting open-cell foams can be made from different metals and alloys, for example, from aluminum alloys [33–35], and have a wide range of desired cell sizes, relative densities, and porosities, which are replicated from the initial PU foam. The porosity typically ranges from 80 % to 97 %.

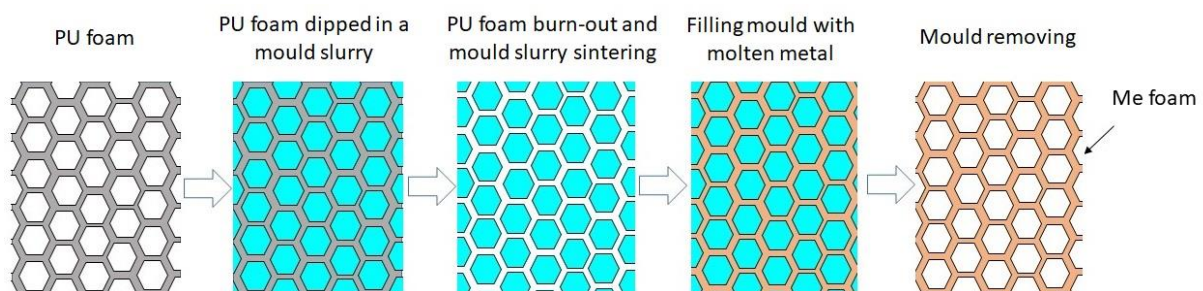


Figure 3 Schematic illustration of the production of open-cell metal foams by investment casting (adapted from [36]).

Despite these advantages, there are some challenges, such as non-uniform filling of the mould with molten metal. To overcome this problem, high pressure in a gravity field and preheating of the mould is used to fill the mould with molten metal [33–35]. Changing the gravity ratio can also improve mould filling. It has been shown in [33] that the structural integrity of pores, surface morphology, and thickness of aluminum columns improve after increasing the gravity coefficient. In addition, the fabrication of metal foams in the supergravity field makes it possible

to obtain open-porous metal foams with a smaller cell size. The authors also varied the cell size from 4.5 mm to 0.1 mm. However, the removal of materials from the mould was ineffective for foams with a cell size of 0.1 mm.

The production of metal foams by investment casting has a size limitation due to the incomplete filling of the moulds and the uneven heating of large moulds, which affects the filling of pores with liquid metals, macrostructure, and phase distribution of metal alloys [32,35]. In addition, the foam structure may be damaged when the heat-resistant mould is removed.

**Manufacturing of open-cell metal foams by casting with space holders** is shown in Figure 4. In the first process step, metal powder is mixed with space holders. This mixture is further heated. After the melt metal is solidified, the space holders are removed with acids or leached in solvents. Sodium chloride, sugar, carbonates or sand can be used as space holders. The resulting foams replicate the shape and size of the space holders, and foams with a porosity of >90 % can be obtained. The space holder casting is used to prepare foams, for example, from aluminum, magnesium, zinc, lead, tin [2].

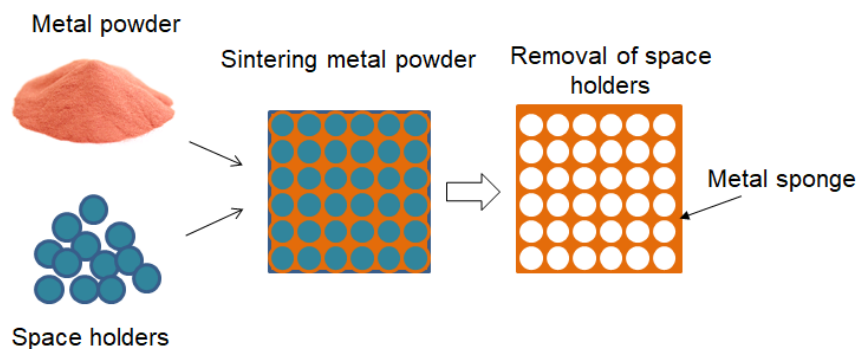


Figure 4 Schematic illustration of the fabrication of open-cell metal foams by space holder casting (adapted from [36]).

There are some challenges in making foams with this method: the voids between the particles of the space holders may not be completely filled with the metal melt due to the high surface tension of liquid metals. High-pressure melt infiltration, vacuum, and preheating of the space holders are used to increase their wettability with the molten metal and to prevent the molten metal from solidifying before the preform is completely filled [37,38]. These production process optimizations improve the stability of the foams and help to obtain foams with the desired functional properties.

Another way to manufacture open-cell metal foams is the **electrodeposition technique**, which is carried out in an electrolyte solution with dissolved metal ions [2]. Polymer foams are used

as templates for the electrodeposited metal. Before electrodeposition, the polymer foam must have a certain electrical conductivity. For this purpose, the polymer foam is usually immersed in an electrically conductive slurry based on graphite or carbon black for chemical coating. Then, after electrodeposition, the polymer is removed by heat treatment. The result is a three-dimensional arrangement of metal struts. The struts become hollow, after the polymer is removed. These foams have a wide range of cell sizes from 6 ppi to 70 ppi and a surface area of  $500 \text{ m}^2 \cdot \text{m}^{-3}$  to  $7500 \text{ m}^2 \cdot \text{m}^{-3}$  [2]. Basically, this method is used to produce nickel or nickel-chromium foams and copper foams.

Although the electrodeposition process can easily create a three-dimensional dendritic metal structure, it is difficult to control the microstructure with the desired characteristics [39]. This is because the trunks and branches in a porous dendritic structure are often unable to support the weight of multiple subbranches. As a result, the produced structure begins to collapse even with minimal convective forces. Another problem associated with this method is an overgrowth of dendritic structures, which form a thick film with very low porosity. This, in turn, makes it difficult for the transport of gases and/or liquids through this type of foam.

**Manufacturing of open-cell foams by the sponge replication technique.** Initially, the sponge replication method was used to produce ceramic foam [40]. This method consists of three production steps, which are shown in Figure 5. In the first step, an aqueous suspension of metallic powder, mixed with a binder, is applied to a PU template foam. After that, the PU template and the binder are burned out. The last step is the sintering of the metal foam. As a result of this manufacturing method, the foam is characterized by a hollow strut, as illustrated in Figure 5. This type of foam has a high porosity (up to 90 %) and a controlled pore size, which depends on the shape and size of the original PU template foam. In addition, the foams have a high surface area to volume ratio, which makes these foams attractive for the chemical industry in catalytic reactions, as a support template for various coatings, filters, and heat exchangers.

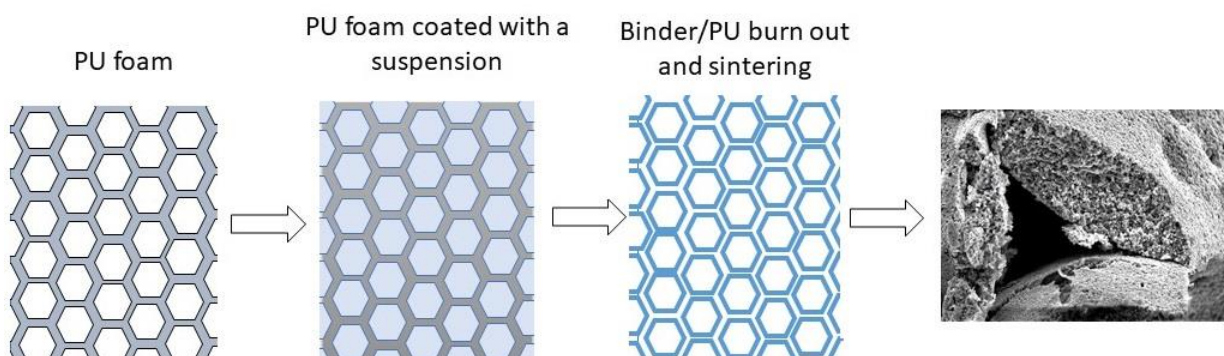


Figure 5 Schematic illustration of manufacturing of open-cell metal foams by the sponge replication technique (adapted from [36]).

Despite many advantages, this production method has limitations. One of them is the thin oxide layer on the initial metal powders (an example of rapidly oxidizing metals is aluminum), which is difficult to disrupt [41]. This leads to incomplete sintering of the powder particles and a heterogeneous microstructure of the foam. As a result, the foam may have poor mechanical properties and low thermal/electrical conductivity. Various additives, different sintering temperatures and atmospheres are used to dissolve the thin oxide layer [42,43].

### **2.3.1 Open-cell metal foams prepared by the sponge replication technique**

The sponge replication technique has a widespread application in the production of ceramic foams. Recently, this technique has also started to be used for the production of metal foams; in contrast to ceramic foams, sponge replicated metal foams have been less studied. It has been used to obtain open-porous titanium [7,30,44], Ti6Al4V [31], steel [9,45] and aluminum foams [46,47].

Since metal powders have a high density, it is important to obtain a suspension that is uniformly coated on the PU template foam and does not drain during drying. Therefore the slurry's rheological properties, which can be varied by using additives (such as polyvinyl alcohol (PVA), polyethylene glycol (PEG) carboxyl methylcellulose), dispersants (Dolapix), dispersion liquids (mostly water), and powder loading, are of great importance in the production of foams with this manufacturing technology [7,9,44]. For instance, it was shown in [44] that PVA and particle loading had a major influence on the viscosity of a titanium suspension. However, Dolapix did not affect the viscosity but prevented the metal particles from rapid sedimentation. A mixture of water and ethanol was used in [48] as a solvent or a dispersion liquid, respectively, to increase the compressive strength of titanium scaffolds by improving compactness where the compressive strength reached  $83.6 \pm 4.0$  MPa with a total porosity of  $66.4 \pm 1.8$  %. The addition of ethanol resulted in a homogeneous porous titanium scaffold structure and fully interconnected foam cells.

The composition of the PU template foam can also influence the uniformity of the suspension coating, the chemical composition of the sintered foam, and their mechanical properties. Titanium foams were manufactured using three different PU foam templates in [49]: polyether- and no-degraded polyester-based PU template foams and degraded polyester-based PU template foams. Coating a titanium slurry on polyester-based PU template foams provided a uniform coating because it was more hydrophilic than polyether-based PU template foams due to the increase in polarity of the carboxylic acid group. A positive coating characteristic during

the manufacturing of titanium foams with the polyester-based PU template foam had a positive effect on the mechanical properties of the resulting Ti foams. The compressive stress-strain curve of the titanium foams based on degraded polyester-based PU foams was characterized by a brittle behavior, no initial elastic response at low strain levels, and no stress plateau was observed. This was due to the formation of titanium carbide during PU template burn-out. Consequently, the type, chemical and surface chemical characteristics of the PU template foam have a significant influence on the resulting foams; the formation of undesirable compounds must be considered that may impair the properties of the reticulated foams.

Figure 6 shows a typical foam strut and its cross-section. It can be seen that the material around the hollow strut pore is unevenly distributed, and struts are characterized by an edge defect, which can also be seen in the cross-section (oval highlighted area) and the presence of pores in the strut. The edge defects form due to insufficient coating of the PU foams with a suspension. Strut pores can occur in form of gas bubbles as a result of the interaction between powder and additives. All these features can have a negative effect on the mechanical properties of foams compared to bulk or cast material [45]. It was observed a tensile failure of steel foams in [45], in which the influence of strut pores and edge defects on the failure of the foam was studied in detail. The results showed that hollow struts fail by zipping along with the corners of the strut (Figure 7 a,b). The opening of the strut occurred in areas with less solid material as strut corners and edge defects. Pores, which are located near the strut corner (Figure 7 c,d), contributed to cracking especially in areas with thinner struts and leading to the opening of the strut corner (marked with an \*).

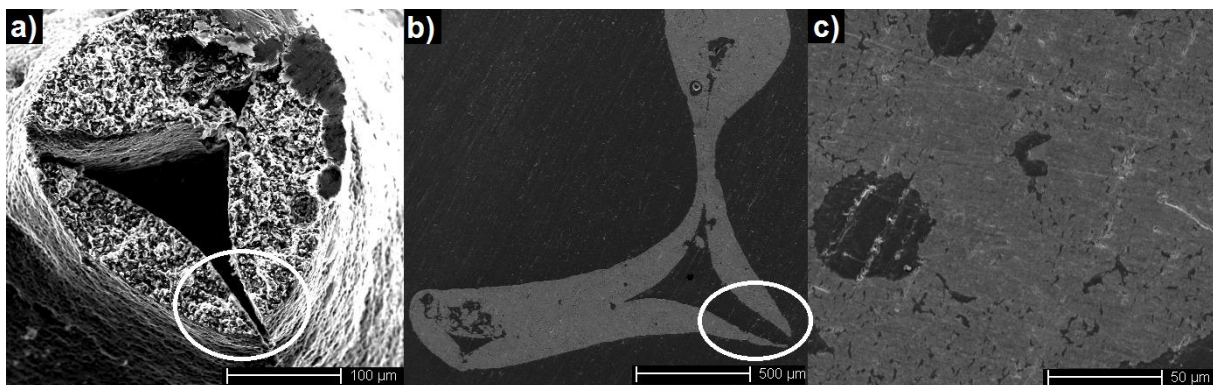


Figure 6 SEM image of a typical strut and cross-section of metal foams prepared by the sponge replication technique (here: aluminum foams).

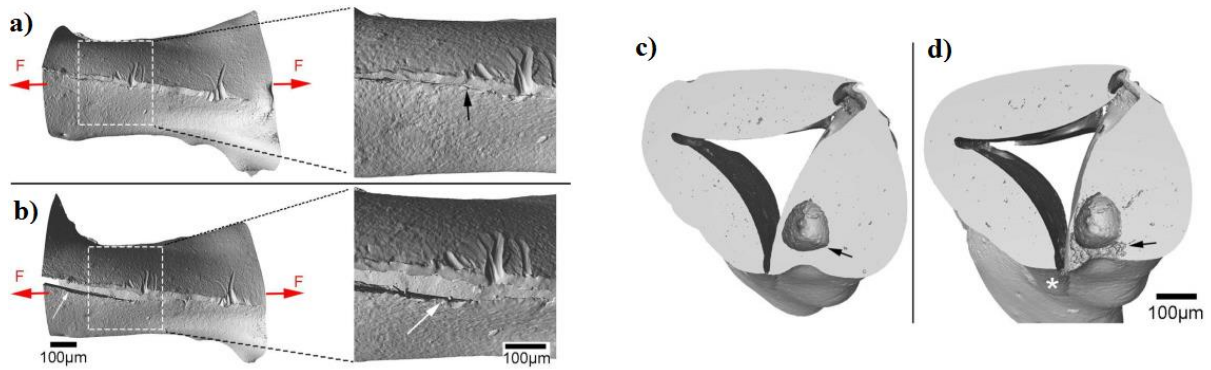


Figure 7 Tomographic imaging of the strut before loading, showing the sutured area of the strut (black arrow) (a); strut after loading at 4 % deformation strain, showing unzipping along the struts (white arrow) (b); development of cracks around the pore: unloaded strut (black arrow) (c) and crack development around the pore after loading at 1.4 % strain (unzipping (\*) is marked) (d) [45].

One of the most important parameters in foam production is the cell size of PU template foams. Varying this parameter affects porosity, mechanical properties, water and gas permeability, and surface area. In [7], the microstructure and mechanical properties of titanium foams with different cell sizes ranging from 25 ppi to 40 ppi with a total porosity of 86 % to 92 % were studied. It was found that, as the number of pores increased, i.e. as the cell size decreased, the porosity decreased and the compressive strength increased non-linearly.

The sponge replication technique also allows the production of metal matrix composite foams. A homogeneous distribution of  $\text{TiC}_{0.7}\text{N}_{0.3}$  particles in a 316L matrix was obtained in [9], which worked as a reinforcing material, increasing the compressive strength from 4.5 MPa to 16.5 MPa at 4 wt. % of  $\text{TiC}_{0.7}\text{N}_{0.3}$ . The compression strain curves of the 316L stainless steel metal matrix composite had a typical compression strain behavior for an open-cell metal foam shown in Chapter 2.2.

The possibility of processing aluminum foams prepared by the sponge replication method was demonstrated in [47]. Relatively stable aluminum foams sintered in air at 620 °C for 4 h and 7 h showed a porosity between 94.4 % and 95.5 %. The focus of this work was mainly on determining the suspension composition. Despite the general possibility of obtaining stable aluminum foams, no further studies were carried out.

## 2.4 Freeze-drying as a method to manufacture porous materials

Freeze-drying is a method of manufacturing porous materials from a ceramic, polymers, or metal suspension by ice-crystal driven particle movement during freezing and subsequent

sublimation of the solidified liquids (solvents) at low pressure and temperature; this leads to a porous structure. The pore structures formed after these processing steps replicate the morphology of the solidified liquid. The advantage of this method is its flexibility since this method allows the volume fraction, size, shape, and orientation of pores to be varied by changing the characteristics of the suspension, such as the type of solvents, additives, the fraction of particles, and by the solidification conditions such as freezing temperature, freezing front direction, mold design and substrate material [50,51].

This chapter deals with the basic principles of the freeze-drying method. The basic parameters affecting pore shape, pore thickness, and pore direction are presented. The main applications of porous materials are discussed. An overview of recent research on freeze-dried foams is presented.

#### **2.4.1 Basic principles: anisotropic and isotropic freezing**

Freezing is divided into anisotropic and isotropic freezing [50,51]. The anisotropic type includes unidirectional freezing. This method has been studied more extensively than isotropic freezing. A diagram of this type of freezing is shown in Figure 8. First, a suspension consisting of solids and a liquid is placed in a mould, sidewise to a thermally insulating material such as Teflon (a). The base of this mould consists of thermally conductive materials such as copper, which is cooled. This leads to the nucleation of a solidification front and its directional propagation (b). At the beginning of the solidification front, the solidification rate is very high and dispersed particles are captured by the freezing front forming a dense layer at the base of the sample (c). As the solidification front propagates, particles are pushed out of the liquid and concentrate in the interdendritic space (d). As a result, areas of high concentration of frozen particles and frozen liquid are formed. The frozen liquid is then removed by sublimation after completion of the freezing process (e). The formed pores replicate the morphology of the solidified liquid, have an elongated shape and have a direction co-directed to the freezing front. The resulting samples are sintered after sublimation of the frozen liquid (f).

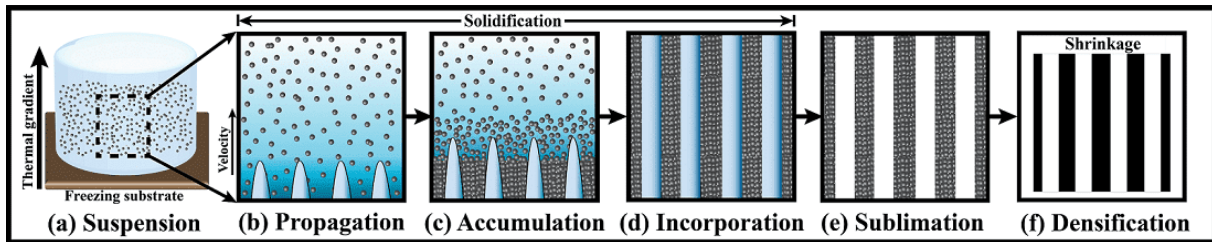


Figure 8 An anisotropic freeze casting process consisting of placing a suspension in a thermally insulated mould (a), freezing the suspension (b), accumulation and pushing the particles out of the liquid into the interdendritic space (c) and their incorporation (d), sublimation of frozen samples (e), and densification of the sample via sintering (f) [50].

The isotropic freezing method is used to obtain irregular porosity [50,51]. In isotropic freezing shown in Figure 9, the slurry is also placed in a heat-insulating mould and placed in a freezer (a). In contrast to the anisotropic method, freezing of the particles occurs randomly and has no direction, since nucleation (b) and solidification (c) occur simultaneously throughout the suspension in a random orientation. The resulting pores have an isotropic structure after sublimation (d) and densification and/or sintering (e). In this type of freezing the shape of pores may vary from closed equiaxed cells to open reticular networks [50]. In particular cases, freezing is carried out in thermally conductive forms to obtain directional freezing in a predominantly bottom-up and radial direction. Despite the presence of relatively directional freezing, the pores are generally isotropic in this kind of freezing. Figure 10 shows the most common types of pores after anisotropic freezing having a lamellar (a), a dendritic (b) or a honeycomb structure (c), and after isotropic freezing having a honeycomb (d), an equiaxed (e) or a cellular (f) structure [50].

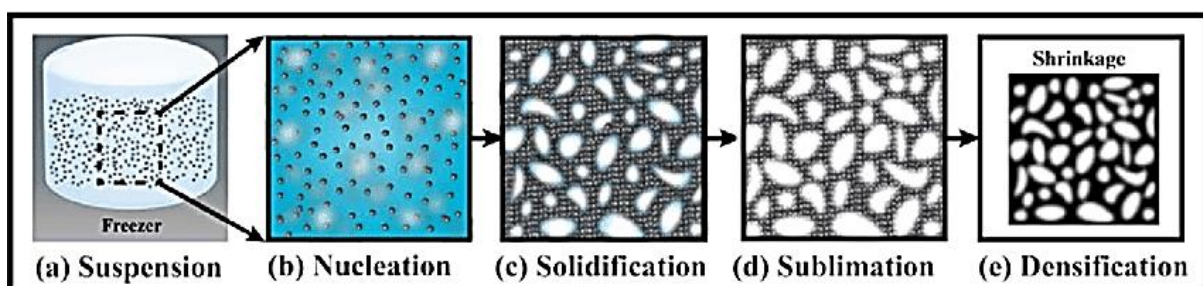


Figure 9 An isotropic freeze casting process consisting of placing a suspension in a thermally insulated mould (a), solid nucleation in suspension (b), random solidification (c), sublimation of frozen samples (d) and densification via sintering (e) [50].

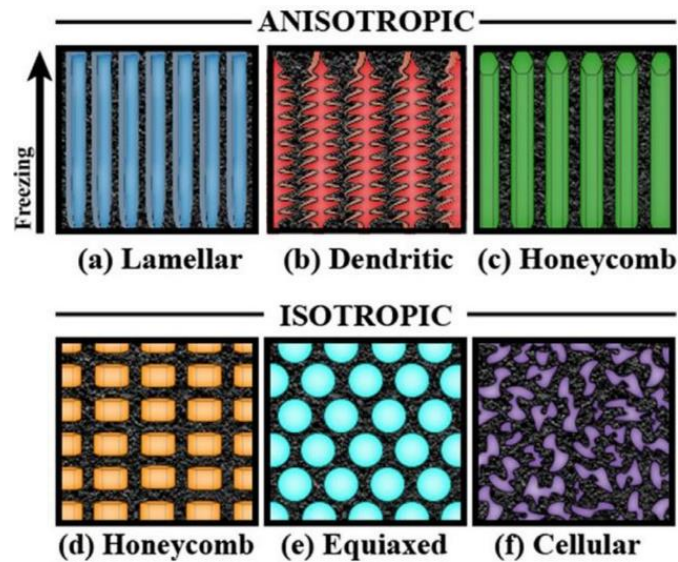


Figure 10 Schematic representation of pores in sublimated materials during anisotropic (top) and isotropic freezing (bottom). The colored areas indicate the region with solidified liquid, which determines the morphology of the pores after sublimation. The dark areas are the solid material particles [50].

#### 2.4.2 Influence of freezing parameters, solid loading, solvents and additives on the microstructure of freeze-dried porous materials

One of the parameters significantly influencing the pore size is the freezing front velocity. It was found that as the freezing rate increased, the pore size decreased as a result of the temperature gradient formation, which, in turn, increased the strength of ceramics [52]. Figure 11 shows the dependence of the structure wavelength on the ice front velocity [53]. The higher the freezing rate, the finer the microstructure of the lamellar pores and material lamellae. The speed of the freezing front can be controlled by the solid load, the cooling rate, and the freezing temperature. It was reported in [54] that increasing the solid loading decreased the freezing onset temperature resulting in a shorter wavelength and increased the lamella wall thickness. By varying the temperature from  $-30\text{ }^{\circ}\text{C}$  to  $-196\text{ }^{\circ}\text{C}$  during freezing a suspension yttria-stabilized zirconia (YSZ) with tert-butyl alcohol (TBA), porous ceramics with unidirectional pore channels were obtained [55]. The pore size decreased in proportion to the freezing temperature and increased in proportion to the distance from the cooling plate (Figure 12).

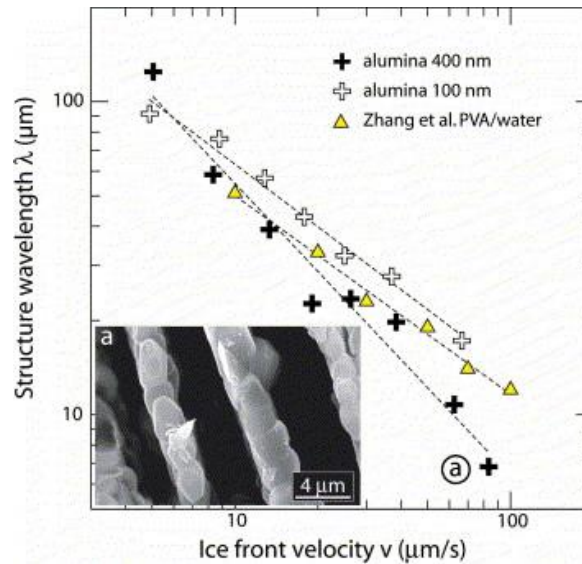


Figure 11 Wavelength variation of the material structure as a function of the ice front velocity. The SEM image of the cross-section of the sample parallel to the ice front with the smallest lamellae thickness of  $\sim 2 \mu\text{m}$  is shown in inset (a) [53].

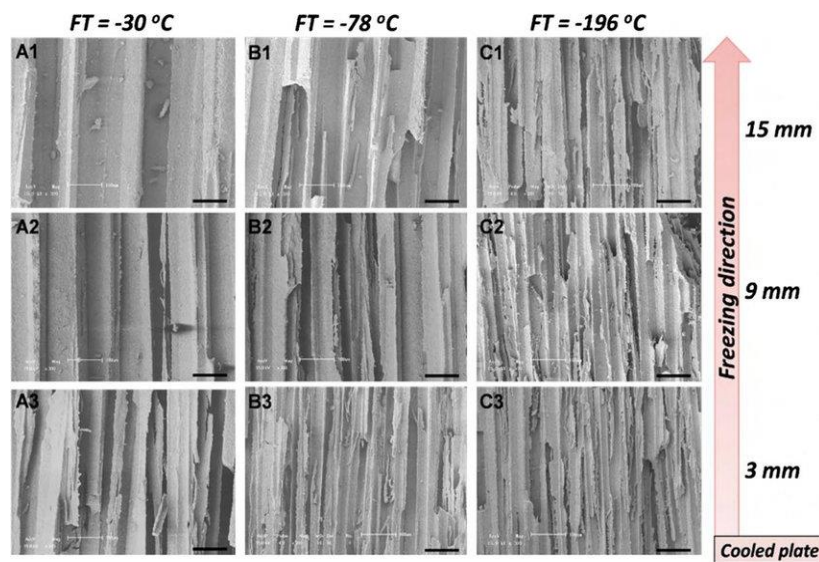


Figure 12 Microstructure of unidirectionally aligned pore channels in YSZ ceramics at different distances from the cooled plate from 15 mm to 3 mm and at freezing temperatures varied from  $-30 \text{ }^{\circ}\text{C}$  to  $-196 \text{ }^{\circ}\text{C}$  [56].

Varying the ratio of liquid to solid part in the initial suspension also affects the microstructure of the samples (Figure 13) [53]. The pores formed after sublimation were initially ice formed from the liquid part. Thus, the total porosity of the material and size of pores depended directly on the liquid/solid ratio in the suspension. A high solid content did not result in lamellar pores (Figure 13 c). It was observed that higher solid loading increased the compressive strength by forming thicker walls in [57].

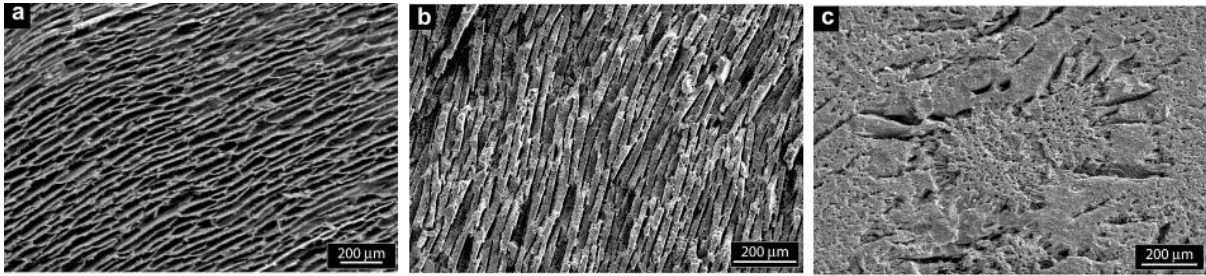


Figure 13 SEM micrograph of a cross-section parallel to the ice front showing the effect of the suspension water content on the microstructure; total porosity of the samples: (a) 70 %, (b) 40 %, (c) 24 % [53].

The size of the original solid particles also influence the microstructure of the pores [12,58–60]. This was because solids act as nucleation sites for ice crystals and influence the velocity of the freezing front. With decreasing particle size, the number of ice crystal nucleation sites increases leading to the formation of numerous small pores. It is difficult to obtain a homogeneous morphology of the final frozen structure at particle sizes with the order of the size of the interdendritic spaces. Therefore, the particle size has to be lower than the wavelength of the desired structure. Consequently, micron-sized particles cannot be used to create structures with nanometre wavelengths. In order to achieve a homogeneous and well-defined structure, it must be considered that an irregular particle size distribution (presence of large particles or agglomerates of particles) has a negative effect on the uniformity of the final structure.

Additives can also influence the pore morphology. They can be used to change the phase diagram of the liquides, the anisotropy of the solid/liquid interfacial energy, the viscosity of the suspension, the freezing temperature of the suspension and the volume expansion of the system [58]. One of these additives is glycerol, which is the most commonly used one. Its advantages include non-toxicity, low cost, good solubility in water, as well as a low freezing point [61]. In addition, the use of glycerol can prevent the formation of defects associated with the water expansion and the particle push back during freezing. This leads to an increase in suspension viscosity and good bonding between lamellae, which, in turn, increases the mechanical properties of the system [62]. Polyethylene glycol (PEG) is also referred to as one of the additives in water-based suspensions, which, in turn, can also be used as a binder [63]. PEG led to a reduction in the local equilibrium solidification temperature and stabilizes the growth of dendrite tips. The addition of PEG also reduced the pore size in [64]. PVA is used to regulate the pore morphology. That made it possible to obtain small pores in [65,66]. Gelatin is an additive for regulating the pore morphology and increases the viscosity of the suspension [67,68]. The addition of gelatin helps to prevent abnormal ice growth and to obtain a homogeneous microstructure. In addition, gelatin bounds the solid particles together and

prevented their breakdown in the green body before sintering [68]. Another additive is polyacrylamide (PAM), which changes the pore structure from lamellar pores with dendrites to columnar ones without dendrites, decreasing the pore size and increasing the material wall thickness [69].

The liquid part, called the solvent, disperses the solids in suspension and acts as a binder between the solid particles during freezing [50]. The most common solvents include water, camphor, tert-butyl alcohol (TBA), and the naphthalene-camphor binary system. The type of solvent used during freezing is the main factor affecting the pore structure; this is because they have different freezing points, viscosity, surface tension, and hydrophilicity.

Water is a widely used solvent due to its low cost, the convenience of use, environmental friendliness, the unique morphology of ice crystals, and compatibility with functional additives [70]. The obtained pores after freeze casting have a lamellar channel shape. However, due to its anisotropy, the lamellar structure can have undesirable properties for some applications. In this case, additives such as camphene and TBA are used. Camphene is used to obtain dendritic-shaped pores [71]. In contrast to the lamellar structure of frozen water or camphene, frozen TBA usually has the shape of long, straight prismatic crystals without branching at the crystallization point, which is useful for the production of porous materials with membrane-like structures for the separation process [72]. TBA is infinitely soluble in water. The obtained ice crystals do not have a uniform shape after the solidification of this suspension. The shape of the crystal changes depending on the ratio of TBA to water. Another solvent is a binary compound of naphthalene and camphor. This binary compound has low viscosity and is used for manufacturing macroporous structures [73]. Table 1 summarises the above-mentioned freezing parameters and their effect on freeze-dried materials.

Table 1 Influence of freezing direction, freezing front velocity, temperature, solid loading, solvents and additives on the microstructure of freeze-dried porous materials.

Control Parameter	Structural feature	Effect	Reference
freezing direction: anisotropic and isotropic	pore direction pore shape	<b>anisotropic:</b> pores direction co-directed to the freezing front; pore shape: lamellar, dendritic, honeycomb. <b>isotropic:</b> random orientations, irregular porosity; pore shape: honeycomb, equiaxed, cellular.	[50,51,59]
freezing front velocity	structure wavelength	higher freezing rate - finer microstructure	[52,53,59]
freezing temperature	pore thickness	pore size decreases in proportion to the freezing temperature;	[23,56,74]
solid loading	total porosity	total porosity, pore size, wavelength, pore morphology, compressive strength, freezing onset temperature	[23,54,57,75]
particles size	velocity of freezing front, nucleation sites for ice crystals	morphology, wavelength	[12,58–60]
additives (glycerol, PEG, PVA, gelatin, PAM)	viscosity of the suspension, freezing temperature, phase diagram of solvents, solid/liquid interfacial energy	morphology of pores (reduce rejection of particles, reduced growth of dendrite tips out into the melt), bonding between lamellas, mechanical properties, shape of pores, wavelength	[58,61–69]
solvents (water, camphor, TBA, naphthalene-camphor)	freezing onset, viscosity, surface tension, hydrophility	pore morphology (lamellar structure, porous with membrane-like structures, dendritic-shaped pores)	[70–73]

### 2.4.3 Application of freeze-casted ceramic and metal porous materials

Freeze-drying forms porous materials, which have found applications in various fields such as biomedicine, thermal insulation and interface materials, electrically conductive materials and piezoresistive sensors, energy storage and conversion, structural materials, water and air filters, heavy metal adsorption and smart materials (self-healing, self-monitoring, shape memory, shape programming) [59]. Varying the suspension composition, total porosity, pore size, shape and direction of pores affects the specific surface area, the strength, the thermal and the electrical conductivity of porous materials [12]. All of this makes it possible to cover the above-mentioned application areas.

In structural applications, highly ordered porous structures of freeze-casted materials promote very high recoverable compressive deformations compared to random porous systems. These materials provide high levels of mechanical energy dissipation (damping) in a weight-dependent system and achieve high levels of elasticity. Deformation and energy dissipation of cellular materials are used to develop shock and vibration protection and acoustic insulation systems [59].

In energy storage and conversion structures, the electronic, thermal, mass-transport properties of energy materials can be optimized by additional pores. Freeze-dried materials are used in the development of new electrode structures. Highly ordered porous electrode structures provide high active material loading and provide efficient ion transport channels compared to conventional densely packed structures [76,77]. Also, the high porosity of materials formed after freeze casting reduces deformation caused by volume changes during charge/discharge cycles [77,78]. In the field of lithium-ion batteries, vertically aligned  $\text{LiFe}_{0.7}\text{Mn}_{0.3}\text{PO}_4$  nanoplates and graphene hybrid frameworks contributed to 2.5 times higher ion transport and better cycling performance compared to electrodes with random structure [76].

A series of papers have demonstrated the use of Cu foams with well-aligned porous structures as anode current collectors for a lithium-ion battery [23,79–81]. The possibility of replacing the copper foil with a frozen Cu foil coated with Si or Sn active material was discussed in [80]. The excellent thermal and electrical conductivity of copper makes copper freeze-dried foams ideal for applications such as heat exchangers, catalyst supports, and electromagnetic shields [79]. The Cu-Ni combination can be used in the field of high-temperature filters with high load-bearing capability and as electrodes with good corrosion resistance [81].

Biomimetic pore structures created by freezing can be used to fabricate microbial fuel cells to recycle organic waste partially into hydrogen [82,83]. The high surface area and efficient mass/electron transfer of the obtained porous materials are advantages in this application. Another widespread application is the use of ceramic and metal porous structures as filters. The high surface area of aligned porous materials can be used to clean water [84,85] and air [86]. Due to the aligned pore structure, these filters provide efficient transfer of liquids and gases compared to random porous materials. Nowadays, there are many research works where such filters are used to remove dyes [87], oil and organic solvents [88,89], and heavy metals [90] from water and air.

#### 2.4.4 Freeze-drying of metals

Freeze-drying or casting was originally used for the making of ceramic porous materials; therefore there is at present a high number of works about the influence of freezing parameters, additives, solvents, etc. on their porosity, strength, mechanical and thermal characteristics [12]. However, in the last decade, this method has been applied for the manufacture of metallic porous materials despite the tendency of metal particles in suspension to rapidly settle and oxidize in water. At present, freeze-drying is actively applied to obtain titanium [91,92], Ti-Al alloy [93], iron [94–96], copper [23,74,75,79], nickel [81,97,98] foams, and Cu-Ni porous materials [81].

In the manufacturing of copper foams copper oxide powders are usually used, which are converted to pure copper after sintering in an argon atmosphere with hydrogen [23,75]. Copper foams with oriented lamellar macropores and micropore walls were obtained for the use in electrochemical cells in [23]. The authors varied the processing parameters such as the proportion of powder in suspension from 13 vol. % to 19 vol. %, the freezing temperature from  $-10\text{ }^{\circ}\text{C}$  to  $-30\text{ }^{\circ}\text{C}$ . This resulted in foams with a porosity ranging from 45 % to 73 %. The amount of porosity was inversely related to the proportion of powder in the suspension. It was also found that with decreasing solid loading and increasing freezing temperature, the width of oriented lamellar macropores increased from  $15\text{ }\mu\text{m}$  to  $64\text{ }\mu\text{m}$  and the width of the Cu material lamellae decreased from  $63\text{ }\mu\text{m}$  to  $19\text{ }\mu\text{m}$ . A linear decrease in porosity from 50 % to 31% with an increase in the proportion of CuO powder from 20 vol. % to 40 vol. % was also observed in [75]. Copper foams with a high porosity of ~80 % with aligned, elongated pores from 40 nm to 80 nm were obtained from copper oxide powders with an initial solid particle load of 15 vol. % in the processing suspension. The pore diameter was approximately  $91\text{ }\mu\text{m}$ . Three types of porosity were found in these foams: aligned, elongated pores repeating ice dendrites; microporosity in partly sintered copper walls; and cracks in these copper walls formed due to shrinkage during sintering. Copper foams with an oriented pore structure were also obtained in [74]. Similar to the previously observed work [23], the pore size decreased with decreasing freezing temperature and the effect of pore direction and compressive loading relative to each other was shown. It was found that the yield strength decreased from 25.4 MPa to 12.6 MPa and from 23.7 MPa to 8.6 MPa in directions parallel or normal to the freezing direction, respectively.

It was discussed in Chapter 2.4.2 that different additives affect the freezing process. The effect of PVA additive on the morphology and the macro- and microstructure of NiO foams made by

reduction and sintering of a directionally frozen water suspension of nanometric NiO powders was studied in [98]. It was found that the addition of PVA led to the formation of dendrites and the accumulation of NiO powder in the interdendritic space, respectively, creating Ni walls with micropores after sintering. As a result, the Ni walls with the additive were characterized by less dense walls, more closed pores, and a rougher surface than the foams without PVA addition. The addition of PVA reduced the nickel wall size from  $75 \pm 13 \mu\text{m}$  to  $21 \pm 5 \mu\text{m}$ . In this way, the addition of PVA can also be used to vary the surface area.

Pure copper or nickel is not as corrosion resistant as an alloy based on it. That may prevent the application of pure open-cell metal foams in areas requiring high strength and corrosion resistance such as anode in a fuel cell [98,99]. Cu-Ni freeze-dried foams with vertically aligned lamellar macro-pores were manufactured to solve this problem in [81]. The foams were prepared from mixed powders of NiO (<20 nm) and CuO (40–80 nm) with 100, 90, 70, 50, 30, 10, and 0 wt. % Cu. The Cu–Ni alloy was formed after oxide powder reduction/sintering processing at 800 °C to 1000 °C in Ar with 5 vol. % H<sub>2</sub>. The results of corrosion resistance in sulphuric corrosive environment showed that the weight loss rate of Cu<sub>7</sub>Ni<sub>3</sub> alloy foam was six times and five times slower than that of pure Ni and pure Cu foam, respectively.

It was previously shown in Chapter 2.4.2 that, when a suspension is frozen, there is a pore-size-width gradient along the freezing direction. This results from the fact that there is a decrease in the rate of solidification with distance from the cooling source at a constant substrate freezing temperature. As a result, there are the smallest pores from the side closer to the substrate-cooler, which gradually grow further away from the cooler. Depending on the foam applications, this pore gradient may be undesirable. In order to avoid it and to obtain a more homogeneous porous structure, it was proposed the use of double-sided cooling instead of a one-sided cooling, leading to a more homogeneously distributed cooling rate to minimize the pore width gradient in [94]. It helped to control the temperature gradient in the suspension and to obtain more uniform width of pores and pore walls.

For controlling the velocity of the freezing front, a continuous directional freeze casting technique based on liquid metal cooling (LMC) has been developed, which is called “LMC-like freeze-casting” [100]. This method is based on immersing a mould with a slurry in a low-temperature bath at a constant rate. The solidification rate and the immersion rate of the mould were equal, due to a special freezing mould made of quartz.

Pore size and direction, wall thickness, total porosity, and sintering parameters of green bodies as mentioned above influence the mechanical properties of the final-sintered foams. Iron foams with lamellar aligned channels made from a  $\text{Fe}_2\text{O}_3$  suspension sintered at different temperatures were investigated in [96]. Increasing the sintering temperature from 900 °C to 1100 °C resulted in a reduction of the foam porosity from ~ 70 % to ~ 60 % and a reduction of the lamellar pore thickness from ~ 46  $\mu\text{m}$  to ~ 40  $\mu\text{m}$  at a constant  $\text{Fe}_2\text{O}_3$  loading of the slurry of 18.5 vol. %. It was found that the maximum strength of the foams changed from 8 MPa to 20 MPa with increasing the sintering temperature and a corresponding decrease in porosity.

## **2.5 Manufacturing of open-cell foams via sponge replication technique and freeze-drying**

Open-cell porous metal and ceramic foams are actively used in the fields of heat exchangers, heat pumps, filters, catalyst substrates, where high air and liquid permeability combined with high specific surface area play an important role [4,5,101]. Metal or ceramics foams can be coated for these applications with active materials such as zeolites or MOFs [4,5,102]. Therefore, the high specific surface area of the foams allows the amount of coated active material to be increased, thereby increasing the efficiency of the composite in related applications [103,104]. The formation of additional porosity in the foam struts can increase the specific surface area of the foam. A possible method of manufacturing additional strut porosity can be a combination of sponge replication and freeze-drying methods. This manufacturing way was first applied in 2010 in [105] for aqueous  $\text{SiO}_2$  suspension. PU foams were coated with the suspension, the excess slurry was removed as a preparation step from the sponge replication technique, then the foams were frozen to obtain aqueous crystals in the struts as a preparation step from the freeze-drying technique. After that, the samples were sublimated and sintered. As a result, this technique allowed to obtain open-celled ceramic foams with additional porosity in foam struts. The combination of replication and freezing techniques was successfully applied for a tert-butyl alcohol- $\text{Ca}_{10}(\text{PO}_4)_6(\text{OH})_2$  slurry [106].

A more detailed study of the effect of freezing temperature, additives, and solid loading on total porosity, pore morphology and size, specific surface area, and compressive strength was presented in [10,11]. These works were focused on obtaining highly porous alumina ceramics. Sample preparation also proceeded by slurry coating onto the PU foam, freezing, sublimation, and sintering.

In [10], PU foams were coated with aqueous suspensions with different solid loadings from 20 vol. % to 40 vol. % with guar gum as a thickener and afterward, the samples were frozen at temperatures between  $-196\text{ }^{\circ}\text{C}$  in liquid nitrogen and  $-20\text{ }^{\circ}\text{C}$  in a laboratory freezer. After sublimation and sintering of the foams, it was found that the size and morphology of the pores inside the struts strongly depend on the solid loading of the alumina suspension and the freezing temperature. When the freezing temperature decreased from  $-20\text{ }^{\circ}\text{C}$  to  $-80\text{ }^{\circ}\text{C}$ , the pores had a lamellar structure, typical for aqueous suspensions. The direction of the lamellar pores was not homogeneous across the sample due to nondirectional freezing. When foams were frozen in liquid nitrogen, the formation of a high number of small round-shaped pores without lamellar pores was observed due to the high freezing rate. Changing the freezing temperature from  $-20\text{ }^{\circ}\text{C}$  to  $-80\text{ }^{\circ}\text{C}$  with the solid load of 20 vol. % had no significant effect on the material lamellae thickness, which varied from  $28.6\text{ }\mu\text{m}$  to  $29\text{ }\mu\text{m}$  but there was a thickness increase from  $28.6\text{ }\mu\text{m}$  to  $40\text{ }\mu\text{m}$  at the solid load of 40 vol. %. The growth of the solid loading from 20 vol. % to 40 vol. % at  $-20\text{ }^{\circ}\text{C}$  reduced the thickness of the lamellar pore from  $62\text{ }\mu\text{m}$  to  $18\text{ }\mu\text{m}$ . Additional pores obtained by this production method increased the total strut porosity (closed and open pores), as an example from 25.8 % to 54.8 % for foams with a slurry loading of 30 vol. % at  $-20\text{ }^{\circ}\text{C}$ . Due to additional lamellar pores in the struts, the specific surface area of the foams increased from  $70\text{ cm}^2\text{ g}^{-1}$  to  $113\text{--}259\text{ cm}^2\text{ g}^{-1}$ .

The results of the compressive strength study have shown that with the increase of the solid loading the compressive strength increased too, due to a decreased porosity and resulting densification of the struts [10]. Despite a high total porosity, the compressive strength of the foams after freezing ranged from 0.2 MPa to 1 MPa. It was found that the pore morphology had a significant effect on the compressive strength. Samples frozen in liquid nitrogen had a higher strength compared to samples prepared by the sponge replication technique without and with freezing steps. It was suggested that the reason for the increased compressive strength in liquid nitrogen might be due to the formation of the small spherical shape pores. The presence of lamellar pores at  $-20\text{ }^{\circ}\text{C}$  or  $-80\text{ }^{\circ}\text{C}$  conversely decreased the compressive strength. A possible failure mechanism described in the article was the breaking of interconnections between the individual material lamellae due to weak bonding of the material lamellae, which may have caused the material lamellae to slip off from each other, as well as the accumulation of stress at the ends of the lamellar pores, which led to failure in the foam material.

In a further study, different thickeners (guar gum, wallpaper paste, methylcellulose, potato starch) were added to a 30 vol. % and a 40 vol. % aluminum oxide slurry and was suspended

to a freezing temperature of  $-20\text{ }^{\circ}\text{C}$  to produce foams [11]. Formation of lamellar pores was observed regardless of the type of thickener. However, the microstructure of the foams was characterized by the formation of numerous round voids when the loading was increased to 40 vol. %, this was especially obvious for guar gum. However, after drying at room temperature and sintering without freeze processing, the foam struts had a homogeneous structure when guar gum was added [10]. The formation of these voids may be caused by a higher viscosity compared to foams from slurries with 30 vol. % alumina solid loading. Accordingly, this might have prevented gas bubbles to escape from the slurries after coating the PU foams. Increasing the solid loading reduced the open strut porosity and the lamellar pore thickness, but increased the material lamellae thickness. That behavior was also observed in [10]. Varying the thickeners did not lead to significant changes in lamellar pores size and material lamellae size.

It was found that the compressive strength increased with higher slurry loading. The highest compressive strength values were obtained for samples with methyl cellulose. It was 1.3 MPa at 40 vol. % solid alumina loading with a total porosity of  $\sim 91\%$ . This dispersion had the highest viscosity, which contributed to a homogeneous and almost defect-free coating of the PU foam, which consequently had a positive effect on the compressive strength. The formed bubble voids reduced the compressive strength, especially in the samples with guar gum.

The performed works in [10,11] showed the successful application of the combination of the sponge replication and freezing techniques to obtain ceramic foams with additional porosity in their struts. The results demonstrated that foams obtained by this novel method have the potential for the use as carriers for active materials due to the possibility to increase the specific surface area, which may allow achieving high loading of active materials, respectively increase the ratio of active material mass to support mass. This manufacturing technique may be attractive for metal foams, which may be used in heat pumps, as carriers in catalysts, as heat exchangers and filters, or in general, where a large specific surface area and highly porous struts are required.

Up to now, the combination of sponge replication and freeze processing as described in [10,11] was not applied yet for the manufacturing of open porous replica metal foams, and the systematics of the aforementioned parameter studies for alumina foams was adapted for the manufacturing of aluminum and copper foams within this work.

## 2.6 Micro-macroporous composite materials based on open-cell foams

More than 70 different composite materials based on macroporous foam (ceramic, metal and polymer substrates) and microporous material (pore size less than 2 nm [107]) applied to support struts are currently represented [6]. Micro-macro-porous composite materials cover the fields of materials science (cellular materials) and chemistry (microporous compounds). Microporous compounds have a high internal specific surface area and can adsorb molecules in their micropores. Well-known and well-understood microporous crystalline compounds include zeolites (ZSM-5, Zeolite A, Silicalite-1, SAPO-5, SAPO-34, etc.) and MOFs such as HKUST-1, MOF-5, CAU-10, MIL-101.

Zeolites are crystalline framework materials consisting of tetrahedral primary building units  $[TO_4]$  with common angles, where  $T = Si, Al, P, Ti, \dots$  [6]. There are also compounds where some of the  $T$  atoms in the tetrahedral are substituted, e.g. as  $[(Si/Al)O_4]$  [108]. These tetrahedral primary  $[TO_4]$  blocks are connected in larger structures (rings, cells) resulting in a three-dimensional porous structure (Figure 14). As a result, zeolites are characterized by a well-defined three-dimensional pore network with interconnected spherical cavities or channels. The zeolite's pore size can range from 0.41 nm (zeolite A) to 0.74 nm (zeolite X/Y).

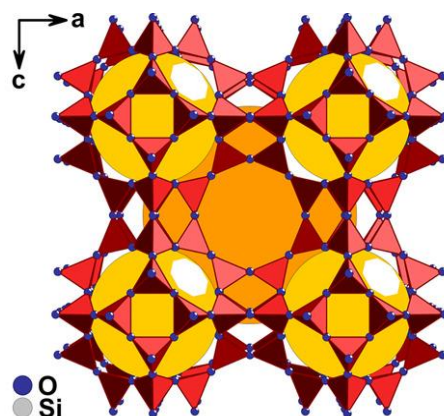


Figure 14 Zeolite framework structure for zeolite A, formed by joining sodalite cages (yellow) through four-membered and six-membered rings. The diameter of the pore opening (orange) is 0.41 nm (the cations in the pores are not specified in the frame structure) [6].

MOFs are nanoporous materials consisting of metal ions and polyatomic organic bridging ligands. Their basic structure consists of bound inorganic nodes (metal ions or metal-oxide cluster ions) with linking to organic molecules such as polydentate carboxylic acids, to form a porous structure. For MOFs, there is no clear unambiguous structure like for zeolite frameworks due to the fact that there is a great number of possibilities for variations in the nodes and bonding

links. Figure 15 shows an example of one of the MOFs (HKUST-1). The pore size of them can vary from microporous to mesoporous. For example, HKUST-1 copper trimesate has a pore diameter of 1.0 nm [109], while MIL-101(Cr) has larger pores of 2.7 nm and 3.2 nm [110]. Due to the larger pore size, MOFs have a higher inner specific surface area compared to zeolites. However, the presence of organic building blocks affects their thermal stability, which in most cases does not exceed 300 °C [6].

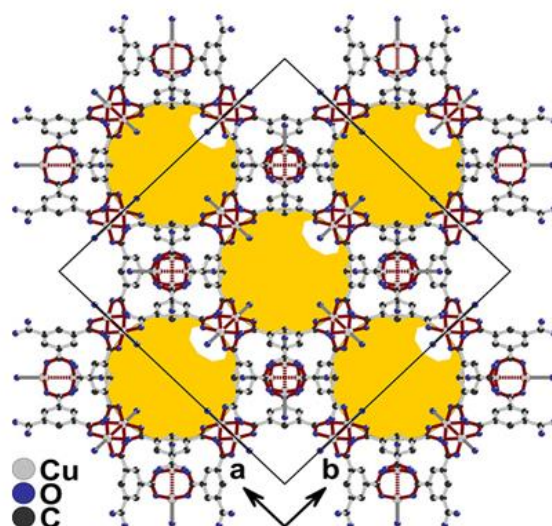


Figure 15 A MOF example HKUST-1: the porous structure consists of  $[\text{Cu}\cdots\text{Cu}]^{4+}$  dumbbells that are connected by trimesate anions (pore diameter 1.0 nm, yellow spheres) [6].

MOFs and zeolites are used or suggested to be in adsorption-driven heat pumps, sorptive extraction of organic sulphides, hydrogen and methane storage, gas separation,  $\text{CO}_2$  capture, microreactor device, or in methanol to olefin conversion [6]. The combination of open-porous ceramic or metal foams with active materials can increase the efficiency of those applications in their systems also due to the irregular pore geometry of the open-porous foam cells, which allows efficient transport of gases or liquids to the microporous adsorbent layer due to a high degree of turbulent flow and radial mixing [111,112]. Thanks to the heat-conductive foam substrate, the sorption heat can be transferred away.

### 2.6.1 SAPO-34: Hydrothermal synthesis, properties, and application

SAPO-34 is an effective catalyst for the conversion of methanol to light olefins and a promising material for adsorption heat pumps, due to its low regeneration temperature ( $T_{\text{reg}} < 100$  °C), suitable S-shaped adsorption isotherm, and sufficient hydrothermal stability [104,113–115].

The crystallization of SAPO-34 on different porous support materials was demonstrated in a great number of studies.

**SAPO-34 crystallization on ceramic and metal foams.** Zeolite/silicone foams with high adsorption capacity without hindering the porous structure of the pure zeolite were obtained in [104], in which 96 % of zeolite in the foam was active for water adsorption. The addition of zeolite had a positive effect on the mechanical properties of the composite.

SAPO-34 was successfully crystallized on SiC open-cell foams with linear cell densities of 10 ppi and 30 ppi by direct hydrothermal crystallization at different crystallization times, 30 h and 45 h [116], which did not affect the thickness of the zeolite coating and the amount of loaded material. The pore size of the ceramic foam did not influence the quality of the crystallized zeolite. At the same time, the amount of deposited zeolite grew with the number of pores due to an increase in the surface area of the foam. Measurements of N<sub>2</sub> sorption showed that the coatings had a Brunauer-Emmett-Teller (BET) surface area equal to pure zeolite powder.

SAPO-34 was also coated on graphite cell structures used in heat exchangers [117]. This composite was obtained by hydrothermal synthesis on pre-oxidized graphite foams to increase the chemical affinity to the zeolite. Zeolite crystallization did not affect the thermal conductivity of the graphite composites. It was also found that the weight fraction of zeolite mainly depended on the volume of the support macropores. The adsorption behavior of the composite was similar to pure SAPO-34.

In [118], SAPO zeolite was crystallized on an aluminum foam using two methods: hydrothermal and microwave heating. The synthesis of the coating by microwave heating significantly reduced the crystallization time from 72 h to 6 h. There were no significant differences in terms of purity and amount of deposited SAPO-34 coatings. However, the SAPO-34 crystallites during microwave heating were characterized by a smaller crystal size. In both cases, the foam weight increased by 15 % and the coatings were homogeneous. The adsorption results showed that there was no difference between the hydrothermal and microwave generated zeolites, despite the different morphology of the coatings. The measured water absorption values were comparable to pure SAPO-34.

**Hydrothermal synthesis of SAPO-34.** There are different methods for the synthesis of SAPO-34 which include rapid high-temperature synthesis, dry gel conversion, microwave, sonochemical and hydrothermal syntheses [119]. One of the easy-to-carry-out and widespread

methods is the hydrothermal synthesis, which was used in this work. Such parameters as temperature and crystallization time, Si source in the reaction mixture, type and concentration of the molecular template are used to control the synthesis kinetics, the morphology and the size of the SAPO-34 crystals [119].

The hydrothermal method is based on the solubility of minerals in water at a temperature above 100 °C and a pressure higher than 1 bar [120]. To create these conditions, the aqueous system for the SAPO-34 synthesis is placed in a stainless steel autoclave with Teflon linings. The mechanism of crystallization is complex, and it is possible to control composition and charge within internal regions in a crystal. This is, however, rather complex and is described elsewhere [121].

From studies of the effect of crystallization time [120,122–124] on crystal synthesis, it follows that there is mainly an increase in crystal size with the crystallization time. This is attributed to the Ostwald ripening phenomenon, in which small crystals dissolve and precipitate onto larger particles. It is seen also from reviewed studies that at short crystallization time, an amorphous phase is formed, which disappears with increasing time. For example, Askari et al. showed in [122] that with a crystallization time of 3 hours at 200 °C an amorphous phase was predominant. Further increase of the crystallization time from 6 h to 24 h produced pure SAPO-34, improved crystallinity and increased crystal size. In the synthesis of SAPO-34, the aggregation of particles occurred rapidly after nucleation, so the crystallization time is the most important parameter in adjusting the size of the crystals. At the same time, a longer crystallization time increased the crystallinity and the surface area in [122,123]. It was also shown in [124] that the surface area and the crystallinity increased with the crystallization temperature.

### **2.6.2 HKUST-1: Properties, crystallization on open-cell foams, and applications**

HKUST-1 was first reported in [109]. It consists of 1,3,5 benzenetricarboxylate (BTC) ligands coordinating copper ions in a cubic lattice with a pore size of 1 nm and has a sky-blue color (Figure 15). Advantages of HKUST-1 include its relatively low crystallization temperature and a high surface area with a theoretical value of 2153 m<sup>2</sup>g<sup>-1</sup>, and a water adsorption capacity of 0.55 g·g<sub>MOF</sub><sup>-1</sup> at 90 % relative humidity [125,126]. The adsorption of nitrogen in HKUST-1 is a two-step process in which first of all small pores with a higher affinity for nitrogen are filled followed by the filling of larger pores [127]. During water adsorption, larger and more hydrophilic pores are filled first [126]. HKUST-1 can be used for hydrogen [128] and methane

storage [129,130]. The combination of open-cell foams with HKUST-1 can be used as heat pumps for sorption cooling, due to adsorption and desorption of water [131], and for gas separation [132].

**HKUST-1 crystallization on ceramic and metal foams.** HKUST-1 was directly crystallized in a polytetrafluoroethylene (PTFE) or Teflon container at 80 °C for 96 h on oxide bond (ob) SiC foams and alumina foams with different cell sizes, varied from 20 ppi to 35 ppi [133]. The influence of an alumina coating, which provides OH groups on the surface, or a silanization process on the foam's surface and the influence on the growth of MOFs was also studied. Differences in the amount of crystallized HKUST-1 depending on the initial substrate were observed. The weight fraction of HKUST-1 in ob-SiC was almost twice that of HKUST-1@alumina coated foam due to a more pronounced surface roughness, which increased the specific surface area of foams for coating and improved the mechanical anchoring of the MOF crystals. An effect of the surface roughness on the crystallization was described in [134]. The alumina coating formed before the silanization also increased the mass fraction of HKUST-1 compared to foams without such coating and decreased the crystal size of HKUST-1, thus for HKUST-1@SiC composite the crystallite size changed from 50 nm to 15 nm. It was discussed that smaller crystals are advantageous for applications based on sorption processes in MOF materials because the diffusion pathways are shorter [132].

An increase of the linear cell pore number of the porous support increased the HKUST-1 loading, consequently the water adsorption, by increasing the specific surface area of the MOF [133]. The alumina sol treatment resulted in increased HKUST-1 loading but led to the formation of non-porous byproducts, which reduced the water uptake capacity of the MOF layer. Composites without alumina sol coating showed water uptake of  $0.53 \text{ g} \cdot \text{g}_{\text{MOF}}^{-1}$  on average, which was in good agreement with the water uptake of pure HKUST-1. The HKUST-1 coating had no significant effect on the thermal conductivity of the composite when compared with the original foams.

HKUST-1 was crystallized on a copper open-cell foam with pore sizes of 20, 40, 60 and 80 ppi, by electrochemical deposition in [132]. The MOF loading varied from 8.7 wt. % for the foam with 20 ppi to 17.6 wt. % for the foam with 60 ppi. With a further increase in the pore number up to 80 ppi, a decrease in the MOF loading was observed, due to the limitation of the reagent transport in the fine porous structure that in [134] led to the formation of  $\text{Cu}(\text{Hbtc})(\text{H}_2\text{O})_3$  needles. The use of copper foam as a support template increased the effective thermal

conductivity by a factor of 1.59 to 27.52, compared to HKUST-1 synthesized by microwave-assisted hydrothermal synthesis and shaped into spheres with a size of 2-3 mm. The time of total water desorption (above 373.15 K) for the composite was shorter as for the MOF powder and the temperature homogeneity within the foam/MOF composite was higher than in the pure HKUST-1 crystalline material. And also the selectivity in gas separation/selective adsorption of CO<sub>2</sub>/N<sub>2</sub> and CH<sub>4</sub>/N<sub>2</sub> at 60 ppi and 80 ppi composites, respectively, was higher for HKUST@copper composite.

## 3 Materials

In this chapter starting materials are described. The sponge replication process based on foam-like polymer templates is shown more in detail, which is the basic manufacturing route within this work. The sponge replication process was combined with freeze processing steps in order to increase the replica foam's strut porosity and, consequently, its specific surface area. To demonstrate a proof of principle for a potential application, the zeolite SAPO-34 and the MOF material HKUST-1 were direct-crystallized on the metal foam surface.

### 3.1 Specimen preparation of metal foams

The preparation of metal foams consists of two main manufacturing routes: sponge replication and a combination of sponge replication and freezing techniques. Each of them is divided into several production steps: preparation of a suspension, coating of the PU template foam with a metal suspension, drying, binder and PU burn-out, and thermal processing. Depending on the starting material (aluminum or copper) and the manufacturing route, such parameters as the suspension composition and thermal processing parameters (temperature, atmosphere, time) were varied. PU templates with different cell sizes (ppi) were used to vary the cell size of the resulting metal foams. The description of the characteristics of the original PU foams is presented in detail in [135].

#### 3.1.1 Starting aluminum and copper powders

As a starting material for the preparation of aluminum foams, two types of aluminum powders were used. The first powder was obtained from Aldrich Aluminum 11010-250G-R (Aldrich Chemie GmbH, Steinheim/Germany), which had the median diameter of the particle size distribution  $d_{50} = 16.6 \pm 0.8 \mu\text{m}$  with 10 vol. % of the particles  $< 5.0 \mu\text{m}$  and 90 vol. %  $< 51.8 \mu\text{m}$ . The second powder was an air-atomized aluminum powder supplied by Ecka Granules (MEP103 RE903, Ecke Granules, Ranshofen, Austria) with a 99.5 % purity with Ti  $< 0.25$  wt. %. The Ecka powder was characterized by a particle amount: 10 vol. %  $< 2.7 \mu\text{m}$ ,  $d_{50} = 6.2 \pm 0.3 \mu\text{m}$ , and 90 vol. %  $< 13.4 \mu\text{m}$ . For manufacturing of the copper foams a powder supplied by Ecka Granules (ECKA Kupfer CH UF 10, Ranshofen, Austria) with 99.81 % purity was used. The powder particle distribution was  $d_{50} = 10.5 \pm 0.5 \mu\text{m}$  with 10 vol. %  $< 3.7 \mu\text{m}$  and 10 vol. %  $> 64.6 \mu\text{m}$ . Detailed characterisation of the as-received powders are performed in Chapters 5.1.1 and 5.3.1.

### 3.1.2 Specimen preparation of aluminum and copper foams by the sponge replication technique

A schematic preparation illustration of the sponge replication technique is shown in Figure 16. For the preparation of replication processed foams (RP foams) metal powders and a 10.7 wt. % solution of a PVA binder (1.2 wt. %, Optapix PA 4G, Zschimmer and Schwarz Chemie GmbH, Lahnstein, Germany) were suspended in distilled water. The solid content of the metal powder in the slurries is shown in Table 2. The metal-containing slurries were mixed in a planetary centrifugal mixer (THINKY Mixer ARE-250, THINKY Corp. Tokyo, Japan) at 2000 rpm for 6 min and cooled to room temperature. After slurry preparation the PU template foams were dipped into the metal slurries. The excess slurry was removed manually. The metal slurry coated PU template foams were dried for 24 hours in air.



Figure 16 Schematic illustration of RP foams preparation.

Table 2 Slurry content and thermal processing conditions of RP foams.

Sample	Metal powder, wt. %	Thermal processing		Atmosphere
		T, °C	Time, h	
Aluminum Aldrich	57.0	750	3	Vacuum
Aluminum Ecka	70.6	600-900		Air, vacuum, Ar
Copper	83.0	500, 900	6	Ar/H <sub>2</sub> with 2 vol. % H <sub>2</sub>

For the preparation of samples, open-cell PU foams (Koepp Schaum GmbH, Oestrich Winkel, Germany) with different linear cell counts (10 ppi, 20 ppi, and 30 ppi) were used. A geometric size of PU template foams was 15 mm × 15 mm × 20 mm and 20 mm × 20 mm × 20 mm; the corresponding metal foams were characterized with respect to their porosity, cellular morphology, and mechanical properties. Metal foams resulting from PU template foams with a geometric template size of 20 mm × 50 mm × 50 mm were used for the thermal conductivity measurement.

After drying the green foams in air the binder and the PU template foams were burned-out in air at 250 °C for 3 h and at 500 °C for 3 h in a circulating air furnace (KU 40/ 04/A,

THERMCONCEPT Dr. Fischer GmbH, Bremen, Germany) with a heating rate of  $1 \text{ K}\cdot\text{min}^{-1}$ . The last step was thermal processing of the metal foams in a conventional tube furnace (alumina tube, HTRH 70-600/1800, Carbolite-Gero GmbH and Co. KG, Neuhausen, Germany). For the aluminum foams, this step was carried out for 3 h in air, vacuum and Ar (purity 99.999 %) atmospheres at  $600 \text{ }^\circ\text{C}$  to  $900 \text{ }^\circ\text{C}$ . The thermal processing of copper foams was carried out for 6 h in Ar/H<sub>2</sub> atmosphere (2 vol. % H<sub>2</sub>) at  $500 \text{ }^\circ\text{C}$  and at  $900 \text{ }^\circ\text{C}$ , respectively (Table 2). The heating and cooling rates were set to  $3 \text{ K}\cdot\text{min}^{-1}$  for both metal-type foams. The flow rate of Ar was  $25 \text{ mL}\cdot\text{min}^{-1}$ , in the case of Ar/H<sub>2</sub> this value was  $80 \text{ mL}\cdot\text{min}^{-1}$ .

### 3.1.3 Specimen preparation of aluminum and copper foams by a combination of sponge replication and freezing techniques

A schematic illustration for the manufacturing of foams by a combination of sponge replication and freeze-drying techniques is presented in Figure 17. The combined replication processed and freeze-dried processed foams were prepared by almost the same manufacturing route as the RP foams but with an additional freezing step and a freeze-drying step in order to generate additional pores in the foam struts. The replication processed and freeze-dried processed foams will be further defined as RP/FP foams.

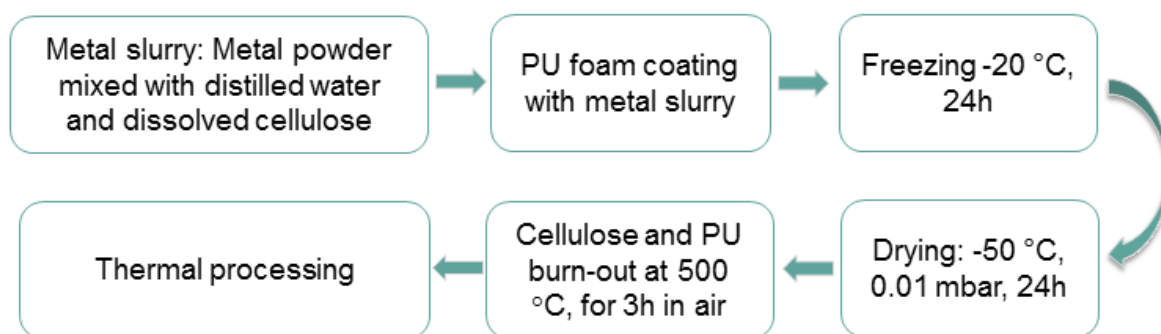


Figure 17 Schematic illustration of RP/FP foam preparation.

The slurry for the preparation of copper foams contained ~73 wt. % of copper powder. The aluminum slurry contained ~54 wt. % of aluminum powder. The slurry content and thermal processing conditions of the RP/FP foams is shown in Table 3. The slurries were prepared in the following way. Methyl-cellulose (Tylose 3000 P, methyl hydroxyethylcellulose, Carl Roth GmbH & Co, KG, Karlsruhe, Germany) was used as an additional thickener to adjust the viscosity of the slurry to a level suitable to prevent drainage off of the aqueous slurry from the PU template foam. 1.5 g of methylcellulose were dissolved in 25 ml distilled water and mixed

with metal powders in a planetary centrifugal mixer at 2000 rpm for 6 min. The PU template foams were dipped into the metal slurries after cooling to room temperature and squeezed to remove the excess slurry. The coated PU template foams with different linear cell count (10, 20 and 30 ppi) were frozen for 24 h at  $-20\text{ }^{\circ}\text{C}$  to obtain water ice dendrites. Drying of the RP/FP foams was carried out in a freeze dryer (Gefriertrockenschrank BETA 1-16 LMC 2, Martin Christ Gefriertrocknungsanlagen GmbH, Osterode, Germany) for 24 h in a vacuum of 0.1 mbar at  $-50\text{ }^{\circ}\text{C}$  to remove residual dendritic water ice crystals from lamellar pores by sublimation. Afterwards, the cellulose and PU burn-out was carried out in air at  $250\text{ }^{\circ}\text{C}$  for 3 h and at  $500\text{ }^{\circ}\text{C}$  for 3 h (Figure 17). Thermal processing of the foams was in Ar atmosphere for 3 h at  $650\text{ }^{\circ}\text{C}$  and  $750\text{ }^{\circ}\text{C}$  for aluminum foams; for copper thermal processing was in Ar/H<sub>2</sub> atmosphere (2 vol. % H<sub>2</sub>) for 6 h at  $900\text{ }^{\circ}\text{C}$ .

Table 3 Slurry content and thermal processing conditions of RP/FP foams.

Sample	Metal powder, wt. %	Thermal processing		Atmosphere
		T, $^{\circ}\text{C}$	Time, h	
Aluminum Ecka	54	650, 750	3	Ar
Copper	73	900	6	Ar/H <sub>2</sub> with 2 vol. % H <sub>2</sub>

### 3.2 Direct crystallization of zeolites and MOFs onto the surface of aluminum and copper foams

In this subsection, direct crystallization of the SAPO-34 zeolite and HKUST-1 MOF on RP and RP/FP aluminum and copper foams is described including post-processing. Materials characterization and properties analysis will follow in a separate chapter.

#### 3.2.1 Direct crystallization of SAPO-34 onto the surface of aluminum foams

RP and RP/FP aluminum foams were used for direct crystallization of SAPO-34 after their thermal processing. The in situ crystallization procedure by hydrothermal synthesis was adapted from the approach described in [136]. The starting materials used to synthesize SAPO-34 were catapal B (Sasol) as an alumina source, orthophosphoric acid (85 %), morpholine (Sigma-Aldrich,  $\geq 99\text{ }%$ ) as an organic template, and fumed silica (Aerosil 200, Evonik Industries). The molar composition of the initial reaction mixture is given as  $\text{Al}_2\text{O}_3 : \text{SiO}_2 : \text{P}_2\text{O}_5 : 2\text{ morpholine} : 60\text{ H}_2\text{O}$ . Phosphoric acid and alumina were mixed with distilled water and stirred for 6 h to form a homogeneous gel. A second mixture was prepared by mixing fumed silica and morpholine in distilled water while stirring. This mixture was then added dropwise to the first mixture while stirring. The resulting gel was aged for 24 h at  $27\text{ }^{\circ}\text{C}$ . The aluminum

foams were then placed in a PTFE lined stainless steel autoclave with the reaction mixture on an additional Teflon distance holder on the bottom of the autoclave so that the remaining crystallized material was underneath the sample (Figure 18 a). This was to obtain a more uniform distribution of the crystallized SAPO-34 on the metal foam. For comparison, Figure 18 b,c shows the prepared samples without and with Teflon distance holder. A large amount of crystallized SAPO-34 can be seen on the part of the samples that was immersed in the formed crystallized zeolite compared to the sample placed on the Teflon substrate.

The total volume of the autoclave was 60 mL. For the preparation of the synthesis gel per autoclave filling 2.41 g Catapal B, 3.93 g phosphoric acid, 1.02 g fumed silica, 2.97 g morpholine, and 16.22 g water were taken. Crystallization was performed under autogenic pressure at 200 °C for 5, 15, and 24 h. Afterward, the coated foams as well as the solid part accumulated at the bottom of the autoclave were washed and dried at 110 °C for 24 h. The samples were finally calcined at 550 °C for 2 h to remove the organic template (Figure 18 d).

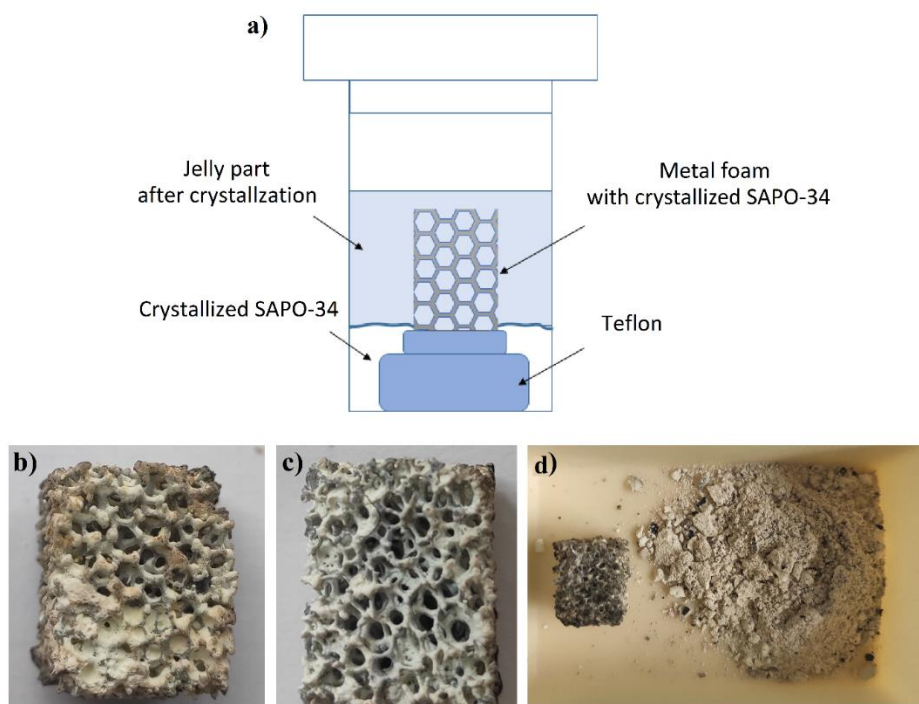


Figure 18 Schematic illustration of a PTFE-lined stainless steel autoclave with a Teflon distance holder after crystallization of SAPO-34 on the surface of aluminum foam (a); RP/FP aluminum foam with SAPO-34 after calcination for 15 h without (b) and on (c) Teflon distance holder; RP/FP aluminum foam with SAPO-34 and collected SAPO-34 powder after calcination (d).

### 3.2.2 Direct crystallization of HKUST-1 onto the surface of copper foams

The HKUST-1 coating was carried out by direct crystallization by placing conditioned foam samples into the HKUST-1 synthesis gel. The crystallization was carried out in a PTFE-lined

stainless steel autoclave and/or in a polyvinylfluoride (PVF) container with a total volume of 60 ml. The synthesis gel per autoclave filling was obtained by mixing 1.957 g (8.1 mmol)  $\text{Cu}(\text{NO}_3)_2 \cdot 3\text{H}_2\text{O}$  dissolved in 15 ml distilled water with a solution of 0.968 g (4.6 mmol) trimesic acid and 15 ml ethanol. The crystallization step was at 80 °C for 6, 14, 24, and 96 h in a circulating air oven (KU 40/04/A, Thermconcept Dr. Fischer GmbH, Bremen, Germany). After cooling to room temperature, the coated samples were washed with demineralized water. Traces of trimesic acid in the HKUST-1 framework were removed by an activation procedure in ethanol in the autoclave/container at 70 °C for 24 h. After that, samples were placed in a lab furnace to dry at 110 °C for 24 h. The weight of the deposited HKUST-1 was calculated as a weight difference between the initial thermal processed copper foams before and after crystallization and drying.

## 4 Characterization

In this chapter the methods for the materials characterizing the aluminum and copper powders, the RP and RP/FP foams without and with crystallized zeolites and MOFs are described. After a brief description of the theoretical background of the respective method, the instrumental parameters for each method/for the equipment are described.

### 4.1 Thermal analysis

#### 4.1.1 Differential scanning calorimetry and thermogravimetric analysis

Differential scanning calorimetry (DSC) and thermogravimetric analysis (TGA) are two of the most used thermal analysis methods for the characterization of materials. DSC is used to determine how much energy a sample absorbs or releases during heating or cooling, which indicates exothermic or endothermic reactions; a chemical reaction is related to a mass change, while phase transitions show no weight change but are accompanied by release or absorption of energy. A mass change is detected by TGA. Thus, with a combination of DSC and TGA temperature intervals of chemical reactions, phase transitions or decomposition processes can be identified. In this context it is important to select the right atmosphere for the carrier gas; this is typically synthetic air, argon or nitrogen.

In this work, DSC and TG analysis was carried out using a STA 449 F3 Jupiter thermal analyzer (Netzsch-Gerätebau GmbH, Selb, Germany) to study the change in weight and the onset of oxidation of the metal powders in air. The metal powders were heated from room temperature to 600 °C (aluminum powders) and to 1000 °C (copper powder) with a heating rate of 10 K min<sup>-1</sup> and an airflow rate of 50 ml min<sup>-1</sup>.

#### 4.1.2 Thermal conductivity

Typically, metal foams have a significantly lower thermal conductivity coefficient than bulk materials. Porosity, impurities, and grain size can adversely affect the thermal properties of the samples. The well-established Hot Disk Transient Plane Source TPS 2500 S (Hotdisk SE, Gothenburg, Sweden) was used for the measurement of the thermal conductivity of metal foams [137]. It is a fast, non-destructive and accurate method for measuring the thermal conductivity. The calculation of the thermal conductivity coefficient is carried out using a temperature change sensor [138].

During the measurements, the sensor with a diameter of 9.868 mm was placed between two polished samples made with PU templates with a geometric size of 20 mm × 50 mm × 50 mm, Figure 19. The heating power of the sensor was 150–200 mW for 5–10 s per measurement. Each combination of the largest sides was measured five times. Then the samples were turned to measure all combinations of sides. A total of 20 measurements from four combinations of sides were obtained per series of samples for the calculation of the average thermal conductivity.

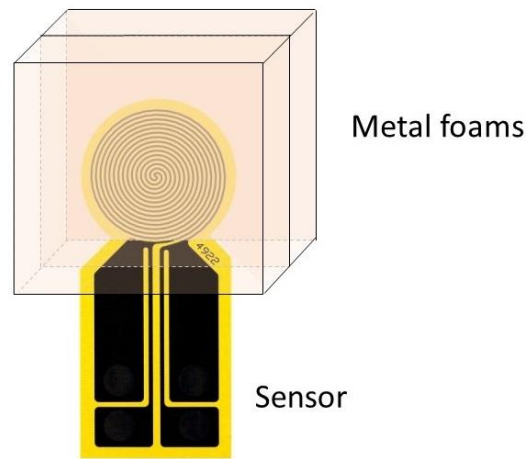


Figure 19 Schematic illustration of the thermal conductivity measurement.

With the values of the thermal conductivity, it is possible to evaluate the effect of pores in struts, impurities, and microstructure on it. A model derived by Ashby [19] was used to estimate the influence of porosity in struts on the thermal conductivity, Equation (2):

$$\lambda_s = \frac{\lambda_f - P_{cell} \cdot \lambda_g}{1/3 \cdot (1 - P_{cell})}, \quad (2)$$

where  $\lambda_s$  is the thermal conductivity of the porous strut material excluded the porosity within the strut,  $\lambda_g$  is the thermal conductivity of the gas phase (air) which is 0.0264 W·m<sup>-1</sup>K<sup>-1</sup> [19], and  $P_{cell}$  is the cell porosity. A model derived by Eucken was used to compare the thermal conductivity of the bulk strut material  $\lambda_b$  and the bulk material [139]:

$$\lambda_s = \lambda_b \frac{1 + 2P_s \cdot (1 - \frac{\lambda_g}{\lambda_b}) / (2\frac{\lambda_g}{\lambda_b} + 1)}{1 - 2P_s \cdot (1 - \frac{\lambda_g}{\lambda_b}) / (2\frac{\lambda_g}{\lambda_b} + 1)}, \quad (3)$$

where  $P_s$  is the strut porosity excluding the hollow strut cavities and  $\lambda_s$  is the thermal conductivity of the porous strut material as calculated in Equation (2). The difference between

the thermal conductivity of the bulk strut material and the bulk material may be used to indicate impurity and grain boundary effects on the thermal conductivity of metal foams.

## 4.2 Micro- and macrostructure characterization

### 4.2.1 X-ray diffraction analysis

The main purpose of this method of analysis is to identify the different phases in their mixtures based on the analysis of the diffraction pattern of the samples studied. A compound in the mixture is identified by the set of its interplanar distances and the relative intensities of the corresponding lines in the X-ray diffractogram. Coherently scattered X-rays interfere with each other, with the crystal lattice as a diffraction lattice for X-rays, because the interplanar distances in the crystal are comparable to the wavelength of the radiation [140].

For X-ray diffraction analysis (XRD), an X'Pert Pro diffractometer (PANalytical GmbH, Kassel, Germany, Co  $K\alpha_{1/2}$  radiation,  $2\theta$ , 10–85°) with a Bragg–Brentano reflection geometry was used. The Topas Academic V5 software package was used to determine the phase composition with subsequent Rietveld analysis [141]. Prior to the phase analysis, the samples were prepared for measurements. The aluminum foams were thermally processed in air and vacuum and copper foams after the binder and PU were crushed and milled, the resulting powders were loaded into sample holders with reverse loading. Thermally processed aluminum foams in argon and copper foams in Ar/H<sub>2</sub> atmosphere were compressed to obtain a planar surface for measurement in reflection geometry.

Phase analysis of HKUST-1 and SAPO-34 was carried out from as-collected material from the autoclave's bottom, partially from material scratched off from the metal foam struts. The theoretical powder diffractograms were calculated from HKUST-1 and SAPO-34 crystal structure data obtained from the Crystallographic Open Database (COD) [142] and the IZA Atlas [143] of Zeolite Compounds using the computer program VESTA Ver. 3.5.7. The COD identifier is 2300380 for HKUST-1; for SAPO-34 the structural data for the chabazite (CHA) framework was used.

### 4.2.2 Scanning electron microscopy

A scanning electron microscope (SEM) is a tool for surface imaging of an object with a high spatial resolution of up to 0.4 nanometers. In combination with specific wavelength disperse or energy disperse X-ray detector (EDX) compositional analysis can be carried out with a small detection area of some ten  $\mu\text{m}^2$ . SEM is based on the principle of the interaction of an electron

beam with an object. The principle of operation of the SEM is as follows: the electrons emitted by the electron gun aligned in the SEM pillar are accelerated to an energy of 2 keV to 40 keV; a set of magnetic lenses and deflecting scan coils form a small diameter electron beam that is scanned into a raster on the sample surface. When this surface is irradiated with these electrons, three types of radiation are generated: reflected or backscattered electrons, secondary electrons, and X-rays. Typically, secondary and/or reflected (backscattered) electrons are used to obtain topology information from the surface and near the surface regions of the samples. The contrast of secondary electrons depends most of all on the surface topography, while the reflected electrons carry information about the electron density distribution in an object (e.g. areas enriched with an element with a higher atomic number appear brighter). Consequently, backscattered electrons, which are generated simultaneously with secondary electrons, contain information about the composition. Irradiation of the sample with an electron beam leads not only to the formation of secondary and reflected electrons but also to a characteristic X-ray emission. EDX detectors allow the analysis of the elemental composition of a sample, either by spot or by line and area scanning.

A SEM of the type XL30 ESEM-FEG (FEI, Hillsboro, USA) with an integrated EDX analysis system (DX-4, EDAXBusinessUnit, AmetekGmbH, Meerbusch, Germany) was used for sample analysis and characterization. For the analyses of powders and the single strut morphology of foams, polycarbonate/graphite adhesive plates (Plano GmbH) were used to mount the samples. For cross-sectional analysis the foams were immersed in an epoxy resin, and after hardening of the resin, the surface was ground with grinding paper with increasing mesh number (180, 320, 600, 800, 1200, 2500, 4000 mesh; in this sequence), and polished with diamond suspension with an average particle size of 3  $\mu\text{m}$  and 1  $\mu\text{m}$ . For the grains structure investigation of the copper samples, the foams were chemically etched in a solution of 100 ml of distilled water with 10 g of ammonium persulfate  $(\text{NH}_4)_2\text{S}_2\text{O}_8$  for 30 s. The ImageJ 1.48s software (National Institutes of Health, USA) was used to measure the average grain size.

A sputter coater (K550 Sputter Coater, Quorum Technologies Ltd, Kent, USA) was used to sputter gold on the surface of samples embedded in epoxy. This was necessary to provide electric conductivity to the foams in order to avoid charging effects during secondary electron bombardment.

### 4.2.3 Microcomputer tomography

Optical and scanning electron microscopy are useful tools for microstructural analysis. However, both methods provide surface or near-surface information of a sample. Since the wall strut thickness, the thickness of material lamellae, and the lamellar pore thickness in metal foams are not uniformly distributed, a cross-section microscopy analysis is insufficient for a three-dimensional characterization of these structural elements. Methods for measuring the total porosity, such as the Archimedes method or pycnometer, do not provide sufficient information to characterize the size, shape, and location of pores throughout the foams. X-ray microcomputed tomography ( $\mu$ -CT), in contrast to the methods mentioned before, is a reliable tool for non-destructive layer-by-layer examination of the internal structure of objects, which makes it possible to determine defects, pore size and their distribution in materials, estimate the surface area of objects, and obtain a three-dimensional image after reconstruction and stacking of layer images.

X-ray  $\mu$ -CT became the technique of choice for the reconstruction of an image obtained by circular scanning of an object with an X-ray beam. The method is based on the measurement and complex computer processing of the difference in the attenuation of X-ray radiation with different materials. With the help of a Fourier transform algorithm, 2D side-view projection images create a set of horizontal cross-sectional images that are combined to produce a complete 3D map of a specimen.

The structural analysis and determination of geometric values were carried out using a  $\mu$ -CT (Phoenix Nanotom S, GE Sensing&Inspiration, Wunstorf, Germany) with the Fast Scan mode and with an exposure time of 1000 ms per projection image. Different values for the current and the voltage of the X-ray tube were adjusted for the measurement of copper and aluminum foams. Copper foams were measured with a current of 50  $\mu$ A and a voltage of 100 kV, and 60  $\mu$ A and 120 kV were applied for aluminum foams. A 0.1 mm copper sheet was used as a filter to avoid beam hardening artifacts for measurements of copper specimens.

Single struts were analyzed instead of larger foam pieces for the calculation of the wall strut thickness ( $D_{ws}$ ), the thickness of material lamellae ( $D_{ml}$ ), lamellar pore thickness ( $D_{lp}$ ), and the ratio of the foams surface area-to-the-volume of the foam material ( $Obj.S/Obj.V.$ ), see Figure 20. This resulted in a higher resolution, and an example is shown in Figure 20. The voxel size of the measured struts was 3  $\mu$ m. The strut thickness ( $D_s$ ) and the cell size were measured and

calculated from intact foams thermally processed from  $15\text{ mm} \times 15\text{ mm} \times 20\text{ mm}$  PU template foams. An adjusted voxel size was  $7\mu\text{m}$ .

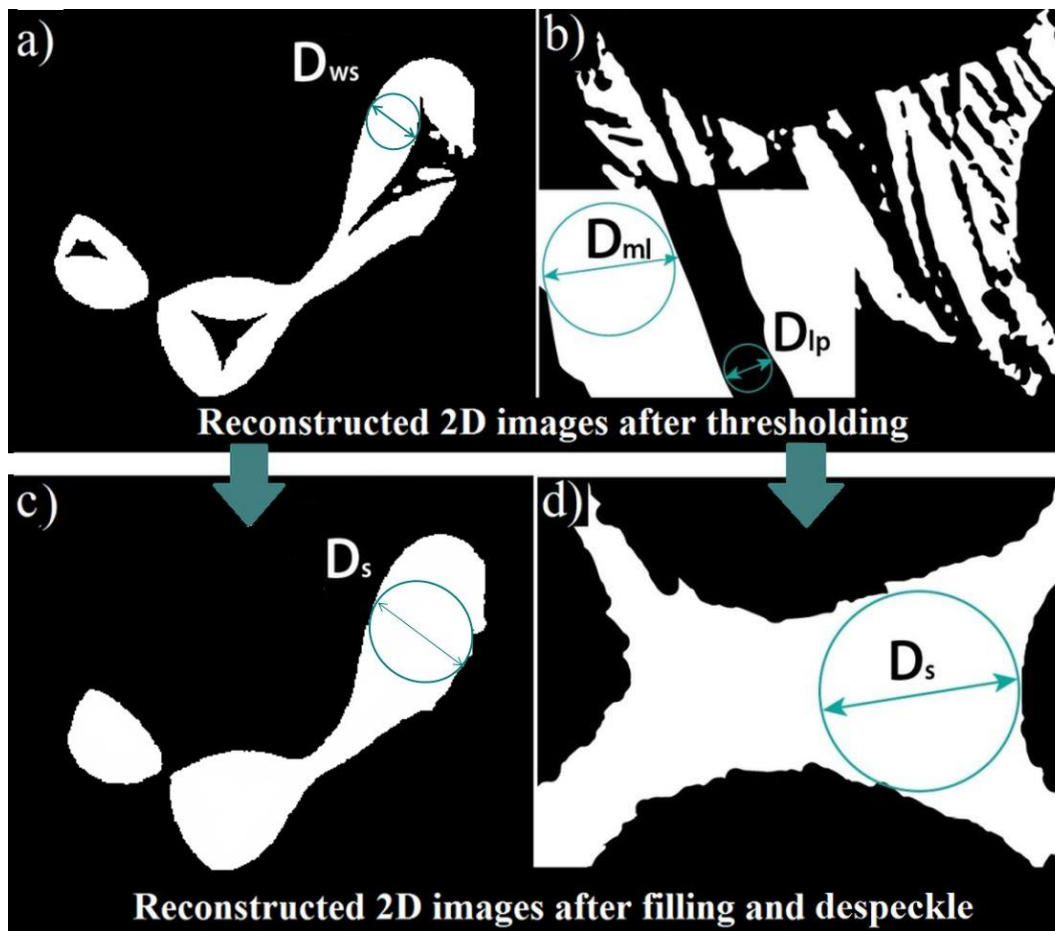


Figure 20. Example of a 2D image reconstruction after thresholding (a,b) and after filling and despeckle (c,d) of a foam manufactured by the sponge replication technique (a,c) and of a foam manufactured by the combination of sponge replication and freezing techniques (b,d). Schematic illustration of wall strut thickness ( $D_{ws}$ ), thickness of material lamellae ( $D_{ml}$ ), lamellar pore thickness ( $D_{lp}$ ), and strut thickness ( $D_s$ ) measurements (adapted from [13]).

The reconstruction of the 3D sample volume from the collected radiographs was carried out using the software PhoenixDatos|XV2.0 (GE Sensing & Inspection Technologies GmbH, Wunstorf, Germany). The reconstructed data were evaluated either with the software myVGL 2.1.4 (Version 4.0.0, Volume Graphics GmbH, Heidelberg, Germany), which was mainly used to view the reconstruction models and create cross-sections with false-color images depending on the gray value histogram or with the software CTAnalyzer 1.16 (CTAn, Skyscan/Bruker microCT, Kontich, Belgium).

The software package CTAnalyzer (CTAn V1.16, Skyscan/Bruker microCT, Kontich, Belgium) was applied to perform calculations of the distribution of the cell size,  $D_{ws}$ ,  $D_s$ ,  $D_{ml}$ , and  $D_{lp}$ . A differential thresholding technique described in [144] was used to adjust the

CTAnalyzer data import and binarization steps prior to the actual morphological calculations. After the binarization was completed, a threshold step was implemented, and a 3D analysis was performed using the CTAnalyzer to calculate the geometric parameters of the foams. A reconstructed 2D image of foams after thresholding is shown in Figure 20 a,b.

The foams were filled in the 2D space after thresholding using the closing function called morphological operation for the calculation of the cell size,  $D_s$ , and  $Obj.S/Obj.V$ . The kernel type with a radius of  $\sim 6-10$  was used for copper foams and aluminum foams. Afterwards, the remaining cavities, e.g. air bubbles, within the area up to 8000–10000 pixels were removed with the despeckle operation. The strut filling and despeckle are illustrated in Figure 20.

The calculation of the specific surface area per mass was carried out through the measured surface-area-to-volume ratio  $Obj.S/Obj.V$  divided by the material density. In this work,  $Obj.S/Obj.V$  values after thresholding (with hollow struts and lamellar pores) and after filling and despeckle (without hollow struts and lamellar pores) were used to compare the influence of hollow strut and lamellar pores on the specific surface area of the foams, Figure 20. The bulk density of pure aluminum and copper and the actual material density after thermal processing can have different values. Aluminum and copper tablets were prepared from the metal slurries described in Chapter 3.1.2 to determine the material density. These tablets were dried for 24 h. The thermal processing after binder burn-out was carried out for 3 h in Ar at 650 °C for aluminum tablets and for 6 h in Ar/H<sub>2</sub> atmosphere at 900 °C for copper tablets. The material density of the thermally processed tablets was  $\sim 8.7 \text{ g}\cdot\text{cm}^{-3}$  for copper and  $\sim 1.6 \text{ g}\cdot\text{cm}^{-3}$  for aluminum.

#### 4.2.4 Determination of the foam porosity

Pores in a porous material are one of the most important structural characteristics, since they largely determine the mechanical, thermal or electrical properties, etc. The porosity is divided into open and closed. Open pores are connected to each other and to the external environment. Closed pores are sealed/isolated in the foam struts. Various methods are used and combined to measure both types of porosity. This part shows methods that have been used to determine the porosity of copper foams and aluminum foams.

**Total porosity.** The total porosity ( $P_{total}$ ), consisting of open and closed pores, is based on the calculation of the geometric foam density and the skeletal relative density ( $\rho_{rel}$ ) of the strut

material and is defined as the ratio of the total pore volume ( $V_{pores}$ ) to the total foam volume ( $V_{foam}$ ) [145]. The calculation of  $P_{total}$  is defined in the equation:

$$P_{total} = 1 - \rho_{rel} = \frac{V_{pores}}{V_{foam}}. \quad (4)$$

There is a great number of methods to measure the total porosity of struts, open or closed porosity in various size ranges, such as the Archimedes method or ultrasonic methods [146,147], gas pycnometry [148,149], and  $\mu$ -CT [32,33]. The most common non-destructive methods for the porosity analysis are the Archimedes method and  $\mu$ -CT, which were used in this work.

**Archimedes method.** This method determines the density of foams by measuring the foam mass in air and in an infiltrating fluid of known density. This measurement was carried out with water as an infiltrating fluid according to DIN EN 623-2:1993-11 standard procedure [152]. The Archimedes method is the most economic and fastest procedure for determining porosity [150]. In the first step, the sample is weighted in air ( $m_{dry}$ ). Then the sample is submerged in the liquid to get  $m_{sub}$ . The sample is soaked with the liquid by wetting and infiltration and weighted again ( $m_{wet}$ ). The open porosity of the foam ( $P_{open}$ ) is the difference between  $m_{wet}$  and  $m_{dry}$  divided by the difference between  $m_{wet}$  and  $m_{sub}$ :

$$P_{open} = \frac{m_{wet} - m_{dry}}{m_{wet} - m_{sub}}. \quad (5)$$

The above-obtained results of the foam weight can be used to calculate the total foam porosity ( $P_{total}$ ) and the closed porosity ( $P_{closed}$ ):

$$P_{total} = 1 - \rho_{rel} = 1 - \frac{\rho_{bulk}}{\rho_{theo}}, \text{ where } \rho_{bulk} = \rho_{water} \frac{m_{dry}}{m_{wet} - m_{sub}} \quad (6)$$

$$P_{closed} = P_{total} - P_{open}, \quad (7)$$

where  $\rho_{theo}$  is the theoretical density of bulk material and  $\rho_{bulk}$  is the bulk material density of foams. The cell porosity ( $P_{cell}$ ) of the foams consists of the cavities after PU template burn-out ( $V_{hollow\ strut\ pores}$ ), open and closed materials pores ( $V_{material\ pores}$ ) surrounded by the volume of material without any pores ( $V_{material}$ ):

$$P_{cell} = \frac{V_{foam} - V_{material} - V_{material\ pores}}{V_{foam}}, \quad (8)$$

$$V_{material} = \frac{m_{dry}}{\rho_{theo}}, \quad (9)$$

$$V_{material\ pores} = \frac{m_{dry}}{\rho_{bulk}} - \frac{m_{dry}}{\rho_{theo}} - V_{hollow\ strut\ pores}. \quad (10)$$

The total strut porosity ( $P_s$ ) is related to the overall strut volume:

$$P_s = \frac{V_{hollow\ strut\ pores} + V_{material\ pores}}{V_{material} + V_{material\ pores} + V_{hollow\ strut\ pores}}. \quad (11)$$

The cavities volume  $V_{hollow\ strut\ pores}$  is based on the volume of the PU template foam calculated in [153], which was corrected by the volumetric shrinkage of the manufactured foams after thermal processing.

There are some challenges associated with the method, such as the attachment of air bubbles to the foam surface leading to lower density values. In addition, it is not possible, as described in DIN EN 623-2: 1993-11, to release adhered water from the partially rough surface of a sample, which leads to an overestimated porosity. To solve these problems, the foams were placed in an ultrasonic bath to completely fill the foam pores with water. A small amount of surfactant was added to the water to reduce the surface tension and to improve the wettability.

### 4.3 Mechanical properties

Figure 21 illustrates a typical stress-strain curve of an aluminum or copper foam in the compression mode. The compressive strength of metal foams is characterized by the elastic-plastic deformation, which can be generally divided into three regions, see Chapter 2.2 [20,21]. The compressive yield strength ( $\sigma$ ) is equal to  $\sigma_{pl}^*$  (Figure 2) in foams developed in this work.

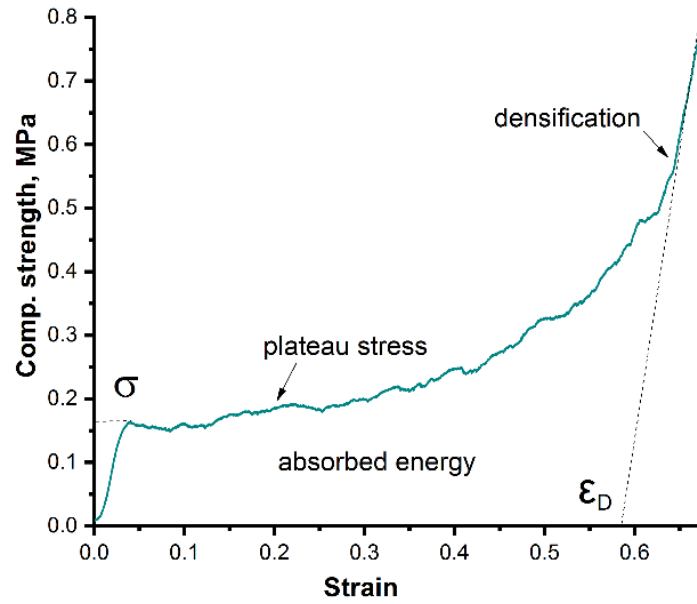


Figure 21 Compressive stress-strain curves of copper foams manufactured by the sponge replication technique, where  $\sigma$  is the compressive yield strength and  $\epsilon_D$  is the densification strain.

A TIRAtest 2825 testing machine (TIRA GmbH, Schalkau, Germany) was used for the uniaxial compressive strength test, in which foams were placed between loading plates with 150 mm in diameter. The applied load was  $2 \text{ mm} \cdot \text{min}^{-1}$ . At least ten foams were measured to calculate the compressive yield strength [154]. The software package Visual-XSe114.0 (CRGRAPH, Starnberg, Germany) was applied to determine the average value of the compressive yield strength. For the calculation of the energy absorption capacity of the foams the integrated area under the stress-strain curve was used according to Equation (12) [20]:

$$W = \int_0^{\epsilon_D} \sigma(\epsilon) d\epsilon, \quad (12)$$

where  $W$  is the energy absorption per unit volume and  $\epsilon_D$  is the densification strain, which is schematically shown in Figure 21.

For the comparison of the relative strength of the samples with different cell sizes and different preparation techniques (sponge replication technique and its combination with freeze-drying), the Gibson and Ashby model, Equation (1), was used in [19,20]. Since in this work  $\sigma = \sigma_{pl}^*$ , the Gibson-Ashby equation has the form:

$$\frac{\sigma}{\sigma_b^*} = C \cdot \left( \frac{\rho^*}{\rho} \right)^n, \quad (13)$$

where  $\sigma_b^*$  and  $\rho$  were 69 MPa and  $8.96 \text{ g cm}^{-3}$  for the copper foams, respectively, and 29.4 MPa and  $2.73 \text{ g cm}^{-3}$  for the aluminum foams [155]. The empirical values of these constants were

taken for the Gibson-Ashby model curve with  $C = 0.3$  and  $n = 1.5$ . The  $n$  parameter was varied for the obtained results of the measured compressive yield strength.

#### 4.4 Analysis of the microporous-component HKUST-I and SAPO-34 and water adsorption capacity

The crystallized-material loading was determined according to the following equation:

$$\text{Material loading} = \frac{m_{\text{foam+material}} - m_{\text{foam}}}{m_{\text{foam+material}}} \cdot 100\%, \quad (14)$$

where  $m_{\text{foam+material}}$  is the weight of the foam after crystallization and drying at 110 °C for 24 h;  $m_{\text{foam}}$  is the weight of the initial metal foam after thermal processing.

Water adsorption measurements were carried out in saturated brine at 75 % RH for 24 h at room temperature for aluminum composite foams and for 7 days at the same RH level for the copper composite foams. Then the samples were weighted to calculate the absorbed water by the microporous component according to the equation:

$$\text{Water uptake} = \frac{m_{\text{after water adsorption}} - m_{\text{foam+material}}}{m_{\text{foam+material}}} \cdot 100\%, \quad (15)$$

where  $m_{\text{after water adsorption}}$  was the weight of the foam with crystallized material after water adsorption.

Aluminum foams with crystallized SAPO-34 used for cycle water adsorption/desorption testing were dried at 110 °C for 24 h before starting the next water adsorption cycle in saturated brine at 75 % RH for 24 h at room temperature. After that, the samples were stored in a desiccator over silica gel (0% RH) [156].

#### 4.5 Determination of the specific surface area by the BET-method of foam composites

Brunauer-Emmett-Teller (BET) surface area analysis is used to measure the surface area of solid or porous materials based on the physical adsorption of gas molecules on a solid surface. In this method, the specific surface area of samples, which includes surface irregularities and pores, is determined on an atomic level by the adsorption of an inert gas. Nitrogen is usually used as the gaseous adsorbate; therefore, the standard BET analysis is carried out at the boiling point of nitrogen. Argon, carbon dioxide, or water may also be used as an adsorbate. For proper interaction of gas and surface, the sample is cooled in liquid nitrogen (-196 °C) and kept

constant while the partial pressure gas increases stepwise. As the relative pressure increases, more and more molecules are adsorbed by the surface of the sample. The result is that the surface of the sample is covered by a thin monolayer of gas molecules. The number of gas molecules in the monolayer is then recorded by the adsorbed volume, which is used to calculate the specific surface area by knowing the cross-sectional area of the adsorbate. In this study, the specific surface area of aluminum foams with crystallized SAPO-34 was measured with a Micromeritics ASAP 2020 at  $-196\text{ }^{\circ}\text{C}$  ( $p/p_0 \geq 0.005$ ).

## 5 Results and discussion

In this chapter, results will be presented, discussed, and evaluated within the scope of this work. The characterization of the starting metal powders (aluminum and copper) for further manufacturing of the RP and RP/FP foams are presented. A comparison of the RP and RP/FP foams after thermal processing is carried out, and the influence of the processing parameters and cell size of the initial PU foam on the porosity, phase content, geometrical, mechanical, and thermal properties is discussed. The last subsection is focused on the direct crystallization of SAPO-34 and HKUST-1 onto RP and RP/FP aluminum and copper foams. Part of the results is taken from [13,36,157–160], which were published in the frame of this work.

### 5.1 Aluminum foams manufactured by the sponge replication technique and investigation of their properties

Starting powders and thermal processing parameters such as atmosphere, temperature, and processing time have a significant influence on the properties of the resulting foams [29,47]. RP aluminum foams were prepared from different aluminum powder and at varying temperatures and atmospheres in this part. The structure, powder sintering behavior, porosity, phase content, mechanical and thermal properties of the foams were analyzed. The most optimal thermal processing parameters were selected for further preparation of RP/FP foams. The influence of the cell size of the PU template on the total porosity, specific surface area, mechanical and thermal properties of RP foams was also investigated and evaluated.

#### 5.1.1 As-received aluminum powders

The SEM images of the Aldrich and Ecka powders and the XRD phase analyses are shown in Figure 22. The Aldrich powder was characterized by a flaky and irregular shape of the particles. Some cracks were identified on the powder surface. From the SEM image of the Ecka powder, it was followed that the particles' surface was smooth and had a spheroidal geometry. The results of the XRD phase analyses showed an aluminum phase only for both types of aluminum powders. No impurities or oxides were detected, possibly due to their amount was below the resolution of the XRD method or the oxides were in an amorphous state.

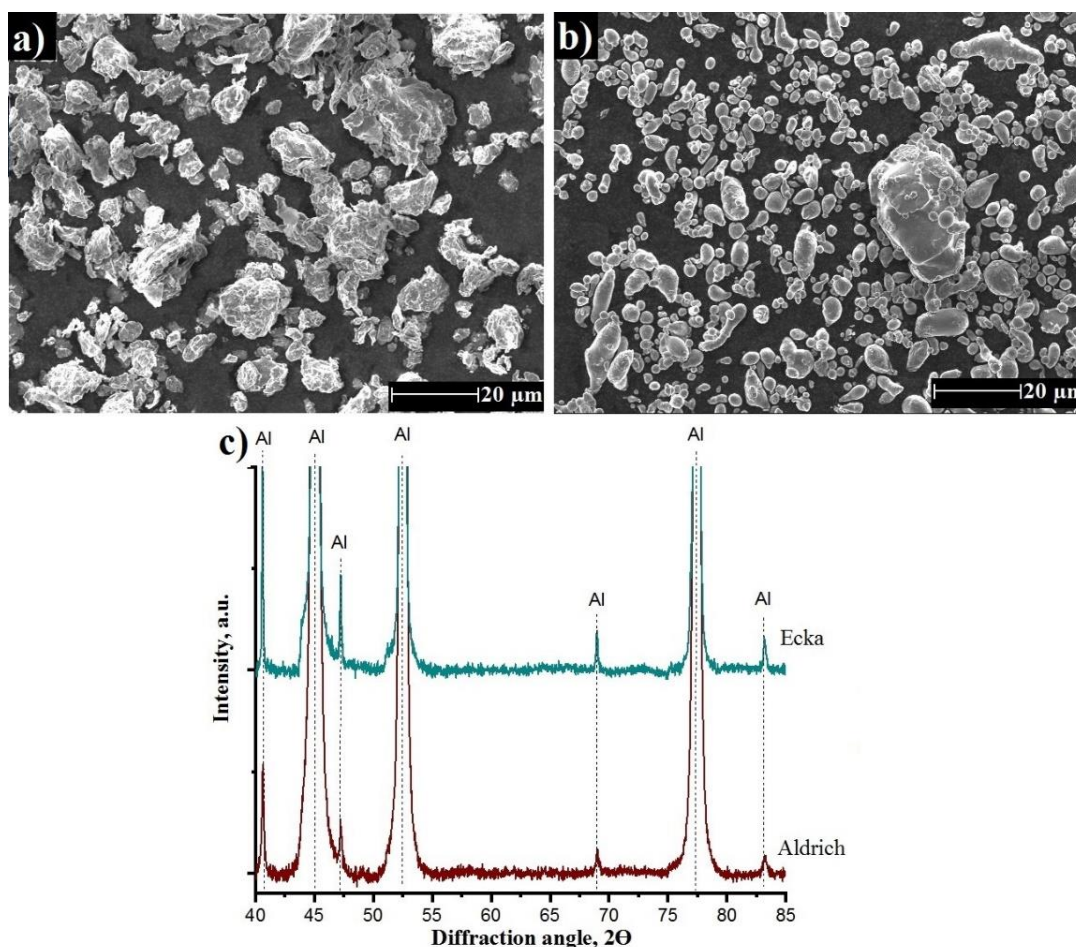


Figure 22 SEM images of the Aldrich (a) and Ecka (b) powders; XRD diffractograms of as-received Aldrich powder (red curves) and Ecka powder (green curves) (c) (adapted from [157]).

The results of the TG and DSC analysis of both powders are shown in Figure 23. The mass loss below 400 °C may be caused by desorption of adsorbed gaseous species or water vapor from the powders' surface. DSC analyses showed an exothermic peak for both powders, which were assigned to the oxidation of aluminum in the presence of air, and an endothermic peak at slightly higher temperatures, which were assigned to the melting of the aluminum powders. The flake-shaped Aldrich powder's oxidation peak was located at ~586 °C, and that of the spheroidal-shaped Ecka powder was at ~580 °C. The melting peaks were at ~660 °C for the Aldrich powder and at ~665 °C for the Ecka powder. This difference in melting temperatures of the Ecka powder and the melting temperature of plain aluminum ( $T_m \approx 660$  °C [161]) might be associated with some impurities, which were not detected by XRD analyses. According to the supplier's information, the Ecka powder contained a small amount of titanium (< 0.25 wt. %).

An intensive weight gain was observed with the onset of the oxidation reaction until the onset of the endothermic reaction of both powders. The Aldrich powder was characterized by higher weight gain in comparison with the Ecka powder. For the Aldrich powder, the total weight gain

was 18 wt. % at 750 °C, for the Ecka powder this value was 3 wt. %. It follows that the Aldrich flaky powder with larger powder particles oxidized more quickly than the Ecka spheroidal powder with smaller powder particles. However, active oxidation up to 500 °C, a temperature necessary for the binder and PU template burn-out step, was not found for the aluminum powders. The oxidation behavior of the starting powders in air has to be taken into account for the manufacturing of the metal foams.

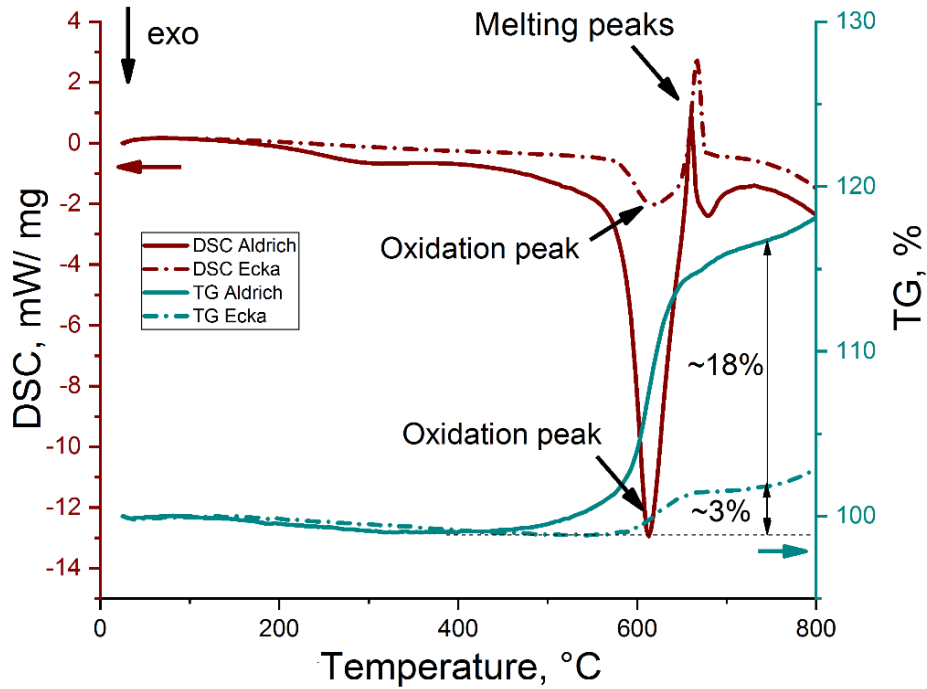


Figure 23 TG (green) and DSC (red) curves of as received Aldrich (straight line) and Ecka (dash dot line) powders in air; the heating rate was 10 K min<sup>-1</sup> (adapted from [157]).

### 5.1.2 Aluminum foams prepared from different starting powders

SEM images of selectively broken struts and cross-sections of the aluminum foams after thermal processing at 750 °C for 3 h in vacuum are shown in Figure 24. A PU template foam with a cell size of 20 ppi and a geometric size of 20 × 20 × 20 mm was used for the manufacturing of foams. It can be seen from Figure 24 that the struts of the foam were hollow and were characterized by a non-uniform porous microstructure. The microstructure of the foams manufactured from the Ecka powder appeared denser packed than that of the struts of the foams made from the Aldrich powder. This incomplete sintering after thermal processing of the foams from different aluminum powders may be related to the existence of a thin oxide layer on the powder surface [41,162].

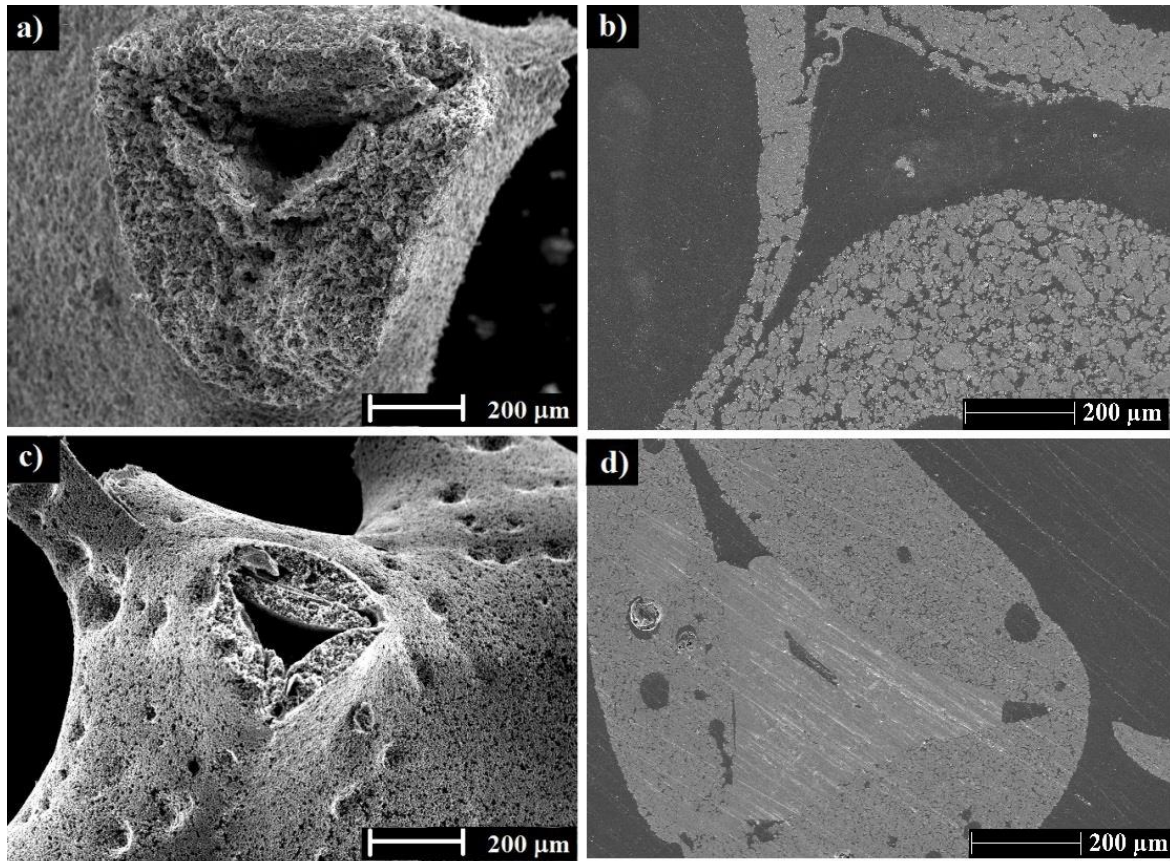


Figure 24 SEM images of selectively broken struts and cross sections of the foams made from the Aldrich powder (a, b) and from the Ecka powder (c, d) after thermal processing at 750 °C for 3h in vacuum; PU template foams with a cell size of 20 ppi (adapted from [157]).

The results of the XRD phase analyses indicated that after thermal processing the aluminum foams consisted, besides metallic aluminum, of the  $\alpha$ - and the  $\gamma$ - $\text{Al}_2\text{O}_3$  phase (Figure 25). In the foams made from the Aldrich powder, these values were ~29.1 wt. % for  $\gamma$ - $\text{Al}_2\text{O}_3$  and ~11.1 wt. % of the  $\alpha$ - $\text{Al}_2\text{O}_3$  phase. For the foams prepared from the Ecka powder, only  $\gamma$ - $\text{Al}_2\text{O}_3$  (19.1 wt. %) was detected besides metallic aluminum. The  $\alpha$ - $\text{Al}_2\text{O}_3$  phase was also found but the quantification was not possible due to the Rietveld technique's limitation to measure low phase amounts.

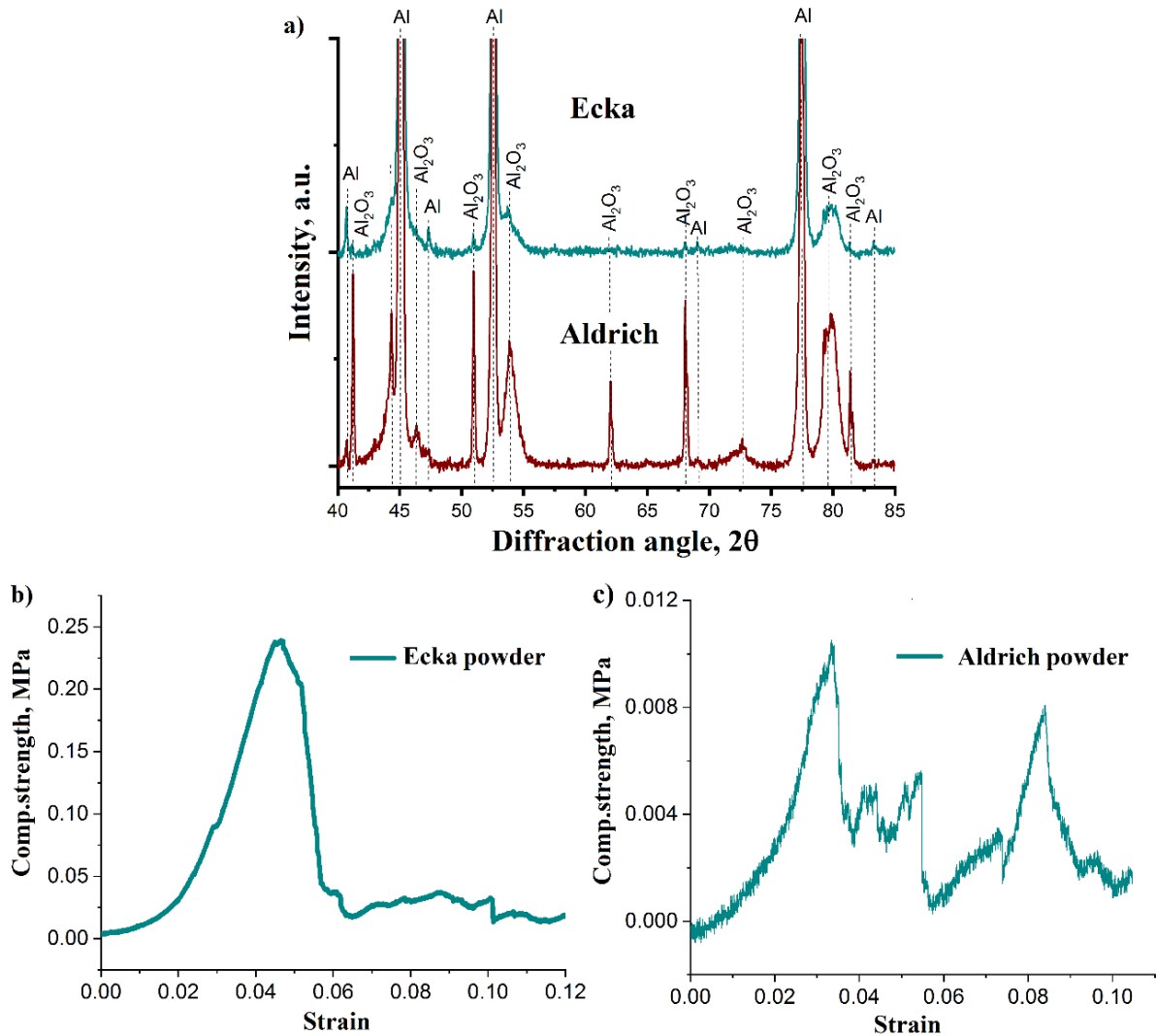


Figure 25 X-ray diffraction analysis (a) and an example of the compressive strength curve (b,c) of the foams prepared from the Aldrich powder and from the Ecka powder after thermal processing at 750 °C for 3h in vacuum; PU template foams with a cell size of 20 ppi (adapted from [157]).

Table 4 shows the values of the compressive yield strength of the foams. The behavior of the compressive strength curve of the foam prepared from the Ecka powder is demonstrated in Figure 25 b,c, which was characterized by higher compressive yield strength ( $0.266 \pm 0.082$  MPa) in comparison with the foams made from the Aldrich powder ( $0.011 \pm 0.002$  MPa). Archimedes' measurements indicated a total porosity ranging from 90 % to 91 % (Table 4). It was observed that the foams made from Aldrich powder had a higher total strut porosity ( $\sim 64.9$  %) than those made from Ecka powder ( $\sim 52.6$  %), see also SEM images in Figure 24.

Table 4 Porosity and compressive yield strength of the aluminum foams prepared from Aldrich powder and from Ecka powder; PU template foams with a cell size of 20 ppi.

Sample	Total porosity, %	Cell porosity, %	Total strut porosity, %	Compressive yield strength, MPa
Foams prepared from the Aldrich powder	91.1 ± 0.1	77.3 ± 0.1	64.9 ± 0.1	0.011 ± 0.002
Foams prepared from the Ecka powder	90.3 ± 0.1	82.2 ± 1.6	52.6 ± 3.4	0.266 ± 0.082

### 5.1.3 Chapter summary

Open-cell aluminum foams were manufactured with a cell size of a PU template of 20 ppi by the sponge replication technique from two different aluminum powders supplied by Ecka und Aldrich. The aluminum foams were thermally processed at 750 °C, which is higher than the melting point of aluminum. Despite this, the resulting samples kept their shape. From the literature is known that it is a challenge to disrupt or dissolve the oxide layer formed on the powder surface; this is one of the key problems of the thermal process of aluminum powders [163,164]. Aluminum oxides around powder particles have a melting point of 2072 °C [165], therefore they are stable at the thermal processing temperature used in the work. In this way, the oxide shell around the aluminum powder acted as an oxide skeleton [29,166], which, on one hand, may have constrained the sintering of the particles, and, on the other hand, it may have kept the foam structure stable at temperatures above the aluminum melting point. This became evident from the SEM results in Figure 24. As a result, the thermal processing of the aluminum foams may be described as follows: aluminum oxide has a coefficient of thermal expansion of  $\sim 7.4 \cdot 10^{-6} \text{ K}^{-1}$ , which is lower than that of pure aluminum ( $\sim 24.4 \cdot 10^{-6} \text{ K}^{-1}$ ) [167]. During heating, the oxide shells around the aluminum particles were ruptured due to the stress created by the difference in the coefficient of thermal expansion [29]. Molten aluminum flowed out, which led to a joining of the particles and their oxide shells, their fusion during melting, formation of agglomerates of joined aluminum (Figure 24). It is also possible that residual oxygen in the furnace led to a partial oxidation of molten aluminum resulting in partial healing of the cracks formed in the oxide shells, thereby increasing the resistance of the foams against complete melting.

It follows from these results that the particle size and shape of the starting materials have a great influence on the microstructure, the phase content, the porosity, and the mechanical properties. It was found that foams made from the spheroidal shaped Ecka powder is characterized by

higher mechanical strength compared to the foams made from the irregularly shaped flaked Aldrich powder. Liu et al [168] discussed that stress concentrations generated on the surface of the powders cause the oxide shell to rupture. Also in a study by Patnaik [165], a higher rate of rupture of the oxide shell of a more irregularly shaped powder was observed. Thus, a powder with a less regular shape may have a higher rate of oxide shell rupture during heating and consequently can react more actively with residual oxygen in the furnace during thermal processing. This behavior is in good agreement with the TGA and XRD results (Figure 23 and Figure 25) which show that the irregularly shaped Aldrich flake powder oxidized significantly faster than the spheroidal-shaped Ecka powder when it reached the oxidation onset temperature. Thus, the oxide shell grows much faster for Aldrich particles compared to the oxide shell on the surface of the Ecka powder. Consequently, the oxide shell of the Ecka powder is thinner than that of the Aldrich powder. This may have led to the effect that molten aluminum more easily broke the oxide shell of the Ecka powder when it reached its melting point. Therefore, the molten aluminum joined the particles faster. As a result, the powder particles in the foam made from the Ecka powder have a higher structural connectivity, a higher stability, and a higher strength than that of the irregularly shaped Aldrich powder. This, in turn, reduced the porosity of the struts and increased the strength of the aluminum foams.

It followed from the above that the microstructure of the foams, the phase content, the porosity, and the mechanical properties depended on the particle size and shape of the original aluminum powders. The Ecka powder with a spheroidal shape is thus more attractive as a starting material for further manufacturing of open-cell aluminum foams than the Aldrich flake powder with an irregular shape.

#### **5.1.4 Aluminum foams thermally processed in different atmospheres**

Figure 26 shows an example of RP foams after thermal processing in air, vacuum, and Ar atmosphere at 750 °C for 3 h. A PU template foam with a cell size of 20 ppi and a geometric size of 20 × 20 × 20 mm was used for the manufacturing of foams. Small aluminum beads on the surface of the struts after thermal processing in air were found. Foams thermally processed in Ar were characterized by a shrinkage in all directions and some larger, formerly molten aluminum beads located in their interior of the strut's surface. The morphology of the strut surface after thermal processing is presented more detail in the Appendix, Figure A 1.

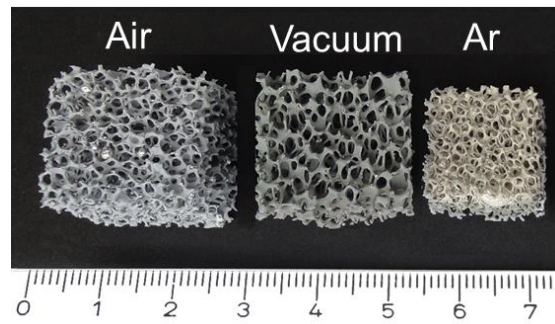


Figure 26 Aluminum foams after thermal processing for 3h at 750 °C in air, vacuum and Ar atmosphere; PU template foams with a cell size of 20 ppi (adapted from [158]).

SEM cross-section images of Al foams thermally processed at 750 °C in air, vacuum, and Ar atmosphere are shown in Figure 27. As expected from the manufacturing process, the struts were hollow. The cavity in the struts formed after PU template burn-out. However, the foams were characterized by the presence of molten aluminum beads inside and outside the strut, and cracks were identified along the walls of struts of foams thermally processed in air and vacuum. The microstructure is described by the presence of microporosity in the walls of the struts. The struts did not result from a homogeneous melt. A high number of voids remained in the foams after thermal processing. A decrease in microporosity was observed when the thermal processing atmosphere was changed from air to Ar. After heat treatment in Ar atmosphere, the powder particles were closer and more connected to each other forming conglomerations of formerly molten powders particles. These foams possess a denser structure than foams processed in air or in vacuum.

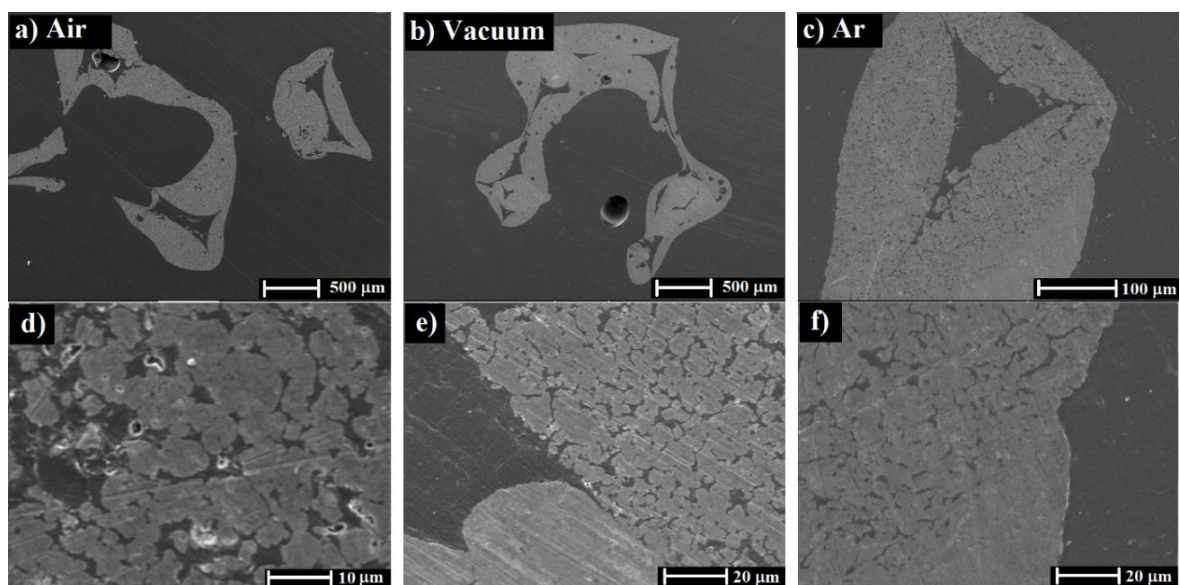


Figure 27 SEM images of aluminum RP foams thermally processed for 3h at 750 °C in air (a,d), in vacuum (b,e), and in Ar (c,f); PU template foams with a cell size of 20 ppi.

For the XRD phase analyses, the foams, thermally processed in air and vacuum, were milled and the resulting powders were analyzed. The foams processed in Ar were compressed to obtain a planar surface prior to analysis for proper measurement. From the XRD phase analyses (Figure 28), it was found that aluminum oxides ( $\alpha$ -,  $\gamma$ - $\text{Al}_2\text{O}_3$ ) were formed after thermal processing of the foams in different atmospheres. The foams thermally processed in air were characterized by the highest amount of aluminum oxide, it was  $\sim 20.2$  wt. % of the  $\alpha$ - $\text{Al}_2\text{O}_3$  phase and  $\sim 2.4$  wt. % of the  $\gamma$ - $\text{Al}_2\text{O}_3$  phase. Further thermal processing in vacuum and Ar showed that the aluminum oxide concentration decreased from  $\sim 19.1$  wt. % of the  $\gamma$ - $\text{Al}_2\text{O}_3$  phase in vacuum to  $\sim 4.6$  wt. % of the  $\gamma$ - $\text{Al}_2\text{O}_3$  phase in Ar. Although trace formation of the  $\alpha$ - $\text{Al}_2\text{O}_3$  phase was observed in these samples, its quantification by the Rietveld method was impossible due to its low concentration ( $\gg 1$  wt. %). The total oxide concentration is given in Table 5.

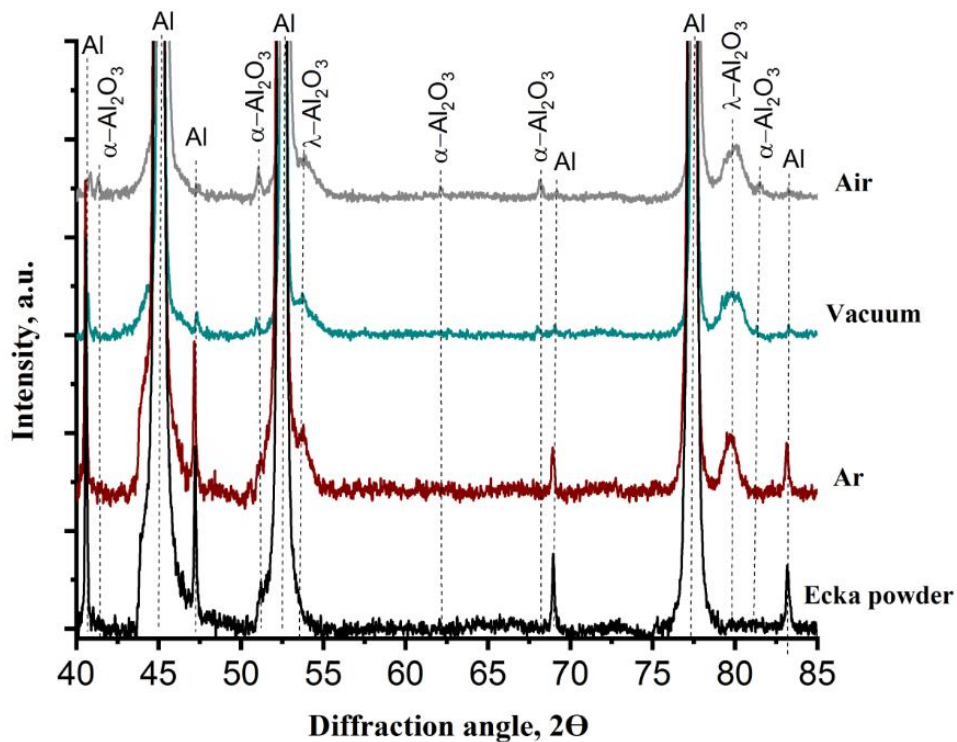


Figure 28 X-ray diffraction patterns of as received aluminum powder and RP aluminum foams after thermal processing in air, vacuum and Ar at 750 °C for 3 h.

Table 5 Oxide concentration, volumetric shrinkage, porosity, compressive yield strength and thermal conductivity of RP aluminum foams thermally processed in air, vacuum and Ar atmospheres at 750 °C for 3 h; PU template foams with a cell size of 20 ppi.

Sample	Air	Vacuum	Ar
Aluminum oxides, wt. %	22.6	19.1	4.6
Volumetric shrinkage ( $S_v$ ), %	0	0	49.7 ± 2.3
Total porosity ( $P_{total}$ ), %	90.4 ± 0.3	90.3 ± 0.1	90.7 ± 0.6
Cell porosity ( $P_{cell}$ ), %	78.6 ± 0.8	82.2 ± 1.6	86.9 ± 0.8
Strut porosity ( $P_s$ ), %	58.4 ± 1.0	52.6 ± 3.4	40.8 ± 2.1
Compressive (yield) strength, MPa	0.13 ± 0.02	0.27 ± 0.08	0.34 ± 0.08
Therm. Cond. of foam $\lambda_f$ , W·m <sup>-1</sup> K <sup>-1</sup>	0.45 ± 0.05	1.79 ± 0.11	2.32 ± 0.14
Therm. Cond. of porous strut material $\lambda_s$ , W·m <sup>-1</sup> K <sup>-1</sup>	7.8	36.3	63.2
Therm. Cond. of bulk material $\lambda_b$ , W·m <sup>-1</sup> K <sup>-1</sup>	21.1	82.4	114.9

All foams were prepared with a similarly high total porosity ranging from 90 % to 91 % to compare the compressive yield strength and the thermal properties (Table 5). The results of measurements of geometric parameters and the porosity by the Archimedes method are presented in Table 5, from which it follows that the foams thermally processed in Ar atmosphere are characterized by volumetric shrinkage of ~49.7 %, see also Figure 26. The high shrinkage of aluminum foams processed in Ar correlates to the amount of alumina; this is significantly less compared to foams processed in air and in vacuum. Thus, the “fusion rate” of molten Al is higher because of a lower constraint caused by the alumina’s lower concentration (Figure 27). This resulted in a decrease in the strut porosity from 58.4 % to 40.8 %.

The thermal conductivity coefficient of the foams  $\lambda_f$  ranged from 0.45 ± 0.05 W·m<sup>-1</sup>K<sup>-1</sup> to 2.32 ± 0.14 W·m<sup>-1</sup>K<sup>-1</sup> (Table 5). It can be seen that  $\lambda_f$  increased with a decreasing oxide content and a decreasing strut porosity of the foams. Equations (2) and (3) were used to evaluate the effect of porosity and purity on the measured  $\lambda_f$  of the foams, see Chapter 4.1.2. From the calculated values of the thermal conductivity of the porous strut material  $\lambda_s$ , it was found that with increasing  $P_s$  the value of  $\lambda_s$  decreased from 63.2 W·m<sup>-1</sup>K<sup>-1</sup> (Ar atmosphere) to 7.8 W·m<sup>-1</sup>K<sup>-1</sup> (air). The sample thermally treated in air had the lowest bulk thermal conductivity  $\lambda_b \approx 21.1$  W·m<sup>-1</sup>K<sup>-1</sup>. Reduction of oxygen in the processing atmosphere significantly increased this value to  $\lambda_b \approx 114.9$  W·m<sup>-1</sup>K<sup>-1</sup> (Ar atmosphere). These calculated  $\lambda_b$  values were much lower than that for  $\lambda_b$  of pure bulk aluminum ~205 W·m<sup>-1</sup>K<sup>-1</sup> [169]. This discrepancy between the thermal

conductivity of pure bulk aluminum and the calculated  $\lambda_b$  can be explained by the presence of impurities, such as oxide shells (alumina) around the powder particles formed during the thermal processing of aluminum powders [153,170,171], which have a low thermal conductivity of  $24\text{--}39\text{ W}\cdot\text{m}^{-1}\text{K}^{-1}$  [172]. These low values of the calculated  $\lambda_b$  might also be due to a change in the number of grain boundaries in the heat flow path with decreasing grain size compared to pure bulk aluminum. This is due to the fact that the mean free path of phonons decreases due to an increase in intra-grain phonon scattering with a smaller grain size [173].

Figure 29 shows the visual appearance of the foams after measuring the compressive strength and the behavior of the curves. The foams thermally processed in air and vacuum collapsed into small pieces after the test. The stress-strain curves of these aluminum foams indicated brittle behavior with shear fracture typical for ceramic foams. The compressive strength of the foams thermally processed in air reached  $0.13 \pm 0.02\text{ MPa}$ ; this value was  $0.27 \pm 0.08\text{ MPa}$  for the foams processed in vacuum. After thermal processing in Ar, the foams were characterized by a more ductile behavior of the stress-strain curve, which is typical for metal foams, with a compressive yield strength of  $0.34 \pm 0.08\text{ MPa}$ . The highest value of the compressive yield strength of foams in Ar may be reached by a higher structural interconnection of the powder particles through the formation of molten aluminum agglomerations, which consequently reduced the porosity of the strut.

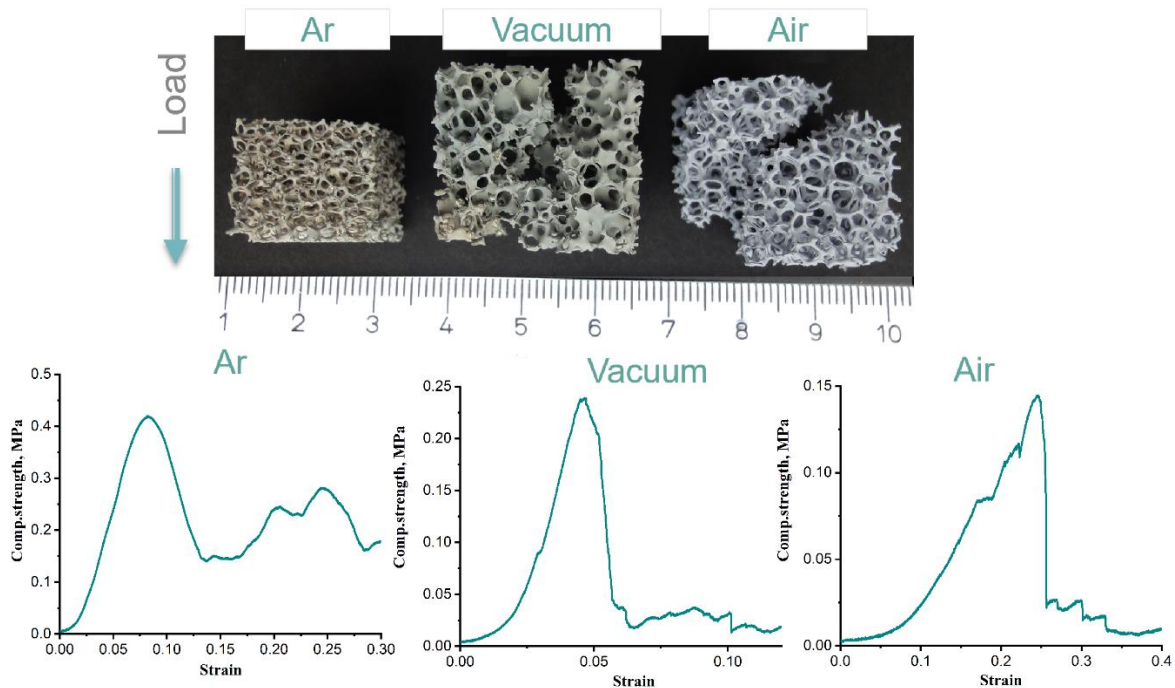


Figure 29 RP aluminum foams after compressive strength test (top) and stress-strain curves (bottom) typical for foams thermally processed in air, vacuum, and Ar at  $750\text{ }^{\circ}\text{C}$  for 3 h; PU template foams with a cell size of 20 ppi (adapted from [158]).

It was concluded from these results that the thermal processing atmosphere significantly influenced the microstructure formation of the samples, the oxide phase content, the thermal conductivity, and the mechanical properties. Reducing the amount of oxygen in the thermal processing atmosphere significantly reduced the strut's microporosity and improved the thermal processing of aluminum powder particles, which, in turn, increased the thermal conductivity and the compressive yield strength of the foams. Therefore, further work was carried out in Ar atmosphere.

### 5.1.5 Aluminum foams manufactured by the sponge replication technique at different temperatures in Ar atmosphere

Figure 30 shows the RP foams before PU burn-out and after thermal processing at 600 °C, 650 °C, and 750 °C for PU template foams with a cell size of 20 ppi and a geometric size of 15 × 15 × 20 mm (for RP foams thermally processed at 750 °C to 900 °C for PU template foams with a geometric size of 20 × 20 × 20 mm please see also the Appendix, Figure A 2). A slight volumetric shrinkage of ~8.8 % was found after processing at 600 °C. A further increase in the thermal processing temperature resulted in an increase in volumetric shrinkage in all directions of 45.3 % at 650 °C and 51.2 % at 750 °C, see also Table 6. Most of the foams showed small aluminum beads after processing at 650 °C (Figure 30), the bead size and number increased with increasing processing temperature. The surface morphology of the struts after thermal processing is presented more detailed in the Appendix, Figure A 3.

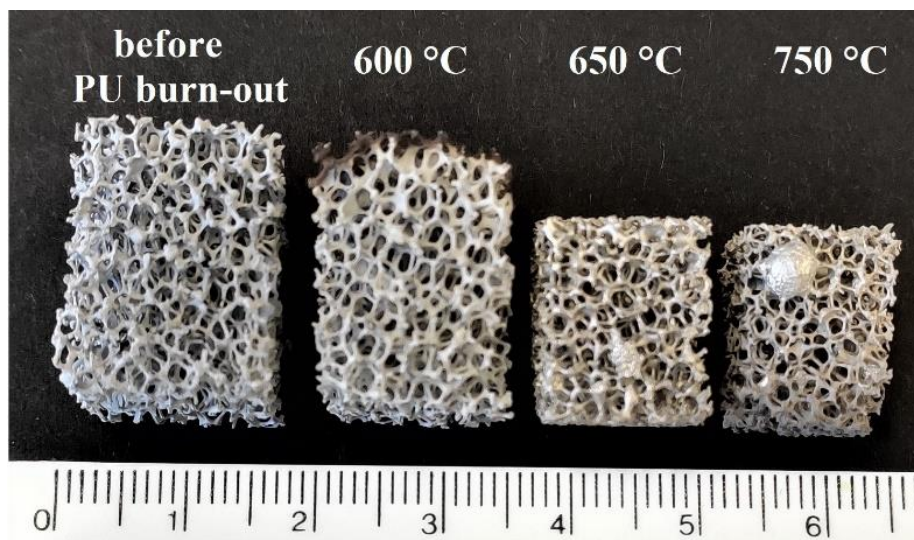


Figure 30 Aluminum foams before PU burn-out and after thermal processing for 3 h in Ar at 600 °C to 750 °C; PU template foams with a cell size of 20 ppi.

Table 6 Volumetric shrinkage, porosity, compressive yield strength, and thermal conductivity of Al foams thermally processed for 3 h in Ar at 600 °C, 650 °C, and 750 °C; PU template foams with a cell size of 20 ppi.

Sample	600 °C	650 °C	750 °C
Volumetric shrinkage ( $S_v$ ), %	$8.8 \pm 3.5$	$45.3 \pm 4.1$	$51.2 \pm 1.9$
Total porosity ( $P_{total}$ ), %	$94.3 \pm 0.4$	$90.5 \pm 0.7$	$90.4 \pm 0.4$
Cell porosity ( $P_{cell}$ ), %	$85.5 \pm 3.3$	$85.7 \pm 1.3$	$85.1 \pm 1.7$
Strut porosity ( $P_s$ ), %	$65.9 \pm 4.8$	$43.1 \pm 3.3$	$44.3 \pm 5.8$
Compressive (yield) strength, MPa	$0.09 \pm 0.05$	$0.29 \pm 0.05$	$0.27 \pm 0.03$
Absorbed energy per volume, MJ m <sup>-3</sup>	-	0.093	0.095
Therm. Cond. of foam $\lambda_f$ , W·m <sup>-1</sup> K <sup>-1</sup>	-	$2.26 \pm 0.14$	$2.32 \pm 0.14$
Therm. Cond. of porous strut material $\lambda_s$ , W·m <sup>-1</sup> K <sup>-1</sup>	-	65.1	63.2
Therm. Cond. of bulk material $\lambda_b$ , W·m <sup>-1</sup> K <sup>-1</sup>	-	115.6	114.9

SEM images of cross-sections of aluminum RP foams thermally processed in Ar at 600 °C to 850 °C are shown in Figure 31. Despite the thermal processing temperature (above the melting point of bulk aluminum ~660 °C [161]), the struts of all foams were still hollow up to the highest applied processing temperature of 850 °C. At temperatures up to 750 °C, some formerly molten aluminum and aluminum beads were observed, which were located not only outside but also inside the foam struts (Figure 31 e–k). In addition, a visible deformation of the foams was found after processing at 850 °C. The microstructure of the foam struts generally was not homogeneous and incomplete joining of aluminum powder particles was observed, despite the high thermal processing temperatures. The struts possessed a high number of pores in their microstructure, which may have been formed due to a thin layer of alumina on the powder surface [41,162]. However, in general, the foams thermal processed at temperatures at 650 °C and above (Figure 31 c,d) were characterized by fewer voids, more aluminum particles joined together, and a denser packed microstructure compared to the foams thermal processed at 600 °C (Figure 31 a,b).

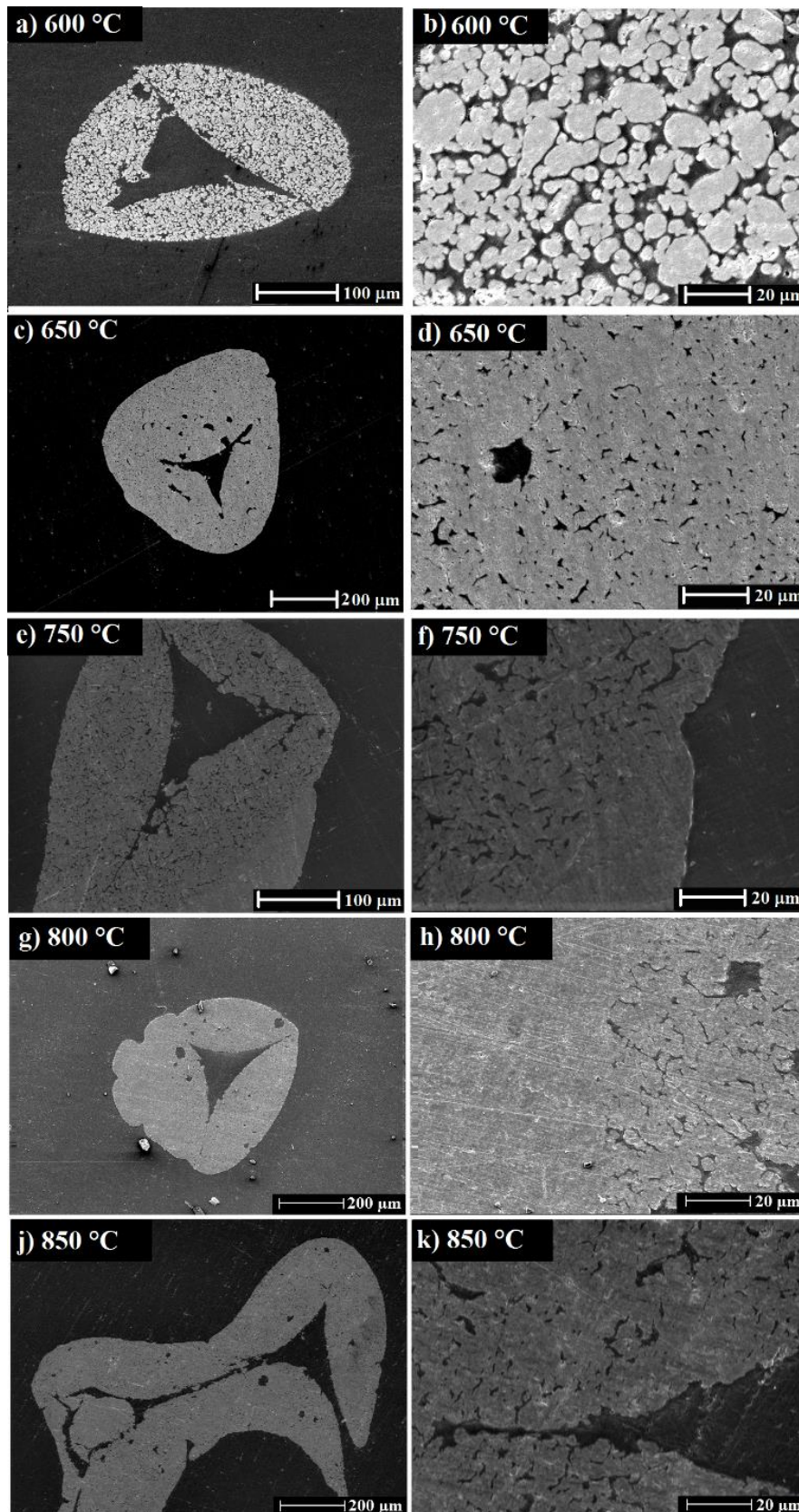


Figure 31 SEM images of aluminum RP foams thermally processed for 3 h in Ar at 600 °C (a,b), 650 °C in (c,d), 750 °C (e,f), 800 °C (g,h), and 850 °C (j,k); PU template foams with a cell size of 20 ppi (adapted from [158]).

XRD patterns of the phase analyses of as-received aluminum powder and the aluminum foams after thermal processing for 3 h in Ar at 600 °C to 900 °C are shown in Figure 32. Aluminum oxides ( $\alpha$ -,  $\gamma$ - $\text{Al}_2\text{O}_3$ ) were found after thermal processing. Phase analyses were obtained from a planar surface after compression of the thermally processed aluminum foams. The phase compositions were calculated from X-ray measurements using the Rietveld analysis. The results are shown in Table 7. A slight increase of the aluminum oxide amount with temperature is evident. The highest amount of aluminum oxide after thermal processing in Ar at 900 °C was 28.8 wt. % for the  $\alpha$ - $\text{Al}_2\text{O}_3$  phase and ~7.4 wt. % for the  $\gamma$ - $\text{Al}_2\text{O}_3$  phase. The foam processed at 900 °C collapsed during thermal processing, see in the Appendix, Figure A 2, and was excluded from further discussion.

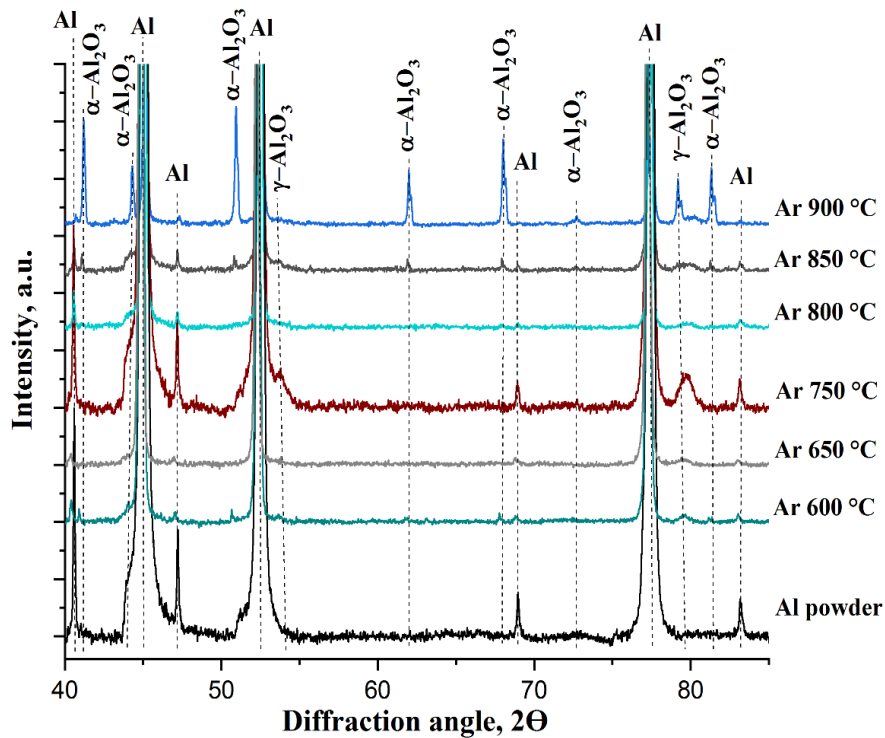


Figure 32 X-ray diffraction patterns of as received aluminum powder and RP aluminum foams after thermal processing for 3 h in Ar at 600 °C to 900 °C (adapted from [158]).

Table 7 Phase composition of the as-received powder and the aluminum foams thermally processed for 3 h in Ar at 600–900 °C.

Sample	$\alpha$ - $\text{Al}_2\text{O}_3$ , wt. %	$\gamma$ - $\text{Al}_2\text{O}_3$ , wt. %
Al powder	-	-
Ar 600 °C	-	2.6
Ar 650 °C	-	2.5
Ar 750 °C	-	4.6
Ar 800 °C	-	3.8
Ar 850 °C	1.5	4.3
Ar 900 °C	28.8	7.4

Table A 1 in the Appendix shows the volume shrinkage, the porosity, the compressive yield strength, and the thermal conductivity of Al foams thermally processed for 3 h in Ar at 750–900 °C. These results were obtained for the foams prepared from PU template foams with a geometric size of 20 mm × 20 mm × 20 mm. A comparison of the samples prepared at 750 °C from PU template foams with a geometric size of 15 mm × 15 mm × 20 mm in Table 6 and the foams in Table A 1 made from larger PU template foams shows that the geometric size of the initial PU foam slightly affected the shrinkage of the samples, the porosity, and the mechanical properties of the foams.

From the results of porosity measurements by the Archimedes method (Table 6) it follows that the total porosity of aluminum foams was 94.3 % after thermal processing at 600 °C and within 90 % to 91 % after treatment at 650 °C to 750 °C. A significant decrease in the strut porosity from 65.9 % to 43.1 % was observed with the increase in temperature because of the higher joining degree of the aluminum powder particles. Due to the deformation of the samples at thermal processing temperatures above 750 °C, further work was mainly focused on the samples made at 650 °C and 750 °C.

From the compressive (yield) strength results shown in Table 6 and Figure 33, it follows that the temperature of thermal processing had a significant influence on the compressive strength behavior. The stress-strain curves of aluminum foams at 600 °C were characterized by a brittle behavior with shear fracture (Figure 33 a), which is more typical for ceramic foams (the same stress-strain curve behavior was observed after thermal processing in air and in vacuum, see Figure 29). Foams processed at 650 °C and higher temperatures had a more ductile stress-strain curve behavior typical for aluminum and metals in general (Figure 33 b,c). The curves can be characterized by three distinct regions [20,21]: an elastic region up to the compressive yield point  $\sigma$ , a large plateau region with plastic cell failure. The mode of deformation in the second region was the result of a repetitive failure of the pore layers, so the stress-strain curve had a very uneven character [174]. These long plateaus were the result of the open-cell construction of the foams. In the third region, the flow stress increased rapidly as the cell pores in the deformation zone were flattened.

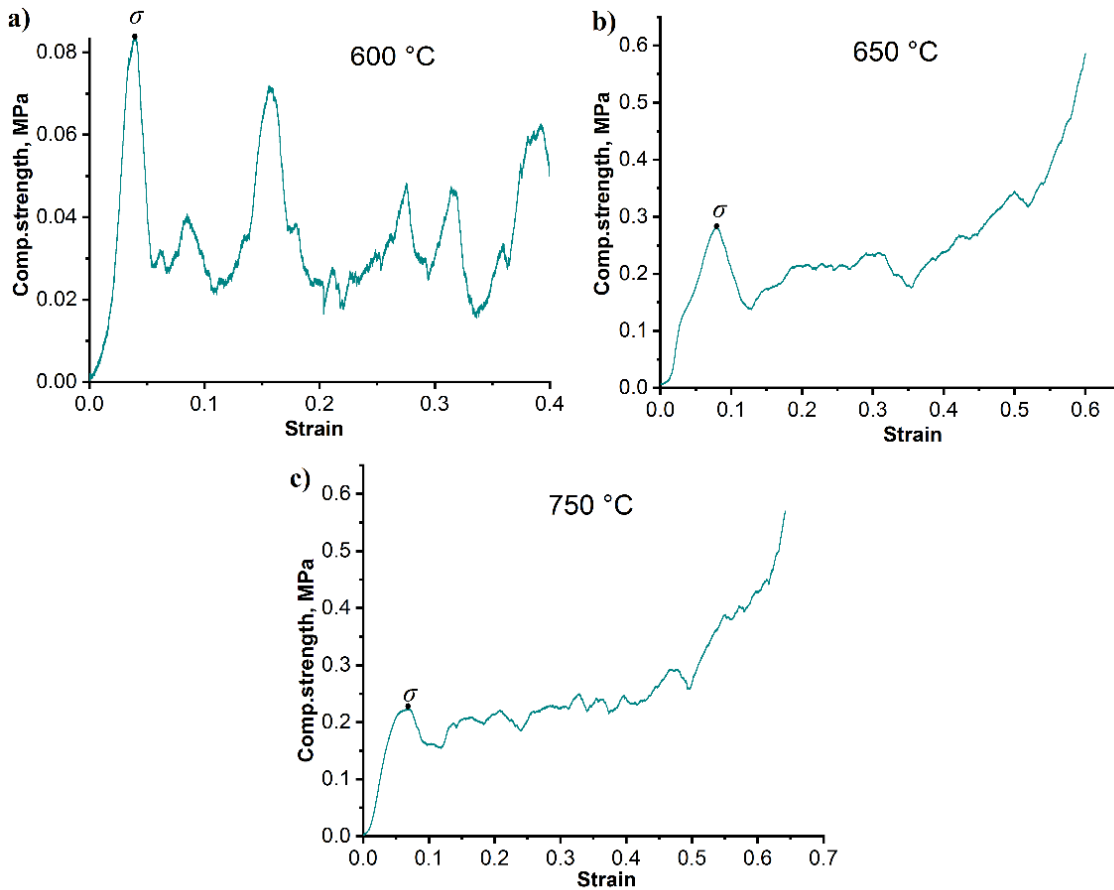


Figure 33 Compressive stress-strain curves of the RP aluminum foams after processing at 600 °C (a), 650 °C (b), and 750 °C (c) for 3 h in Ar for PU template foams with a cell size of 20 ppi.

The average compressive (yield) strength and absorbed energy after thermal processing at 650 °C and 750 °C increased compared to foams processed at 600 °C from  $0.09 \pm 0.05$  MPa to  $0.29 \pm 0.05$  MPa due to better structural interconnectivity of the former powder particles at higher thermal processing temperatures (Table 6). There was no major difference in the mechanical properties for the foams thermally processed at 650 °C and 750 °C and the values were within the measurement error. Increasing the thermal processing temperature slightly increased the absorbed energy per volume from  $0.093 \text{ MJ m}^{-3}$  at 650 °C to  $0.095 \text{ MJ m}^{-3}$  at 750 °C. This value was calculated from Equation (12). Since the samples at 600 °C were brittle, this made it difficult to correctly calculate the absorbed energy per volume. From the results presented in the Appendix, Table A 1, it can be seen that a further increase in temperature above 750 °C led to lower compressive yield strength values, which might be the result of the formation of more molten aluminum beads outside the struts and the subsequent reduction in the size of the strut walls and their ability to withstand mechanical loads.

The results of the thermal conductivity showed that an increase in the thermal processing temperature led to a slight increase in  $\lambda_f$ . This value ranged from  $2.26 \pm 0.14 \text{ W m}^{-1} \text{ K}^{-1}$  after  $650 \text{ }^\circ\text{C}$  to  $2.32 \pm 0.14 \text{ W m}^{-1} \text{ K}^{-1}$  after  $750 \text{ }^\circ\text{C}$  (Table 6). Since  $P_{cell}$  and  $P_s$  had almost the same values for foams processed at  $650 \text{ }^\circ\text{C}$  and  $750 \text{ }^\circ\text{C}$ , the calculated  $\lambda_S$  and  $\lambda_b$ , see Chapter 4.3, were not significantly different. At  $650 \text{ }^\circ\text{C}$  and  $750 \text{ }^\circ\text{C}$   $\lambda_S$  ranged from  $\sim 65.1 \text{ W m}^{-1} \text{ K}^{-1}$  to  $\sim 63.2 \text{ W m}^{-1} \text{ K}^{-1}$ , respectively. The value of  $\lambda_b$  value was  $\sim 115.6 \text{ W m}^{-1} \text{ K}^{-1}$  at  $650 \text{ }^\circ\text{C}$  and  $\sim 114.9 \text{ W m}^{-1} \text{ K}^{-1}$  at  $750 \text{ }^\circ\text{C}$ . Despite the difference in the thermal processing temperature,  $\lambda_b$  did not significantly change at  $650 \text{ }^\circ\text{C}$  and  $750 \text{ }^\circ\text{C}$ . Therefore, it can be concluded that for these samples, the thermal processing with increasing temperature did not significantly generate impurities or grain boundary effects within the struts of the foams that affect the value of thermal conductivity  $\lambda_b$ . The discrepancy between the thermal conductivity of pure bulk aluminum and the calculated  $\lambda_b$  was discussed in detail in Chapter 5.1.4. The thermal conductivity of foams thermally processed at  $600 \text{ }^\circ\text{C}$  was not investigated due to the destruction of the foam during the measurement under load, which was applied to increase the contact area between the samples and the Hot Disk detector.

### 5.1.6 Aluminum foams manufactured by the sponge replication technique with different total porosity

The specific surface area, the mechanical and the thermal properties of the resulting foams depend on their total porosity [175,176]. In this part, RP aluminum foams with different total porosity, which were thermally processed at  $650 \text{ }^\circ\text{C}$  for 3 hours in Ar, made with PU template foams with a cell size of 20 ppi and with a geometric size of  $15 \text{ mm} \times 15 \text{ mm} \times 20 \text{ mm}$ , were manufactured and characterized.

Table 8 shows the porosity, the geometric characteristics, the mechanical and the thermal properties of RP aluminum foams thermally processed for 3 h at  $650 \text{ }^\circ\text{C}$  in Ar with different  $P_{total}$  (90.5 % and 86.6 %). There was an increase in volumetric shrinkage from 41.9 % to 45.3 % and  $P_{cell}$  from 80.9 % to 87.5 % with total porosity increasing. It might be due to less material suspension loaded into the initial PU template foams to reduce  $P_{total}$ . As a result, the strut porosity  $P_s$  was also higher (43.1 % for  $P_{total}$  of 90.5 % and 37.6 % for  $P_{total}$  of 86.6 %), due to the hollow struts had a higher contribution to  $P_s$  at the fixed thermal processing parameters.

Table 8 Porosity, geometrical characteristics, mechanical and thermal properties of RP aluminum foams thermally processed for 3 h at 650 °C in Ar with total porosity 90.5 % and 86.6 % for PU template foams with a cell size of 20 ppi.

Cell size of PU template foams	20 ppi	20 ppi
Volumetric shrinkage ( $S_v$ ), %	45.3 ± 4.1	41.9 ± 2.5
Total porosity ( $P_{total}$ ), %	90.5 ± 0.7	86.6 ± 0.7
Cell porosity ( $P_{cell}$ ), %	85.7 ± 1.3	80.9 ± 1.5
Strut porosity ( $P_s$ ), %	43.1 ± 3.3	37.6 ± 2.7
Mean diameter of wall strut wall ( $D_{ws}$ ), μm	130 ± 55	136 ± 45
Mean diameter of struts ( $D_s$ ), mm	0.50 ± 0.32	0.52 ± 0.24
Mean cell size, mm	1.97 ± 0.16	1.96 ± 0.28
Specific surface area by μ-CT, cm <sup>2</sup> g <sup>-1</sup>	126	114
Compressive yield strength, MPa	0.29 ± 0.05	0.34 ± 0.07
Absorbed energy per volume, MJ m <sup>-3</sup>	0.093	0.095
Therm. Cond. of foam $\lambda_f$ , W m <sup>-1</sup> K <sup>-1</sup>	2.26 ± 0.14	3.21 ± 0.18

The μ-CT 3D reconstruction image of the RP aluminum foams indicates the foam to be open porous, Figure 34 a. The distribution of the strut thickness, strut wall thickness, and cell size is shown in Figure 34 b and c. Their mean values determined by applying a Gaussian approximation to the distance histogram, obtained from CTAnalyser calculations of CT data (Chapter 4.2.3), are presented in Table 8. The mean cell size of the RP aluminum foam with  $P_{total}$  of 90.5 % was  $1.97 \pm 0.16$  mm, the diameter of the struts  $D_s$  was  $0.50 \pm 0.32$  mm, and the diameter of the strut wall thickness  $D_{ws}$  was  $130 \pm 55$  μm. For the RP aluminum foams with a lower  $P_{total}$  of ~86.6 %, the cell size was  $1.96 \pm 0.28$  mm,  $D_s = 0.52 \pm 0.24$  mm, and  $D_{ws} = 136 \pm 45$  μm. The slight difference of these mean calculated values and their distribution in Figure 34 a and c are associated with a higher slurry load on the initial PU foam to prepare foams with  $P_{total}$  of 86.6 %.

The specific surface area calculated from the μ-CT reconstruction data, as shown in Figure 34 d (green), increases from 114 cm<sup>2</sup> g<sup>-1</sup> to 126 cm<sup>2</sup> g<sup>-1</sup> with increasing porosity. The specific surface area was calculated also after filling and despeckle of the hollow struts, see Chapter 4.2.3, to evaluate the effect of the hollow strut surface formed after PU burn-out on the specific surface areas, Figure 34 d, gray. It was found that the hollow struts formed after PU burn-out further increased the specific surface area of the foam by about factor two.

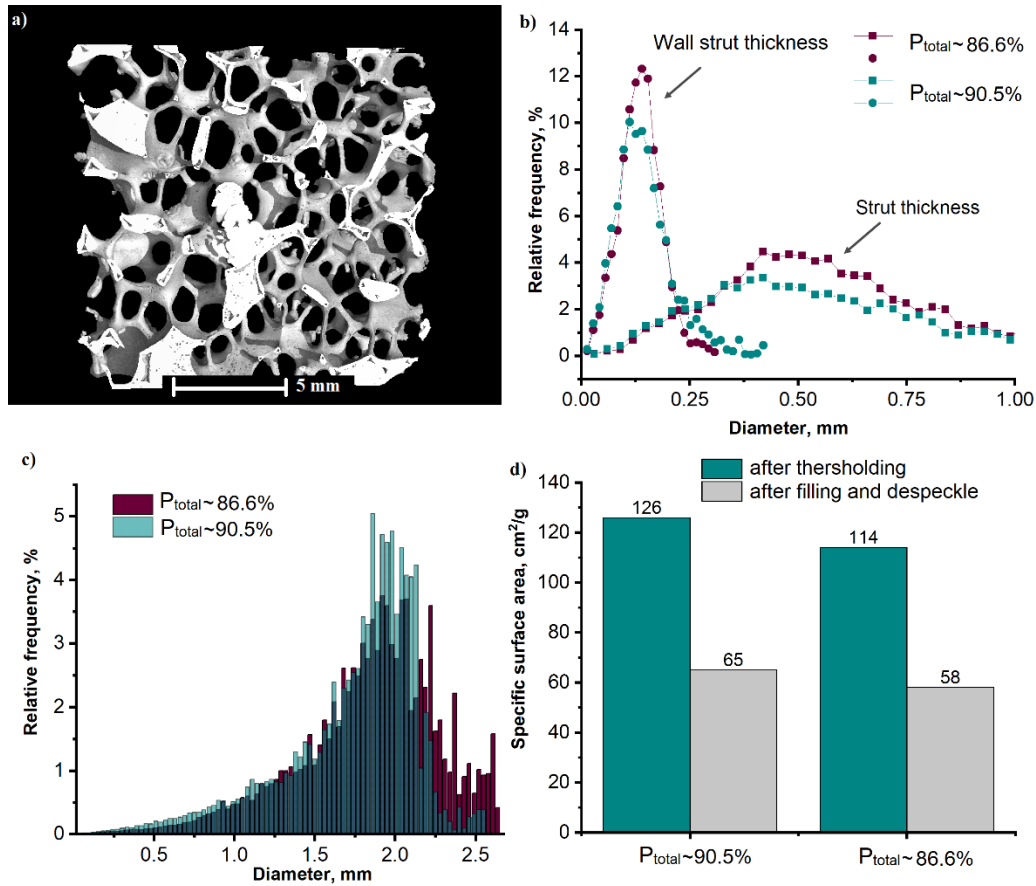


Figure 34  $\mu$ -CT reconstruction image of the RP aluminum foams with  $P_{total} \approx 90.5\%$  (a); distributions of the wall strut thickness and the strut thickness (b) and the cell size (c) of the RP aluminum foams with  $P_{total} \approx 90.5\%$  (red) and  $P_{total} \approx 86.6\%$  (green), both thermally processed at 650 °C for 3h; specific surface area after thresholding (green) and after filling and despeckle (gray) (d); PU template foams with a cell size of 20 ppi.

It follows from the measurements of mechanical properties (Table 8) that there was a slight decrease in the compressive yield strength from  $0.34 \pm 0.07$  MPa to  $0.29 \pm 0.05$  MPa as well as the absorbed energy per volume from  $0.095 \text{ MJ} \cdot \text{m}^{-3}$  to  $0.093 \text{ MJ} \cdot \text{m}^{-3}$  with an increase in  $P_{total}$  of RP aluminum foams. Moreover, a slight reduction in porosity significantly increased  $\lambda_f$  of RP aluminum foams from  $2.26 \pm 0.14 \text{ W} \cdot \text{m}^{-1} \text{K}^{-1}$  to  $3.21 \pm 0.18 \text{ W} \cdot \text{m}^{-1} \text{K}^{-1}$  (Table 8).

It follows from the above results that a slight change in the total porosity from 90.5 % to 86.6 % of the RP aluminum foams improved the mechanical properties and thermal conductivity, affected by reducing the strut porosity, the cell porosity, and increasing the strut thickness.

### 5.1.7 Chapter summary

Open-cell aluminum foams were manufactured by the sponge replication technique in the temperature range from 600 °C to 900 °C in air, vacuum, and argon. The thermal processing

conditions significantly influenced the microstructure, the phase content, the porosity, the thermal conductivity, and the mechanical properties of the as-received aluminum foams.

Open-cell aluminum foams thermally processed in Ar had a denser microstructure, a lower porosity, a higher thermal conductivity, and a higher compressive strength compared to samples processed in vacuum or in air (Figure 27 and Table 5). This was assigned to the lower amount of aluminum oxide formed during thermal processing. As a result, the oxide shell of the aluminum powder was thinner and was broken more easily during thermal processing in Ar. The effect of residual oxygen and the destruction of the oxide shells during heating was discussed more detailed in Chapter 5.1.3. Consequently, the aluminum particles in Ar had a higher joining degree when the processing temperature was above the melting point of aluminum, which, in turn, decreased the strut porosity and increased the compressive yield strength and the thermal conductivity of the foams (Table 5).

During thermal processing of the RP aluminum foams at 600 °C in Ar atmosphere, the foams were characterized by a brittle and porous structure. With an increasing thermal processing temperature, there was a decrease in strut porosity; mechanical properties and thermal conductivity of foams were enhanced. This may be due to a more intense process of oxide shell rupture and a more intense joining of the powder particles with increasing temperature [5]. Despite this, aluminum foams did not melt even at 850 °C, which was related to the oxide shells surrounding the aluminum particles acting as a support for the foam structure in the sense of a skeleton in this system [29,166].

From the obtained results, it was concluded that the most optimal thermal processing parameters for the manufacture of RP foams were at 650 °C and 750 °C for 3 h in Ar atmosphere. Under these conditions, the RP foams with a total porosity in the order of 90 % to 91 % retained their shape and were characterized by relatively high mechanical stability and a high thermal conductivity in comparison to foams processed with parameters deviating from the above.

## **5.2 Aluminum foams manufactured by a combination of sponge replication and freezing techniques**

This chapter presents the manufacturing of RP/FP aluminum foams based on the results from Chapter 5.1. Ar atmosphere and thermal processing temperatures of 650 °C and 750 °C were applied for thermal processing. The samples were made with a PU template foam with cell pore sizes of 10 ppi, 20 ppi, and 30 ppi, and a geometric size of 15 × 15 × 20 mm. The influence of the additional freezing/freeze-drying processing steps on the strut porosity, the microstructure,

the thickness of material lamellae and lamellar pores, the specific surface area, the mechanical and thermal properties was investigated in this chapter.

### 5.2.1 Aluminum foams manufactured by a combination of sponge replication and freezing techniques at different temperatures and solid loading

The RP/FP aluminum foams are shown in Figure 35 before binder and PU template burn-out and after thermal processing at 650 °C and 750 °C in Ar. The foams kept their shape after thermal processing but they significantly shrunk (~55 % at 650 °C and ~63 % at 750 °C). Larger aluminum beads were found on the surface of the struts after thermal processing at 750 °C. The deformation of the struts is a result of the formation of these molten aluminum beads. Since it is known from alumina foams that the size of the lamellar pores depends on the water content in the coating slurry [10,11], aluminum foams with 70 vol. % and 80 vol. % water were prepared. Their appearance after thermal processing for 3 h in Ar at 650 °C is shown in Figure 36. The RP/FP foams are characterized by higher shrinkage in all directions than the RP foams. Increasing the water content to 80 vol. % resulted in shrinkage of the aluminum foam and destruction of their struts. The foams collapsed under a low load.

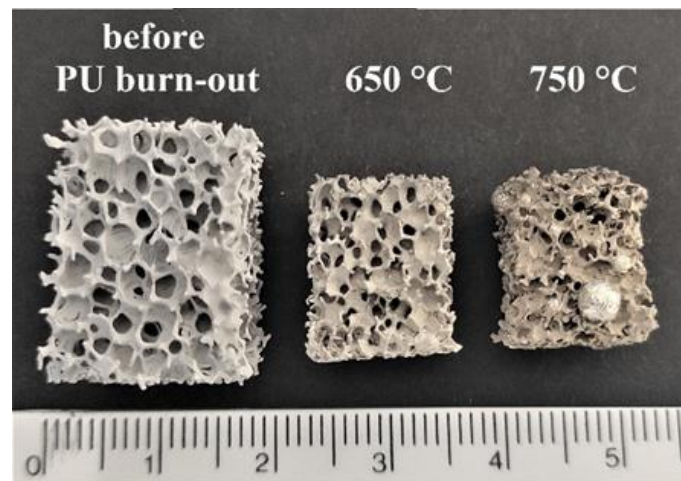


Figure 35 RP/FP aluminum foams before binder and PU burn-out and after thermal processing for 3 h in Ar at 650 °C and 750 °C; PU template foams with a cell size of 20 ppi.

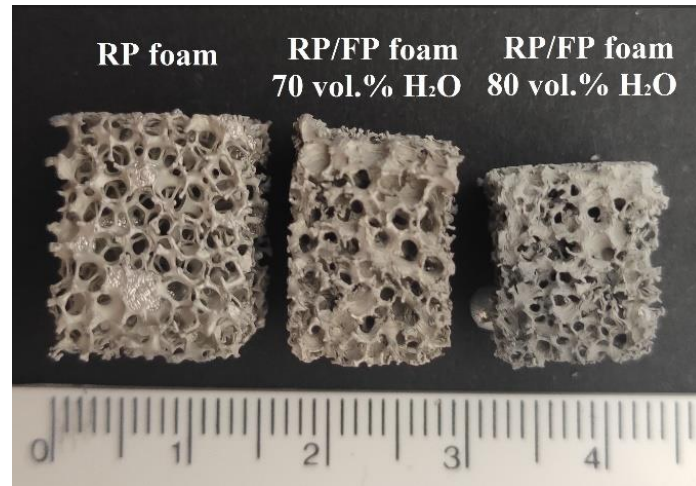


Figure 36 RP foam and RP/FP foam with 70 vol. % of water and RP/FP foam with 80 vol. % of water after thermal processing for 3 h in Ar at 650 °C; PU template foams with a cell size of 20 ppi.

X-ray diffraction analysis detected the presence of  $\gamma\text{-Al}_2\text{O}_3$ . The amount of aluminum oxide after thermal processing in Ar at 650 °C was ~3.0 wt.% and at 750 °C it was ~4.2 wt. %. This increase can be associated with a decrease in the amount of pure aluminum as a result of the formation of molten aluminum beads and a corresponding increase in wt. % of the  $\gamma\text{-Al}_2\text{O}_3$  phase. A similar behavior was observed in Table 7, Chapter 5.1.5. Consequently, this thermal processing condition at 750 °C was appropriate for the manufacturing of the RP foams, but not for the RP/FP foams. Therefore, RP/FP foams prepared from a coating slurry with 70 vol. % of water were carried out at 650 °C.

### 5.2.2 Aluminum foams manufactured by a combination of sponge replication and freezing techniques with different cell size

Figure 37 shows SEM images of the strut surface and cross-sections of RP/FP aluminum foams after thermal processing at 650 °C. The images demonstrate the formation of lamellar pores and material lamellae, typical for aqueous slurries, generated by freezing and subsequent freeze-drying. These lamellar pores are characterized by a random direction and orientation due to non-directional freezing and random orientation of the foam struts (Figure 37 b,c). A similar lamellar pore orientation after manufacturing RP/FP ceramic foams after non-directional freezing and freeze-drying was found in [10,11]. The microstructure of the material lamellae in the aluminum foams is not uniform after thermal processing (Figure 37 d). There are areas with a high degree of particle joining having a higher material density, and those where the pores dominated.

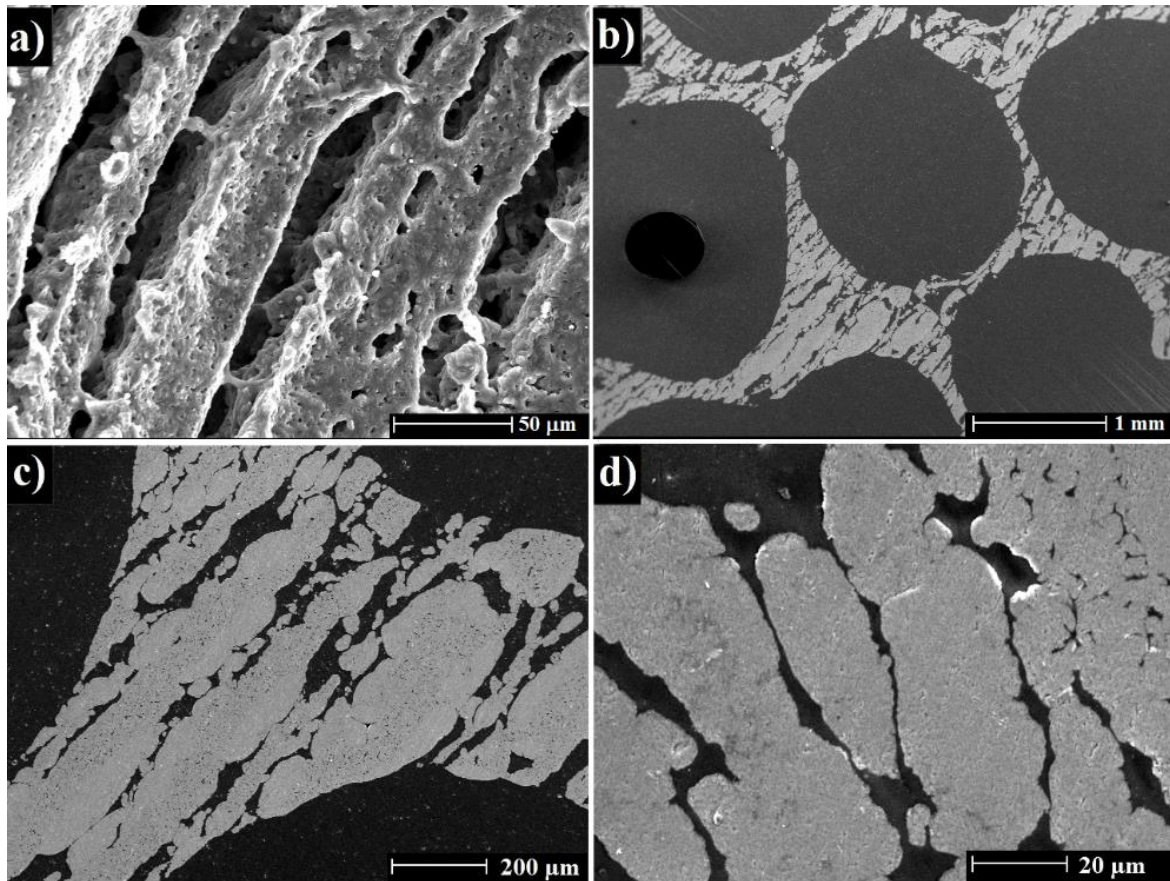


Figure 37 SEM images of the surface of RP/FP aluminum foams (a) and their cross sections after thermal processing for 3h in Ar at 650 °C (b–d).

In Table 9 most relevant properties of RP/FP aluminum foams after thermal processing at 650 °C are listed. They possess a high volumetric shrinkage of 56.1 % to 57.6 %. The total porosity was between 86.4 % and 86.6 %. The cell porosity increased from 68.6 % to 76.8 % with increasing cell size of the PU template foams. The aluminum foams were characterized by high strut porosity ranging from 47.3 % (10 ppi) to 59.8 % (30 ppi) because of the additional formation of lamellar pores in the RP/FP foams.

Table 9 Geometrical, mechanical and thermal properties of RP/FP aluminum foams thermally processed for 3 h at 650 °C in Ar for PU template foams with a cell size of 10 ppi, 20 ppi, and 30 ppi.

Cell size of PU template foams	10 ppi	20 ppi	30 ppi
Volumetric shrinkage ( $S_v$ ), %	$57.6 \pm 2.8$	$56.1 \pm 3.7$	$56.4 \pm 1.4$
Total porosity ( $P_{total}$ ), %	$86.4 \pm 0.9$	$86.6 \pm 1.1$	$86.5 \pm 0.6$
Cell porosity ( $P_{cell}$ ), %	$76.8 \pm 2.1$	$73.5 \pm 2.5$	$68.6 \pm 4.1$
Strut porosity ( $P_s$ ), %	$47.3 \pm 2.7$	$53.8 \pm 3.4$	$59.8 \pm 4.5$
Mean diameter of struts, mm	$0.80 \pm 0.53$	$0.52 \pm 0.23$	$0.24 \pm 0.11$
Mean cell size, mm	$2.54 \pm 0.84$	$1.91 \pm 0.22$	$0.99 \pm 0.13$
Material lamellae thickness, $\mu\text{m}$	$80 \pm 39$	$81 \pm 35$	$78 \pm 35$
Lamellar pore thickness, $\mu\text{m}$	$39 \pm 15$	$24 \pm 6$	$30 \pm 10$
Specific surface area by $\mu$ -CT, $\text{cm}^2 \cdot \text{g}^{-1}$	231	219	238
Compressive yield strength, MPa	$0.44 \pm 0.18$	$0.49 \pm 0.13$	$0.72 \pm 0.19$
Absorbed energy per volume, $\text{MJ} \cdot \text{m}^{-3}$	0.13	0.15	0.29
Therm. Cond. of foam $\lambda_f$ , $\text{W} \cdot \text{m}^{-1} \text{K}^{-1}$	$2.18 \pm 0.05$	$2.32 \pm 0.05$	$2.97 \pm 0.18$
Therm. Cond. of porous strut material $\lambda_s$ , $\text{W} \cdot \text{m}^{-1} \text{K}^{-1}$	34.6	32.1	34.8
Bulk therm. Cond. of bulk material $\lambda_b$ , $\text{W} \cdot \text{m}^{-1} \text{K}^{-1}$	70.6	80.3	102.7

Figure 38 shows  $\mu$ -CT 3D reconstruction images of RP/FP aluminum foams with a cell size of the PU template foam of 10 ppi, 20ppi, and 30 ppi after thermal processing at 650 °C in Ar for 3 h. No directionally aligned lamellar pores were observed along with the foams. The RP/FP aluminum foams are characterized by open cells and windows.

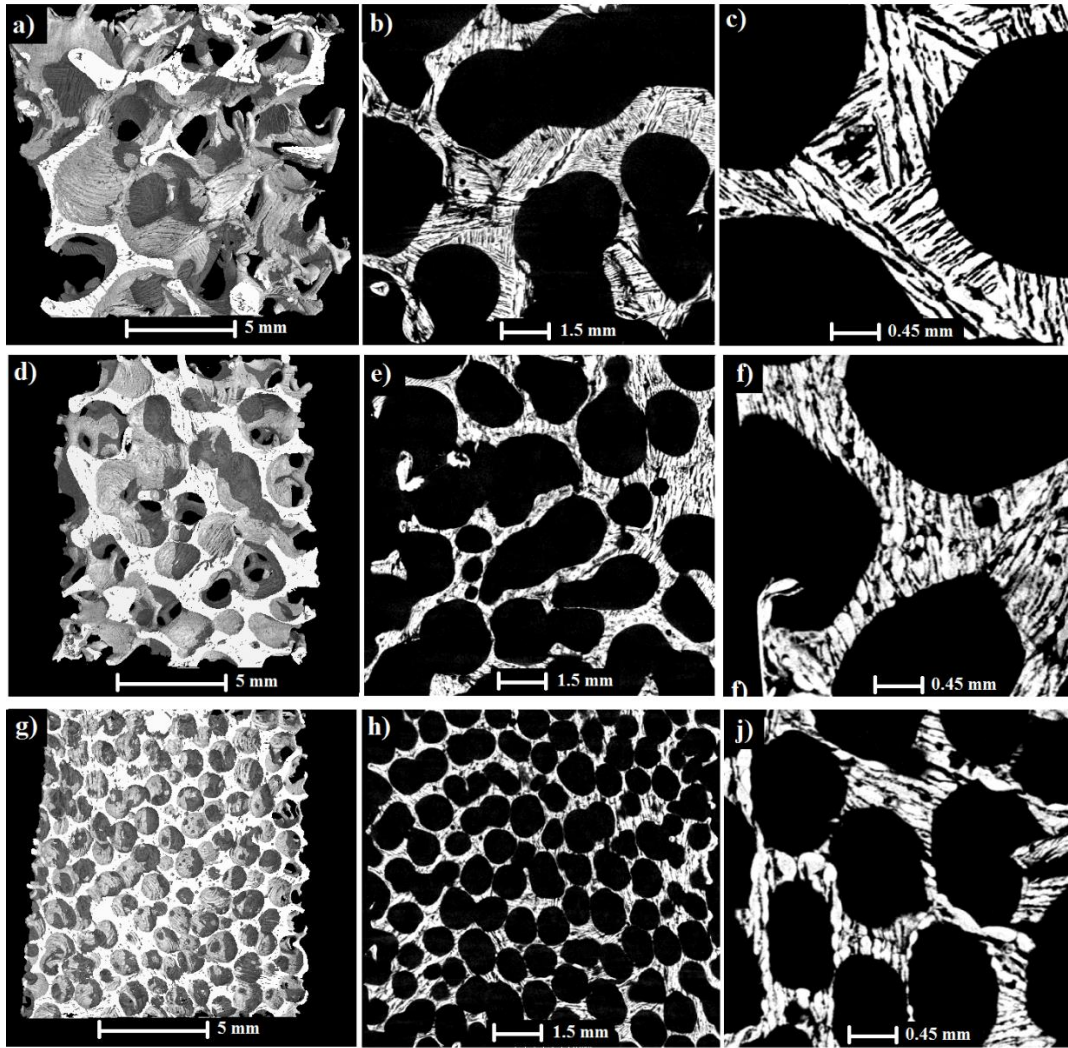


Figure 38  $\mu$ -CT reconstruction images of the RP/FP aluminum foams after thermal processing at 650 °C in Ar for 3 h as a function of the PU template foam cell size: 10 ppi (a–c), 20 ppi (d–f), and 30 ppi (g–j).

The distribution and the mean value of the cell size, the strut thickness, the material lamellae thickness, and the lamellar pore thickness are shown in Figure 39 and listed in Table 9. The distribution curve of the cell size shifted to the left with a decrease in the cell size of the PU templates (Figure 39 a). The mean cell size of the RP/FP aluminum foams was  $2.54 \pm 0.84$  mm for the 10 ppi templated foam,  $1.91 \pm 0.22$  mm for the 20 ppi templated foam, and  $0.99 \pm 0.13$  mm for the 30 ppi templated foam. The strut thickness of the RP/FP foams increased with increasing cell size of the PU template from  $0.24 \pm 0.11$  mm (30 ppi) to  $0.80 \pm 0.53$  mm (10 ppi), see Figure 39 b and Table 9. The thickness of the material lamellae for all samples was approximately the same laying between 78  $\mu$ m and 81  $\mu$ m, see Figure 39 c and Table 9. The same direction of change was observed for the lamellar pores, they were in the range from 24  $\mu$ m to 39  $\mu$ m, Figure 39 d and Table 9. Since slurries with the same metal powder load were used and the same freezing temperature was applied for the manufacturing of RP/FP aluminum

foams, no significant difference in the results was obtained. The thickness and type of lamellar pores might be changeable by varying the solvent amount, the freezing temperature and/or the binder amount and type [10,11].

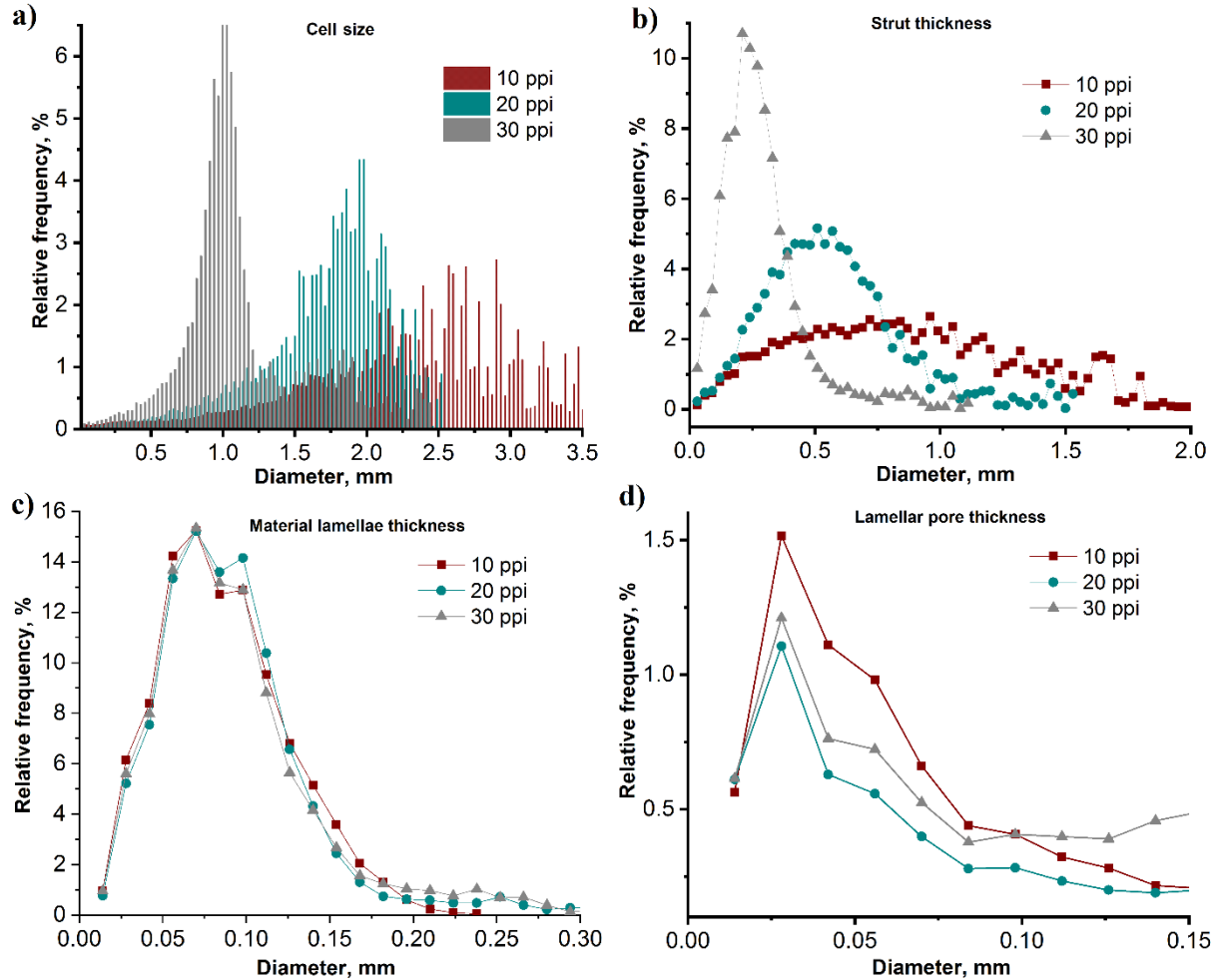


Figure 39 Distributions of the cell size (a), strut thickness (b), material lamellae thickness (c), and lamellar pore thickness (d) of the RP/FP aluminum foams thermally processed at 650 °C for 3h in Ar; the PU template foam cell size was 10 ppi, 20 ppi, and 30 ppi (adapted from [159]).

Table 9 and Figure 40 show the specific surface area calculated from  $\mu$ -CT reconstruction data. It can be seen comparing the samples after thresholding and after filling and despeckle steps that the additional lamellar pores and hollow struts significantly increased the specific surface areas for all samples. The highest difference was observed for the 10 ppi templated foam, in which the specific surface area increased from 33  $\text{cm}^2 \cdot \text{g}^{-1}$  to 231  $\text{cm}^2 \cdot \text{g}^{-1}$ , see a more detailed description of the thresholding, filling, and despeckle steps in Chapter 4.2.3 and Figure 20.

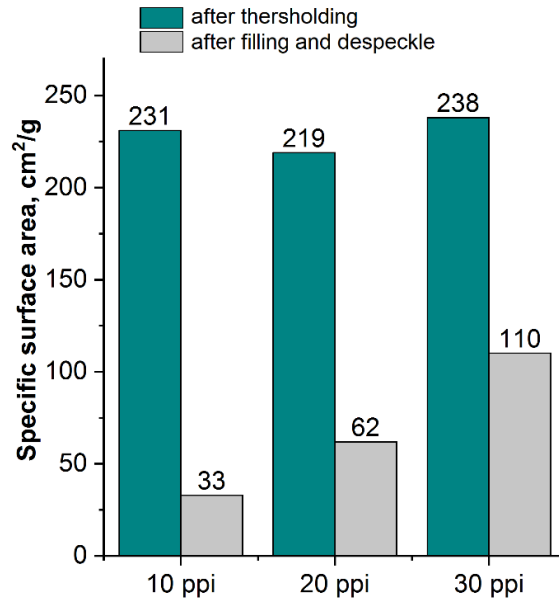


Figure 40 Specific surface area of the RP/FP aluminum foams thermally processed at 650 °C for 3h in Ar depending on the cell size of the PU template foam (10 ppi, 20 ppi, and 30 ppi); measured using  $\mu$ -CT (adapted from [159]).

Compressive strength testing showed that the average values of the compressive yield strength increased with decreasing foam cell size of the RP/FP foams (Table 9); the 10 ppi templated aluminum foam had  $0.44 \pm 0.18$  MPa, and the 30 ppi templated foam possessed a compressive yield strength of  $0.72 \pm 0.19$  MPa. The typical compressive strength behavior of RP/FP foams is shown in Figure 41. The shape of the compressive curves demonstrated that the stress-strain behavior in the initial compression stage had an elastic deformation region, a long plateau where plastic cell failure occurred and a further increase in compressive strength caused by densification [20,21]. The calculated absorbed energy, Equation (12), also grew with the increase of the ppi value of the initial PU template foams: from  $0.13 \text{ MJ m}^{-3}$  for the 10 ppi templated foam to  $0.29 \text{ MJ m}^{-3}$  for the 30 ppi templated foam (Table 9).

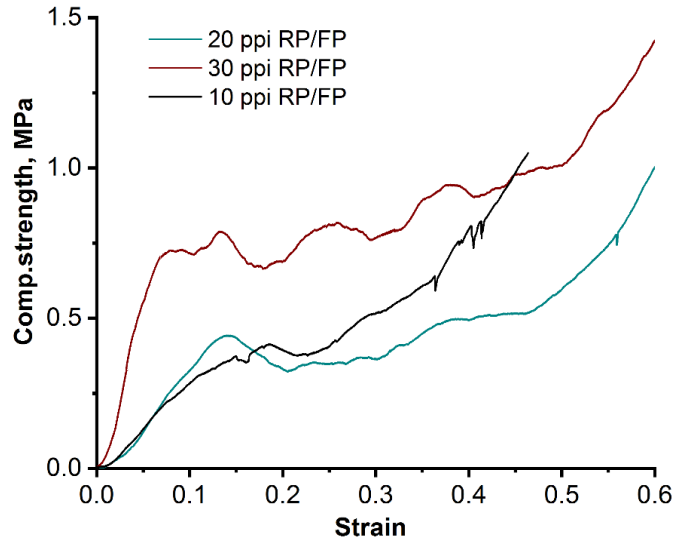


Figure 41 Compressive stress-strain curves of RP/FP aluminum foams after thermal processing at 650 °C for 3 h in Ar; PU template foams cell sizes were 10 ppi, 20 ppi, and 30 ppi.

The results of the measured and calculated thermal conductivity are shown in Table 9. The thermal conductivity of foam  $\lambda_f$  was  $2.18 \pm 0.05 \text{ W}\cdot\text{m}^{-1}\text{K}^{-1}$  for the 10 ppi,  $2.32 \pm 0.05 \text{ W}\cdot\text{m}^{-1}\text{K}^{-1}$  for the 20 ppi, and  $2.97 \pm 0.18 \text{ W}\cdot\text{m}^{-1}\text{K}^{-1}$  for the 30 ppi templated foams. The calculated thermal conductivity of porous strut material  $\lambda_s$  using a model from Ashby [19], Equation (2), did not change significantly and ranged from  $32.1 \text{ W}\cdot\text{m}^{-1}\text{K}^{-1}$  (20 ppi) to  $34.8 \text{ W}\cdot\text{m}^{-1}\text{K}^{-1}$  (30 ppi). A model derived by Eucken [139], Equation (3), was used to estimate the thermal conductivity of the bulk strut material  $\lambda_b$ . The obtained values of  $\lambda_b$  varied from  $76.0 \text{ W}\cdot\text{m}^{-1}\text{K}^{-1}$  (10 ppi) to  $102.7 \text{ W}\cdot\text{m}^{-1}\text{K}^{-1}$  (30 ppi). These low values of  $\lambda_b$  for the aluminum foams compared to the thermal conductivity of pure bulk aluminum ( $\sim 205 \text{ W}\cdot\text{m}^{-1}\text{K}^{-1}$  [169]) might be related to an increase in the number of grain boundaries in the heat flow path or the residual aluminum oxide that was also observed in Chapters 5.1.4 and 5.1.5.

### 5.2.3 Aluminum foams: sponge replication vs. combination of sponge replication and freezing techniques

In this section, 20 ppi templated RP and RP/FP aluminum foams thermally processed at 650 °C for 3 hours in Ar are compared with respect to their most relevant properties, Table 10. The aluminum foams had a total porosity of 86.6 %. The RP/FP aluminum foams were characterized by higher volumetric shrinkage of 56.1 % and a lower cell porosity of 73.5 % in comparison with the RP aluminum foams with  $S_v$  of 41.9 % and  $P_{cell}$  of 80.9 %. An additional formation of lamellar pores within the struts of the aluminum foams raised the strut porosity by  $\sim 1.4$  times.

The results of  $\mu$ -CT measurements of cell size and strut thickness are also shown in Table 10 and in Figure 42. The calculated mean cell size and strut thicknesses demonstrated no significant differences between the RP and RP/FP foams, Table 10. The additional lamellar pores significantly increased the specific surface area from  $114 \text{ cm}^2 \cdot \text{g}^{-1}$  to  $219 \text{ cm}^2 \cdot \text{g}^{-1}$ , Figure 42 c and Table 10. However, the specific surface area for both samples, whereby hollow struts and lamellar pores after filling and despeckle were not taken into account, was in the range between  $58 \text{ cm}^2 \cdot \text{g}^{-1}$  for the RP foams and  $62 \text{ cm}^2 \cdot \text{g}^{-1}$  for the RP/FP foams. Consequently, the combination of the sponge replication and freezing techniques increased the specific surface area by 3.5 times compared to foams without hollow struts and lamellar pores (after filling and despeckle).

Table 10 Geometrical, mechanical and thermal properties of RP and RP/FP aluminum foams thermally processed for 3 h at  $650 \text{ }^\circ\text{C}$  in Ar, templated with PU foams with a cell size of 20 ppi.

Sample	RP/FP	RP
Volumetric shrinkage ( $S_v$ ), %	$56.1 \pm 3.7$	$41.9 \pm 2.5$
Total porosity ( $P_{total}$ ), %	$86.6 \pm 1.1$	$86.6 \pm 0.7$
Cell porosity ( $P_{cell}$ ), %	$73.5 \pm 2.5$	$80.9 \pm 1.5$
Strut porosity ( $P_s$ ), %	$53.8 \pm 3.4$	$37.6 \pm 2.7$
Mean diameter of struts, mm	$0.52 \pm 0.23$	$0.48 \pm 0.25$
Mean cell size, mm	$1.91 \pm 0.22$	$1.96 \pm 0.28$
Specific surface area by $\mu$ -CT, $\text{cm}^2 \cdot \text{g}^{-1}$	219	114
Compressive yield strength, MPa	$0.49 \pm 0.13$	$0.34 \pm 0.07$
Absorbed energy per volume, $\text{MJ} \cdot \text{m}^{-3}$	0.15	0.10
Therm. Cond. of foam $\lambda_f$ , $\text{W m}^{-1} \cdot \text{K}^{-1}$	$2.32 \pm 0.05$	$3.21 \pm 0.18$
Therm. Cond. of porous strut material $\lambda_s$ , $\text{W m}^{-1} \cdot \text{K}^{-1}$	32.1	61.7

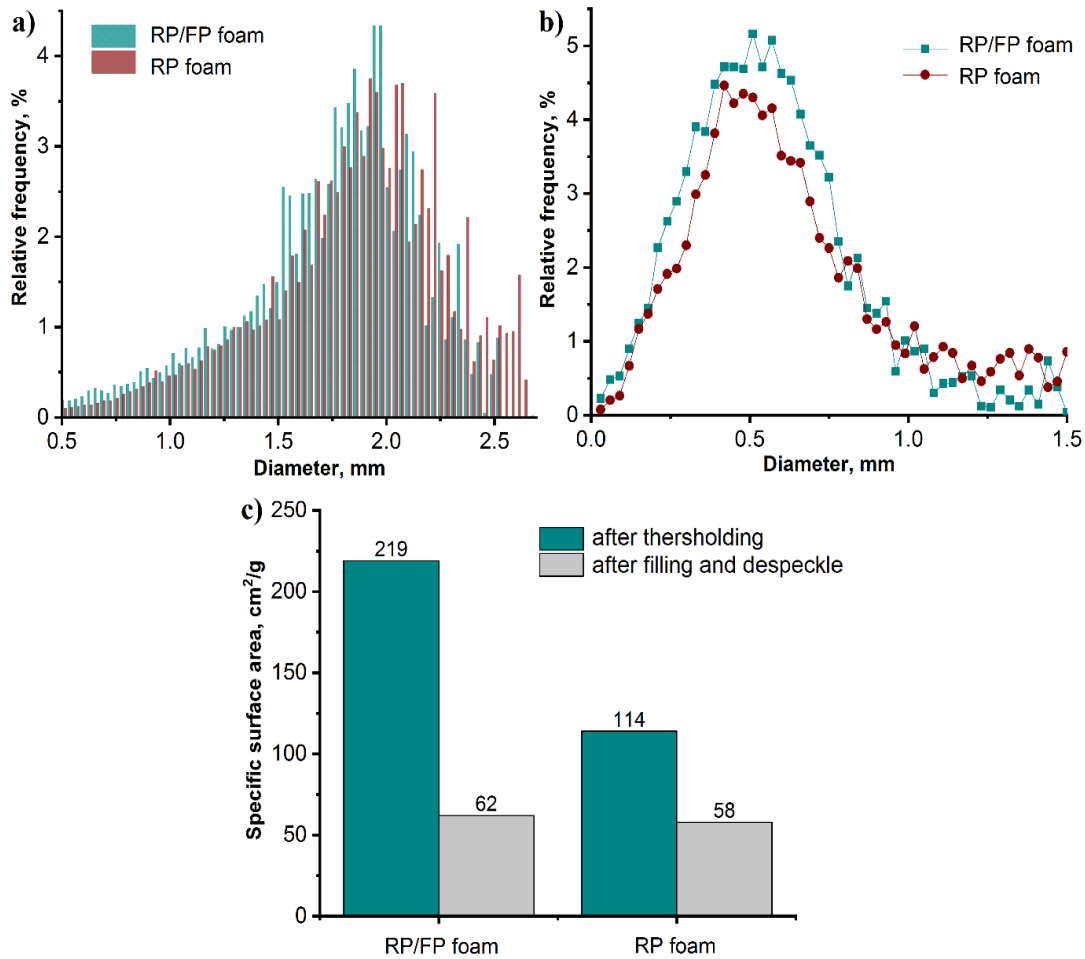


Figure 42 Distributions of the cell size (a) and the strut thickness (b) of the RP (red) and RP/FP (green) aluminum foams; specific surface area of the RP and RP/FP aluminum foams after thresholding (green) and filling and despeckle (gray) (c) measured using  $\mu$ -CT; PU template foams with a cell size of 20 ppi (adapted from [159]).

From Table 10 it can be seen that, despite approximately the same total porosity  $P_{total}$ , the compressive yield strength and the absorption energy were higher for the RP/FP foams than for the RP foams. Figure 42 indicates a distribution of the strut thickness and the cell size for both foams to be similar. However,  $P_{cell}$  and  $P_s$  had a more noticeable difference. On the one hand, the RP/FP foams had a lower cell porosity than the RP foams. This might be a reason for the increased compressive strength up to  $0.49 \pm 0.13$  MPa, Table 10. On the other hand, these foams were characterized with higher strut porosity that usually has a negative effect on the mechanical properties. However, the RP/FP foams are characterized by lamellar pores along with the foams. It was found in [177] that the direction and thickness of the lamellar pores significantly influenced the compressive strength, which depended on the orientation of the material lamellae relative to the direction of load: compressive strength increased in parallel direction of load of the lamellar pores and decreased with perpendicular orientation. However, in this case, the lamellar pores had an anisotropic orientation, Figure 38, that might enhance the

compressive yield strength and the absorbed energy despite the high strut porosity ( $P_s \approx 54.4\%$ ) via a load sharing mechanism [174,178].

Figure 43 shows the relative compressive strength  $\sigma_{pl}^*/\sigma_b^*$  of the different sample series for the RP and RP/FP foams depending on the relative density  $\rho^*/\rho_s$ , Equation (13). For all foams, the plastic collapse strength  $\sigma_{pl}^*$  was equal to the compressive yield strength  $\sigma$ . It has been mentioned in Chapter 4.3 that the proportionality constant  $C$  demonstrated the pore geometry effect and the density exponent  $n$  showed the deformation mechanisms; these values are usually near 0.3 and 1.5, respectively [20,23,24,179]. However, they depend on the pore geometry, on the material, etc. and they may vary [178,180,181]. The Gibson-Ashby model was plotted for fixed  $C = 0.3$  and  $n = 1.5$  values (dash line). The Gibson-Ashby model was plotted with fixed  $C = 0.3$  and varying  $n$  values for the manufactured foams. For the Gibson-Ashby plot of the RP and RP/FP foams,  $n$  was  $\sim 1.54$ ; this is in good agreement with the model. There was no difference between fitted curves for both types of foams. The discrepancy between the experimental  $n$  value and empirically defined value may be caused by the original open-cell metal foams having no pores in their struts [20]. In the case of aluminum foams with hollow struts, lamellar pores, and material pores, a variation of the  $n$  value is expectable. Several authors observed a significant influence of the pore size on the mechanical behavior of metal foams [25,182]. It was discussed in [174,178] that small pores can impact the mechanical strength via a load sharing mechanism. All above can change the foams' deformation modes such as yielding, bending, and buckling, which results in a variation of the  $n$  value [20,183]. A further systematic study is required to investigate the compression behavior of these foams under load to identify the deformation mechanisms more detailed.

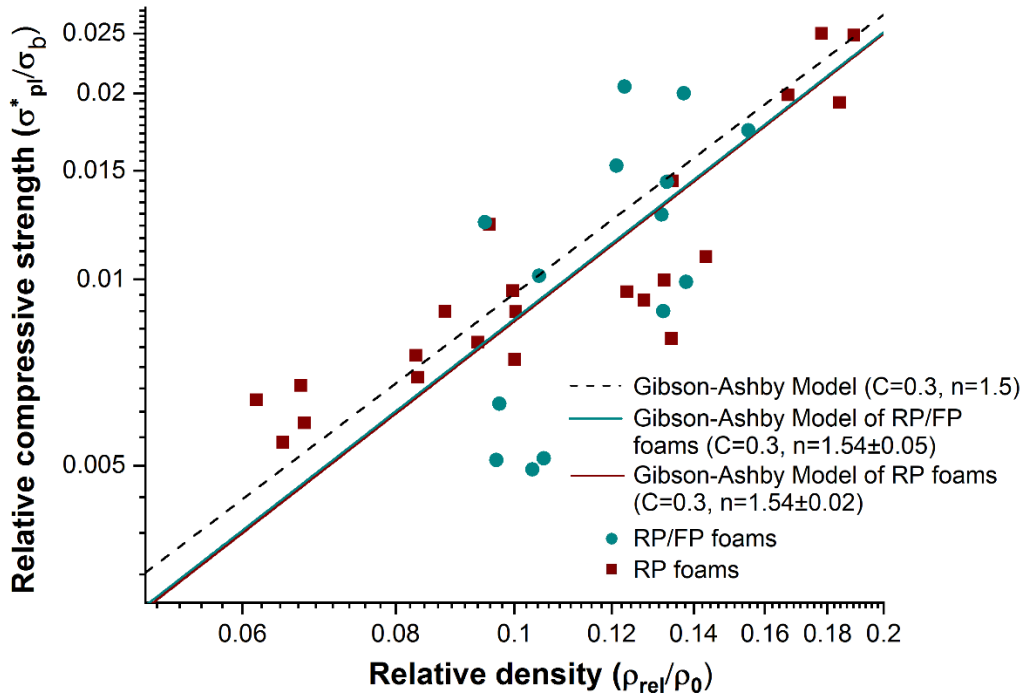


Figure 43 Relationship between the relative compressive strength and the relative density of RP (red dots) and RP/FP (green dots) aluminum foams thermally processed at 650 °C for 3 h in an Ar atmosphere; the Gibson-Ashby models were obtained by fitting experimental results with  $C$  and  $n$  variables (red line for RP foams and green line for RP/FP foams); and Gibson-Ashby model with  $C = 0.3$ ,  $n = 1.5$  (black dash line); PU template foams with a cell size of 20 ppi (adapted from [159]).

The thermal conductivity of foams  $\lambda_f$  ranged from  $2.32 \pm 0.05 \text{ W}\cdot\text{m}^{-1}\text{K}^{-1}$  for the RP/FP foams to  $3.21 \pm 0.18 \text{ W}\cdot\text{m}^{-1}\text{K}^{-1}$  for the RP foams, Table 10. To estimate the effect of additional lamellar pores on  $\lambda_f$ , the thermal conductivity of the porous strut material  $\lambda_s$  was calculated, Equation (2). As a result of the increase in the strut porosity from 37.6 % to 53.8 % due to lamellar pores,  $\lambda_s$  decreased from  $61.7 \text{ W}\cdot\text{m}^{-1}\text{K}^{-1}$  to  $32.1 \text{ W}\cdot\text{m}^{-1}\text{K}^{-1}$ .

## 5.2.4 Chapter summary

Aluminum foams were manufactured by a combination of sponge replication and freezing techniques. The foams were thermally processed at 650 °C in argon atmosphere for 3 h. The foam cell pores were varied by using PU template foams with a cell size of 10 ppi to 30 ppi. The RP/FP foams possessed lamellar pores in their struts along with the entire samples having a random orientation of lamellar pores with a pore thickness of 24  $\mu\text{m}$  to 39  $\mu\text{m}$  and material lamellae with a thickness of 78  $\mu\text{m}$  to 81  $\mu\text{m}$ . When comparing the RP/FP and the RP foams with approximately the same total porosity of 86.6 % for the 20 ppi templated foams, it was

found that the formation of lamellar pores increased the strut porosity by a factor of 1.4 and the specific surface area by a factor of 1.9 in comparison with the RP foams. The variation of the pore size of the initial PU foams led to a slight change of the specific surface area of the RP/FP foams from  $219 \text{ cm}^2 \cdot \text{g}^{-1}$  to  $238 \text{ cm}^2 \cdot \text{g}^{-1}$ .

Despite the increased strut porosity after the formation of additional strut pores, the RP/FP foams showed a higher energy absorption capability and a higher compressive yield strength compared to the RP foams, both with PU template foam cell size of 20 ppi. This effect may be related to the arrangement of the lamellar pores, which built the strut, because the compressive strength depends directly on the direction of the applied load in those materials [177]. The lamellar pores in the RP/FP samples did not have an orientation as a result of non-directional freezing. This might be an advantage for the mechanical properties of specimens with additional strut pores [21,22]. The increase in mechanical properties may be explained by the load sharing mechanism resulting from the formation of non-directional pores [174,178]. It was also found that a decrease in cell size of the RP/FP foams led also to an increase in the energy absorption capability and in the compressive yield strength, despite an increase in  $P_s$  from 47.9 % to 60.6 %; this indicates an influence of the number of struts and its architecture in a given volume element.

The relative compressive strength  $\sigma_{pl}^*/\sigma_b^*$  of the different sample series for the RP and RP/FP foams depending on the relative density  $\rho^*/\rho_s$  was in a good agreement with the Gibson-Ashby model. A slight variation of the value  $n$  may be associated with changes in the deformation modes (yielding, bending, and buckling) in the aluminum foams due to a different strut porosity (lamellar pores, hollow strut pores, and material pores) [20,183].

Finally, an increase of the strut porosity after the formation of lamellar pores led to a decrease in the thermal conductivity of the foams. Samples with finer cell pores possessed a higher thermal conductivity at the same total porosity.

### **5.3 Copper foams manufactured by the sponge replication technique and a combination of sponge replication and freezing techniques**

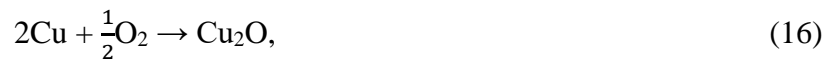
This chapter presents the manufacturing of RP and RP/FP copper foams processed at 500 °C and 900 °C for 6 h in Ar/H<sub>2</sub> atmosphere. A PU template foam with cell pore sizes of 10 ppi, 20 ppi, and 30 ppi, and a geometric size of 15 × 15 × 20 mm was used. The influence of the thermal processing temperature and the additional freezing/freeze-drying processing steps on the strut

porosity, the microstructure, the thickness of material lamellae and lamellar pores, the specific surface area, the mechanical and thermal properties were investigated in this chapter.

### 5.3.1 As-received copper powder

The X-ray diffraction patterns, TG and DSC, and the powder morphology characterization results are shown in Figure 44. As-received copper powder contained copper as the only phase; no impurities or copper oxides were observed; which may be detectable by XRD analysis. The copper powder particles were characterized by a nonspheroidal geometry and a flaky shape.

The TG and DSC indicated a continuous weight gain with a temperature increase above ~183 °C. The powder had two oxidation peaks, Figure 44. The first peak appeared at ~193 °C and the second peak was found at ~474 °C, which could be associated with the formation of Cu<sub>2</sub>O and CuO according to the following chemical reactions [185]:



The weight gain steadily increased until the onset of the second oxidation peak. The total weight gain of the copper powder was ~24 wt. %. This value is in good agreement with the quantitative oxidation of Cu to CuO having a theoretical weight increase of ~25.2 wt. %.

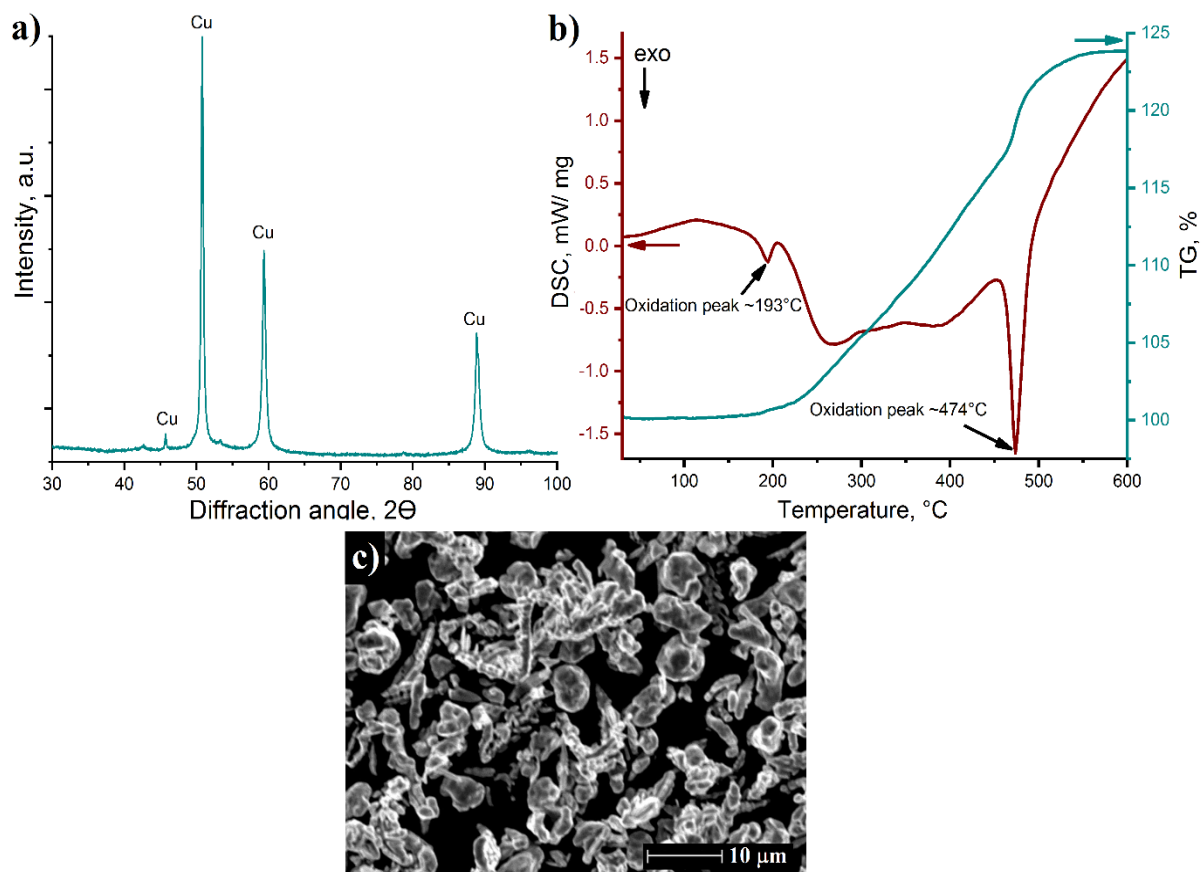


Figure 44 As-received copper powder: XRD phase analyse (a), TG and DSC curves in air (b) and SEM image of the powder (c); the heating rate was 10 K min<sup>-1</sup> (adapted from [13]).

### 5.3.2 Copper foams manufactured by the sponge replication technique at different temperatures

After binder and PU burn-out, X-ray diffraction analysis of the RP copper foams showed that the foams oxidized to ~50 wt. % of CuO and ~50 wt. % of Cu<sub>2</sub>O, Figure 45 a. A colour change of the copper foam to black was due to the removal of the PU template foam in air at 500 °C, Figure 45 b, resulting in a set of complex oxidation reactions, see Chapter 5.3.1. However, after further thermal processing in Ar/H<sub>2</sub> atmosphere, copper was the only phase detected for the RP copper foams thermally processed at 500 °C and 900 °C. A complete reduction of copper oxides to copper powders after sintering for 6–8 h in Ar/H<sub>2</sub> atmosphere was discussed in [23]. The chemical reduction of copper oxides is explained in [186] by the following chemical reaction:



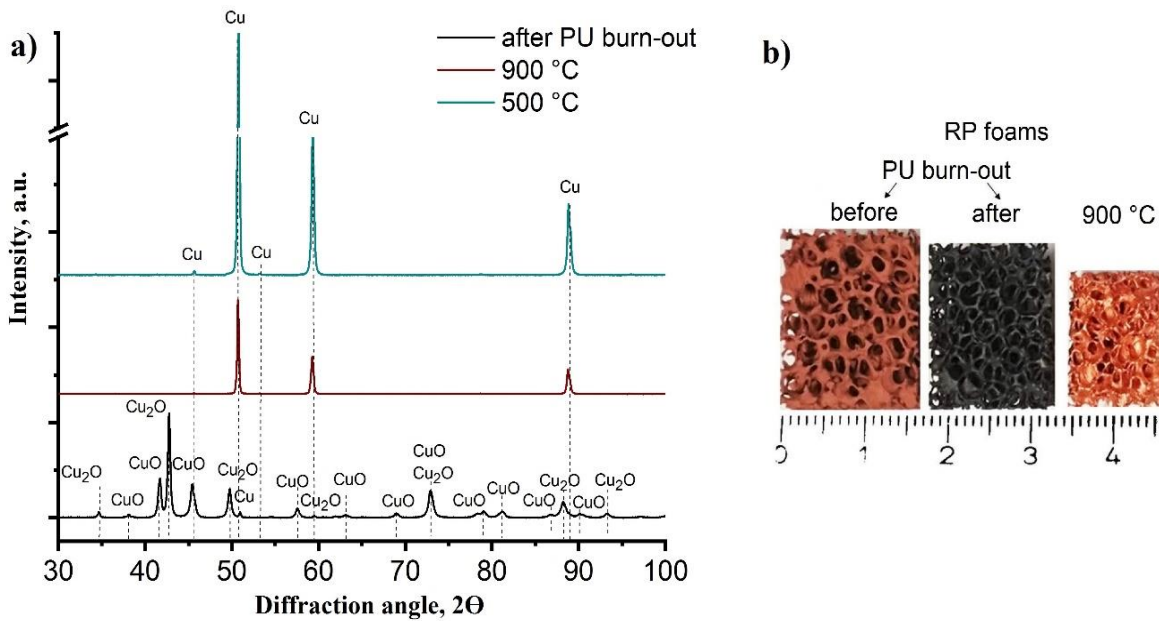


Figure 45 X-ray diffraction patterns of the RP copper foams after PU burn-out in air (a); photographs of the RP copper foams before and after binder and PU burn-out and after thermal processing at 900 °C for 6 h in Ar/H<sub>2</sub> atmosphere (b); PU template foams with a cell size of 20 ppi (adapted from [13]).

It was found that the copper struts had hollow cavities after PU burn-out and thermal processing from SEM cross-sectional images of the RP foams in Figure 46 a–d. The microstructure of the struts before binder and PU burn-out was more porous in comparison with the foams afterward due to the oxidation of the copper powder particles in air during PU burn-out in Figure 46 e,f. After the thermal processing in Ar/H<sub>2</sub> atmosphere, the microstructure of the RP foams was characterized by a higher joining degree of the powder particles, a grain growth, a decreased porosity, pore rounding, and a microstructure, which became more homogeneous with "an increase" of the processing temperature from 500 °C to 900 °C, Figure 46 g,h. These aforementioned microstructural changes may be related to enhancing atomic diffusion along grain boundaries, over the surfaces, and through the crystalline lattice at higher thermal processing temperatures [187,188].

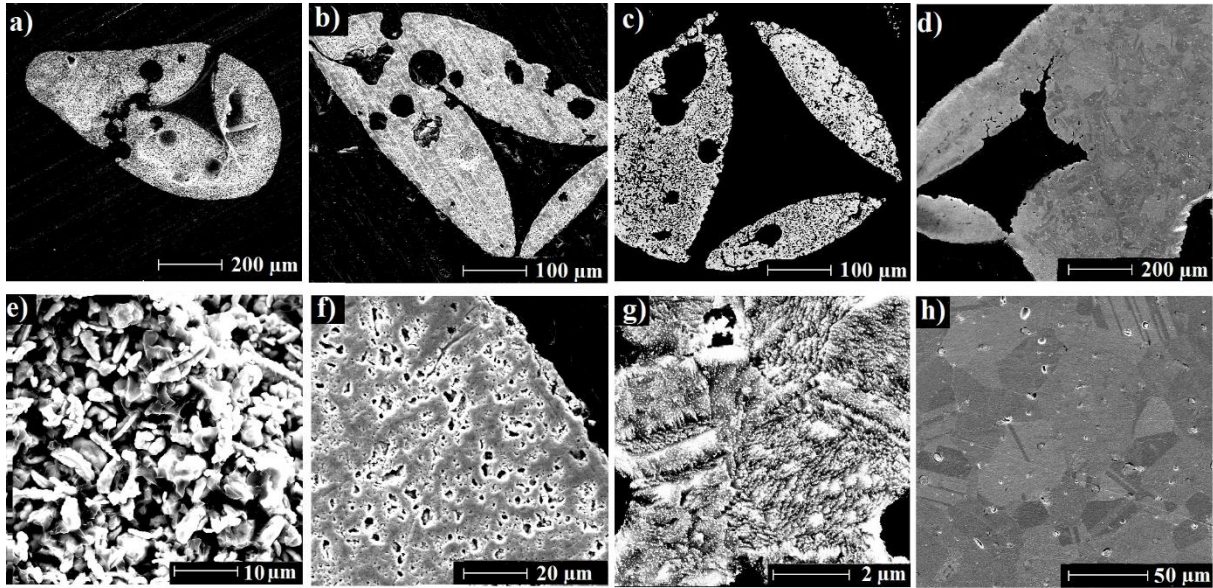


Figure 46 SEM images of RP copper foams: before (a,f) and after (b,g) binder and PU burn-out; after processing at 500 °C (c,h) and 900 °C (d,i) for 6 h in Ar/H<sub>2</sub> (adapted from [13]).

Table 11 shows values for volumetric shrinkage, porosity, and mechanical properties of the RP copper foams after thermal processing at 500 °C and at 900 °C. With increasing temperature, the volumetric shrinkage changed from 26.0 % at 500 °C to 42.6 % at 900 °C. From the results of the porosity measurements with the Archimedes method, it followed that the total porosity of the copper foams was 94.6 % after processing at 500 °C and 93.1 % after processing at 900 °C. The higher joining degree of the copper powder particles at higher processing temperatures that led to a decrease of the strut porosity from ~62.3 % at 500 °C to ~58.7 % at 900 °C, Figure 46 g,h.

Table 11 Volumetric shrinkage, porosity and mechanical properties of the RP copper foams thermally processed for 6 h at 500 °C and 900 °C in Ar/H<sub>2</sub>; PU template foams with a cell size of 20 ppi.

Sample	RP foams	
	500	900
Thermal processing temperature, °C	500	900
Volumetric shrinkage ( $S_v$ ), %	26.0 ± 4.0	42.6 ± 2.5
Total porosity ( $P_{total}$ ), %	94.6 ± 0.4	93.1 ± 0.3
Cell porosity ( $P_{cell}$ ), %	87.7 ± 5.7	85.6 ± 3.0
Strut porosity ( $P_s$ ), %	62.3 ± 7.8	58.7 ± 5.3
Compressive yield strength, MPa	0.14 ± 0.03	0.28 ± 0.07
Absorbed energy per volume, MJ·m <sup>-3</sup>	0.05	0.10

Figure 47 shows the stress-strain behavior of the selected RP copper foams. Their shapes demonstrate that the stress-strain behavior is characterized by elastic deformation up to the compressive yield point  $\sigma$ . With a load increase, the stress-strain curve changed its behavior to a long plateau with plastic deformation of the cell walls (plastic cell collapse) with a slow stress increase until the densification strain point ( $\varepsilon_D$ ) [20]. There was an increase in the mean compressive yield strength and the absorbed energy with an increase of the thermal processing temperature from  $0.14 \pm 0.03$  MPa and  $0.05 \text{ MJ}\cdot\text{m}^{-3}$  at  $500 \text{ }^\circ\text{C}$  to  $0.28 \pm 0.07$  MPa and  $0.10 \text{ MJ}\cdot\text{m}^{-3}$  at  $900 \text{ }^\circ\text{C}$  (Table 11).

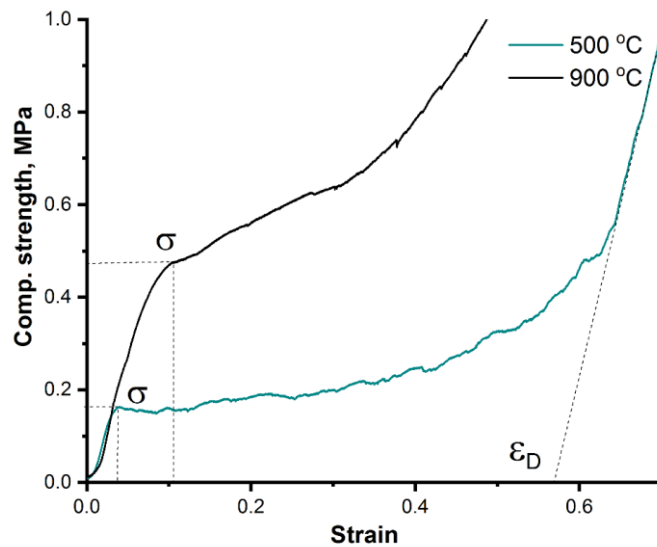


Figure 47 Compressive stress-strain curves of the RP copper foams after processing at  $500 \text{ }^\circ\text{C}$  (green) and  $900 \text{ }^\circ\text{C}$  (black) for 6 h in  $\text{Ar}/\text{H}_2$  ( $\sigma$  – compressive yield strength,  $\varepsilon_D$  – densification strain); PU template foams with a cell size of 20 ppi (adapted from [13]).

The RP copper foams thermally processed at  $900 \text{ }^\circ\text{C}$  were characterized by a higher compressive yield strength and a higher energy absorption capability than the foams processed at  $500 \text{ }^\circ\text{C}$  due to the more intense joining of the powder particles resulting in a higher powder particle connectivity, and as a consequence, a decrease of the material strut porosity. It must be noted that a processing temperature of  $500 \text{ }^\circ\text{C}$  was not sufficient for proper microstructure formation, and the thermal processing was carried out at  $900 \text{ }^\circ\text{C}$  for ongoing work.

### 5.3.3 Copper foams manufactured by the sponge replication technique with different cell size

Table 12 shows geometrical data, mechanical and thermal properties of RP copper foams thermally processed for 6 h at  $900 \text{ }^\circ\text{C}$  in  $\text{Ar}/\text{H}_2$  for PU template foams with a cell size of 10 ppi, 20 ppi, and 30 ppi. The RP copper foams were prepared almost the same total porosity, ranging

between 92 % and 93 %. The RP copper foams were characterized by a high volumetric shrinkage varied from 42.5 % (20 ppi) to 60.5 % (10 ppi). It was found an increase of the cell porosity from 78.8 % to 89.2 % and a decrease of the strut porosity from 68.2 % to 46.5 % with an increase of the cell size of the PU template foams from 30 ppi to 10 ppi. The strut porosity was lower due to the fact that the volume fraction of pores after PU burn-out decreased and the thickness of the struts increased at the same load of the slurry, as a result, the surface area of the PU template foam covered by the suspension was less for the PU template foam with a cell size of 10 ppi than with a cell size of 30 ppi.

Table 12 Geometrical, mechanical and thermal properties of the RP copper foams thermally processed for 6 h at 900 °C in Ar/H<sub>2</sub> for PU template foams with a cell size of 10 ppi, 20 ppi, and 30 ppi.

Cell size of PU template foams	10 ppi	20 ppi	30 ppi
Volumetric shrinkage ( $S_v$ ), %	60.5 ± 4.0	42.6 ± 2.5	46.5 ± 5.6
Total porosity ( $P_{total}$ ), %	92.8 ± 0.8	93.1 ± 0.3	92.6 ± 0.7
Cell porosity ( $P_{cell}$ ), %	89.2 ± 1.0	85.6 ± 3.0	78.8 ± 5.2
Strut porosity ( $P_s$ ), %	46.5 ± 3.9	58.7 ± 5.3	68.2 ± 4.4
Mean cell size, mm	2.63 ± 0.20	1.89 ± 0.12	1.61 ± 0.15
Mean diameter of wall struts, μm	124 ± 57	135 ± 66	94 ± 41
Mean diameter of struts, mm	0.56 ± 0.33	0.44 ± 0.15	0.21 ± 0.09
Specific surface area by μ-CT, cm <sup>2</sup> ·g <sup>-1</sup>	24	25	41
Compressive yield strength, MPa	0.22 ± 0.07	0.28 ± 0.07	0.56 ± 0.14
Absorbed energy per volume, MJ·m <sup>-3</sup>	0.09	0.10	0.14
Therm. Cond. of foam $\lambda_f$ , W·m <sup>-1</sup> K <sup>-1</sup>	2.41 ± 0.14	3.15 ± 0.18	3.44 ± 0.20
Therm. Cond. of porous strut material $\lambda_s$ , W·m <sup>-1</sup> K <sup>-1</sup>	108.1	96.7	81.4

Figure 48 shows μ-CT 3D reconstruction images of the RP copper foams after thermal processing for 6 h at 900 °C in Ar/H<sub>2</sub> for different cell sizes of the PU template foam (10 ppi, 20 ppi, and 30 ppi). The RP copper foams possess open cells. The distribution and the average value of the cell size, the wall strut thickness, and the strut thickness are shown in Figure 49 and Table 12. The mean cell size was 2.63 ± 0.20 mm for the 10 ppi, 1.89 ± 0.12 mm for the 20 ppi, and 1.61 ± 0.15 mm for the 30 ppi templated foams. The strut thickness and the wall strut thickness increased with the cell size of PU template foams, Figure 49 b,c and Table 12.

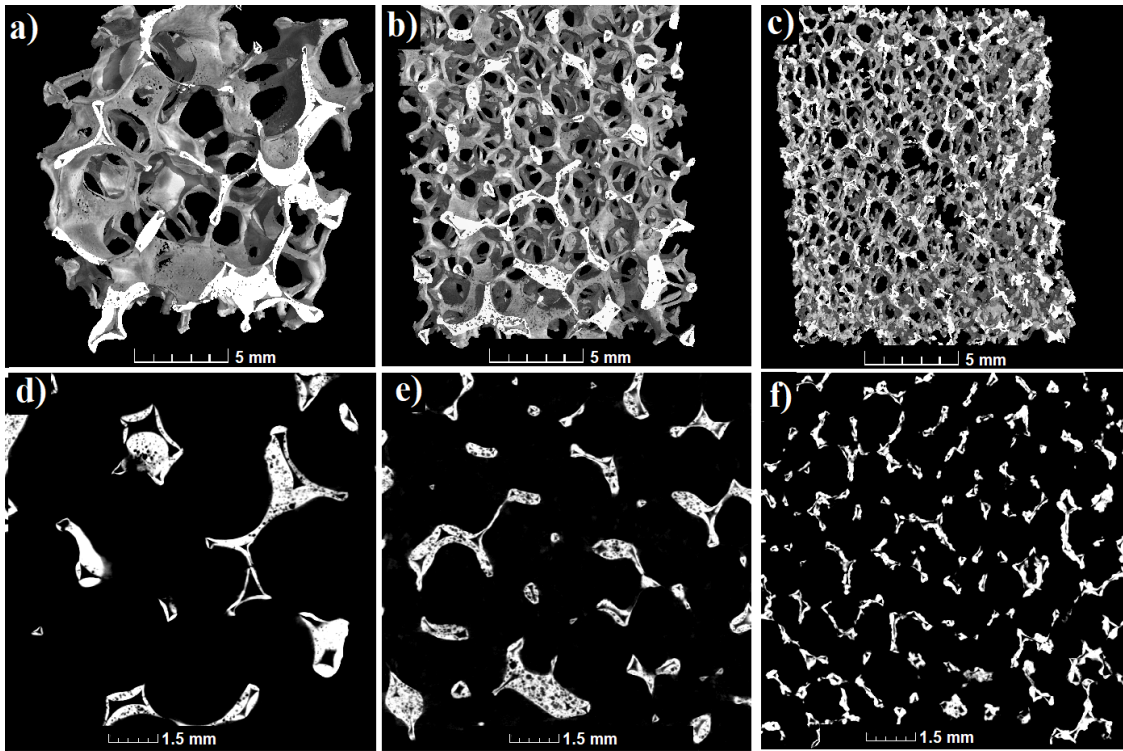


Figure 48 3D reconstructed images of the RP copper foams after thermal processing at 900 °C for 6 h in Ar/H<sub>2</sub> atmosphere for different cell sizes of the PU template foams: 10 ppi (a,d), 20 ppi (b,e), and 30 ppi (c,f).

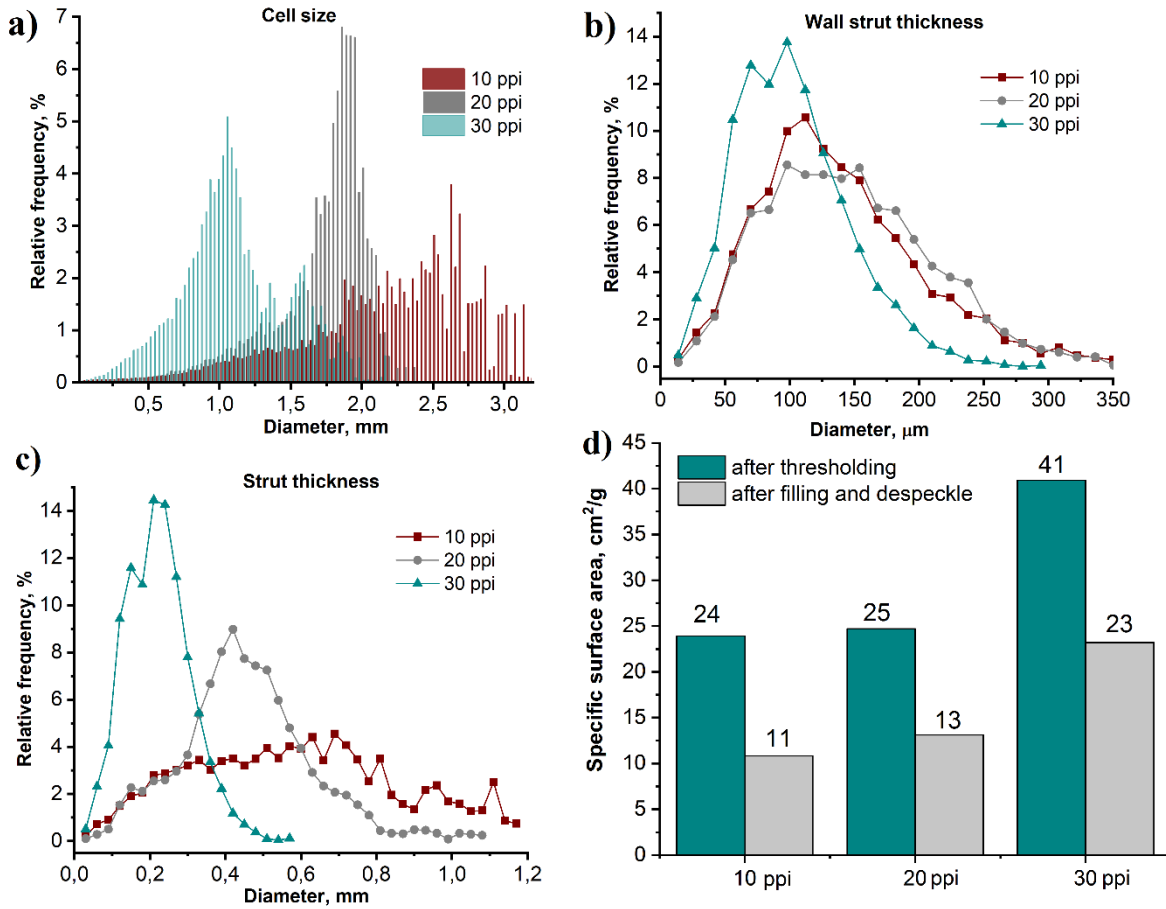


Figure 49 Distributions of the cell size (a), wall strut thickness (b), and strut thickness (c) of the RP copper foams thermally processed at 900 °C for 6 h in Ar/H<sub>2</sub> atmosphere for different PU template foam sizes (10 ppi, 20 ppi, and 30 ppi); data obtained from  $\mu$ -CT measurements.

The calculation of the specific surface area from the  $\mu$ -CT reconstruction data is shown in Figure 49 d and Table 12. The specific surface area increased with decreasing cell size of the PU template foams from 24 cm<sup>2</sup>·g<sup>-1</sup> to 41 cm<sup>2</sup>·g<sup>-1</sup>. To estimate the impact of hollow struts on the specific surface area,  $\mu$ -CT reconstructions of the RP copper foams were filled and despeckled after thresholding, see Chapter 4.2.3. The hollow struts contributed significantly to the specific surface area, Figure 49 d. In the 10 ppi templated foam, for example, the specific surface area increased from 11 cm<sup>2</sup>·g<sup>-1</sup> to 24 cm<sup>2</sup>·g<sup>-1</sup> due to the hollow struts. The difference in the specific surface area before and after filling and despeckle for the finer pored foams was smaller because the surface area of the foam in general increases with the number of foam cells. This was also observed for the RP/FP aluminum samples in Chapter 5.2.2.

The compressive strength results in Table 12 show that the average values of compressive yield strength and absorbed energy increased with decreasing pore size of the RP/FP copper foams. The compressive yield strength varied from  $0.22 \pm 0.07$  MPa for the 10 ppi to  $0.56 \pm 0.14$  MPa

for the 30 ppi templated copper foams. The absorbed energy slightly increased from  $0.09 \text{ MJ}\cdot\text{m}^{-3}$  (10 ppi) to  $0.14 \text{ MJ}\cdot\text{m}^{-3}$  (30 ppi). The typical compressive stress-strain curves of the RP copper foams had a shape similar to the curves shown in Figure 47. They also contained an elastic deformation region, a long plateau, and a densification region.

A Gibson-Ashby plot was carried out to compare the relative compressive strength  $\sigma_{pl}^*/\sigma_b^*$  of different series of the RP foams as a function of the relative density  $\rho^*/\rho_s$  with  $C = 0.3$  and  $n = 1.5$ , both,  $C$  and  $n$  were fixed (dashed line), and with fixed  $C = 0.3$  and varying  $n$  for the copper foams in Figure 50. It can be seen that the RP foams had a high scattering of the parameter  $n$  for the plotted curves, related to the foam cell size (10 ppi:  $n \approx 1.69$ , 20 ppi:  $n \approx 1.54$ , 30 ppi:  $n \approx 1.38$ ). The discrepancy between the fitted functions and between the experimental values of  $n$  and the empirical value of  $n$  may be due to several factors: 1) the Gibson-Ashby model used in this work was originally applied to metal foams with open-cell pores without strut porosity [20], this was also stated for aluminum foams and their deviating  $n$ ; 2) due to the high density of copper ( $\rho_{Cu} = 8.96 \text{ g cm}^{-3}$ ) homogeneous coating of the PU template foam with the copper powder containing suspension was challenging/less reproducible as for aluminum foams; and 3) during the thermal processing, a very high shrinkage of the foams with low relative density was observed, especially for foams with a cell size of 10 ppi, in several cases their shape underwent a deformation. These factors may affect the mechanical strength of the foams and may change their deformation mechanism during loading such as yielding, bending, and buckling, leading to a change in the value of  $n$  [20,183]. Therefore, for these foams, the fitted curves had this scattering between each other and the Gibson-Ashby model.

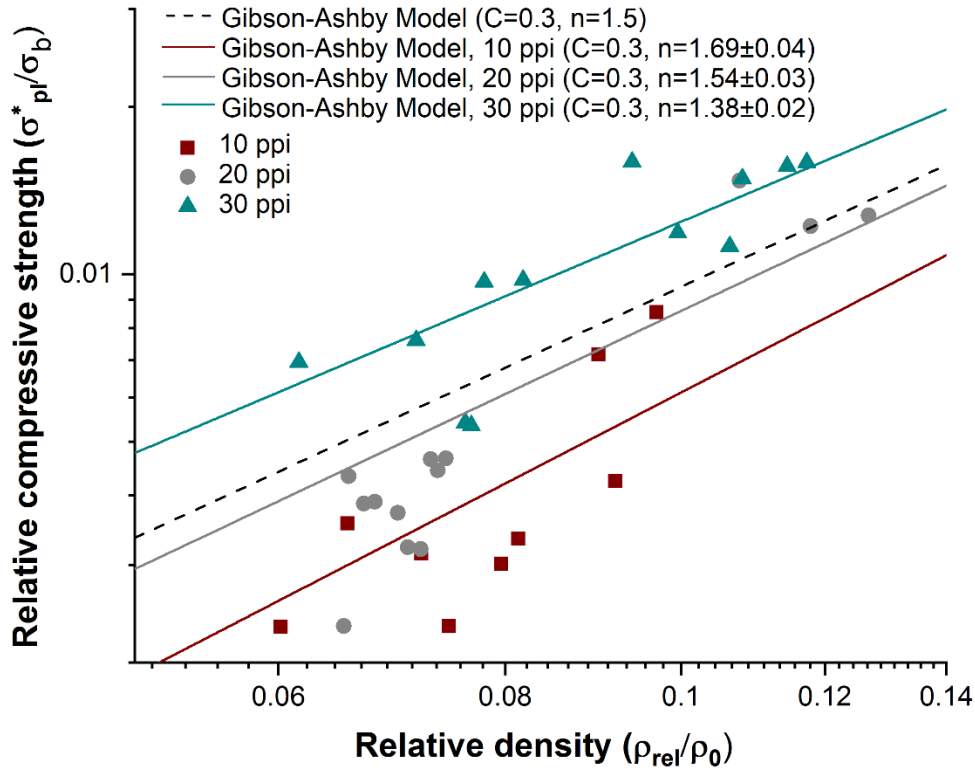


Figure 50 Relationship between the relative compressive strength and the relative density of the RP copper foams thermally processed at 900 °C for 6 h in Ar/H<sub>2</sub> atmosphere for different cell sizes of the PU template foams (10 ppi, 20 ppi, and 30 ppi); Gibson-Ashby models obtained by fitting experimental results with  $C = 0.3$  and variable  $n$ ; and Gibson-Ashby model with  $C = 0.3$ ,  $n = 1.5$  (black dash line).

The measurement of the thermal conductivity  $\lambda_f$  of the RP copper foams ranged from  $2.41 \pm 0.14 \text{ W}\cdot\text{m}^{-1}\text{K}^{-1}$  to  $3.44 \pm 0.20 \text{ W}\cdot\text{m}^{-1}\text{K}^{-1}$  with decreasing cell size of the PU template foams from 10 ppi to 30 ppi, Table 12. The results show that  $\lambda_f$  is significantly lower than that of bulk copper, which is  $\sim 413 \text{ W}\cdot\text{m}^{-1}\text{K}^{-1}$ , influenced by several levels of foam porosity. The thermal conductivity calculations of the porous strut material  $\lambda_s$  were performed according to a model from Ashby [19], Equation (2). The thermal conductivity of the porous strut material decreased from  $108.1 \text{ W}\cdot\text{m}^{-1}\text{K}^{-1}$  to  $81.4 \text{ W}\cdot\text{m}^{-1}\text{K}^{-1}$  with an increasing  $P_s$  from 45.6 % (10 ppi) to 68.2 % (30 ppi).

### 5.3.4 Copper foams manufactured by a combination of sponge replication and freezing techniques with different cell size

Figure 51 shows SEM images of the cross-sections and surfaces of the RP/FP copper foams after thermal processing at 900 °C. The images demonstrate the formation of lamellar pores and material lamellae with random orientation as for the RP/FP aluminum foams, Chapter 5.2.2.

The microstructure of the material lamellae appeared heterogeneously after thermal processing. Some areas with pores in material lamellae were observed, Figure 51 c,e. Grain boundaries between thermally processed copper particles can be seen in Figure 51 f.

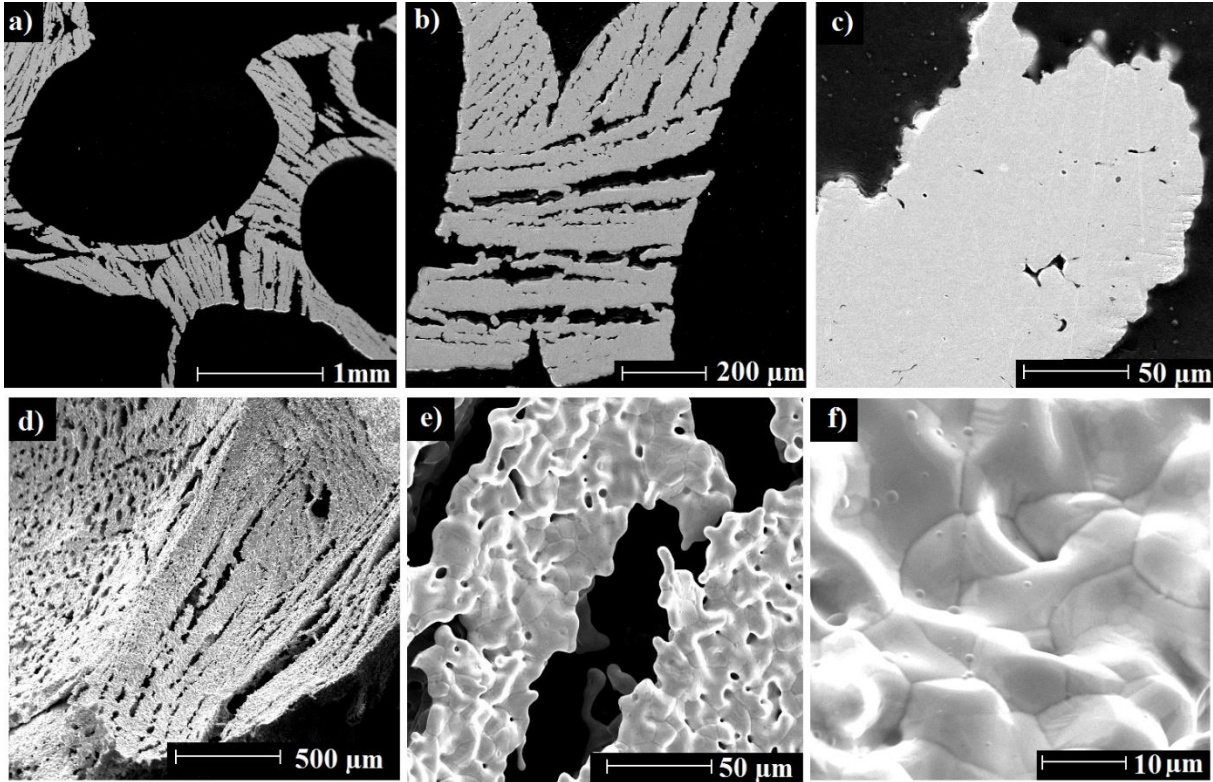


Figure 51 SEM images of the cross section of RP/FP copper foams for 20 ppi templated foams (a–c) and their surfaces (d–f) after thermal processing for 6h in Ar/H<sub>2</sub> at 900 °C (adapted from [13]).

For further investigation of the influence of the foam pore size on geometrical, mechanical, and thermal properties of the RP/FP copper foams were prepared with almost the same porosity ranging between ~86.4 % and 87.4 %. The results are listed in Table 13. The RP/FP foams were characterized by high volumetric shrinkage of about 58.3 % to 62.6 %. The cell porosity decreased from 72.9 % for the 10 ppi templated foam to 61.0 % for 30 ppi templated foam and correlated with the foam cell size. The strut porosity varied from 57.2 % (10 ppi) to 66.7 % (30 ppi).

Table 13 Geometrical, mechanical, and thermal properties of RR/FP copper foams thermally processed for 6 h at 900 °C in Ar/H<sub>2</sub> atmosphere; templated with different cell sizes of the PU foams (10 ppi, 20 ppi, and 30 ppi).

Cell size of PU template foams	10 ppi	20 ppi	30 ppi
Volumetric shrinkage ( $S_v$ ), %	58.3 ± 4.6	59.5 ± 2.3	62.6 ± 1.5
Total porosity ( $P_{total}$ ), %	87.2 ± 1.4	87.4 ± 0.8	86.4 ± 0.9
Cell porosity ( $P_{cell}$ ), %	72.9 ± 4.2	68.0 ± 2.6	61.0 ± 6.2
Strut porosity ( $P_s$ ), %	57.2 ± 1.1	64.1 ± 2.5	66.7 ± 3.9
Mean diameter of struts, mm	0.90 ± 0.47	0.49 ± 0.27	0.30 ± 0.16
Mean cell size, mm	2.72 ± 1.15	1.61 ± 0.22	1.28 ± 0.60
Material lamellae thickness, μm	80 ± 38	87 ± 41	72 ± 37
Lamellar pore thickness, μm	56 ± 49	38 ± 24	40 ± 26
Specific surface area by μ-CT, cm <sup>2</sup> ·g <sup>-1</sup>	42	48	53
Compressive yield strength, MPA	0.95 ± 0.22	1.16 ± 0.29	1.61 ± 0.53
Absorbed energy per volume, MJ·m <sup>-3</sup>	0.23	0.30	0.36
Therm. Cond. of foam $\lambda_f$ , W m <sup>-1</sup> ·K <sup>-1</sup>	5.09 ± 0.27	4.95 ± 0.27	5.94 ± 0.32
Therm. Cond. of porous strut material $\lambda_s$ , W m <sup>-1</sup> ·K <sup>-1</sup>	68.8	59.1	55.5
Bulk therm. Cond. of bulk material $\lambda_b$ , W m <sup>-1</sup> ·K <sup>-1</sup>	191.0	192.8	213.6

Figure 52 shows μ-CT 3D reconstruction images of the foams after thermal processing at 900 °C for different cell sizes of the PU template foam (10 ppi, 20 ppi, and 30 ppi). A random orientation of lamellar pores along with the foams can be recognized. The RP/FP copper foams possess open cells. From the distribution of the cell size and the strut thickness in Figure 53 a,b, it is evident their increase with decreasing PU template foam cell size. The mean cell size decreased from 2.72 ± 1.15 μm for the 10 ppi templated foam to 1.28 ± 0.60 μm for the 30 ppi templated foam, Table 13. The RP/FP copper foams possess strut thicknesses varied from  $D_s \approx 0.90 \pm 0.47$  mm (10 ppi) to  $D_s \approx 0.30 \pm 0.16$  mm (30 ppi), Table 13. Material lamellae thickness and lamellar pore thickness are shown in Figure 53 c,d, and their calculated mean values are listed in Table 13. The material lamellae varied from 72 μm to 87 μm and the lamellar pores were in the range from 38 μm to 56 μm.

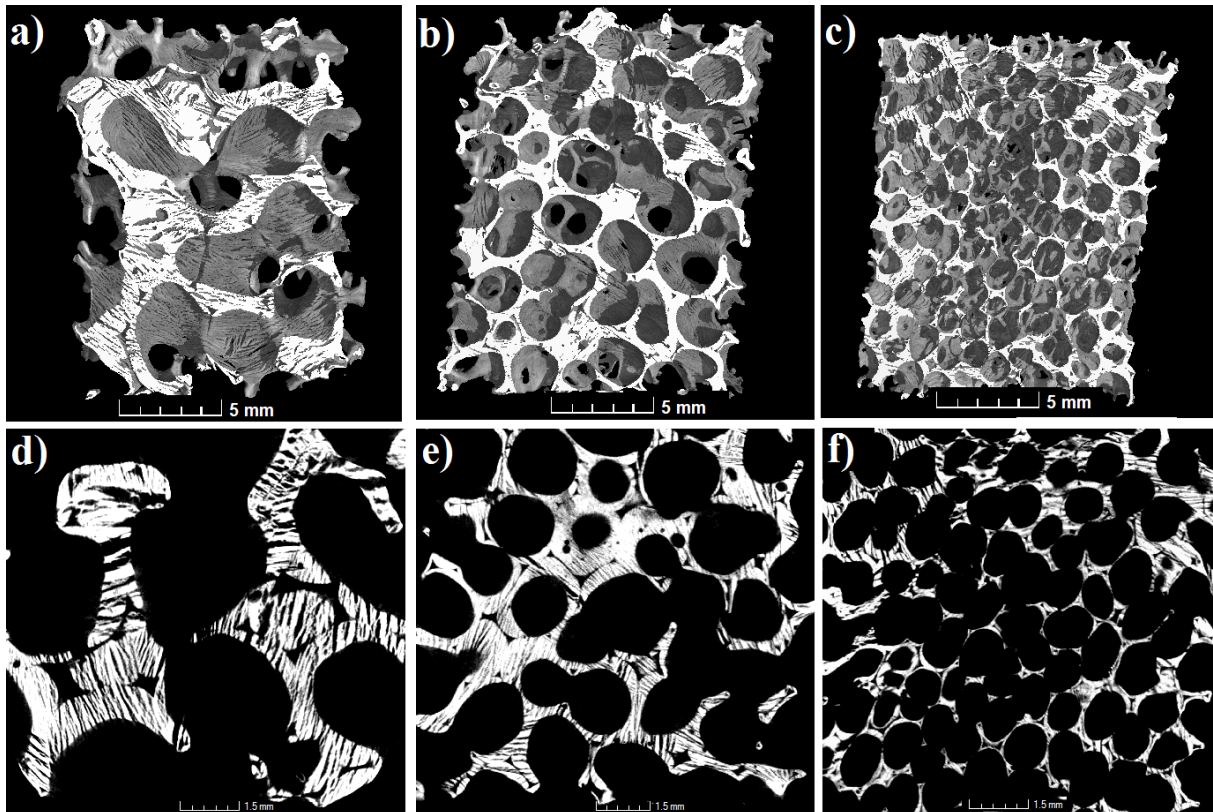


Figure 52  $\mu$ -CT reconstruction images of the RP/FP copper foams after thermal processing at 900 °C for 6 h in Ar/H<sub>2</sub> atmosphere; different cell sizes of the PU template foams: 10 ppi (a,d), 20 ppi (b,e), and 30 ppi (c,f).

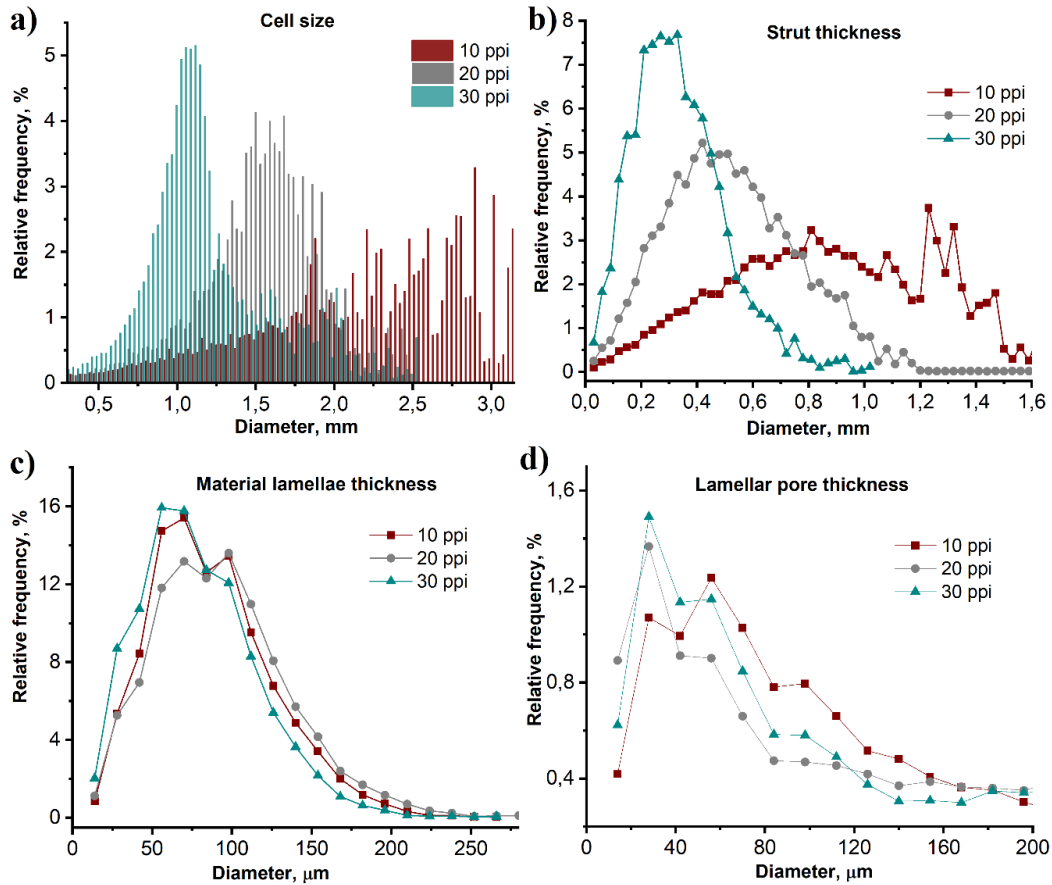


Figure 53 Distributions of the cell size (a), the strut thickness (b), the material lamellae (c), and lamellar pores (d) of the RP/FP copper foams thermally processed at 900 °C for 6 h in Ar/H<sub>2</sub> atmosphere for foams templated with different cell sizes of the PU foams (10 ppi, 20 ppi, and 30 ppi); measurements were carried out with  $\mu$ -CT (adapted from [160]).

The specific surface area calculated from  $\mu$ -CT reconstruction data after thresholding increased with decreasing foam cell size from 42 cm<sup>2</sup>·g<sup>-1</sup> (10 ppi) to 53 cm<sup>2</sup>·g<sup>-1</sup> (30 ppi), Figure 54 and Table 13. Comparing these results after the filling and despeckle step with the results after thresholding, see Chapter 4.2.3, it can be seen that the additional lamellar pores and hollow struts significantly increased these values for all samples by a factor of  $\sim$ 7 for the 10 ppi, a factor of  $\sim$ 3.4 for the 20 ppi, and a factor of  $\sim$ 3.5 for the 30 ppi templated foams.

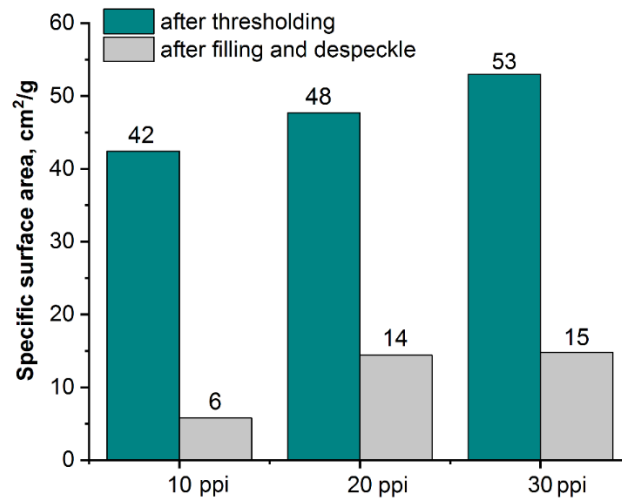


Figure 54 Specific surface area of the RP/FP copper foams thermally processed at 900 °C for 6 h in Ar/H<sub>2</sub> atmosphere for different template cell sizes of the PU foams (10 ppi, 20 ppi, and 30 ppi); data obtained from  $\mu$ -CT analysis.

Compressive strength testing showed an increase of the compressive yield strength and the adsorbed energy with a decreasing foam cell size of the RP/FP foams; this was from  $0.95 \pm 0.22$  MPa and  $0.23 \text{ MJ}\cdot\text{m}^{-3}$  (10 ppi) to  $1.61 \pm 0.53$  MPa and  $0.36 \text{ MJ}\cdot\text{m}^{-3}$  (30 ppi), Table 13. The Gibson-Ashby model was applied also for the RP/FP copper foams with fixed  $C = 0.3$  and  $n = 1.5$  (dashed line) and with fixed  $C = 0.3$  and varying  $n$  values for the prepared foams, see Figure 55. It can be seen that the RP/FP foams had a small scatter of the values for the parameter  $n$  for the fitting functions (10 ppi:  $n \approx 1.51$ ; 20 ppi:  $n \approx 1.46$ , 30 ppi:  $n \approx 1.45$ ). With a decrease in the cell size and a corresponding increase in the number of struts, a slight increase in the relative compressive strength was observed. The experimental values of  $n$ , as well as the fitted functions for the experimental data, were in good agreement with the Gibson-Ashby model. The discrepancy between the experimental values of  $n$  and the empirical value ( $n = 1.5$ ) can be attributed to the presence of open struts and lamellar pores, as the model is initially applied to homogeneous foams without pores [20]. In a variety of publications also deviations of experimental values from empirical values were observed as a result of changes in the cell size and the presence of pores in the struts [25,174,178,182]. All these factors might modify the deformation mechanism of the foams such as yielding, bending, and buckling, which results in a variation of the  $n$  value [20,183].

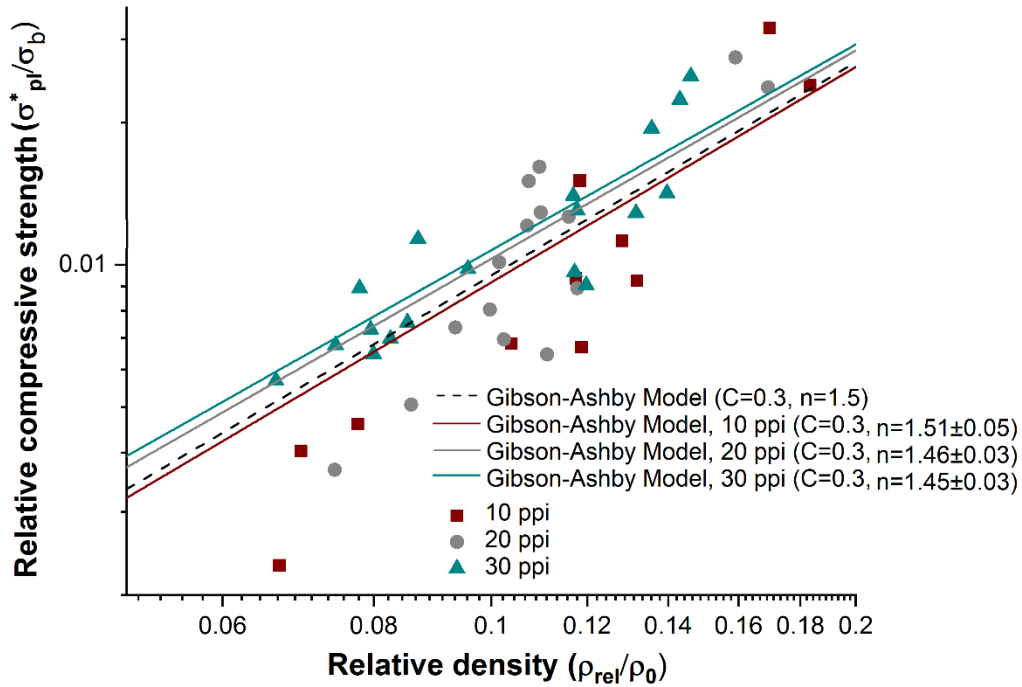


Figure 55 Relationship between the relative compressive strength and the relative density of the RP/FP copper foams thermally processed at 900 °C for 6 h in Ar/H<sub>2</sub> atmosphere; foams from different cell size of the PU template foams (10 ppi, 20 ppi, and 30 ppi); Gibson-Ashby models obtained by fitting experimental results with  $C = 0.3$  and variable  $n$ ; and Gibson-Ashby model with  $C = 0.3$ ,  $n = 1.5$  (black dash line).

The thermal conductivity  $\lambda_f$  of the RP/FP copper foams was  $5.09 \pm 0.27 \text{ W}\cdot\text{m}^{-1}\text{K}^{-1}$  for the 10 ppi,  $4.95 \pm 0.27 \text{ W}\cdot\text{m}^{-1}\text{K}^{-1}$  for the 20 ppi, and  $5.94 \pm 0.32 \text{ W}\cdot\text{m}^{-1}\text{K}^{-1}$  for the 30 ppi templated foams. The calculated thermal conductivity of porous strut material  $\lambda_s$  using a model from Ashby [19], Equation (2), ranged from  $55.5 \text{ W}\cdot\text{m}^{-1}\text{K}^{-1}$  (10 ppi) to  $68.8 \text{ W}\cdot\text{m}^{-1}\text{K}^{-1}$  (30 ppi). A model derived by Eucken [139], Equation (3), was used to estimate the thermal conductivity of the bulk strut material  $\lambda_b$ . The calculated values of  $\lambda_b$  varied from  $191.0 \text{ W}\cdot\text{m}^{-1}\text{K}^{-1}$  (10 ppi) to  $213.6 \text{ W}\cdot\text{m}^{-1}\text{K}^{-1}$  (30 ppi). These low values of  $\lambda_b$  for the RP/FP foams compared to the thermal conductivity of pure bulk copper ( $\sim 413 \text{ W}\cdot\text{m}^{-1}\text{K}^{-1}$ ) may be related to an increase in the number of grain boundaries in the heat flow path with decreasing grain size compared to bulk copper or the residual copper oxide(s) not detected by X-ray diffraction due to a concentration below the detection limit. Thus, copper oxides have low thermal conductivity ( $\text{CuO} \approx 76.5 \text{ W}\cdot\text{m}^{-1}\text{K}^{-1}$  [189],  $\text{Cu}_2\text{O} \approx 4.5 \text{ W}\cdot\text{m}^{-1}\text{K}^{-1}$  [190]).

### 5.3.5 Chapter summary

Copper foams were manufactured by the sponge replication technique and a combination of sponge replication of freezing techniques at 500 °C and 900 °C for 6 h in Ar/H<sub>2</sub> atmosphere in order to reduce oxidic copper species to form elemental copper. The foams were templated with

different foam cell sizes of the PU template foam ranging from 10 ppi to 30 ppi. The final temperature for thermal processing was set to 900 °C. That made it possible to manufacture foams with a comparatively higher compressive yield strength and a higher energy absorption capability than at 500 °C.

The formed lamellar pores in the RP/FP foams had a random direction along with the foam sample. The mean thickness of the lamellar pores was between 38 μm and 56 μm, and the material lamellae possessed a thickness of 72–87 μm. The formation of lamellar pores increased the specific surface area for all samples, for example, by a factor of ~1.9 for the 20 ppi templated foam.

The increase in compressive yield strength, absorbed energy, and thermal conductivity of the RP/FP foams compared to the RP foams may be associated with lower total porosity and smaller cell sizes, despite a higher porosity of the struts. It seems possible that the formation of non-directional lamellar pores improved the mechanical properties of the foams by a load sharing mechanism [174,178]. The results of the relative compressive strength  $\sigma_{pl}^*/\sigma_b^*$  for the RP/FP foams as a function of the relative density  $\rho^*/\rho_s$  agreed well with the Gibson-Ashby model. Variations of  $n$  values were observed compared to empirical values, which might be associated with changes in the deformation modes (yielding, bending, and buckling) and this model was originally used for open-cell porous foams without strut porosity. In general, the compressive yield strength and the energy absorption capacity increased with the number of cell pores.

#### **5.4 Direct crystallization of active coatings onto the surface of aluminum and copper foams**

This section presents the results of the coatings on RP and RP/FP aluminum and copper foams with SAPO-34 and HKUST-1, respectively. Microporous coatings on macroporous supports are under discussion for heat transformation applications such as adsorption heat storage or as materials in adsorption heat pumps [6]. The effect of the crystallization time on the morphology of the obtained coatings, weight gain of crystallized materials, and their water adsorption are investigated. It must be noted that the loading of the microporous component plays a crucial role in the adsorption capacity of the resulting composite materials; thus, it is important to know the share of both components: the support and the microporous active component. This is, however, a challenge, since part of the support may be dissolved in direct crystallization processes and transferred into an active component. In a first approximation, it was assumed that dissolution of the support does not take place and thus, the weight gain after crystallization

and molecular template burn-out (in case of SAPO-34; 550 °C in air) was taken to estimate the load of the microporous components, and deviations found after analysis have been assigned to support dissolution processes.

#### **5.4.1 Direct crystallization of SAPO-34 onto the surface of aluminum foams**

In this part, the RP and RP/FP aluminum foams with approximately the same total porosity of 86.6 % and the same pore size of the initial PU template foam of 20 ppi are discussed. A more detailed comparison of the samples is given in Chapter 5.2.3.

Figure 56 shows SEM images after crystallization of SAPO-34 on the RP/FP aluminum foams after different crystallization times 5 h, 15 h, and 24 h. For a crystallization time of 5 h and 15 h, there were areas where the openings of the lamellar pores are still visible (Figure 56 a,e). With increasing crystallization time, the openings of the lamellar pores were completely covered with SAPO-34 (Figure 56 i). It can be seen that on the surface of all samples crystals were cube-shaped with varying crystal sizes. The average crystal size was ~18  $\mu\text{m}$  after crystallization for 5 h, ~16  $\mu\text{m}$  for 15 h, and ~13  $\mu\text{m}$  for 24 h. The SAPO-34 crystals grow on top of each other, forming cascades of crystals. A similar morphology and arrangement of the crystals were found in [116], in which the same solution was used for the synthesis of SAPO-34 on the surface of open cellular silicon carbide foams. The X-ray diffraction patterns of the crystallized material in Figure 57 were in good agreement with the calculated SAPO-34 pattern, see the calculation procedure in Chapter 4.2.1. No amorphous phases were detected even with a crystallization time of 5 h.

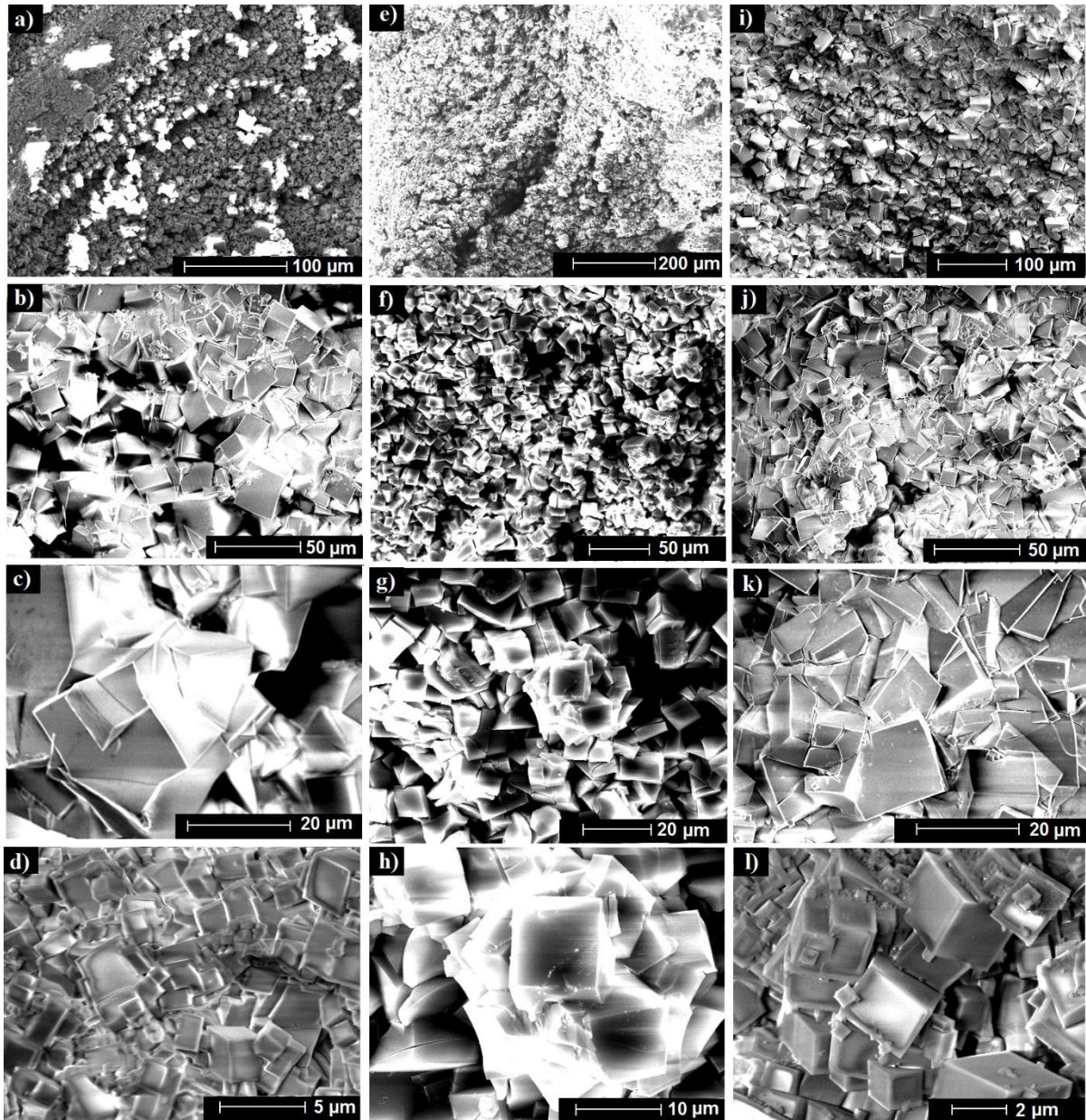


Figure 56 SEM images of the RP/FP aluminum foams after crystallization of SAPO-34 for 5 h (a–d), 15 h (e–h), and 24 h (i–l).

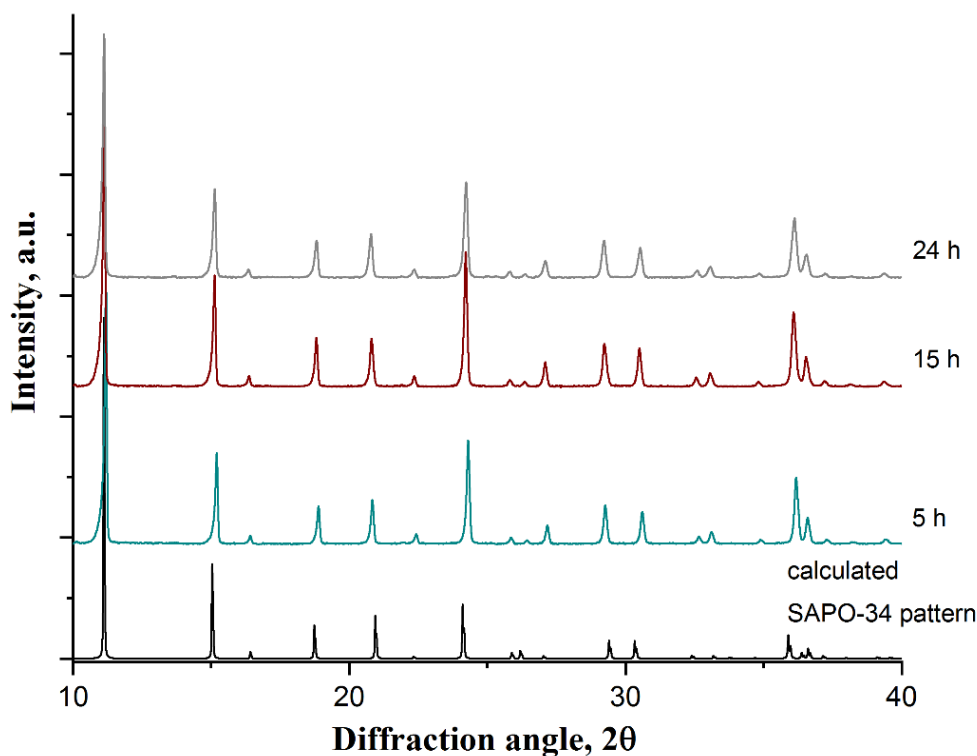


Figure 57 X-ray diffraction patterns of SAPO-34 calculated patterns (black), after crystallization for 5 h (green), 15 h (red), and 24 h (grey).

The cross-section images of the RP and RP/FP aluminum foams in Figure 58 indicate that SAPO-34 crystals were not only formed on the outside of the struts but also on the surface inside the hollow struts and in the lamellar pores of the foams. After crystallization for 5 hours (Figure 58 a,d), a non-homogeneous formation of coated islands was observed. The highlighted areas (white rectangles) show images at a higher resolution where the boundary between the crystallized SAPO-34 and the strut is visible. The formation of crystals inside the struts might be related to edge defects, which are typical for sponge replicated foams. These defects may allow hollow strut pores to be accessed by the crystallization solution for the SAPO-34 formation. SAPO-34 crystals were observed along all material lamellae in the RP/FP foams. With increasing crystallization time, a gradual growth of SAPO-34 was seen on the surface of the struts, inside the hollow pores, and in the lamellar pores.

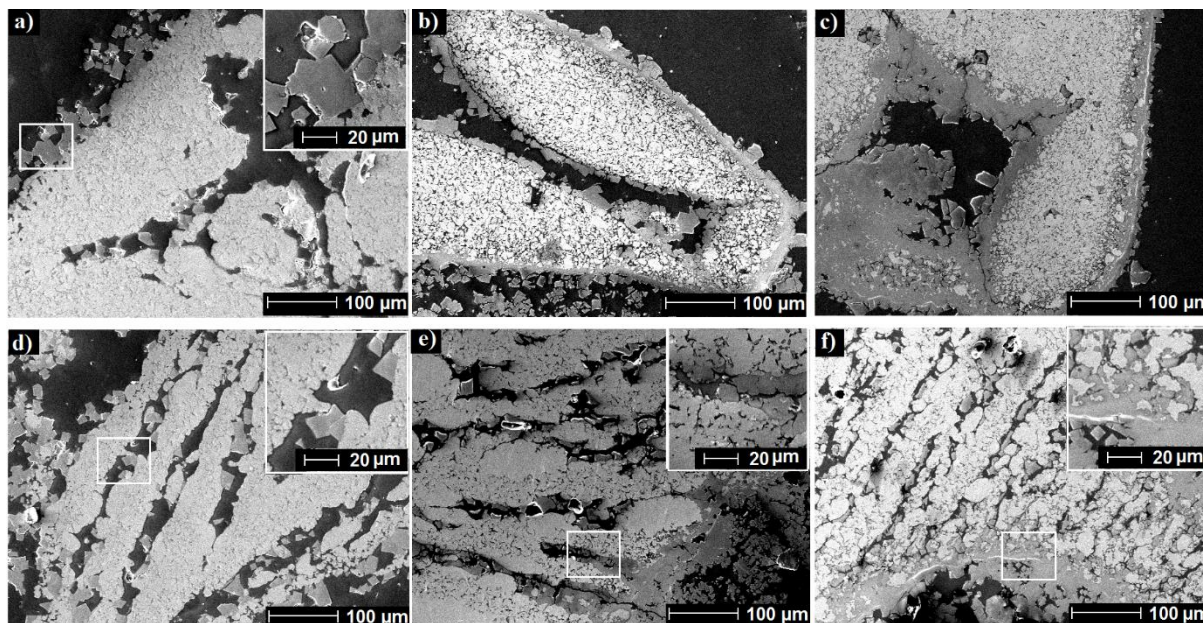


Figure 58 SEM cross section images of the RP (top) and RP/FP (bottom) aluminum foams after crystallization of SAPO-34 for 5 h (a,d), 15 h (b,e), and 24 h (c,f); PU template foams with a cell size of 20 ppi.

Figure 59a shows the SAPO-34 loading as a function of the crystallization time. It can be seen that zeolite loading also increased with the crystallization time. However, a scatter of these values was observed. With the same crystallization time, some foams had different amounts of the crystallized SAPO-34. This may be due to the fact that small fragments of the foams were broken during loading the foams into the autoclave, by a subsequent washing procedure; or due to a nonuniformity of the SAPO-34 coating on the surface of the foams. The maximum weight increase after 24 h was 44.1 wt. % for the RP/FP foams and 38.5 wt. % for the RP foams that was measured after calcination for the molecular template burn-out and after drying, see Chapters 4.4 and 3.2.1.

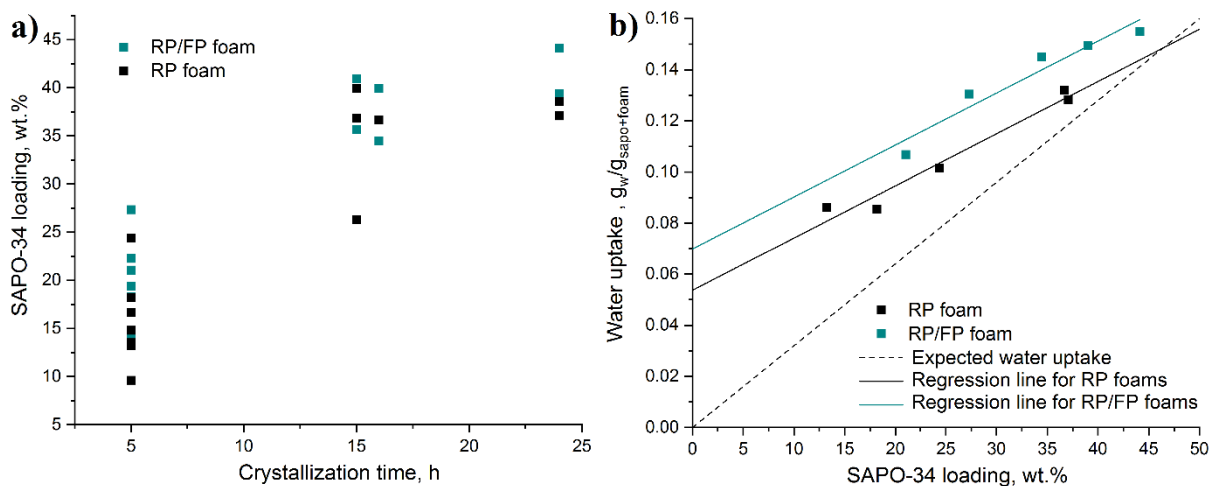


Figure 59 Dependence of the SAPO-34 loading on crystallization time (a), and water uptake of the SAPO-34 aluminum composite foams as a function of SAPO-34 loading (b) for the RP (black) and RP/FP foams (green); PU template foams with a cell size of 20 ppi.

The results of the water uptake of the SAPO-34 aluminum composite foams are shown in Figure 59 b. To evaluate the adsorption capacity of the foams an expected water uptake based on the load of SAPO-34 (dashed lines) was plotted, where 1g of SAPO-34 adsorbs 0.32 g of water at 20 °C [114]. It can be seen that the water adsorption capacity of the SAPO-34 coated aluminum foam composite increased with the SAPO-34 loading. The water uptake was higher for the RP/FP aluminum foams than for the RP samples. The maximum water uptake was  $\sim 0.15 \text{ g} \cdot \text{g}_{\text{foam}+\text{SAPO}}^{-1}$  for the RP/FP foams at a zeolite loading of  $\sim 44.1 \text{ wt. \%}$  and  $\sim 0.13 \text{ g} \cdot \text{g}_{\text{foam}+\text{SAPO}}^{-1}$  for the RP foams at a loading of  $\sim 37.1 \text{ wt. \%}$ . The calculations of the SAPO-34 loading and the water uptake are presented more detailed in Chapter 4.4. However, these measured values for the water uptake were above the expected/calculated values for the water uptake, which is explained by a partial dissolution of the aluminum foams during crystallization. It can be seen that this discrepancy decreased with increasing SAPO-34 loading. This behavior of the regression curves may indicate that a partial dissolution of the foam took place at the beginning of the crystallization time when the reagents for nucleation of the SAPO-34 crystals reacted with the surface of the foam and may have dissolved it. As the zeolite crystals nucleated on the foam surface, the dissolution effect may have been stopped during the continued crystallization process. It can also be observed from the fitted lines for the RP and RP/FP foams that the divergence of the water uptake for the RP/FP foams was higher than that for the RP foams. This effect was related to the RP/FP foams' higher specific surface area compared to the RP foams, thus, more aluminum was dissolved in these samples compared to the RP foams.

Data derived from the N<sub>2</sub>-sorption measurement of selected composite foams are listed in Table 14. The BET surface area ( $S_{\text{BET}}$ ) of the samples increased with increasing crystallization time;

the SAPO-34 loading was obtained according to Equation (14). Values of the BET surface area of pure SAPO-34 powder can be up to  $\sim 645 \text{ m}^2 \cdot \text{g}^{-1}$  [191]. Based on these data, the SAPO-34 loading in the composite foams was calculated by dividing  $S_{\text{BET}}$  of coated foams by the  $S_{\text{BET}}$  of pure SAPO-34 (Table 14). The results show that the load of SAPO-34 was lower than the calculated load, which confirmed the effect of aluminum dissolution in the initial period of the crystallization.

Table 14 Properties of selected RP and RP/FP aluminum foams after crystallization for 5 and 24 h; PU template foams with a cell size of 20 ppi.

Sample	$S_{\text{BET}}$ of coated foam, $\text{m}^2 \cdot \text{g}^{-1}$	Measured SAPO-34 loading, wt. %	Calculated SAPO-34 loading, wt. %
RP foam 5 h	126	14.8	19.5
RP/FP foam 5 h	188	19.4	29.1
RP foam 24 h	304	38.5	47.1
RP/FP foam 24 h	316	39.3	49.0

A crucial parameter when zeolites are used in heat pump applications is their stability during repeated water adsorption/desorption. In a first attempt, three adsorption/desorption cycles were carried out, see Chapter 4.4. The duration of one adsorption cycle was 24 h. Figure 60 shows the RP/FP samples after crystallization for 5 h with three adsorption/desorption cycles (a) and after crystallization for 24 h with one adsorption/desorption cycle (b). These results show that the crystallized coatings were stable, no major cracks or crystal breakage were observed. There was also no significant decrease in the water-uptake values. As an example, the results of water uptake after three adsorption/desorption cycles for the RP/FP aluminum foam with a crystallization time of 5 h and a SAPO-34 loading of  $\sim 27.3$  wt. % are shown in Table 15. Only a small variation of the water-uptake values was recognized. This shows the proof of principle for the composite materials, and further investigations have to be carried out.

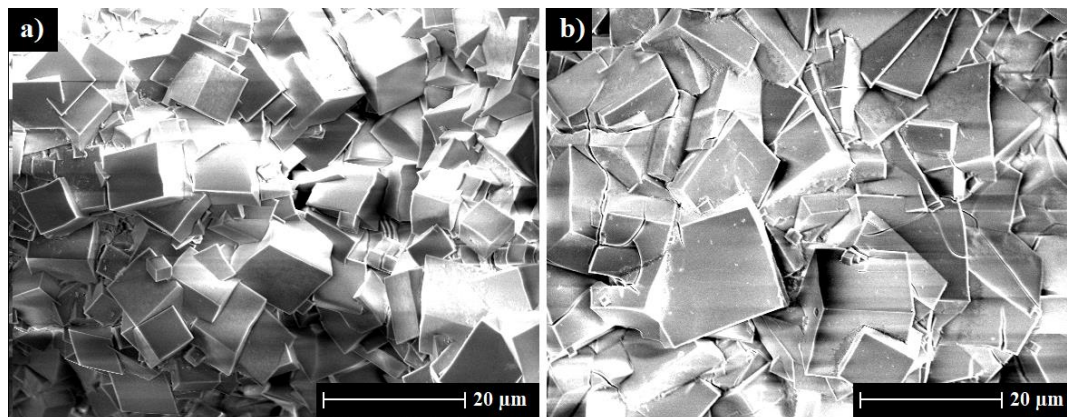


Figure 60 SEM images of aluminum foams with SAPO-34 crystallized for 5 h (a) and for 24 h (b) after water adsorption for three cycles (a) and one cycle (b); PU template foams with a cell size of 20 ppi. The cycle time for the water adsorption was 24 h.

Table 15 Water uptake of RP/FP aluminum foam after crystallization for 5 h with a SAPO-34 loading of ~27.3 wt. % after three water adsorption/desorption cycles; PU template foams with a cell size of 20 ppi.

Foam weight with SAPO-34, g	Foam weight with SAPO-34 and water, g	Water uptake, $\text{g} \cdot \text{g}_{\text{foam+SAPO}}^{-1}$	Cycle
0.9466	1.0701	0.13047	1
0.9438	1.0665	0.13001	2
0.9430	1.0657	0.13012	3

#### 5.4.2 Direct crystallization of HKUST-1 onto the surface of copper foams

In this part the crystallization results of the HKUST-1 MOF on the surface of RP and RP/FP copper foams with a total porosity of ~93 % and ~87 %, respectively, are discussed. The foams were templated with a 20 ppi PU foam.

The HKUST-1 coatings crystallized well in layers with a good adherence on the foam samples. Figure 61 shows the RP/FP copper foam samples after crystallization of HKUST-1 for 6 h, 14 h, 24 h, and 96 h with different magnifications. After a crystallization time of 6 h, openings of the lamellar pores were still observed in some parts of the foam, e. g. Figure 61 a. However, when the crystallization time was increased, the active material covered the pore openings (Figure 61 d, j). The crystal size of HKUST-1 increased from ~3  $\mu\text{m}$  for 6 h of crystallization to ~54  $\mu\text{m}$  for a crystallization time of 96 h. The shape of the HKUST-1 crystals is octahedral. The increase in crystal size on silicon carbide ceramic foams with increasing crystallization time was also observed in [134]; the authors used the same synthesis gel. The thickness of the HKUST-1 after crystallization for 24 h was ~250  $\mu\text{m}$  (Figure 61 h), and X-ray diffraction patterns of the crystallized material shown in Figure 62 were in good agreement with the calculated HKUST-1 pattern, see the calculation procedure in Chapter 4.2.1. No amorphous phases were detected.

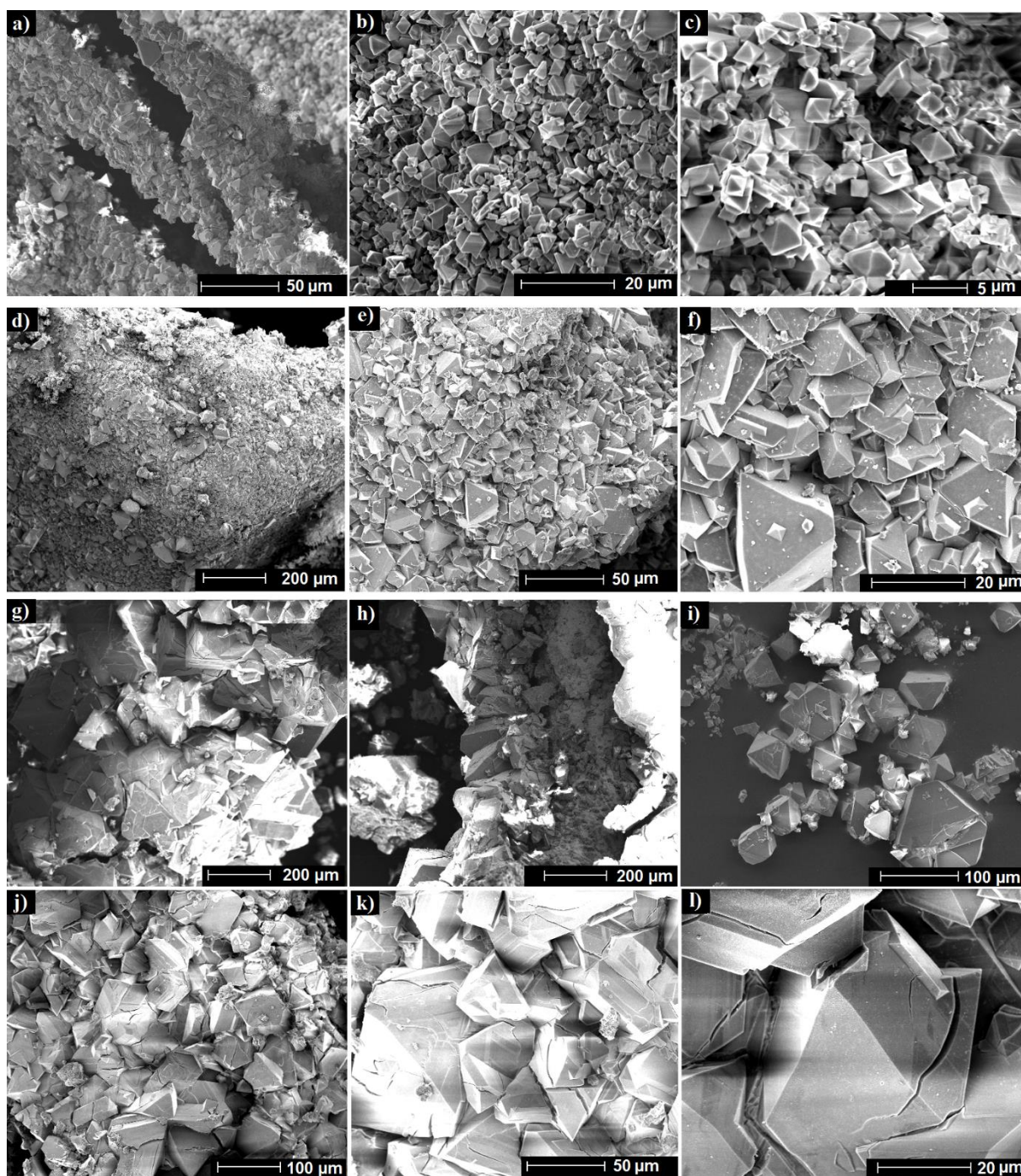


Figure 61 SEM images of the surface of RP/FP copper foams after crystallization of HKUST-1 for 6 h (a–c), 14 h (d–f), 24 h (g–h), and 96 h (j–l); HKUST-1 powder after crystallization for 24 h (i).

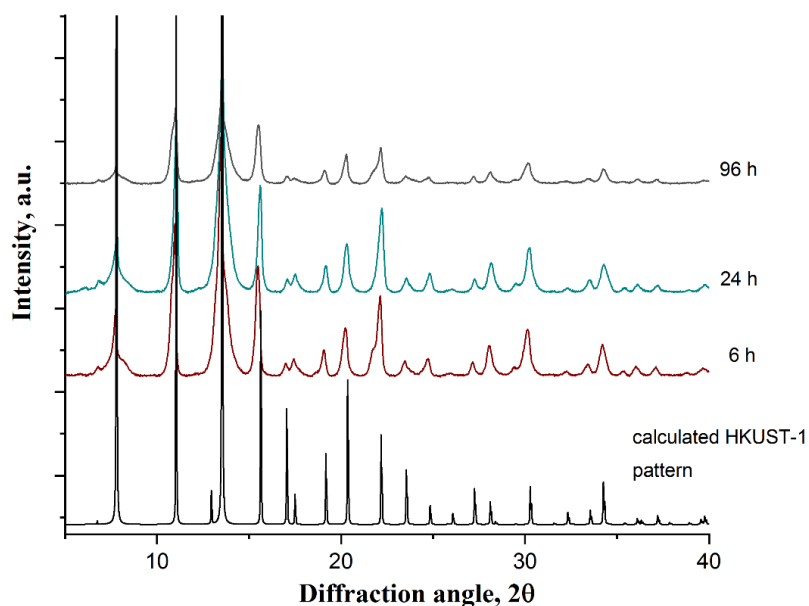


Figure 62 X-ray diffraction patterns of HKUST-1: calculated patterns (black); after crystallization for 6 h (red), 24 h (green), and 96 h (grey).

It can be seen from the cross-section of the RP/FP copper foam after crystallization for 96 h in Figure 63 a,b that HKUST-1 crystal formation occurred outside of the struts but also along the material lamellae in the lamellar pores. The crystal growth, however, was not homogeneous. The lamellar pores were only partially filled with HKUST-1. Relatively small pores did not contain any crystals at all. Mostly a dense layer was formed on the outer side of the foam struts, Figure 63 c, covering the lamellar pores from the outer surface of the struts.

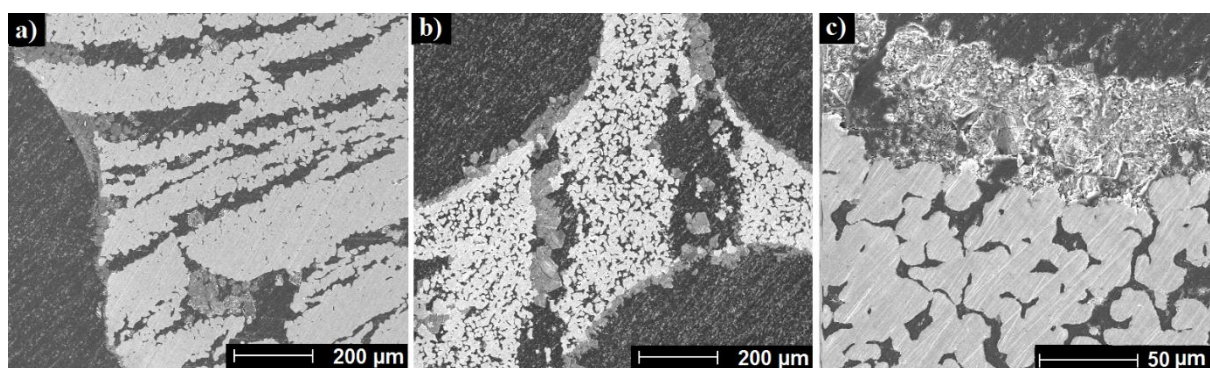


Figure 63 SEM cross-section images of RP/FP copper foam after crystallization of HKUST-1 for 96 h.

The amount of HKUST-1 loading on the RP and RP/FP copper foams increased with increasing crystallization time, Figure 64 a. There was some variation of these values due to a non-uniform coating of the samples. Some samples were characterized with areas without HKUST-1 layer, Figure 64. However, it was obvious that the material loading was higher for the RP foams; the maximum weight increase after 96 h was 21.3 wt. % for the RP/FP foams and 33.4 wt. % for

the RP foams. This may be due to the formation of areas without crystallized material or with a small amount of it on the RP/FP foams, Figure 64 c. The non-uniform crystallization of the active material on the surface of the RP/FP foams and in their lamellar pores is explained by a part of windows and lamellar pores being very small, see Table 13, Figure 52 and Figure 63, which, in turn, hindered an access of the crystallization solution [134]. The influence of pore size on the crystallization behavior of HKUST-1 was studied in [134], where  $\text{Cu}(\text{Hbtc})(\text{H}_2\text{O})_3$  needles were found in foams with a cell size of 30 ppi. Those needles, however, were not detected in foams with a cell size of 10 ppi. The authors explained this by the fact that the concentration of  $\text{Cu}^{2+}$  ions and trimesate ions might decrease faster during the crystallization of HKUST-1 in foams with smaller cells. This was justified with the mass transfer and the concentration balance equilibria in the cell space of the foam and the crystallization solution. With decreasing cell size, the number of struts increased resulting in smaller hollow struts, which acts as a diffusion barrier for the crystallization solution within the foams with smaller cells and thus smaller hollow struts.

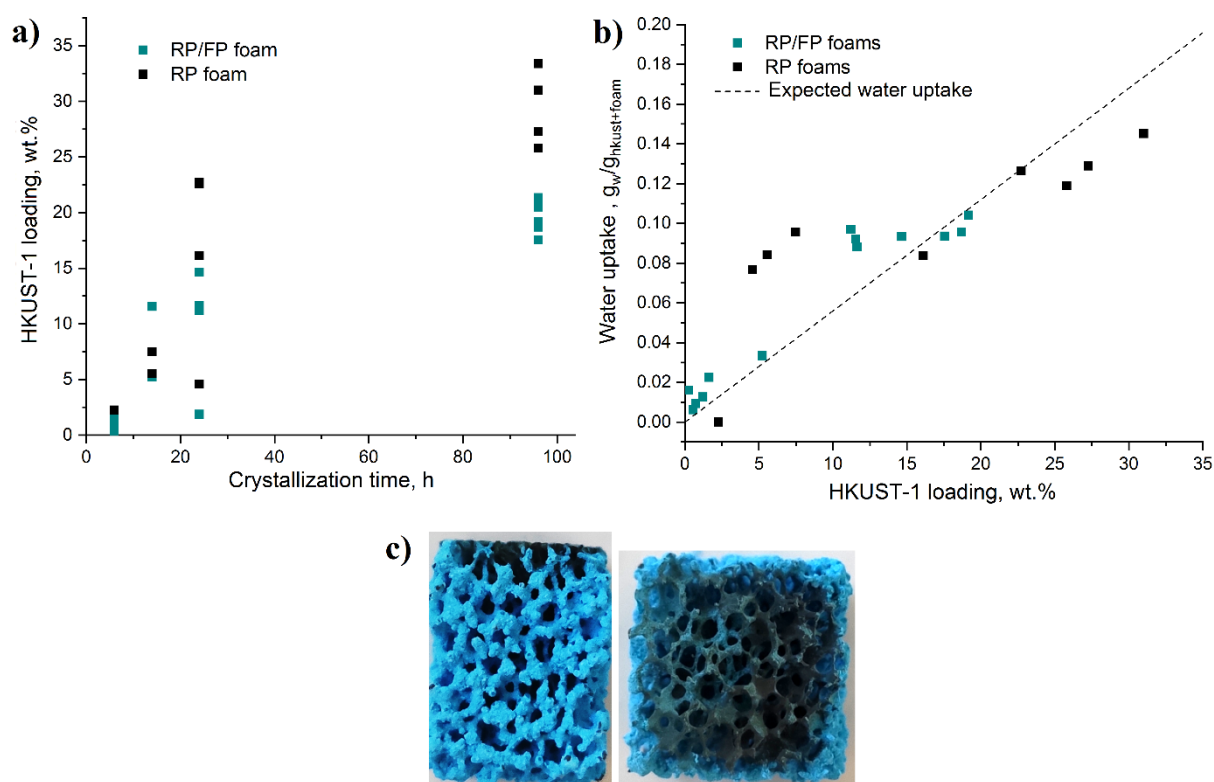


Figure 64 Dependence of HKUST-1 loading on crystallization time (a) and the water uptake of the HKUST-1 copper composite foams as a function of the HKUST-1 loading (b) for the RP (black rectangles) and RP/FP (green rectangles) foams; RP/FP copper foam with HKUST-1 after crystallization for 14 h (c); PU template foams with a cell size of 20 ppi.

Figure 64 b shows the relationship between the water uptake and the HKUST-1 loading. It was observed that as the weight of the active coating increased, the water uptake also increased with

crystallization time and HKUST-1 load, respectively. Similar to SAPO-34 zeolite, the expected water uptake function of the composites (dashed line) was plotted to compare the adsorption capacity of the resulting foams with the expected water absorption of the HKUST-1 copper foam composite, where 1 g HKUST-1 adsorbs 0.55 g of water at room temperature [125,126,134]. The water uptake of the real composites was higher than the expected/calculated water uptake, which was assigned to a partial dissolution of the copper foams during crystallization in the initial phase of the crystallization. As the MOF loading increased, the water adsorption of the composite was close to the expected adsorption line. As well as for the aluminum foams with crystallized SAPO-34, this behavior of the water uptake curve indicated that a partial dissolution of the foam at the beginning of crystallization led to an overestimation of the HKUST-1 loading. As the crystals nucleated on the copper foam surface and the HKUST-1 layer grew, the dissolution process may have stopped. With a load higher than 25 wt. %, the water uptake was below the expected/calculated water uptake line. This is believed to be a result of the formation of non-porous by-products, which may clog MOF pores when the HKUST-1 coating thickness increased. The water uptake values after 7 days were  $0.09 \text{ g} \cdot \text{g}_{\text{foam}+\text{HKUST}}^{-1}$  at a HKUST-1 load of 14.6 wt. % for the RP/FP foams and  $0.13 \text{ g} \cdot \text{g}_{\text{foam}+\text{HKUST}}^{-1}$  for the RP foams with a MOF load of  $\sim 22.7$  wt. % after 24 h of crystallization. Figure 65 shows SEM images of a HKUST-1 loaded RP copper foam after water uptake over 7 days and long-term storage. HKUST-1 crystals were destroyed.

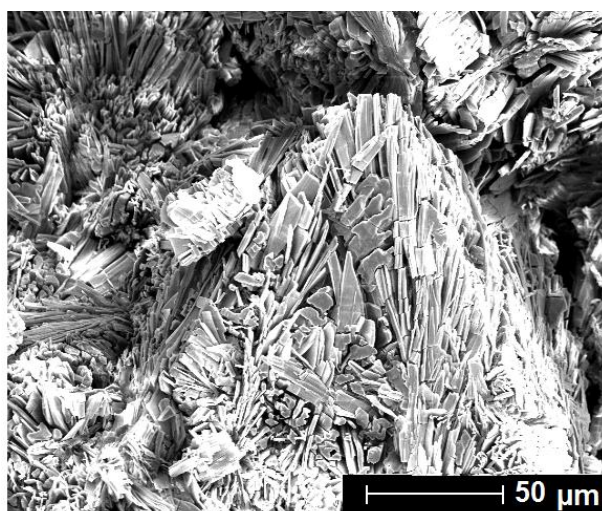


Figure 65 SEM images of the surface of the RP copper foams after crystallization of HKUST-1 for 96 h and water adsorption for 7 days and long-term storage.

### 5.4.3 Chapter summary

The direct crystallization of SAPO-34 and HKUST-1 was successful on the surface of the RP and RP/FP aluminum and copper foams; the microporous component was crystallized for

different times. Cube-shaped SAPO-34 crystals were observed on the surface of the aluminum foam struts, in the hollow struts, and along the material lamellae in RP/FP foams. In copper foams, octahedral HKUST-1 crystals significantly increased in their size with increasing crystallization time; and there was non-uniform crystal growth in lamellar pores and hollow struts of the RP/FP foams (Figure 63). The non-uniformity was tentatively assigned to possible difficulties in mass transfer and imbalance between the concentration of  $\text{Cu}^{2+}$  and trimesate ions in these small pores. This seems to hinder the crystallization as also found in [134]. This resulted in partially HKUST-1 free lamellar pores. The belonging pore openings were covered by a MOF layer.

With increasing crystallization time for MOF and zeolite coatings, an intensive increase in active-material loading was observed at the beginning of the crystallization process, which gradually changed with increasing crystallization time. For the RP/FP aluminum foams the higher specific surface area (~1.92 times, see Chapter 5.2.3) increased the loading of the SAPO-34 compared to the RP foams due to a good accessibility of small pores. For the copper foams, the RP samples had a higher HKUST-1 loading than the RP/FP foams, which was assigned to a shift of the reaction conditions by hindered diffusion of the crystallization solution into small pores.

The water uptake study showed higher values as expected for the initial phase of the crystallization process, which might result from a partial dissolution of aluminum and copper, respectively, in this phase. As the crystallization time increased and the load of the active material increased as well, the water adsorption capacity approximated the expected/calculated water uptake. Higher active material loadings of the RP/FP aluminum foams resulted in higher water adsorption capacities compared to the RP foams. The zeolite coating showed resistance to the water adsorption during repeated adsorption/desorption. For the copper foams, the water adsorption of the RP/FP and the RP foams did not differ significantly, which was assigned to a non-uniform crystallization of the active material in lamellar pores and partially MOF free strut areas in the RP/FP foams. After water adsorption and long-term storage, it was found that the HKUST-1 crystals were not stable.

## 6 Summary and outlook

Aluminum and copper foams were manufactured from metal powders by the sponge replication technique and by a combination of the sponge replication technique and two additional freeze processing steps: freezing and freeze-drying. The freeze processing steps were added to generate an additional porosity within the foam struts. The influence of the initial particle size and shape of the starting powders, the thermal treatment parameters, the cell size of the polymeric template foams, and the additional strut pores on the macrostructure, the porosity, the mechanical properties, the thermal conductivity, and the specific surface area of the as-processed foams was investigated.

Those foams are discussed as support materials for microporous active coatings such as metal-organic frameworks and/or zeolites for heat conversion applications. Advantages of such macroporous-microporous composite materials, compared to molded bodies, are a high tortuosity in fluid dynamic applications, a fast accessibility of the active components, and a high heat conductivity. In the case of foams with additional strut porosity, generated by the additional freezing steps, an additional amount of the active component can be accommodated within these pores. First direct crystallization experiments for the loading of copper and aluminum foams have shown, that microporous materials can be adhered to the outer and the inner surface of aluminum and copper foams.

In the aluminum foam manufacturing process, the shape and the size of the starting powder particles influenced the foam properties significantly. Spheroidal-shaped aluminum particles led to a higher joining degree of powder particles and a lower content of alumina in contrast with irregularly shaped starting powder particles, which resulted in a denser strut structure and a higher compressive strength. However, during the manufacturing of aluminum foams by the replication process a certain amount of alumina seems necessary to prevent the foam structure from collapsing during thermal treatment. Optimized processing conditions – heat treatment for three hours under argon atmosphere in a temperature range from 650 °C to 750 °C – led to aluminum foams with a total porosity of up to 91 %. Aluminum foams manufactured by the sponge replication process and the additional freeze processing steps – RP/FP foams – showed a significantly higher strut porosity of up to 54 %. These foams, however, showed a distinct deformation behavior when they were processed at temperatures above 650 °C.

Copper foams were also demonstrated to be processable via the sponge replication process – RP foams – and via the combination of the reticulation process with additional freezing steps. In order to obtain copper foams, a chemical reduction in argon/hydrogen atmosphere was necessary for the conversion of copper-(I, II) oxides into the metal. Optimized thermal processing conditions after template burn-out were found to be 900 °C in a hydrogen-containing atmosphere. This resulted in RP copper foams with a total porosity of up to 93 % and a thermal conductivity of up to 3.15 W m<sup>-1</sup> K<sup>-1</sup> for RP foams with varying foam cell sizes. RP/FP copper foams showed a smaller total porosity of ~ 87 %, and the thermal conductivity was found to be 4.95 W m<sup>-1</sup> K<sup>-1</sup>.

The struts of both types of RP/FP metal foams possess lamellar pores with random orientation; the average thickness in aluminum foams was found to be 24 μm to 39 μm, and it was 38 μm to 56 μm for copper foams. The average thickness of the strut's material lamellae was 72 μm to 87 μm for both types of RP/FP foams. These additional pores resulted in an increase of the specific surface area of the RP/FP foams of a factor ~1.9 for both, Al- and Cu-RP/FP foams compared to their RP foams manufactured from a 20 ppi PU template foam. In spite of the increase in the strut porosity of the RP/FP foams a higher compressive strength was measured. This effect was explained with different pore sizes, pore orientations, and arrangements of the pores on different porosity levels but has not been quantified within this work. In general, the relative compressive strength  $\sigma_{pl}^*/\sigma_b^*$  as a function of the relative density  $\rho^*/\rho_s$  was found to be in good agreement with the Gibson-Ashby model for all types of foams; a slight variation of the value of  $n$  in this model points to a change in the deformation mechanism under load as a function of the share of the different levels of porosity.

The direct crystallization processes of microporous materials on metal foam supports – SAPO-34 on aluminum foams and HKUST-1 on copper foams – demonstrated a load with a microporous component on the outer strut surface, in the inner strut surface, and in the interlamellar space of the strut pores generated by the additional freezing steps. Even if these processes are not optimized yet, they point out a higher load of the microporous components on/in the RP/FP metal foams; this was already achieved for SAPO-34 on aluminum foams with a SAPO-34 load of 38.5 % for RP and 44.1 % for the RP/FP foams.

From the findings above two major directions have been addressed for future work: a) The mechanical behaviour of the foams under compressive stress indicated a deviation from the

Gibson-Ashby model. This deviation should be studied more in detail under variation of the share of the different levels and characteristics of the porosity. A topological optimization of the RP/FP foam structures may lead to foams with a high porosity and a high compression strength, which, in turn, may result in mechanically highly stable foams with a high loading of the microporous component.

b) In order to achieve homogeneous microporous coatings on the metal foam supports, the different porosity levels should be optimized by the variation of the additional strut pore size and the foam cell size. For a better control of the crystallization processes a surface modification of the metal foams, specifically of the copper foams, may result in dense layers of the microporous component with a uniform layer thickness.

## References

1. Singh, S.; Bhatnagar, N. A survey of fabrication and application of metallic foams (1925–2017). *J. Porous Mater.* **2018**, *25*, 537–554, doi:10.1007/s10934-017-0467-1.
2. Banhart, J. Manufacture, characterisation and application of cellular metals and metal foams. *Prog. Mater. Sci.* **2001**, *46*, 559–632, doi:10.1016/S0079-6425(00)00002-5.
3. Kim, S.; Lee, C.-W. A Review on Manufacturing and Application of Open-cell Metal Foam. *Procedia Mater. Sci.* **2014**, *4*, 305–309, doi:10.1016/j.mspro.2014.07.562.
4. Bortolozzi, J.P.; Banús, E.D.; Milt, V.G.; Gutierrez, L.B.; Ulla, M.A. The significance of passivation treatments on AISI 314 foam pieces to be used as substrates for catalytic applications. *Appl. Surf. Sci.* **2010**, *257*, 495–502, doi:10.1016/j.apsusc.2010.07.019.
5. Gancarczyk, A.; Sintera, K.; Iwaniszyn, M.; Piatek, M.; Macek, W.; Jodłowski, P.J.; Wroński, S.; Sitarz, M.; Łojewska, J.; Kołodziej, A. Metal foams as novel catalyst support in environmental processes. *Catalysts* **2019**, *9*, doi:10.3390/catal9070587.
6. Betke, U.; Lieb, A. Micro-Macroporous Composite Materials – Preparation Techniques and Selected Applications : A Review. **2018**, *1800252*, 1–28, doi:10.1002/adem.201800252.
7. Manonukul, A.; Srikudvien, P.; Tange, M. Microstructure and mechanical properties of commercially pure titanium foam with varied cell size fabricated by replica impregnation method. *Mater. Sci. Eng. A* **2016**, *650*, 432–437, doi:10.1016/j.msea.2015.10.074.
8. Wang, C.; Chen, H.; Zhu, X.; Xiao, Z.; Zhang, K.; Zhang, X. An improved polymeric sponge replication method for biomedical porous titanium scaffolds. *Mater. Sci. Eng. C* **2017**, *70*, 1192–1199, doi:10.1016/j.msec.2016.03.037.
9. Bakan, H.I.; Korkmaz, K. Synthesis and properties of metal matrix composite foams based on austenitic stainless steels -titanium carbonitrides. *Mater. Des.* **2015**, *83*, 154–158, doi:10.1016/j.matdes.2015.06.016.
10. Schelm, K.; Fey, T.; Dammler, K.; Betke, U.; Scheffler, M. Hierarchical-Porous Ceramic Foams by a Combination of Replica and Freeze Technique. *Adv. Eng. Mater.* **2019**, *21*, 1–12, doi:10.1002/adem.201801362.
11. Dammler, K.; Schelm, K.; Betke, U.; Fey, T.; Scheffler, M. Open-cellular alumina foams with hierarchical strut porosity by ice templating: A thickening agent study. *Materials (Basel)*. **2021**, *14*, 1–15, doi:10.3390/ma14051060.
12. Deville, S. Freeze-casting of porous ceramics: A review of current achievements and issues. *Adv. Eng. Mater.* **2008**, *10*, 155–169, doi:10.1002/adem.200700270.
13. Sutygina, A.; Betke, U.; Scheffler, M. Hierarchical-Porous Copper Foams by a Combination of Sponge Replication and Freezing Techniques. *Adv. Eng. Mater.* **2021**, 2001516, doi:10.1002/adem.202001516.

14. Yang, H.; Li, Y.; Ma, B.; Zhu, Y. Review and a theoretical approach on pressure drop correlations of flow through open-cell metal foam. *Materials (Basel)*. **2021**, *14*, doi:10.3390/ma14123153.
15. Giani, L.; Groppi, G.; Tronconi, E. Mass-transfer characterization of metallic foams as supports for structured catalysts. *Ind. Eng. Chem. Res.* **2005**, *44*, 4993–5002, doi:10.1021/ie0490886.
16. Incera Garrido, G.; Patcas, F.C.; Lang, S.; Kraushaar-Czarnetzki, B. Mass transfer and pressure drop in ceramic foams: A description for different pore sizes and porosities. *Chem. Eng. Sci.* **2008**, *63*, 5202–5217, doi:10.1016/j.ces.2008.06.015.
17. Lévêque, J.; Rouzineau, D.; Prévost, M.; Meyer, M. Hydrodynamic and mass transfer efficiency of ceramic foam packing applied to distillation. *Chem. Eng. Sci.* **2009**, *64*, 2607–2616, doi:10.1016/j.ces.2009.02.010.
18. Aguirre, A.; Chandra, V.; Peters, E.A.J.F.; Kuipers, J.A.M.; Neira D'Angelo, M.F. Open-cell foams as catalysts support: A systematic analysis of the mass transfer limitations. *Chem. Eng. J.* **2020**, *393*, 124656, doi:10.1016/j.cej.2020.124656.
19. Ashby, M.F. The properties of foams and lattices. *Philos. Trans. R. Soc. A Math. Phys. Eng. Sci.* **2006**, *364*, 15–30, doi:10.1098/rsta.2005.1678.
20. Gibson, L. J.; Ashby, M. F. *Cellular Solids: Structure and Properties*; Cambridge university press, Cambridge, United Kingdom, 1999.
21. Kavei, G. Mechanical Properties of Aluminum Foam Fabricated by Aluminum Powders with Na or Carbamide Replica. **2015**, *1*, 22–30.
22. Andrews, E.; Sanders, W.; Gibson, L.J. Compressive and tensile behaviour of aluminum foams. *Mater. Sci. Eng. A* **1999**, *270*, 113–124, doi:10.1016/S0921-5093(99)00170-7.
23. Park, H.; Choi, M.; Choe, H.; Dunand, D.C. Microstructure and compressive behavior of ice-templated copper foams with directional, lamellar pores. *Mater. Sci. Eng. A* **2017**, *679*, 435–445, doi:10.1016/j.msea.2016.10.057.
24. Farkas, D.; Caro, A.; Bringa, E.; Crowson, D. Mechanical response of nanoporous gold. *Acta Mater.* **2013**, *61*, 3249–3256, doi:10.1016/j.actamat.2013.02.013.
25. Quadbeck, P.; Kümmel, K.; Hauser, R.; Standke, G.; Adler, J.; Stephani, G.; Kieback, B. Structural and material design of open-cell powder metallurgical foams. *Adv. Eng. Mater.* **2011**, *13*, 1024–1030, doi:10.1002/adem.201100023.
26. Banhart, J. Aluminum foams: On the road to real applications. *MRS Bull.* **2003**, *28*, 290–295, doi:10.1557/mrs2003.83.
27. Yang, X.; Hu, Q.; Du, J.; Song, H.; Zou, T.; Sha, J.; He, C.; Zhao, N. Compression fatigue properties of open-cell aluminum foams fabricated by space-holder method. *Int. J. Fatigue* **2019**, *121*, 272–280, doi:10.1016/j.ijfatigue.2018.11.008.
28. Pang, Q.; Wu, G.H.; Xiu, Z.Y.; Chen, G.Q.; Sun, D.L. Synthesis and mechanical properties of open-cell Ni-Fe-Cr foams. *Mater. Sci. Eng. A* **2012**, *534*, 699–706,

- doi:10.1016/j.msea.2011.12.034.
29. Barg, S.; Soltmann, C.; Schwab, A.; Koch, D.; Schwieger, W.; Grathwohl, G. Novel open cell aluminum foams and their use as reactive support for zeolite crystallization. *J. Porous Mater.* **2011**, *18*, 89–98, doi:10.1007/s10934-010-9359-3.
  30. Manonukul, A.; Srikudvien, P.; Tange, M.; Puncreobutr, C. Geometry anisotropy and mechanical property isotropy in titanium foam fabricated by replica impregnation method. *Mater. Sci. Eng. A* **2016**, *655*, 388–395, doi:10.1016/j.msea.2016.01.017.
  31. Li, J.P.; Li, S.H.; Van Blitterswijk, C.A.; De Groot, K. A novel porous Ti6Al4V: Characterization and cell attachment. *J. Biomed. Mater. Res. - Part A* **2005**, *73*, 223–233, doi:10.1002/jbm.a.30278.
  32. Kulshreshtha, A.; Dhakad, S.K. Preparation of metal foam by different methods: A review. *Mater. Today Proc.* **2020**, doi:10.1016/j.matpr.2020.02.375.
  33. Chang, K.; Gao, J.T.; Wang, Z.; Guo, Z.C. Manufacturing 3-D open-cell aluminum foam via infiltration casting in a super-gravity field. *J. Mater. Process. Technol.* **2018**, *252*, 705–710, doi:10.1016/j.jmatprotec.2017.10.032.
  34. Fischer, S.F.; Groten, V.F.; Brachmann, J.; Fix, C.; Vossel, T.; Bührig-Polaczek, A. Influence of die and casting temperatures and titanium and strontium contents on the technological properties of die-cast A356 in the as-cast and T6 condition. *Miner. Met. Mater. Ser.* **2016**, 1031–1036, doi:10.1007/978-3-319-65136-1\_174.
  35. Schüler, P.; Fischer, S.F.; Bührig-Polaczek, A.; Fleck, C. Deformation and failure behaviour of open cell Al foams under quasistatic and impact loading. *Mater. Sci. Eng. A* **2013**, *587*, 250–261, doi:10.1016/j.msea.2013.08.030.
  36. Sutygina, A.; Betke, U.; Hasemann, G.; Scheffler, M. Manufacturing of open-cell metal foams by the sponge replication technique. *IOP Conf. Ser. Mater. Sci. Eng.* **2020**, 882, doi:10.1088/1757-899X/882/1/012022.
  37. Wang, Z.; Gao, J.; Chang, K.; Meng, L.; Zhang, N.; Guo, Z. Manufacturing of open-cell aluminum foams: Via infiltration casting in super-gravity fields and mechanical properties. *RSC Adv.* **2018**, *8*, 15933–15939, doi:10.1039/c7ra13689g.
  38. Jinnapat, A.; Kennedy, A. Characterisation and mechanical testing of open cell al foams manufactured by molten metal infiltration of porous salt bead preforms: Effect of bead size. *Metals (Basel)*. **2012**, *2*, 122–135, doi:10.3390/met2020122.
  39. Shin, H.C.; Dong, J.; Liu, M. Nanoporous Structures Prepared by an Electrochemical Deposition Process. *Adv. Mater.* **2003**, *15*, 1610–1614, doi:10.1002/adma.200305160.
  40. Jamaludin, A.R.; Kasim, S.R.; Ismail, A.K.; Abdullah, M.Z.; Ahmad, Z.A. The effect of sago as binder in the fabrication of alumina foam through the polymeric sponge replication technique. *J. Eur. Ceram. Soc.* **2015**, *35*, 1905–1914, doi:10.1016/j.jeurceramsoc.2014.12.005.
  41. Kwon, H.; Park, D.H.; Park, Y.; Silvain, J.F.; Kawasaki, A.; Park, Y. Spark plasma sintering

- behavior of pure aluminum depending on various sintering temperatures. *Met. Mater. Int.* **2010**, *16*, 71–75, doi:10.1007/s12540-010-0071-2.
42. Xie, G.; Ohashi, O.; Sato, T.; Yamaguchi, N.; Song, M.; Mitsuishi, K.; Furuya, K. Effect of Mg on the sintering of Al-Mg alloy powders by pulse electric-current sintering process. *Mater. Trans.* **2004**, *45*, 904–909, doi:10.2320/matertrans.45.904.
43. Pieczonka, T.; Schubert, T.; Baunack, S.; Kieback, B. Dimensional behaviour of aluminium sintered in different atmospheres. *Mater. Sci. Eng. A* **2008**, *478*, 251–256, doi:10.1016/j.msea.2007.06.002.
44. Manonukul, A.; Tange, M.; Srikudvien, P.; Denmud, N.; Wattanapornphan, P. Rheological properties of commercially pure titanium slurry for metallic foam production using replica impregnation method. *Powder Technol.* **2014**, *266*, 129–134, doi:10.1016/j.powtec.2014.06.030.
45. Kaya, A.C.; Zaslansky, P.; Nikolaus, A.; Fleck, C. Tensile failure observations in sintered steel foam struts revealed by sub-micron contrast-enhanced microtomography. *Mater. Des.* **2016**, *105*, 190–200, doi:10.1016/j.matdes.2016.05.069.
46. Michailidis, N.; Stergioudi, F.; Omar, H.; Tsipas, D.N. An image-based reconstruction of the 3D geometry of an Al open-cell foam and FEM modeling of the material response. *Mech. Mater.* **2010**, *42*, 142–147, doi:10.1016/j.mechmat.2009.10.006.
47. Zaman, E.; Kele, O. Open cell aluminum foams produced by polymer impregnation method. *Acta Phys. Pol. A* **2014**, *125*, 445–448, doi:10.12693/APhysPolA.125.445.
48. Wang, C.; Chen, H.; Zhu, X.; Xiao, Z.; Zhang, K.; Zhang, X. An improved polymeric sponge replication method for biomedical porous titanium scaffolds. *Mater. Sci. Eng. C* **2017**, *70*, 1192–1199, doi:10.1016/j.msec.2016.03.037.
49. Tange, M.; Manonukul, A.; Srikudvien, P. The effects of organic template and thickening agent on structure and mechanical properties of titanium foam fabricated by replica impregnation method. *Mater. Sci. Eng. A* **2015**, *641*, 54–61, doi:10.1016/j.msea.2015.06.039.
50. Scotti, K.L.; Dunand, D.C. Freeze casting – A review of processing, microstructure and properties via the open data repository, FreezeCasting.net. *Prog. Mater. Sci.* **2018**, *94*, 243–305, doi:10.1016/j.pmatsci.2018.01.001.
51. Du, Y.; Hedayat, N.; Panthi, D.; Ilkhani, H.; Emley, B.J.; Woodson, T. Freeze-casting for the fabrication of solid oxide fuel cells: A review. *Materialia* **2018**, *1*, 198–210, doi:10.1016/j.mtla.2018.07.005.
52. Zamanian, A.; Farhangdoust, S.; Yasaei, M.; Khorami, M.; Hafezi, M. The effect of particle size on the mechanical and microstructural properties of freeze-casted macroporous hydroxyapatite scaffolds. *Int. J. Appl. Ceram. Technol.* **2014**, *11*, 12–21, doi:10.1111/ijac.12031.
53. Deville, S.; Saiz, E.; Tomsia, A.P. Ice-templated porous alumina structures. *Acta Mater.* **2007**,

- 55, 1965–1974, doi:10.1016/j.actamat.2006.11.003.
54. Preiss, A.; Su, B.; Collins, S.; Simpson, D. Tailored graded pore structure in zirconia toughened alumina ceramics using double-side cooling freeze casting. *J. Eur. Ceram. Soc.* **2012**, *32*, 1575–1583, doi:10.1016/j.jeurceramsoc.2011.12.031.
55. Hu, L.; Wang, C.A.; Huang, Y.; Sun, C.; Lu, S.; Hu, Z. Control of pore channel size during freeze casting of porous YSZ ceramics with unidirectionally aligned channels using different freezing temperatures. *J. Eur. Ceram. Soc.* **2010**, *30*, 3389–3396, doi:10.1016/j.jeurceramsoc.2010.07.032.
56. Hu, L.; Wang, C.A.; Huang, Y.; Sun, C.; Lu, S.; Hu, Z. Control of pore channel size during freeze casting of porous YSZ ceramics with unidirectionally aligned channels using different freezing temperatures. *J. Eur. Ceram. Soc.* **2010**, *30*, 3389–3396, doi:10.1016/j.jeurceramsoc.2010.07.032.
57. Liu, R.; Yuan, J.; Wang, C. an A novel way to fabricate tubular porous mullite membrane supports by TBA-based freezing casting method. *J. Eur. Ceram. Soc.* **2013**, *33*, 3249–3256, doi:10.1016/j.jeurceramsoc.2013.06.005.
58. Liu, R.; Xu, T.; Wang, C. an A review of fabrication strategies and applications of porous ceramics prepared by freeze-casting method. *Ceram. Int.* **2016**, *42*, 2907–2925, doi:10.1016/j.ceramint.2015.10.148.
59. Shao, G.; Hanaor, D.A.H.; Shen, X.; Gurlo, A. Freeze Casting: From Low-Dimensional Building Blocks to Aligned Porous Structures—A Review of Novel Materials, Methods, and Applications. *Adv. Mater.* **2020**, *32*, doi:10.1002/adma.201907176.
60. Deville, S.; Maire, E.; Lasalle, A.; Bogner, A.; Gauthier, C.; Leloup, J.; Guizard, C. Influence of particle size on ice nucleation and growth during the ice-templating process. *J. Am. Ceram. Soc.* **2010**, *93*, 2507–2510, doi:10.1111/j.1551-2916.2010.03840.x.
61. Sofie, S.W.; Dogan, F. Freeze Casting of Aqueous Alumina Slurries with Glycerol. *J. Am. Ceram. Soc.* **2001**, *84*, 1459–1464, doi:10.1111/j.1151-2916.2001.tb00860.x.
62. Zhang, Y.; Hu, L.; Han, J.; Jiang, Z. Freeze casting of aqueous alumina slurries with glycerol for porous ceramics. *Ceram. Int.* **2010**, *36*, 617–621, doi:10.1016/j.ceramint.2009.09.036.
63. Pekor, C.M.; Kisa, P.; Nettleship, I. Effect of polyethylene glycol on the microstructure of freeze-cast alumina. *J. Am. Ceram. Soc.* **2008**, *91*, 3185–3190, doi:10.1111/j.1551-2916.2008.02616.x.
64. Pekor, C.; Nettleship, I. The effect of the molecular weight of polyethylene glycol on the microstructure of freeze-cast alumina. *Ceram. Int.* **2014**, *40*, 9171–9177, doi:10.1016/j.ceramint.2014.01.134.
65. Zuo, K.H.; Zeng, Y.P.; Jiang, D. Properties of microstructure-controllable porous yttria-stabilized zirconia ceramics fabricated by freeze casting. *Int. J. Appl. Ceram. Technol.* **2008**, *5*, 198–203, doi:10.1111/j.1744-7402.2008.02190.x.

66. Zuo, K.H.; Zeng, Y.P.; Jiang, D. Effect of polyvinyl alcohol additive on the pore structure and morphology of the freeze-cast hydroxyapatite ceramics. *Mater. Sci. Eng. C* **2010**, *30*, 283–287, doi:10.1016/j.msec.2009.11.003.
67. Fukushima, M.; Yoshizawa, Y.I.; Ohji, T. Macroporous ceramics by gelation-freezing route using gelatin. *Adv. Eng. Mater.* **2014**, *16*, 607–620, doi:10.1002/adem.201400067.
68. Zhang, Y.; Zuo, K.; Zeng, Y.P. Effects of gelatin addition on the microstructure of freeze-cast porous hydroxyapatite ceramics. *Ceram. Int.* **2009**, *35*, 2151–2154, doi:10.1016/j.ceramint.2008.11.022.
69. Ye, F.; Zhang, J.; Zhang, H.; Liu, L. Pore structure and mechanical properties in freeze cast porous Si 3N4 composites using polyacrylamide as an addition agent. *J. Alloys Compd.* **2010**, *506*, 423–427, doi:10.1016/j.jallcom.2010.07.020.
70. Deville, S. Freeze-casting of porous biomaterials: Structure, properties and opportunities. *Materials (Basel)*. **2010**, *3*, 1913–1927, doi:10.3390/ma3031913.
71. Araki, K.; Halloran, J.W. Porous ceramic bodies with interconnected pore channels by a novel freeze casting technique. *J. Am. Ceram. Soc.* **2005**, *88*, 1108–1114, doi:10.1111/j.1551-2916.2005.00176.x.
72. Dong, S.; Wang, L.; Gao, X.; Zhu, W.; Wang, Z.; Ma, Z.; Gao, C. Freeze casting of novel porous silicate cement supports using tert-butyl alcohol-water binary crystals as template: Microstructure, strength and permeability. *J. Memb. Sci.* **2017**, *541*, 143–152, doi:10.1016/j.memsci.2017.06.067.
73. Souza, D.F.; Nunes, E.H.M.; Queiroga, J.A.; Vasconcelos, W.L. Microstructural characterization and gas permeation performance of freeze-cast alumina supports. *J. Eur. Ceram. Soc.* **2018**, *38*, 4020–4025, doi:10.1016/j.jeurceramsoc.2018.04.040.
74. Liu, X.; Wu, J.; Luo, B.; Zhang, L.; Lai, Y. Porous Cu foams with oriented pore structure by freeze casting. *Mater. Lett.* **2017**, *205*, 249–252, doi:10.1016/j.matlet.2017.06.011.
75. Ran, H.; Feng, P.; Liu, Z.; Wang, X.; Niu, J.; Zhang, H. Complex-shaped porous Cu bodies fabricated by freeze-casting and vacuum sintering. *Metals (Basel)*. **2015**, *5*, 1821–1828, doi:10.3390/met5041821.
76. Zhao, Z.; Sun, M.; Chen, W.; Liu, Y.; Zhang, L.; Dongfang, N.; Ruan, Y.; Zhang, J.; Wang, P.; Dong, L.; et al. Sandwich, Vertical-Channeled Thick Electrodes with High Rate and Cycle Performance. *Adv. Funct. Mater.* **2019**, *29*, 1–13, doi:10.1002/adfm.201809196.
77. Zhang, X.; Ju, Z.; Housel, L.M.; Wang, L.; Zhu, Y.; Singh, G.; Sadique, N.; Takeuchi, K.J.; Takeuchi, E.S.; Marschilok, A.C.; et al. Promoting Transport Kinetics in Li-Ion Battery with Aligned Porous Electrode Architectures. *Nano Lett.* **2019**, *19*, 8255–8261, doi:10.1021/acs.nanolett.9b03824.
78. Xue, P.; Liu, S.; Shi, X.; Sun, C.; Lai, C.; Zhou, Y.; Sui, D.; Chen, Y.; Liang, J. A Hierarchical Silver-Nanowire-Graphene Host Enabling Ultrahigh Rates and Superior Long-Term Cycling

- of Lithium-Metal Composite Anodes. *Adv. Mater.* **2018**, *30*, 1–10, doi:10.1002/adma.201804165.
79. Cuba Ramos, A.I.; Dunand, D.C. Preparation and characterization of directionally freeze-cast copper foams. *Metals (Basel)*. **2012**, *2*, 265–273, doi:10.3390/met2030265.
80. Xue, L.; Fu, Z.; Yao, Y.; Huang, T.; Yu, A. Three-dimensional porous Sn-Cu alloy anode for lithium-ion batteries. *Electrochim. Acta* **2010**, *55*, 7310–7314, doi:10.1016/j.electacta.2010.07.015.
81. Nam, K.; Lee, S.; Hong, K.; Kang, J.S.; Jo, H.; Park, H.; Sung, Y.E.; Jenei, P.; Gubicza, J.; Kwon, K.; et al. Freeze Casting is a Facile Method to Create Solid Solution Alloy Foams: Cu–Ni Alloy Foams via Freeze Casting. *Adv. Eng. Mater.* **2019**, *21*, 1–9, doi:10.1002/adem.201801265.
82. Katuri, K.; Ferrer, M.L.; Gutiérrez, M.C.; Jiménez, R.; Del Monte, F.; Leech, D. Three-dimensional microchanneled electrodes in flow-through configuration for bioanode formation and current generation. *Energy Environ. Sci.* **2011**, *4*, 4201–4210, doi:10.1039/c1ee01477c.
83. He, Z.; Liu, J.; Qiao, Y.; Li, C.M.; Thatt, T.; Tan, Y. Nano Lett. **2012**, 10–13.
84. Zhang, P.; Li, J.; Lv, L.; Zhao, Y.; Qu, L. Vertically Aligned Graphene Sheets Membrane for Highly Efficient Solar Thermal Generation of Clean Water. *ACS Nano* **2017**, *11*, 5087–5093, doi:10.1021/acsnano.7b01965.
85. Xu, W.; Xing, Y.; Liu, J.; Wu, H.; Cui, Y.; Li, D.; Guo, D.; Li, C.; Liu, A.; Bai, H. Efficient Water Transport and Solar Steam Generation via Radially, Hierarchically Structured Aerogels. *ACS Nano* **2019**, *13*, 7930–7938, doi:10.1021/acsnano.9b02331.
86. Zhang, S.; Sun, J.; Hu, D.; Xiao, C.; Zhuo, Q.; Wang, J.; Qin, C.; Dai, L. Large-sized graphene oxide/modified tourmaline nanoparticle aerogel with stable honeycomb-like structure for high-efficiency PM2.5 capture. *J. Mater. Chem. A* **2018**, *6*, 16139–16148, doi:10.1039/c8ta05506h.
87. Yu, R.; Shi, Y.; Yang, D.; Liu, Y.; Qu, J.; Yu, Z.Z. Graphene Oxide/Chitosan Aerogel Microspheres with Honeycomb-Cobweb and Radially Oriented Microchannel Structures for Broad-Spectrum and Rapid Adsorption of Water Contaminants. *ACS Appl. Mater. Interfaces* **2017**, *9*, 21809–21819, doi:10.1021/acscami.7b04655.
88. Liao, S.; Zhai, T.; Xia, H. Highly adsorptive graphene aerogel microspheres with center-diverging microchannel structures. *J. Mater. Chem. A* **2016**, *4*, 1068–1077, doi:10.1039/c5ta09540a.
89. Chen, Q.; Tan, X.; Liu, Y.; Liu, S.; Li, M.; Gu, Y.; Zhang, P.; Ye, S.; Yang, Z.; Yang, Y. Biomass-derived porous graphitic carbon materials for energy and environmental applications. *J. Mater. Chem. A* **2020**, *8*, 5773–5811, doi:10.1039/c9ta11618d.
90. Mi, X.; Huang, G.; Xie, W.; Wang, W.; Liu, Y.; Gao, J. Preparation of graphene oxide aerogel and its adsorption for Cu<sup>2+</sup> ions. *Carbon N. Y.* **2012**, *50*, 4856–4864, doi:10.1016/j.carbon.2012.06.013.

91. Chino, Y.; Dunand, D.C. Directionally freeze-cast titanium foam with aligned, elongated pores. *Acta Mater.* **2008**, *56*, 105–113, doi:10.1016/j.actamat.2007.09.002.
92. Trueba, P.; Beltrán, A.M.; Bayo, J.M.; Rodríguez-ortiz, J.A.; Larios, D.F.; Alonso, E.; Dunand, D.C.; Torres, Y. Porous titanium cylinders obtained by the freeze- casting technique: Influence of process parameters on porosity and mechanical behavior. *Metals (Basel)*. **2020**, *10*, doi:10.3390/met10020188.
93. Wang, Q.B.; Hou, Z.P.; Zhang, S.Z.; Feng, H.; Zhang, C.J.; Han, J.C.; Zhang, W.G.; Zhao, R.T. Pore structure and compression behavior of porous TiAl alloys by freeze casting. *Vacuum* **2020**, *175*, 109254, doi:10.1016/j.vacuum.2020.109254.
94. Lloreda-Jurado, P.J.; Wilke, S.K.; Scotti, K.; Paul-Escolano, A.; Dunand, D.C.; Sepúlveda, R. Structure-processing relationships of freeze-cast iron foams fabricated with various solidification rates and post-casting heat treatment. *J. Mater. Res.* **2020**, *35*, 2587–2596, doi:10.1557/jmr.2020.175.
95. Um, T.; Wilke, S.K.; Choe, H.; Dunand, D.C. Effects of pore morphology on the cyclical oxidation/reduction of iron foams created via camphene-based freeze casting. *J. Alloys Compd.* **2020**, *845*, 156278, doi:10.1016/j.jallcom.2020.156278.
96. Plunk, A.A.; Dunand, D.C. Iron foams created by directional freeze casting of iron oxide, reduction and sintering. *Mater. Lett.* **2017**, *191*, 112–115, doi:10.1016/j.matlet.2016.12.104.
97. Lee, S.; Tam, J.; Li, W.; Yu, B.; Cho, H.J.; Samei, J.; Wilkinson, D.S.; Choe, H.; Erb, U. Multi-scale morphological characterization of Ni foams with directional pores. *Mater. Charact.* **2019**, *158*, 109939, doi:10.1016/j.matchar.2019.109939.
98. Jo, H.; Kim, M.J.; Choi, H.; Sung, Y.-E.; Choe, H.; Dunand, D.C. Morphological Study of Directionally Freeze-Cast Nickel Foams. *Metall. Mater. Trans. E* **2016**, *3*, 46–54, doi:10.1007/s40553-016-0068-y.
99. Ting, F.P.; Hsieh, C.W.; Weng, W.H.; Lin, J.C. Effect of operational parameters on the performance of PEMFC assembled with Au-coated Ni-foam. *Int. J. Hydrogen Energy* **2012**, *37*, 13696–13703, doi:10.1016/j.ijhydene.2012.02.142.
100. Lin, T.; Gan, T.; Quan, X.; Cheng, P. Fabricating metal wicks by LMC-like continuous directional freeze casting. *J. Mater. Process. Technol.* **2020**, *282*, 116641, doi:10.1016/j.jmatprotec.2020.116641.
101. García-Moreno, F. Commercial applications of metal foams: Their properties and production. *Materials (Basel)*. **2016**, *9*, 20–24, doi:10.3390/ma9020085.
102. Sanz, O.; Javier Echave, F.; Sánchez, M.; Monzón, A.; Montes, M. Aluminium foams as structured supports for volatile organic compounds (VOCs) oxidation. *Appl. Catal. A Gen.* **2008**, *340*, 125–132, doi:10.1016/j.apcata.2008.02.007.
103. Freni, A.; Frazzica, A.; Dawoud, B.; Chmielewski, S.; Calabrese, L.; Bonaccorsi, L. Adsorbent coatings for heat pumping applications: Verification of hydrothermal and mechanical

- stabilities. *Appl. Therm. Eng.* **2013**, *50*, 1658–1663, doi:10.1016/j.applthermaleng.2011.07.010.
104. Calabrese, L.; Bonaccorsi, L.; Freni, A.; Proverbio, E. Synthesis of SAPO-34 zeolite filled macrocellular foams for adsorption heat pump applications: A preliminary study. *Appl. Therm. Eng.* **2017**, *124*, 1312–1318, doi:10.1016/j.applthermaleng.2017.06.121.
105. Young Yang, T.; Young Kim, W.; Young Yoon, S.; Chae Park, H. Macroporous silicate ceramics prepared by freeze casting combined with polymer sponge method. *J. Phys. Chem. Solids* **2010**, *71*, 436–439, doi:10.1016/j.jpcs.2009.10.017.
106. Lee, J.H.; Choi, H.J.; Yoon, S.Y.; Kim, B.K.; Park, H.C. Processing of porous hydroxyapatite scaffolds containing calcium phosphate glass-ceramics for bone tissue engineering. *J. Ceram. Process. Res.* **2013**, *14*, 544–548, doi:10.36410/jcpr.2013.14.4.544.
107. Wang, T.Q.; Yang, Z.G. Scattering of plane wave from moving body underwater with finite impedance surface. *J. Sound Vib.* **2004**, *273*, 969–987, doi:10.1016/S0022-460X(03)00515-7.
108. Li, Y.; Yu, J. New stories of zeolite structures: Their descriptions, determinations, predictions, and evaluations. *Chem. Rev.* **2014**, *114*, 7268–7316, doi:10.1021/cr500010r.
109. S.S.Y. Chui; S.M.F. Lo; J.P.H. Charmant; A.G. Orpen; I.D. Williams A Chemically Functionalizable Nanoporous Material [Cu<sub>3</sub>(TMA)<sub>2</sub>(H<sub>2</sub>O)<sub>3</sub>]<sub>n</sub>. *Science (80-. )*. **1999**, *283*, 1148.
110. Férey, C.; Mellot-Draznieks, C.; Serre, C.; Millange, F.; Dutour, J.; Surblé, S.; Margiolaki, I. Chemistry: A chromium terephthalate-based solid with unusually large pore volumes and surface area. *Science (80-. )*. **2005**, *309*, 2040–2042, doi:10.1126/science.1116275.
111. Richardson, J.T.; Peng, Y.; Remue, D. Properties of ceramic foam catalyst supports: Pressure drop. *Appl. Catal. A Gen.* **2000**, *204*, 19–32, doi:10.1016/S0926-860X(00)00508-1.
112. Patcas, F.C.; Garrido, G.I.; Kraushaar-Czarnetzki, B. CO oxidation over structured carriers: A comparison of ceramic foams, honeycombs and beads. *Chem. Eng. Sci.* **2007**, *62*, 3984–3990, doi:10.1016/j.ces.2007.04.039.
113. Sun, Q.; Xie, Z.; Yu, J. The state-of-the-art synthetic strategies for SAPO-34 zeolite catalysts in methanol-to-olefin conversion. *Natl. Sci. Rev.* **2018**, *5*, 542–558, doi:10.1093/nsr/nwx103.
114. Calabrese, L.; Bonaccorsi, L.; Bruzzaniti, P.; Frazzica, A.; Freni, A.; Proverbio, E. Adsorption performance and thermodynamic analysis of SAPO-34 silicone composite foams for adsorption heat pump applications. *Mater. Renew. Sustain. Energy* **2018**, *7*, 1–13, doi:10.1007/s40243-018-0131-y.
115. Calabrese, L.; Bruzzaniti, P.; Palamara, D.; Freni, A.; Proverbio, E. New SAPO-34-SPEEK composite coatings for adsorption heat pumps: Adsorption performance and thermodynamic analysis. *Energy* **2020**, *203*, 117814, doi:10.1016/j.energy.2020.117814.
116. Bauer, C.; Scheffler, F.; Schwidder, M. Direct crystallization of silicoaluminophosphates onto the surface of open-celled SiC foam. *Adv. Eng. Mater.* **2015**, *17*, 656–662, doi:10.1002/adem.201400278.

117. Bonaccorsi, L.; Bruzzaniti, P.; Calabrese, L.; Freni, A.; Proverbio, E.; Restuccia, G. Synthesis of SAPO-34 on graphite foams for adsorber heat exchangers. *Appl. Therm. Eng.* **2013**, *61*, 848–852, doi:10.1016/j.applthermaleng.2013.04.053.
118. Bonaccorsi, L.; Calabrese, L.; Freni, A.; Proverbio, E. Hydrothermal and microwave synthesis of SAPO (CHA) zeolites on aluminium foams for heat pumping applications. *Microporous Mesoporous Mater.* **2013**, *167*, 30–37, doi:10.1016/j.micromeso.2012.06.006.
119. Askari, S.; Bashardoust Siahmard, A.; Halladj, R.; Miar Alipour, S. Different techniques and their effective parameters in nano SAPO-34 synthesis: A review. *Powder Technol.* **2016**, *301*, 268–287, doi:10.1016/j.powtec.2016.06.018.
120. Byrappa, K.; Yoshimura, M. Hydrothermal Synthesis and Growth of Zeolites. *Handb. Hydrothermal Technol.* **2013**, 269–347, doi:10.1016/b978-0-12-375090-7.00006-2.
121. Tan, J.; Liu, Z.; Bao, X.; Liu, X.; Han, X.; He, C.; Zhai, R. Crystallization and Si incorporation mechanisms of SAPO-34. *Microporous Mesoporous Mater.* **2002**, *53*, 97–108, doi:10.1016/S1387-1811(02)00329-3.
122. Editorial, G. Membrane reactors – Part I. *Technology* **2009**, 743–753, doi:10.1002/apj.
123. Askari, S.; Halladj, R.; Sohrabi, M. An overview of the effects of crystallization time, template and silicon sources on hydrothermal synthesis of sa-po-34 molecular sieve with small crystals. *Rev. Adv. Mater. Sci.* **2012**, *32*, 83–93.
124. Van Heyden, H.; Mintova, S.; Bein, T. Nanosized SAPO-34 synthesized from colloidal solutions. *Chem. Mater.* **2008**, *20*, 2956–2963, doi:10.1021/cm703541w.
125. Düren, T.; Millange, F.; Férey, G.; Walton, K.S.; Snurr, R.Q. Calculating geometric surface areas as a characterization tool for metal - Organic frameworks. *J. Phys. Chem. C* **2007**, *111*, 15350–15356, doi:10.1021/jp074723h.
126. Küsgens, P.; Rose, M.; Senkovska, I.; Fröde, H.; Henschel, A.; Siegle, S.; Kaskel, S. Characterization of metal-organic frameworks by water adsorption. *Microporous Mesoporous Mater.* **2009**, *120*, 325–330, doi:10.1016/j.micromeso.2008.11.020.
127. Krawiec, P.; Kramer, M.; Sabo, M.; Kunschke, R.; Fröde, H.; Kaskel, S. Improved hydrogen storage in the Metal-Organic Framework Cu<sub>3</sub>(BTC)<sub>2</sub>. *Adv. Eng. Mater.* **2006**, *8*, 293–296, doi:10.1002/adem.200500223.
128. Lin, K.S.; Adhikari, A.K.; Ku, C.N.; Chiang, C.L.; Kuo, H. Synthesis and characterization of porous HKUST-1 metal organic frameworks for hydrogen storage. *Int. J. Hydrogen Energy* **2012**, *37*, 13865–13871, doi:10.1016/j.ijhydene.2012.04.105.
129. Denning, S.; Majid, A.A.A.; Lucero, J.M.; Crawford, J.M.; Carreon, M.A.; Koh, C.A. Metal-Organic Framework HKUST-1 Promotes Methane Hydrate Formation for Improved Gas Storage Capacity. *ACS Appl. Mater. Interfaces* **2020**, *12*, 53510–53518, doi:10.1021/acsami.0c15675.
130. Yildirim, T. Methane Storage in Metal – Organic Frameworks: Current Records, Surprise

- Findings, and Challenges. **2013**.
131. Perea-Cachero, A.; Dechnik, J.; Lahoz, R.; Janiak, C.; Téllez, C.; Coronas, J. HKUST-1 coatings on laser-microperforated brass supports for water adsorption. *CrystEngComm* **2017**, *19*, 1470–1478, doi:10.1039/c6ce02490d.
132. Wang, H.; Qu, Z.G.; Zhang, W.; Zhang, L.Q. A multi-scale porous composite adsorbent with copper benzene-1,3,5-tricarboxylate coating on copper foam. *RSC Adv.* **2016**, *6*, 52888–52897, doi:10.1039/c6ra08622e.
133. Betke, U.; Proemmel, S.; Rannabauer, S.; Lieb, A.; Scheffler, M.; Scheffler, F. Silane functionalized open-celled ceramic foams as support structure in metal organic framework composite materials. *Microporous Mesoporous Mater.* **2017**, *239*, 209–220, doi:10.1016/j.micromeso.2016.10.011.
134. Betke, U.; Proemmel, S.; Eggebrecht, J.G.; Rannabauer, S.; Lieb, A.; Scheffler, M.; Scheffler, F. Micro-Macroporous Composite Materials : SiC Ceramic Foams Functionalized With the Metal Organic Framework HKUST-1. **2016**, 264–273, doi:10.1002/cite.201500141.
135. Schelm, K.; Dammler, K.; Betke, U.; Scheffler, M. Tailoring of the Wetting Behavior of Alumina Dispersions on Polymer Foams by Methylcellulose Addition: A Route Toward Mechanically Stable Ceramic Replica Foams. *Adv. Eng. Mater.* **2019**, *21*, 1–12, doi:10.1002/adem.201900635.
136. Prakash A.M. Synthesis of SAPO-34: High Silicon Incorporation in the Presence of Morpholine as Template. *J. Chem. Inf. Model.* **2013**, *53*, 1689–1699.
137. Log, T.; Gustafsson, S.E. Transient plane source (TPS) technique for measuring thermal transport properties of building materials. *Fire Mater.* **1995**, *19*, 43–49, doi:10.1002/fam.810190107.
138. He, Y. Rapid thermal conductivity measurement with a hot disk sensor: Part 1. Theoretical considerations. *Thermochim. Acta* **2005**, *436*, 122–129, doi:10.1016/j.tca.2005.06.026.
139. Eucken, A. *Die Wärmeleitfähigkeit feuerfester Stoffe. Ihre Berechnung aus der Wärmeleitfähigkeit der Bestandteile*; VDI-Verlag: Berlin, Germany, 1932.
140. <https://www.malvernpanalytical.com/en/products/technology/xray-analysis>.
141. Coelho, A., A. *Topas Academic V5*; Brisbane, Australia, 2012;
142. <http://www.crystallography.net/cod/>.
143. <http://www.iza-structure.org/databases/>.
144. Betke, U.; Dalicho, S.; Rannabauer, S.; Lieb, A.; Scheffler, F.; Scheffler, M. Impact of Slurry Composition on Properties of Cellular Alumina: A Computed Tomographic Study. *Adv. Eng. Mater.* **2017**, *19*, doi:10.1002/adem.201700138.
145. Henon, J.; Alzina, A.; Absi, J.; Smith, D.S.; Rossignol, S. Potassium geopolymer foams made with silica fume pore forming agent for thermal insulation. *J. Porous Mater.* **2013**, *20*, 37–46, doi:10.1007/s10934-012-9572-3.

146. Rieder, H.; Spies, M.; Bamberg, J.; Henkel, B. On- and Offline Ultrasonic Inspection of Additively Manufactured Components. *19th World Conf. Non-Destructive Test.* **2016**, 1–8.
147. Rieder, H.; Dillhöfer, A.; Spies, M.; Bamberg, J.; Hess, T. Online Monitoring of Additive Manufacturing Processes Using Ultrasound 2 . Additive Manufacturing and Quality Assurance Considerations 3 . Ultrasonic Process Monitoring. *Proc. 11th Eur. Conf. Non-Destructive Test.* **2014**, *1*, 2194–2201.
148. Caputo, D.; Aprea, P.; Gargiulo, N.; Liguori, B. The role of materials and products characterization in the additive manufacturing industry. In Proceedings of the 2017 IEEE 3rd International Forum on Research and Technologies for Society and Industry (RTSI); IEEE, 2017; pp. 1–5.
149. Wits, W.W.; Carmignato, S.; Zanini, F.; Vaneker, T.H.J. Porosity testing methods for the quality assessment of selective laser melted parts. *CIRP Ann.* **2016**, *65*, 201–204, doi:10.1016/j.cirp.2016.04.054.
150. Koester, L.W.; Taheri, H.; Bigelow, T.A.; Collins, P.C.; Bond, L.J. Nondestructive testing for metal parts fabricated using powder-based additive manufacturing. *Mater. Eval.* **2018**, *76*, 514–524.
151. Aleshin, N.P.; Grigor'ev, M. V.; Shchipakov, N.A.; Prilutskii, M.A.; Murashov, V. V. Applying nondestructive testing to quality control of additive manufactured parts. *Russ. J. Nondestruct. Test.* **2016**, *52*, 600–609, doi:10.1134/S1061830916100028.
152. Hochleistungskeramik; Monolithische Keramik; Allgemeine und strukturelle Eigenschaften; Teil 2: Bestimmung von Dichte und Porosität; DIN EN 623–2:1993–11; Beuth Verlag: Berlin, Germany, 1993. (In German).
153. Betke, U.; Lieb, A.; Scheffler, F.; Scheffler, M. Manufacturing of Reticulated Open-Cellular Aluminum Nitride Ceramic Foams from Aqueous AlN Suspensions. *Adv. Eng. Mater.* **2017**, *19*, 1–8, doi:10.1002/adem.201600660.
154. WEIBULL, W. A Statistical Distribution Function of Wide Applicability. *J. Appl. Mech.* **1951**, *13*, 293–297.
155. Тихонов Л.В., Кононенко В.А., Прокопенко Г.И. Структура и свойства металлов и сплавов. *Наукова Думка* **1986**, 567.
156. Decoste, J.B.; Peterson, G.W.; Schindler, B.J.; Killops, K.L.; Browe, M.A.; Mahle, J.J. The effect of water adsorption on the structure of the carboxylate containing metal-organic frameworks Cu-BTC, Mg-MOF-74, and UiO-66. *J. Mater. Chem. A* **2013**, *1*, 11922–11932, doi:10.1039/c3ta12497e.
157. Sutygina, A.; Betke, U.; Scheffler, M. Open-Cell Aluminum Foams by the Sponge Replication Technique: A Starting Powder Particle Study. *Adv. Eng. Mater.* **2020**, *1901194*, doi:10.1002/adem.201901194.
158. Sutygina, A.; Betke, U.; Scheffler, M. Open-cell aluminum foams by the sponge replication

- technique. *Materials (Basel)*. **2019**, *12*, doi:10.3390/ma122333840.
159. Sutygina, A.; Betke, U.; Scheffler, M. Manufacturing of Open-Cell Aluminium Foams : Comparing the Sponge Replication Technique and Its Combination with the Freezing Method. *Materials (Basel)*, **2022**, *15*, doi.org/10.3390/ma15062147.
160. Sutygina, A.; Betke, U.; Scheffler, .M. Effect of the cell count on geometrical, mechanical and thermal properties of hierarchical- porous reticulated copper foams from a combination of sponge replication and freeze-drying techniques (Accepted article). *Adv. Eng. Mater.* **2022**, doi.org/10.1002/adem.202200230.
161. S. W. Holman, R. R. Lawrence, L. Barr, Proc. Am. Acad. Arts Sci. **1895**, *31*, 218.
162. Trunov, M.A.; Umbrajkar, S.M.; Schoenitz, M.; Mang, J.T.; Dreizin, E.L. Oxidation and melting of aluminum nanopowders. *J. Phys. Chem. B* **2006**, *110*, 13094–13099, doi:10.1021/jp0614188.
163. Sercombe, T.B.; Schaffer, G.B. Rapid Manufacturing of. **2003**, *301*, 1225–1228.
164. Olakanmi, E.O.; Cochrane, R.F.; Dalgarno, K.W. A review on selective laser sintering/melting (SLS/SLM) of aluminium alloy powders: Processing, microstructure, and properties. *Prog. Mater. Sci.* **2015**, *74*, 401–477, doi:10.1016/j.pmatsci.2015.03.002.
165. Patnaik, P. Handbook of Inorganic Chemicals; McGraw-Hill: New York, NY, USA, 2002.
166. Körner, C.; Arnold, M.; Singer, R.F. Metal foam stabilization by oxide network particles. *Mater. Sci. Eng. A* **2005**, *396*, 28–40, doi:10.1016/j.msea.2005.01.001.
167. Harper, C.A. Handbook of Ceramics, Glasses and Diamond; McGraw-Hill: New York, NY, USA, 2001. No Title.
168. Liu, Z.Y.; Sercombe, T.B.; Schaffer, G.B. The effect of particle shape on the sintering of aluminum. *Metall. Mater. Trans. A Phys. Metall. Mater. Sci.* **2007**, *38*, 1351–1357, doi:10.1007/s11661-007-9153-2.
169. Touloukian, Y.S.; Powell, R.W.; Ho, C.Y.; Klemens, P.G. Thermophysical Properties of Matter—The TPRC Data Series; IFI/Plenum: New York, NY, USA,. **1973**, doi:10.1007/s11665-015-1541-y.
170. McNeil, L.E.; Grimsditch, M.; French, R.H. Vibrational Spectroscopy of Aluminum Nitride. *J. Am. Ceram. Soc.* **1993**, *76*, 1132–1136, doi:10.1111/j.1151-2916.1993.tb03730.x.
171. Slack, G.A.; Tanzilli, R.A.; Pohl, R.O.; Vandersande, J.W. The intrinsic thermal conductivity of AlN. *J. Phys. Chem. Solids* **1987**, *48*, 641–647, doi:10.1016/0022-3697(87)90153-3.
172. Smith, D.S.; Fayette, S.; Grandjean, S.; Martin, C.; Telle, R.; Tonnessen, T. Thermal resistance of grain boundaries in alumina ceramics and refractories. *J. Am. Ceram. Soc.* **2003**, *86*, 105–111, doi:10.1111/j.1151-2916.2003.tb03285.x.
173. Dong, H.; Wen, B.; Melnik, R. Relative importance of grain boundaries and size effects in thermal conductivity of nanocrystalline materials. *Sci. Rep.* **2014**, *4*, 7037, doi:10.1038/srep07037.

174. Bekoz, N.; Oktay, E. Mechanical properties of low alloy steel foams: Dependency on porosity and pore size. *Mater. Sci. Eng. A* **2013**, *576*, 82–90, doi:10.1016/j.msea.2013.04.009.
175. Yu, H.; Guo, Z.; Li, B.; Yao, G.; Luo, H.; Liu, Y. Research into the effect of cell diameter of aluminum foam on its compressive and energy absorption properties. **2007**, *455*, 542–546, doi:10.1016/j.msea.2006.11.091.
176. Inayat, A.; Freund, H.; Zeiser, T.; Schwieger, W. Determining the specific surface area of ceramic foams: The tetrakaidehedra model revisited. *Chem. Eng. Sci.* **2011**, *66*, 1179–1188, doi:10.1016/j.ces.2010.12.031.
177. Mao, H.; Shen, P.; Yang, G.; Zhao, L.; Qiu, X.; Wang, H.; Jiang, Q. 3D highly oriented metal foam: a competitive self-supporting anode for high-performance lithium-ion batteries. *J. Mater. Sci.* **2020**, 11–13, doi:10.1007/s10853-020-04702-7.
178. Zou, L.; Chen, F.; Wang, H.; Shen, Q.; Lavernia, E.J.; Zhang, L. Influence of Porosity on Mechanical Behavior of Porous Cu Fabricated via De-Alloying of Cu–Fe Alloy. *Met. Mater. Int.* **2019**, *25*, 83–93, doi:10.1007/s12540-018-0168-6.
179. Zou, L.; Chen, F.; Chen, X.; Lin, Y.; Shen, Q.; Lavernia, E.J.; Zhang, L. Fabrication and mechanical behavior of porous Cu via chemical de-alloying of Cu<sub>25</sub>Fe<sub>75</sub> alloys. *J. Alloys Compd.* **2016**, *689*, 6–14, doi:10.1016/j.jallcom.2016.07.258.
180. Kaya, A.C.; Fleck, C. Deformation behavior of open-cell stainless steel foams. *Mater. Sci. Eng. A* **2014**, *615*, 447–456, doi:10.1016/j.msea.2014.07.098.
181. Hakamada, M.; Asao, Y.; Kuromura, T.; Chen, Y.; Kusuda, H.; Mabuchi, M. Density dependence of the compressive properties of porous copper over a wide density range. *Acta Mater.* **2007**, *55*, 2291–2299, doi:10.1016/j.actamat.2006.11.024.
182. Günter Stephani, Olaf Andersen, Hartmut Göhler, Cris Kostmann, Kerstin Kümmel, Peter Quadbeck, Matthias Reinfried, Thomas Studnitzky, U.W. Iron Based Cellular Structures – Status and Prospects. *Adv. Eng. Mater.* **2006**, *8*, 847–852, doi:https://doi.org/10.1002/adem.200600078.
183. Yamada, Y.; Wen, C.; Shimojima, K.; Hosokawa, H.; Chino, Y.; Mabuchi, M. Compressive deformation characteristics of open-cell Mg alloys with controlled cell structure. *Mater. Trans.* **2002**, *43*, 1298–1305, doi:10.2320/matertrans.43.1298.
184. Munch, E.; Saiz, E.; Tomsia, A.P.; Deville, S. Architectural control of freeze-cast ceramics through additives and templating. *J. Am. Ceram. Soc.* **2009**, *92*, 1534–1539, doi:10.1111/j.1551-2916.2009.03087.x.
185. Yabuki, A.; Tanaka, S. Oxidation behavior of copper nanoparticles at low temperature. *Mater. Res. Bull.* **2011**, *46*, 2323–2327, doi:10.1016/j.materresbull.2011.08.043.
186. Mahmoud, M.M.; Link, G.; Thumm, M. The role of the native oxide shell on the microwave sintering of copper metal powder compacts. *J. Alloys Compd.* **2015**, *627*, 231–237, doi:10.1016/j.jallcom.2014.11.180.

- 
187. Felege, G.N.; Gurao, N.P.; Upadhyaya, A. Evolution of Microtexture and Microstructure During Sintering of Copper. *Metall. Mater. Trans. A Phys. Metall. Mater. Sci.* **2019**, *50*, 4193–4204, doi:10.1007/s11661-019-05317-7.
188. R.M. German *Powder Metallurgy and Particulate Materials Processing*; Princeton, 2005;
189. Hwang, Y.J.; Ahn, Y.C.; Shin, H.S.; Lee, C.G.; Kim, G.T.; Park, H.S.; Lee, J.K. Investigation on characteristics of thermal conductivity enhancement of nanofluids. *Curr. Appl. Phys.* **2006**, *6*, 1068–1071, doi:10.1016/j.cap.2005.07.021.
190. Timm, H.; Janek, J. On the Soret effect in binary nonstoichiometric oxides-kinetic demixing of cuprite in a temperature gradient. *Solid State Ionics* **2005**, *176*, 1131–1143, doi:10.1016/j.ssi.2005.01.010.
191. Venna, S.R.; Carreon, M.A. Synthesis of SAPO-34 crystals in the presence of crystal growth inhibitors. *J. Phys. Chem. B* **2008**, *112*, 16261–16265, doi:10.1021/jp809316s.

## A Appendix

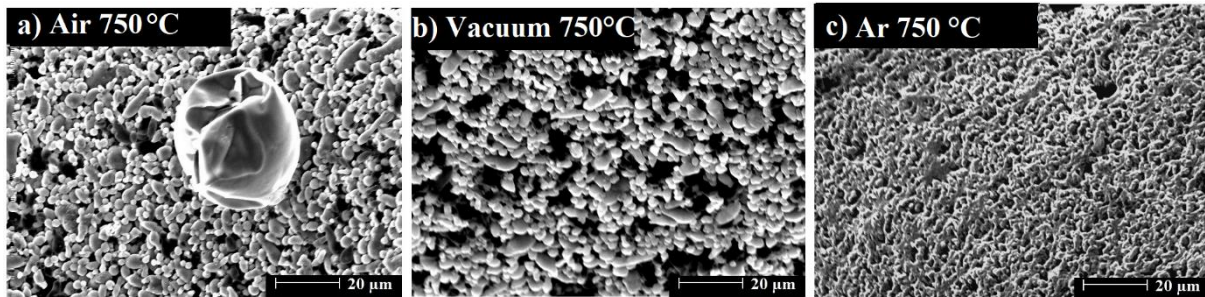


Figure A 1 SEM images of the strut surface of RP aluminum foams thermally processed for 3 h at 750 °C in air (a), vacuum (b), and Ar (c) (adapted from [158]).

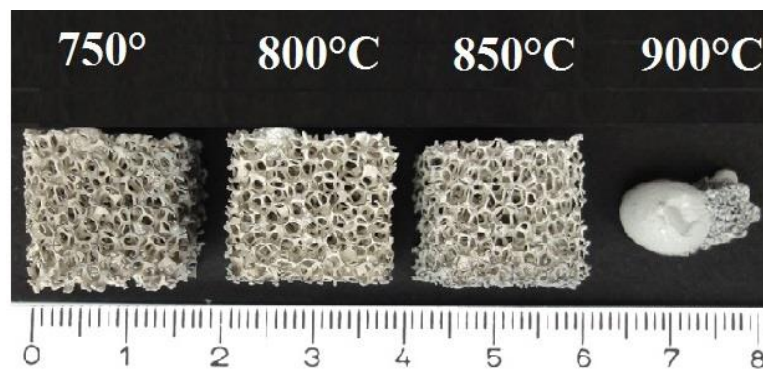


Figure A 2 Aluminum foams after thermal processing for 3 h in Ar at 750–900 °C [158].

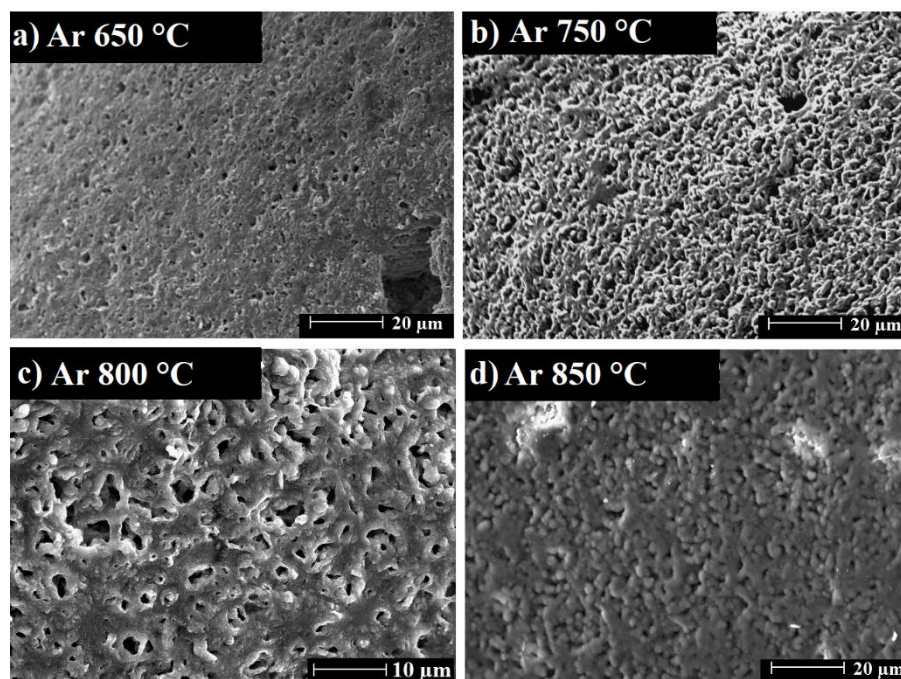


Figure A 3 SEM images of RP aluminum foams strut surface thermally processed for 3h in Ar at 650 °C (a), 750 °C (b), 800 °C (c), and 850 °C (d) (adapted from [158]).

Table A 1 Oxide concentration, volumetric shrinkage, porosity, compressive yield strength, and thermal conductivity of Al foams thermally processed for 3 h in Ar at 750–850 °C; PU template foams with a cell size of 20 ppi and a geometric size of 20 mm × 20 mm × 20 mm.

Sample	750 °C	800 °C	850 °C
Volumetric shrinkage ( $S_v$ ), %	49.7 ± 2.3	50.8 ± 2.9	54.3 ± 3.9
Total porosity ( $P_{total}$ ), %	90.7 ± 0.6	90.2 ± 0.6	90.9 ± 1.0
Cell porosity ( $P_{cell}$ ), %	86.9 ± 0.8	86.1 ± 1.0	86.2 ± 0.4
Strut porosity ( $P_s$ ), %	40.8 ± 2.1	35.6 ± 2.0	40.1 ± 5.8
Compressive yield strength, MPa	0.34 ± 0.08	0.304 ± 0.051	0.224 ± 0.030
Therm. Cond. of foam $\lambda_f$ , W·m <sup>-1</sup> K <sup>-1</sup>	2.32 ± 0.14	2.98 ± 0.17	-
Therm. Cond. of porous strut material $\lambda_s$ , W·m <sup>-1</sup> K <sup>-1</sup>	63.2	76.3	-
Therm. Cond. of bulk material $\lambda_b$ , W·m <sup>-1</sup> K <sup>-1</sup>	114.9	122.4	-

## Declaration of Honour

„I hereby declare that I produced this thesis without prohibited external assistance and that none other than the listed references and tools have been used. I did not make use of any commercial consultant concerning graduation. A third party did not receive any nonmonetary perquisites neither directly nor indirectly for activities, which are connected with the contents of the presented thesis.

All sources of information are clearly marked, including my own publications.

In particular I have not consciously:

- Fabricated data or rejected undesired results
- Misused statistical methods with the aim of drawing other conclusions than those warranted by the available data
- Plagiarized data or publications
- Presented the results of other researchers in a distorted way

I do know that violations of copyright may lead to injunction and damage claims of the author and also to prosecution by the law enforcement authorities. I hereby agree that the thesis may need to be reviewed with an electronic data processing for plagiarism.

This work has not yet been submitted as a doctoral thesis in the same or a similar form in Germany or in any other country. It has not yet been published as a whole.”



Magdeburg, 14.12.21

## Curriculum Vitae

### Personal Information

Name Alina Sutygina  
Date of birth 06.08.1993  
Place of birth Tomsk (Russia)  
Nationality Russia

### Professional Experience

Since 01.2018 **Research associate** at the Chair of Non-Metallic Materials and Compositions in the Faculty of Mechanical Engineering  
*Otto-von-Guericke University, Magdeburg*  
10.2016 – 07.2017 **Technician** at the Faculty of General Physics  
*Tomsk Polytechnic University, Russia*

### Education

01.2018 – 03.2022 **PhD** student at the Faculty of Mechanical Engineering;  
Title "Manufacturing and characterization of cellular metal foam"  
*Otto-von-Guericke University, Magdeburg*  
09.2015 – 06.2017 **Master**, Condensed Matter Physics (Degree with Honors); Title  
"Plasma immersion ion implantation of Ti into Zr-1Nb alloy and  
its influence on physical properties and sorption of hydrogen"  
*Tomsk Polytechnic University, Russia*  
09.2011 – 06.2015 **Bachelor**, Physics; Title "Influence of Ti plasma immersion ion  
implantation to zirconium alloy E-125 on hydrogen sorption rate  
and mechanical properties"  
*Tomsk Polytechnic University, Russia*  
10.2013 – 06.2015 **Translator** "Translation in the field of professional  
communication (English - Russian)"  
*Tomsk Polytechnic University, Russia*  
09.2000 – 05.2011 **Secondary school** (Degree with Honors), Russia

### Internship

03.2017 – 05.2017 **Scientific internship**  
*Vienna University of Technology, Austria*  
08.2016 **Scientific internship**  
*Brandenburg Technical University, Cottbus*  
10.2015 – 12.2015 **Scientific internship**  
*Liberec Technical University, Czech Republic*

### Awards and Achievements

01.2018 – 03.2022 **Promotion** of doctoral studies by the European Structural Fund (ESF) within the framework of the Research Training Group Medical engineering and engineering materials (*MEMoRIAL*)  
03.2017 – 05.2017 **Research scholarship** from Austria's Agency for Education and Internationalisation (*OeAD-GmbH*)  
10.2015 – 12.2015 **Research scholarship** of the *Russian Federation Ministry of Education* for study abroad

## List of publications

1. Sutygina, A.; Betke, U.; Scheffler, M. Effect of the cell count on geometrical, mechanical and thermal properties of hierarchical- porous reticulated copper foams from a combination of sponge replication and freeze-drying techniques (Accepted article). *Adv. Eng. Mater.* **2022**, doi.org/10.1002/adem.202200230.
2. Sutygina, A.; Betke, U.; Scheffler, M. Manufacturing of Open-Cell Aluminium Foams : Comparing the Sponge Replication Technique and Its Combination with the Freezing Method. *Materials (Basel)*, **2022**, *15*, doi.org/10.3390/ma15062147.
3. Sutygina, A.; Betke, U.; Scheffler, M. Hierarchical-Porous Copper Foams by a Combination of Sponge Replication and Freezing Techniques. *Adv. Eng. Mater.* **2021**, 2001516, doi:10.1002/adem.202001516.
4. Sutygina, A.; Betke, U.; Hasemann, G.; Scheffler, M. Manufacturing of open-cell metal foams by the sponge replication technique. *IOP Conf. Ser. Mater. Sci. Eng.* **2020**, *882*, doi:10.1088/1757-899X/882/1/012022.
5. Sutygina, A.; Betke, U.; Scheffler, M. Open-Cell Aluminum Foams by the Sponge Replication Technique: A Starting Powder Particle Study. *Adv. Eng. Mater.* **2020**, *22*, doi:10.1002/adem.201901194.
6. Sutygina, A.; Betke, U.; Scheffler, M. Open-cell aluminum foams by the sponge replication technique. *Materials (Basel)*. **2019**, *12*, doi:10.3390/ma122333840.